

---

---

# Measurement of the Rayleigh Scattering Length and Background contributions during early data taking phases at SNO+

Submitted in partial fulfillment  
of the requirements of the  
Degree of Doctor of Philosophy

by

Stefanie Langrock

School of Physics and Astronomy  
Queen Mary, University of London  
2016

*To Lisa and Christian Schäfer*

*“Neutrinos are fun because they do strange things”*

## **Statement of Originality**

I, Stefanie Langrock, confirm that the research included within this thesis is my own work or that where it has been carried out in collaboration with, or supported by others, that this is duly acknowledged below and my contribution indicated. Previously published material is also acknowledged below.

I attest that I have exercised reasonable care to ensure that the work is original, and does not to the best of my knowledge break any UK law, infringe any third party's copyright or other Intellectual Property Right, or contain any confidential material.

I accept that the College has the right to use plagiarism detection software to check the electronic version of this thesis.

I confirm that this thesis has not been previously submitted for the award of a degree by this or any other university.

The copyright of this thesis rests with the author and no quotation from it or information derived from it may be published without the prior written consent of the author.

Signature: St. Langrock

Date: 02/09/2016

Details of collaboration and publications:

Publication as part of the SNO+ collaboration (SNO+ author list) – S. Andringa et al. "Current Status and Future Prospects of the SNO+ Experiment", *Advances in High Energy Physics* , 2016:6194250

## Contributions of the Author

The scattering length analysis was carried out with the Scattering Module designed by the Oxford group. The author assisted during the initial installation of the system underground and the very first commissioning runs taken in 2013. Any further hardware development and commission runs were carried out by the Oxford group. The system was implemented into the RAT simulation package, used and developed by the SNO+ collaboration, by the author as described in Chapter 5 and Appendix A.1. A basic outline of the scattering length analysis existed prior to this work, but the cut development and systematic considerations as described in Chapter 6 were carried out by the author, including the implementation of the photon flags in RAT.

The target background rates in pure scintillator and water were provided by the SNO+ backgrounds group. The daily leaching rates for two years of scintillator data considering 9 months of water-fill were also provided. The leaching rates for the first 91 days were used to calculate the occurring leaching by the author as described in Chapter 8. Studies on using a coincidence tagging technique to reject Bismuth backgrounds in the region of interest for the Tellurium phase measurements were done prior to this work. Based on these studies, the tagging technique and necessary cuts were adjusted by the author to use for the background contribution measurements as presented in Chapter 7. The production files for the study in Chapter 7 were provided by the collaboration but all the tools to prepare the partial-fill production files used in Chapter 8 were developed by the author for a 91 day fill period with fill levels and background rates based on the calculations in Chapter 8. They are available for the entire collaboration to use.

Further work by the author which is not included in this document included Helium-leak checking of the scintillator purification plant at SNOLAB. Other on-site work comprised of general cavity preparation for water-fill. Additionally, the author was involved in monitoring the official simulation production, which included maintaining the software used to handle submission and grid processing as well as the monitoring of grid sites.

## Abstract

SNO+ is a multipurpose neutrino experiment located at SNOLAB. Its key purpose is investigating the neutrinoless double beta decay of  $^{130}\text{Te}$ , amongst other physics goals such as solar and reactor neutrino oscillations. The success of the experiment depends on the understanding of the optical properties of the detection materials, as well as a good understanding of potential background contributions.

The calibration system used to study the Rayleigh scattering properties of the detector is presented and methods to model the system in Monte Carlo simulations based on commissioning run data are introduced. Furthermore, the analysis of the scattering length in a water-filled detector is described and demonstrated on a fake water-fill data set with an accuracy of the measured scattering length scaling factor of 1.1 %. The evaluation of the systematic uncertainties is presented.

The background contributions originating from the  $^{238}\text{U}$  and  $^{232}\text{Th}$  decay chains during early SNO+ run phases are constrained using  $^{214}\text{Bi}^{214}\text{Po}$  and  $^{212}\text{Bi}^{212}\text{Po}$  delayed coincidences. The methods to identify these coincidences are presented and the challenges to apply them to an intermediate partial water-scintillator phase are discussed. It is shown that for the current target background rates the  $^{238}\text{U}$  and  $^{232}\text{Th}$  chain contents can be determined with an uncertainty of 4.1 % and 27.6 % respectively when combining a 3 months partial-fill with a 6 months scintillator run.

## Acknowledgments

First of all I would like to thank my supervisor Jeanne Wilson for guiding my research for four years and always finding the time for discussions when needed. Her advice on the issues I came across, both related to my thesis and outside of immediate work-related issues, was invaluable and without it completing this work would have been a lot more difficult. I have to extend my thanks also to the SNO+ Oxford group, commonly referred to as the SMELLIE people, especially Armin Reichold and Krishanu Majumdar for all their input to my scattering length analysis. My thanks also extends to Laura Segui, Chris Jones, Jack Dunger, Jeff Lidgard and Esther Turner for all their work and input on the SMELLIE system. I would also like to express my gratitude to all other members of SNO+ whose input contributed to my work, the list of which is too long to mention each one individually.

I also want to mention my colleagues and friends at Queen Mary past and present, for making my time in London enjoyable. Thank you to Evelina Arushanova and Ashley Robert Back and, most recently, Billy Liggins for extensive coffee breaks with productive or not-so productive discussions which sometimes could continue beyond the breaks. You guys are truly fabulous! My thanks also goes to Phil Jones for patiently helping with any problems I had and for letting us regularly invade his place to play Catan and drink his wine. Thank you also Dr. Matt Mottram for always being helpful with code and grid related issues and for being far too nice to enforce tasks when other things were more important.

There is also a few non-SNO+ people I would like to thank. Without the regular Ph.D. distractions provided by Lewis and Tamsin work would have been a lot more productive. I would also like to thank Andrew and his family for their support for the majority of the Ph.D. My thanks also goes to my German friends, Linda, Verena, Xenia, Nancy and Katja for always welcoming me with open arms when I'm back home.

My special thanks goes to Zack Barnard for keeping me (in)sane these last few months, all his support and belief in me and for supplying me with caffeine. And bacon. I would also like to thank Maxwell for insisting I play with him even though I kept telling him there is lots of work to be done and Lola for being the most patient lap cat I have ever come across. Additionally I would like to thank BW, LW, R and

S (you know who you are) for being the most silly bunch I ever encountered. A lot of thanks also to my parents, Cornelia and Andreas, for both their moral and financial support during these last few years.

# Contents

<b>1</b>	<b>Introduction</b>	<b>21</b>
<b>2</b>	<b>Neutrino Physics</b>	<b>23</b>
2.1	Discovery of the Standard Model Neutrinos . . . . .	23
2.2	Neutrino Oscillations . . . . .	25
2.2.1	Theoretical Framework . . . . .	25
2.2.2	Experimental status . . . . .	26
2.3	Mass Measurements . . . . .	30
2.4	Neutrinoless Double Beta Decay . . . . .	31
<b>3</b>	<b>The SNO+ Detector</b>	<b>35</b>
3.1	The Detector . . . . .	35
3.2	The Run Phases and Physics Goals . . . . .	36
3.3	The Electronics System . . . . .	39
3.3.1	Overview . . . . .	40
3.3.2	Timing . . . . .	41
3.4	The Calibration Setup . . . . .	42
3.5	Expected Backgrounds . . . . .	43
3.5.1	Internal Backgrounds . . . . .	43
3.5.2	AV Leaching Backgrounds . . . . .	46
3.5.3	External Backgrounds . . . . .	46
3.5.4	Cosmogenics . . . . .	47
3.5.5	$(\alpha, n)$ Backgrounds . . . . .	47
3.5.6	Instrumental Backgrounds . . . . .	48
3.6	RAT simulation software . . . . .	48
3.6.1	Event generation . . . . .	48

3.6.2	Event reconstruction . . . . .	49
3.7	Summary . . . . .	49
<b>4</b>	<b>The Scattering Module</b>	<b>51</b>
4.1	Rayleigh Scattering . . . . .	53
4.2	The hardware components . . . . .	54
4.2.1	Overview . . . . .	54
4.2.2	The Lasers . . . . .	55
4.2.3	The Fibres . . . . .	57
4.2.4	Hardware Update . . . . .	60
<b>5</b>	<b>Monte Carlo Modeling of the Scattering Module</b>	<b>61</b>
5.1	Note on Coordinate Systems . . . . .	61
5.2	Simulation Principles . . . . .	63
5.3	Tuning of the Simulations using Commissioning Data . . . . .	64
5.3.1	Fibre Directions . . . . .	64
5.3.2	Angular Profiles of Fibre Collimators . . . . .	71
5.3.3	Intensity Measurement . . . . .	77
5.4	Summary . . . . .	88
<b>6</b>	<b>Measurement of the Rayleigh Scattering Length during the Water Phase</b>	<b>90</b>
6.1	Note on Angular Profiles . . . . .	90
6.2	Measurement Principles . . . . .	91
6.2.1	Cut Selection . . . . .	92
6.2.2	Measurement Strategy . . . . .	99
6.2.3	Bias of the Measurement . . . . .	101
6.3	Measurement on a fake data set . . . . .	103
6.4	Systematic Uncertainties . . . . .	104
6.4.1	AV position and scattering . . . . .	105
6.4.2	Intensity . . . . .	106
6.4.3	Angular Profiles . . . . .	106
6.4.4	Fibre Direction . . . . .	109
6.4.5	Noise . . . . .	110
6.5	Summary and Discussion . . . . .	111

<b>7 Internal Background Estimation during the Pure Scintillator Phase</b>	<b>116</b>
7.1 Measurement of Uranium and Thorium chain Backgrounds in Pure Scintillator . . . . .	116
7.1.1 Cut Selection for $^{212}\text{Bi}^{212}\text{Po}$ and $^{214}\text{Bi}^{214}\text{Po}$ Measurements . . . . .	116
7.1.2 Misidentification of other Backgrounds . . . . .	127
7.1.3 Influence of Mistagged events on the Measurement Accuracy . . . . .	135
7.2 Alternative Measurement of the Thorium chain . . . . .	136
7.2.1 The $^{212}\text{Bi}^{208}\text{Tl}$ coincidence . . . . .	136
7.2.2 The triple $\alpha$ -coincidence $^{224}\text{Ra}^{220}\text{Rn}^{216}\text{Po}$ . . . . .	139
7.3 Testing the Bi-Po selection on the Te-loaded one Month Merged Data Set . . . . .	143
7.3.1 Adjusting the Cut Selection . . . . .	143
7.3.2 Applying the Cuts . . . . .	144
7.4 Summary . . . . .	149
<b>8 Evaluation of the Uranium and Thorium chain Backgrounds in Partial-Fill</b>	<b>152</b>
8.1 Calculating the Background Rates in a Partial-filled Detector . . . . .	153
8.1.1 Internal Backgrounds in the Scintillator Volume . . . . .	153
8.1.2 Leaching Backgrounds in the Scintillator Volume . . . . .	153
8.1.3 Backgrounds in the Water Volume . . . . .	155
8.2 Cut Selection on Scintillator Volume Events . . . . .	155
8.2.1 Fiducial Volume Cut . . . . .	157
8.2.2 Cut on the Number of Hits . . . . .	160
8.2.3 Other Cuts . . . . .	162
8.3 Effect of the Cut Selection on Water Volume events . . . . .	166
8.4 Mistagging of Scintillator Volume Events with Water Volume Events	167
8.5 Measurement Uncertainty . . . . .	168
8.6 Summary . . . . .	170
<b>9 Conclusion</b>	<b>172</b>
<b>A Appendix - Scattering Module</b>	<b>174</b>
A.1 Initial definition of the Simulation Parameters . . . . .	174

A.1.1	Extracting the Wavelength and Timing distributions . . . . .	174
A.1.2	Calculating Fibre Directions and Positions . . . . .	174
A.1.3	Implementing the Angular Profiles . . . . .	179
A.2	Commissioning run information . . . . .	183
A.3	Direction Measurement . . . . .	184
A.4	Uncertainties on the Fibre Direction Measurements . . . . .	184
A.5	Uncertainty on the Angle between Fibres . . . . .	186
A.6	Angular Profile Measurement . . . . .	187
A.6.1	Binning of the Angular Profiles . . . . .	187
A.7	Intensity Measurement . . . . .	190
<b>B</b>	<b>Appendix - Rayleigh Scattering Length Measurement</b>	<b>195</b>
B.1	Calculating Crossing Points with the AV and PSUP . . . . .	195
B.2	Evaluating the uncertainties on $c_{\text{scatt}}$ and $c_{\text{in-beam}}$ . . . . .	198
<b>C</b>	<b>Appendix - Background Evaluation</b>	<b>203</b>
C.1	Pure Scintillator Phase . . . . .	203
C.2	Statistical Uncertainties on $^{21x}\text{Bi}^{21x}\text{Po}$ coincidence Measurements . .	208
C.3	Statistical Uncertainties on Mistagged events . . . . .	209
C.4	Tellurium Loaded Phase . . . . .	210
<b>D</b>	<b>Appendix - Partial-fill Background Estimation</b>	<b>212</b>

# List of Figures

2.1	The solar pp chain and the CNO cycle. . . . .	27
2.2	Feynman diagram for neutrinoless double beta decay. . . . .	33
2.3	The effective Majorana neutrino mass $\langle m_{\beta\beta} \rangle$ versus the mass of the lightest neutrino for the inverted and the normal hierarchy. . . . .	34
3.1	Picture of the SNO+ detector. . . . .	37
3.2	Physics energy spectra for the SNO+ water phase. . . . .	38
3.3	Physics energy spectra for the SNO+ pure scintillator phase. . . . .	39
3.4	Physics energy spectra for the SNO+ Tellurium loaded phase. . . . .	40
3.5	Uranium and Thorium decay chains. . . . .	44
4.1	Invisible Proton decay for different reconstruction variables. . . . .	53
4.2	Schematics of the SMELLIE hardware components. . . . .	56
4.3	The four SMELLIE single-wavelength laser heads. . . . .	57
4.4	The SMELLIE mounting plate. . . . .	59
5.1	Definition of the beam angle $\alpha$ . . . . .	62
5.2	The $\Theta$ distributions for all six installed fibres at 495 nm for data and the simulations. . . . .	65
5.3	The $\Phi$ distributions for all six installed fibres at 495 nm for data and the simulations. . . . .	66
5.4	Possible positions of the mounting plate on top of the PMT hex cell.	69
5.5	The $\Theta$ distributions for all six installed fibres at 495 nm for data and the simulations with corrected directions for the simulation. . . . .	72
5.6	The $\Phi$ distributions for all six installed fibres at 495 nm for data and the simulations with corrected directions for the simulation. . . . .	73

5.7	Angular profiles extracted for FS237 at 446 nm at different laser intensities . . . . .	75
5.8	Angular profiles for FS037, FS237 and FS155. . . . .	76
5.9	The $\Theta$ and $\Phi$ distributions for FS037, FS237 and FS155 at 495 nm for data and the simulations with new angular profiles applied to the simulation. . . . .	78
5.10	Mean number of hits versus number of photons simulated per beam pulse for FS237 at 446 nm. . . . .	80
5.11	Refractive index in air and water over the wavelength range covered by the SMELLIE lasers. . . . .	85
5.12	Comparison between the angular profiles in air and the estimated profiles in water for FS037, FS237 and FS155. . . . .	86
5.13	Mean number of hits versus number of photons simulated per beam pulse for FS237 at 446 nm in a water-filled detector for different scattering lengths. . . . .	87
6.1	Average angular profile of SMELLIE fibres in a water-filled detector. . . . .	91
6.2	Optical interactions a photon can undergo in the detector. . . . .	91
6.3	Distances between crossing points. . . . .	93
6.4	Cut selection for the node 07 fibres at 407 nm. . . . .	95
6.5	Control samples for FS025 at 375 nm. . . . .	97
6.6	Scaling factor fits for FS155 at 446 nm. . . . .	100
6.7	Measurement bias for the scaling factor measurement. . . . .	102
6.8	Fits on the generic angular profile. . . . .	107
6.9	Angular profiles of FS155 extracted from different runs converted to water profile. . . . .	108
6.10	Altered generic angular profiles for systematic uncertainty consideration.	109
6.11	Uncertainty combinations on a vector. . . . .	110
6.12	Relative contributions of the systematic uncertainties on the scaling factor measurement. . . . .	113
6.13	Invisible proton decay for different reconstruction variables with the measured scaling factor applied to the data. . . . .	114
7.1	Cut flow scheme for Bi-Po coincidence measurements. . . . .	117

7.2	The $n_{\text{hits}}$ spectra of the four high rate backgrounds and the individual Bi-Po coincidence isotopes. . . . .	118
7.3	Development of the cut efficiencies for the $^{212}\text{Po}$ $n_{\text{hits}}$ cut. . . . .	119
7.4	Development of the cut efficiencies for the $^{214}\text{Po}$ $n_{\text{hits}}$ cut. . . . .	120
7.5	The reconstructed positions of the $^{212}\text{Bi}$ and $^{214}\text{Bi}$ candidates within the AV volume. . . . .	122
7.6	SNO+ position reconstruction resolution demonstrated on $^{130}\text{Te}$ $0\nu\beta\beta$ decays. . . . .	123
7.7	Reconstructed inter-event distance $\Delta r$ between the Bismuth and Polonium candidates for the $^{212}\text{Bi}^{212}\text{Po}$ and $^{214}\text{Bi}^{214}\text{Po}$ coincidences. . . . .	124
7.8	Development of the uncertainties on the $^{212}\text{Bi}^{212}\text{Po}$ and $^{214}\text{Bi}^{214}\text{Po}$ measurements for different leaching and Bi-Po coincidence rates over 181 days.	
7.9	Development of the cut efficiencies for the $^{212}\text{Po}$ $n_{\text{hits}}$ cut for Tellurium loaded scintillator. . . . .	144
7.10	Development of the cut efficiencies for the $^{214}\text{Po}$ $n_{\text{hits}}$ cut for Tellurium loaded scintillator. . . . .	145
7.11	Reconstructed inter-event distance $\Delta r$ between the Bismuth and Polonium candidates for the $^{212}\text{Bi}^{212}\text{Po}$ and $^{214}\text{Bi}^{214}\text{Po}$ coincidences in Tellurium loaded scintillator. . . . .	146
8.1	Schematic of a partial-filled detector. . . . .	154
8.2	Progression of the reconstructed z-coordinate over time of $^{210}\text{Bi}$ scintillator volume events and true z coordinate vs reconstruction accuracy of $^{210}\text{Po}$ scintillator volume events. . . . .	158
8.3	The $z - z_k$ and $n_{\text{hits}}$ distributions for $^{212}\text{Bi}$ water volume events. . . . .	159
8.4	True radial position vs reconstruction accuracy for $^{210}\text{Po}$ scintillator volume events and reconstructed radial distribution of external background events. . . . .	160
8.5	Efficiency progression of the fiducial volume cut. . . . .	161
8.6	The $n_{\text{hits}}$ for different days of filling and the efficiency of the $n_{\text{hits}}^{\text{Po}^{214}}$ cut for all fill levels for $^{210}\text{Bi}$ scintillator volume events. . . . .	161

8.7	Development of cut efficiencies vs fill levels for $^{212}\text{Bi}^{212}\text{Po}$ and $^{214}\text{Bi}^{214}\text{Po}$ coincidences. . . . .	163
8.8	Efficiency of $\Delta r$ cut vs fill level and schematic of the cut volume for $\Delta r$ in a partial-filled detector. . . . .	165
8.9	Development of the uncertainties on the $^{212}\text{Bi}^{212}\text{Po}$ and $^{214}\text{Bi}^{214}\text{Po}$ measurements for different leaching and Bi-Po coincidence rates over 181 days of pure scintillator-fill, including partial-fill analysis. . . . .	170
A.1	Wavelength distributions for the four SMELLIE lasers. . . . .	175
A.2	Intra-pulse timing distributions for the four SMELLIE lasers. . . . .	176
A.3	Geometric considerations used to calculate the fibre positions. . . . .	177
A.4	Dimensions of the SMELLIE mounting plates. . . . .	178
A.5	Example of angular profile measurements carried out by the University of Oxford. . . . .	180
A.6	Angular distribution measurements. . . . .	181
A.7	Measured angular profiles for FS037 covering 10, 7 and 5 PMTs per angular bin. . . . .	188
A.8	Measured angular profiles for FS237 covering 10, 7 and 5 PMTs per angular bin. . . . .	189
A.9	Measured angular profiles for FS155 covering 10, 7 and 5 PMTs per angular bin. . . . .	190
A.10	Oxford angular profiles for FS137, FS255 and FS055. . . . .	191
B.1	Cut selection for the node 25 fibres at 407 nm. . . . .	196
B.2	Cut selection for the node 37 fibres at 407 nm. . . . .	197
B.3	Cut selection for the node 55 fibres at 407 nm. . . . .	198

# List of Tables

2.1	Recent results for the neutrino oscillation parameters. . . . .	30
4.1	Summary of fibre labels. . . . .	60
5.1	Initial fit results from the $\Theta$ and $\Phi$ fits for data and simulation. . . . .	67
5.2	Angles between the center fibre and the two angled fibres for nodes 37 and 55. . . . .	68
5.3	Angles between each fibre direction and the vector $\vec{m}$ pointing from the center of the PMT to the hex cell face. . . . .	70
5.4	Maximum expected occupancy values $P_i^{\max}$ in an air-filled detector for a range of intensities. . . . .	81
5.5	Standard deviation $\sigma$ , the bias $b$ and the uncertainty $u$ on the measured number of photons for the fake data sets for FS037, FS237 and FS155 in air-fill. . . . .	82
5.6	Measured number of photons per beam pulse for March 2014 air-fill data for fibres FS037, FS237 and FS155. . . . .	83
5.7	Maximum expected occupancy values $P_i^{\max}$ in a water-filled detector for 1 000 nppb. . . . .	87
5.8	Standard deviation $\sigma$ , bias $b$ and uncertainty $u$ on the measured number of photons for the low intensity fake data set for FS037, FS237 and FS155 in water-fill. . . . .	88
6.1	SMELLIE cut selection. . . . .	96
6.2	SMELLIE cut values. . . . .	98
6.3	Content of scattered and noise events in several cut regions for different wavelengths. . . . .	99
6.4	Average measured intensities for the fake data set. . . . .	103

6.5	Measured scattering length of the fake data set. . . . .	104
6.6	Fit parameters from the fit on the generic angular profile. . . . .	107
6.7	Signs of the direction systematics. . . . .	111
6.8	Measured scattering length of the fake data set including the systematic uncertainties on the measurement. . . . .	113
7.1	Cuts and cut efficiencies for each cut parameter for the $^{212}\text{Bi}^{212}\text{Po}$ and $^{214}\text{Bi}^{214}\text{Po}$ coincidence selection. . . . .	125
7.2	Expected event yields and measurement uncertainties for the Uranium and Thorium chain measurements for a run period of 181 days. . . . .	126
7.3	Expected Uranium and Thorium chain concentrations in the pure scintillator phase. . . . .	126
7.4	Events selected in 181 days by the $^{212}\text{Po}$ and $^{214}\text{Po}$ cuts including all non-leaching backgrounds and the solar signals. . . . .	129
7.5	Events selected in 181 days by the $^{212}\text{Po}$ and $^{214}\text{Po}$ cuts for all leaching backgrounds. . . . .	130
7.6	Events selected in 181 days by the $^{212}\text{Bi}$ and $^{214}\text{Bi}$ cuts including all non-leaching backgrounds and the solar signals. . . . .	131
7.7	Events selected in 181 days by the $^{212}\text{Bi}$ and $^{214}\text{Bi}$ cuts for all leaching backgrounds. . . . .	132
7.8	Mistagging probabilities of the Bismuth candidate and number of true and misidentified Polonium candidates expected in 181 days for the $^{212}\text{Bi}^{212}\text{Po}$ coincidence measurement. . . . .	133
7.9	Mistagging probabilities of the Bismuth candidate and number of true and misidentified Polonium candidates expected in 181 days for the $^{214}\text{Bi}^{214}\text{Po}$ coincidence measurement. . . . .	134
7.10	Estimated event contributions from mistagging for the $^{212}\text{Bi}^{212}\text{Po}$ selection in 181 days. . . . .	134
7.11	Estimated event contributions from mistagging for the $^{214}\text{Bi}^{214}\text{Po}$ selection in 181 days. . . . .	135
7.12	Cuts and cut efficiencies for each cut parameter for the $^{212}\text{Bi}^{208}\text{Tl}$ coincidence selection. . . . .	138

7.13	Estimated event contributions from mistagging for the $^{212}\text{Bi}^{208}\text{Tl}$ selection in 181 days. . . . .	139
7.14	Cuts and cut efficiencies for each cut parameter for the $^{214}\text{Ra}^{220}\text{Rn}^{216}\text{Po}$ triple $\alpha$ -coincidence selection. . . . .	140
7.15	Mistagging probabilities of the Radon and Polonium candidates and number of true and misidentified Radium candidates expected in 181 days for the $^{224}\text{Ra}^{220}\text{Rn}^{216}\text{Po}$ coincidence measurement. . . . .	141
7.16	Estimated event contributions from mistagging for the $^{224}\text{Ra}^{220}\text{Rn}^{216}\text{Po}$ selection in 181 days. . . . .	142
7.17	Cuts and cut efficiencies for each cut parameter for the $^{212}\text{Bi}^{212}\text{Po}$ and $^{214}\text{Bi}^{214}\text{Po}$ coincidence selection for Tellurium loaded scintillator. . . . .	147
7.18	Estimated mistagged events for the Bi-Po coincidences in the Tellurium phase for 1 month. . . . .	147
7.19	Resulting event yield after applying the $^{212}\text{Bi}^{212}\text{Po}$ cut selection to the Mixed data set. . . . .	148
7.20	Resulting event yield after applying the $^{214}\text{Bi}^{214}\text{Po}$ cut selection to the Mixed data set. . . . .	149
7.21	Purities and measurement uncertainties for the Bi-Po coincidence selection in the Tellurium loaded phase. . . . .	150
8.1	Expected event contributions for all internal and leaching backgrounds in the 91 day partial-fill period. . . . .	156
8.2	Cut efficiencies for each cut parameter for the $^{212}\text{Bi}^{212}\text{Po}$ and $^{214}\text{Bi}^{214}\text{Po}$ coincidence selection in partial-fill. . . . .	164
8.3	Estimated event contributions from mistagging in the scintillator volume during the 91 day partial-fill phase. . . . .	166
8.4	Estimated event contributions from mistagging in the water volume during the 91 day partial-fill phase. . . . .	167
8.5	Estimated event contributions from mistagging of scintillator volume events with water volume events during the 91 day partial-fill phase. .	168
8.6	Event yields and measurement uncertainty for the 91 day partial-fill phase. . . . .	169

A.1	Opening angles of the fibre collimators as measured at the University of Oxford. . . . .	182
A.2	Summary of the SMELLIE runs used for this study. . . . .	183
A.3	Calculated directions from this study and the RAT database for all six installed fibres. . . . .	184
A.4	Fit parameter results for the intensity measurement. . . . .	190
A.5	Fit parameter results for the intensity measurement, upper limit. . . . .	192
A.6	Fit parameter results for the intensity measurement, lower limit. . . . .	192
A.7	Mean number of hits for the March 2014 air-fill data. . . . .	193
A.8	Scattering length in air and water for selected wavelengths. . . . .	193
A.9	Measured number of photons per beam pulse for the March 2014 commissioning data. . . . .	194
B.1	Measured intensity values in nppb from the fake data. . . . .	199
B.2	Scaling factors, scattering region. . . . .	200
B.3	Scaling factors, in-beam region. . . . .	201
B.4	Directions of the node 07 and 25 fibres. . . . .	202
C.1	Internal backgrounds for the pure scintillator phase. . . . .	203
C.2	Pure scintillator Monte Carlo production files. . . . .	204
C.3	Bi-Po coincidence cut selection on RAT 4.5.0 Monte Carlo production files. . . . .	205
C.4	Measurement uncertainty on the $^{212}\text{Bi}^{212}\text{Po}$ and $^{214}\text{Bi}^{214}\text{Po}$ coincidences over time. . . . .	205
C.5	Polonium cut efficiencies $\epsilon^i(n_{\text{hits}})$ for the Bi-Po coincidence measurements. . . . .	206
C.6	Bismuth cut efficiencies $\epsilon^i(n_{\text{hits}})$ for the Bi-Po coincidence measurements. . . . .	207
C.7	Number of mistagged events $N_{\text{mis}}^{\text{coinc}}$ for the $^{212}\text{Bi}^{212}\text{Po}$ and $^{214}\text{Bi}^{214}\text{Po}$ coincidence measurements at different rate scenarios for 181 days. . . . .	208
C.8	Tellurium loaded scintillator Monte Carlo production files. . . . .	210
C.9	Bi-Po coincidence cut selection on RAT 5.0.2 Monte Carlo production files. . . . .	210
C.10	Polonium cut efficiencies $\epsilon^i(n_{\text{hits}})$ for the Bi-Po coincidence measurements in the Tellurium loaded phase. . . . .	211

C.11 Bismuth cut efficiencies $\epsilon^i(n_{\text{hits}})$ for the Bi-Po coincidence measurements in the Tellurium loaded phase. . . . .	211
D.1 Volume and Area covered by the scintillator volume per day during the partial-fill period. . . . .	212
D.2 Fill levels $z_k$ used for the RAT 5.3.1 partial-fill production. . . . .	213
D.3 Internal backgrounds for the pure water phase. . . . .	214
D.4 Partial-fill Monte Carlo production files, scintillator volume. . . . .	215
D.5 Partial-fill Monte Carlo production files, water volume. . . . .	216
D.6 Bi-Po coincidence cut selection on RAT 5.3.1 Monte Carlo production files, scintillator volume. . . . .	217
D.7 Bi-Po coincidence cut selection on RAT 5.3.1 Monte Carlo production files, water volume. . . . .	217
D.8 Polonium cut efficiencies $\epsilon^i(n_{\text{hits}})$ for the Bi-Po coincidence measurements for events occurring in the partial-fill scintillator volume. . . .	218
D.9 Bismuth cut efficiencies $\epsilon^i(n_{\text{hits}})$ for the Bi-Po coincidence measurements for events occurring in the partial-fill scintillator volume. . . .	219
D.10 Fiducial volume cut efficiencies $\epsilon^i(r_{\text{fidvol}})$ for partial-fill water volume events. . . . .	220
D.11 Polonium cut efficiencies $\epsilon^i(n_{\text{hits}})$ for the Bi-Po coincidence measurements for events occurring in the partial-fill water volume. . . . .	221
D.12 Bismuth cut efficiencies $\epsilon^i(n_{\text{hits}})$ for the Bi-Po coincidence measurements for events occurring in the partial-fill water volume. . . . .	222

# 1 Introduction

Ever since the discovery of the neutrino in the last century, a lot of progress has been made in neutrino physics. Multiple experiments have contributed to understanding the nature of the neutrino, proving flavour oscillations in vacuum and matter and continuously improving technology to probe the neutrino masses and the mass nature of the neutrino. Precision measurements of the oscillation parameters and the CP violating phase will help to solve the hierarchy nature of the neutrino masses and double beta decay experiments will help shed light on the nature of the mass giving mechanism for neutrinos.

SNO+ is one of the many experiments designed to expand our existing understanding of the neutrino. It is built to contribute to both the neutrinoless double beta decay and oscillation measurements. These tasks involve high precision measurements in the low energy range. Thus, the detector response must be well understood. This includes understanding both the optical response of all detector materials and the backgrounds to the physics measurements both internal and external to the detector. Understanding both aspects well will improve the energy resolution of the detector and the sensitivity to neutrino results.

This thesis presents work carried out to understand the detector materials at early run phases. To give context to the analysis presented in this document, a brief summary of the important aspects of modern neutrino physics are given and the SNO+ detector and its physics goals are introduced. This is followed by a Chapter discussing the importance of understanding the scattering properties of the detector material and introducing the Scattering Module designed for SNO+ for in-situ measurements of the scattering properties of the detector material. The strategy to measure the scattering properties of the first SNO+ run phase is presented, using air-fill data to describe the simulation of the Scattering Module and then carrying out the scattering length measurement for a water-fill fake data set. Following this, a method is introduced to

measure the backgrounds internal to the scintillator cocktail in both the pure scintillator phase and the partial scintillator-water-fill phase. The method is verified using a one month merged data set for the Tellurium phase and the adjustments necessary for the partial-fill phase are discussed.

# 2 Neutrino Physics

Wolfgang Pauli first proposed the existence of an undetectable particle of neutral charge in 1930 to explain the energy and momentum conservation in  $\beta$ -decays [1]. Initially called neutron by Pauli, it was re-named to neutrino by Fermi [2] after a newly discovered heavier particle found in the nucleus was referred to as neutron by Chadwick [3]. In the Standard Model of particle physics neutrinos are weakly interacting leptons. The number of known light neutrino flavours (neutrinos with  $m_\nu < \frac{m_Z}{2}$ ) was measured from the decay-width of the Z-boson at LEP and determined to be  $N_\nu = 3$  [4].

In the Standard Model, only particles in a left-handed chiral state and anti-particles in a right-handed chiral state interact with the weak force. Investigating electron captures of  $^{152}\text{Eu}$  it was found that neutrinos were always produced with negative helicity, i.e. their spin and momentum vectors always have opposite direction [5]. This implied the massless nature of the Standard Model neutrino, since helicity and chirality are only the same for massless particles. However, the existence of neutrino oscillations indicates that neutrinos are not massless and that neutrinos can be used as a tool to probe physics beyond the Standard Model. In this Chapter, a summary of the discovery of all three known light neutrinos is given, followed by an introduction to neutrino oscillations and mass measurements. The Chapter concludes with a Section on neutrinoless double beta decay.

## 2.1 Discovery of the Standard Model Neutrinos

The first direct detection of Pauli's neutrino was seen by the Cowan-Reines experiment in 1953, which detected anti-neutrinos from fission processes at the Hanford detector

[6]. The anti-neutrinos were detected via inverse  $\beta$ -decay

$$\bar{\nu} + p \rightarrow n + \beta^+ \quad (2.1)$$

and the resulting delayed coincidences from the decay-products in a Cadmium loaded liquid scintillator. The results were confirmed in 1956 [7].

The muon was discovered in 1936. Observations of charged pions<sup>1</sup>  $\pi^\pm$  decaying into muons and other neutral particles [8] gave rise to the question of the nature of this neutral particle (i.e. is it identical to the neutrino observed in  $\beta$ -decays). This question was answered by the discovery of the muon neutrino  $\nu_\mu$  at Brookhaven [9]. A neutrino beam was created from pion decays

$$\pi^\pm \rightarrow \mu^\pm + (\nu/\bar{\nu}) \quad (2.2)$$

and a spark chamber was used to look for  $e^\pm$  and  $\mu^\pm$  from the following interactions:

$$\begin{aligned} \nu + n &\rightarrow p + e^- \\ \bar{\nu} + p &\rightarrow n + e^+ \\ \nu + n &\rightarrow p + \mu^- \\ \bar{\nu} + n &\rightarrow p + \mu^+ \end{aligned} \quad (2.3)$$

Since almost no  $e^\pm$  were detected, it was concluded that the neutrino created alongside the muon was different to the already known electron neutrino  $\nu_e$ .

The third light neutrino, the tau neutrino  $\nu_\tau$ , was implied after the discovery of the tau lepton in the 1970s [10]. The discovery of the tau neutrino was announced by the DONUT collaboration in 2001 [11]. A tau neutrino beam was produced from  $D_s$  meson decays. The neutrinos interacted via charged current interactions with emulsion scintillation targets

$$X + \nu_\tau \rightarrow Y + \tau^- \quad (2.4)$$

creating tau leptons which were subsequently detected.

---

<sup>1</sup>which were discovered in 1947

## 2.2 Neutrino Oscillations

### 2.2.1 Theoretical Framework

Equivalent to the superposition of flavour and mass eigenstates in the down-type quark sector, as e.g. in neutral kaon mixing, a similar oscillation process was suggested for neutrinos [12]. Neutrino oscillations are a result of the misalignment of the weak flavour eigenstates ( $\nu_\alpha = \nu_e, \nu_\mu, \nu_\tau$ ) and the mass eigenstates of the neutrinos ( $\nu_i = \nu_1, \nu_2, \nu_3$ ). The theoretical framework was first proposed for two neutrino flavours [13] and was later expanded to three neutrino flavours. The relation between the two states is described by the Pontecorvo-Maki-Nakagawa-Sakata (PMNS) matrix [14]:

$$|\nu_\alpha\rangle = \sum_i U_{\alpha i} |\nu_i\rangle \quad (2.5)$$

with the matrix components  $U_{\alpha i}$

$$U_{\text{PMNS}} = \begin{pmatrix} 1 & 0 & 0 \\ 0 & c_{23} & s_{23} \\ 0 & -s_{23} & c_{23} \end{pmatrix} \begin{pmatrix} c_{13} & 0 & s_{13}e^{-i\delta_{\text{CP}}} \\ 0 & 1 & 0 \\ -s_{13}e^{i\delta_{\text{CP}}} & 0 & c_{13} \end{pmatrix} \begin{pmatrix} c_{12} & s_{12} & 0 \\ -s_{12} & c_{12} & 0 \\ 0 & 0 & 1 \end{pmatrix} \quad (2.6)$$

where  $c_{ij} = \cos \theta_{ij}$  and  $s_{ij} = \sin \theta_{ij}$ . The CP-violating phase is represented by  $\delta_{\text{CP}}$ . When a neutrino propagates through vacuum, its probability of being detected in any of the flavour eigenstates depends on the mixing angles  $\theta_{ij}$  as well as the energy  $E$  of the neutrino, its travelling distance  $L$  and the difference of the square masses of the mass eigenstates  $\Delta m_{ij}^2 = m_i^2 - m_j^2$  [15]:

$$\begin{aligned} P(\nu_\alpha \rightarrow \nu_\beta) = & \sum_i [U_{\alpha i} U_{\beta i}^*] - 4 \sum_{i>j=1}^3 \left[ \text{Re} (U_{\alpha i} U_{\beta i}^* U_{\alpha j}^* U_{\beta j}) \sin^2 \left( \frac{\Delta m_{ij}^2 L}{4E} \right) \right] \\ & + 2 \sum_{i>j=1}^3 \left[ \text{Im} (U_{\alpha i} U_{\beta i}^* U_{\alpha j}^* U_{\beta j}) \sin \left( \frac{\Delta m_{ij}^2 L}{2E} \right) \right] \end{aligned} \quad (2.7)$$

Matter oscillations are different from vacuum oscillations, due to the interactions of the neutrinos with the material they travel through. If neutrinos are produced in

or travel through matter (as neutrinos produced in the core of the sun) they gain an additional effective mass due to their interactions with matter. This effect is stronger for  $\nu_e$  than for  $\nu_\mu$  and  $\nu_\tau$  since matter contains electrons but no muons or taus. When travelling to the surface of the Sun, the solar neutrino experiences an adiabatic change in electron density of the surrounding matter. Entering the vacuum-like surface of the Sun, its mass eigenstate corresponds now to a different combination of flavour eigenstates. Hence, the survival probability  $P(\nu_e \rightarrow \nu_e)$  of the electron neutrino is lower for matter oscillations in the Sun than for pure vacuum oscillations [16]. This effect was first suggested by Mikheev, Smirnov [17] and Wolfenstein [18] and is called the MSW effect.

### 2.2.2 Experimental status

Neutrinos from different sources can provide a signal for oscillation measurements on Earth. In this Section, the most important sources are described, including key results from oscillation measurements, and the latest results of the oscillation parameters are presented.

#### Solar Neutrinos

One of the largest source of the neutrinos detected on Earth is the Sun, where neutrinos are produced in different fusion processes occurring in the core of the Sun. In the Standard Solar Model (SSM), there are two main fusion chains providing a variety of neutrino sources, each of which emitting neutrinos at different energies: the pp chain and the CNO cycle, which are both shown in Figure 2.1. The neutrinos detected on Earth are named after the fusion process they originate from [19].

Neutrinos from the pep reaction are mono-energetic, with  $E_\nu = 1.442\text{ MeV}$  and have a very well predicted flux. Measuring the survival probability of the neutrinos in this energy range will increase the accuracy of active oscillation parameters and enhance the sensitivity to alternative neutrino mixing models. At this energy, neutrinos from pep reactions are positioned in the transition region of oscillations, where matter dominated oscillation ( $E_\nu > 4\text{ MeV}$ ) shifts to vacuum dominated ( $E_\nu < 1\text{ MeV}$ ) oscillation. Evaluating the survival probability in this region is an essential test for new physics [21].

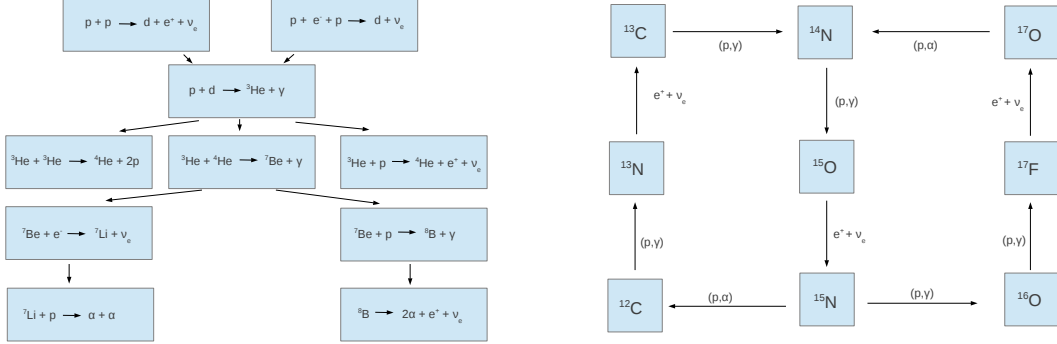


**Figure 2.1:** The solar pp chain (left) and the CNO cycle (right), adapted from [20]

CNO cycle neutrinos provide an excellent measure of the solar metallicity. In recent years, improved solar models have predicted a decreased metallicity of the Sun in comparison to the successful old model. This effect leads to a disagreement between solar model predictions and helioseismology. Neutrinos from the CNO cycle can be used to resolve the metallicity of the Sun's core [22]. Therefore, by measuring pp chain and CNO cycle neutrinos, SNO+ can contribute to the understanding of the nature of neutrino oscillations and the solar model.

Solar neutrinos were first detected in 1968 by the Homestake experiment. The solar  $\nu_e$  were captured on the  ${}^{37}\text{Cl}$  making up the detector material, which had an energy threshold of 0.814 MeV and thus was mainly detecting  ${}^7\text{Be}$  and  ${}^8\text{B}$  neutrinos. It was found that the number of detected  $\nu_e$  neutrinos was about a third of the number predicted by the SSM [23].

The water Cherenkov detectors Kamiokande and Super-Kamiokande measured  ${}^8\text{B}$  with an energy threshold of 7.5 MeV and 5 MeV respectively. Neutrino detection occurred via elastic scattering, therefore the experiment was sensitive to all neutrino types in principle, however, the cross-section of elastic scattering of  $\nu_e$  with matter is 6 times higher than with other neutrino types. The measured solar neutrino flux was approximately half of the predicted flux from the SSM [24][25]. This discrepancy of measured fluxes from both Homestake and Kamiokande with the SSM became known as the solar neutrino problem.

In November 1999, SNO started taking data. Using heavy water as detection ma-

terial, it was sensitive to all three neutrino flavours. Reactions could be detected via charged current (CC), neutral current (NC) and elastic scattering (ES):

$$\begin{aligned}\nu_e + d &\rightarrow p + p + e^- \text{ ( CC)} \\ \nu_\alpha + d &\rightarrow n + p + \nu_\alpha \text{ ( NC)} \\ \nu_\alpha + e^- &\rightarrow \nu_\alpha + e^- \text{ ( ES)}\end{aligned}\tag{2.8}$$

The CC reaction is only sensitive to  $\nu_e$ , however, the NC reaction is equally sensitive to all neutrino types. The resulting flux measurements added for all neutrino types, agreed with the predictions of the electron neutrinos produced in the Sun [26]. The measurements from all three experiments confirmed neutrino oscillations and the MSW effect.

### Atmospheric Neutrinos

Cosmic rays interact with the Earth's atmosphere, producing pions and kaons, which decay into electrons and muons and their respective neutrinos, which are referred to as atmospheric neutrinos. The first atmospheric neutrinos were detected in the 60s, but Kamiokande was the first experiment to observe a discrepancy between the measured atmospheric neutrino flux and the predicted one, hinting that atmospheric neutrinos might oscillate. The ratio of events originating from a  $\nu_\mu$  interaction to events originating from a  $\nu_e$  interaction was smaller than expected by about 60% [27]. The experiments successor Super-Kamiokande could link their results to  $\nu_\mu$  oscillations by detecting a  $\nu_\mu$  flux deficit, which increased with the distance travelled by the neutrinos. The measured  $\nu_e$  flux agreed well with the predictions [28].

### Reactor and Accelerator Neutrinos

Anti-neutrinos produced in fission processes in reactors have been used as a neutrino source for multiple experiments, such as CHOOZ [29] and KamLAND [30]. To produce an accelerator neutrino beam, protons are shot on a fixed target. The resulting pions and kaons decay into muons, which subsequently decay to electrons, providing beams with both muon- and electron-type neutrinos and anti-neutrinos. Dependent on the distance of the detector of an experiment to the neutrino beam facility, they are

referred to as long-baseline or short-baseline experiments. The first long-baseline experiments were K2K and MINOS, which both found evidence for  $\nu_\mu$ -oscillations [31][32]. LSND, a short-baseline experiment, found evidence for  $\bar{\nu}_\mu \rightarrow \bar{\nu}_e$ -oscillations [33].

### Recent results

The parameters measured in any oscillation experiment are  $\Delta m_{ij}^2$  and  $\theta_{ij}$  from the oscillation probability as shown in Equation 2.7. Only two of the three possible  $\Delta m_{ij}^2$  are independent [34], since

$$\Delta m_{21}^2 + \Delta m_{32}^2 - \Delta m_{31}^2 = 0 \quad (2.9)$$

Therefore, only two  $m_{ij}^2$  have to be measured. Measuring oscillations from solar neutrinos provides limits on  $\Delta m_{21}^2$ , which is why it is commonly assigned as  $\Delta m_{\text{sol}}^2$ . The absolute value of  $\Delta m_{32}^2$  can be determined from atmospheric neutrino measurements and is referred to  $|\Delta m_{\text{atm}}^2|$ . Only knowing the absolute value of the mass square difference of  $m_2$  and  $m_3$  leaves ambiguity about the ordering of the neutrino mass states  $m_i$ , offering the following possibilities:

$$m_1 < m_2 < m_3 \quad (2.10)$$

$$m_3 < m_1 < m_2 \quad (2.11)$$

In case of Equation 2.10, the ordering of the mass states is specified as normal hierarchy, whilst in case of Equation 2.11 the ordering is referred to as inverted hierarchy. The most current results as presented at the Neutrino 2016 conference for all oscillation parameters is given in Table 2.1.

The limits on  $\theta_{23}$  and  $m_{32}^2$  were presented by T2K [35]. T2K is a long-baseline neutrino experiment using the beam line structure of the J-PARC accelerator facility [38]. The neutrino beam produced using 30 GeV protons is detected in a near detector as well as the 295 km far away Super-Kamiokande detector. The Super-Kamiokande detector is located off-axis to the neutrino beam (the neutrino beam faces away by about  $2.5^\circ$ ) to provide neutrino energies corresponding to the oscillation minimum of  $\nu_\mu$  at this distance.

**Table 2.1:** Recent results for the neutrino oscillation parameters. The values were taken from [35][36][37].

Parameter	Hierarchy	Value
$\Delta m_{32}^2$	Normal	$2.545^{+0.084}_{-0.082} \times 10^{-3}$ eV $^2$
	Inverted	$2.510^{+0.082}_{-0.083} \times 10^{-3}$ eV $^2$
$\Delta m_{21}^2$	Both	$7.48^{+0.19}_{-0.17} \times 10^{-5}$ eV $^2$
$\sin^2 \theta_{12}$	Both	$0.309 \pm 0.013$
$\sin^2(2\theta_{13})$	Both	$0.111 \pm 0.018$
$\sin^2 \theta_{23}$	Normal	$0.532^{+0.084}_{-0.082}$
	Inverted	$0.534^{+0.041}_{-0.059}$

A combination of results from KamLAND, SNO and Super-Kamiokande generate limits on  $\theta_{12}$  and  $m_{21}^2$  [36]. Current measurements on  $\theta_{13}$  are provided by the Double Chooz experiment [37]. It measures  $\bar{\nu}_e$  disappearance in the neutrino flux from the Chooz Nuclear Power Plant in France using four cylindrical tanks, which are filled with liquid scintillator material [39]. The measurements by Double Chooz agree with the measurements of  $\theta_{13}$  carried out by T2K.

Future measurements of the oscillation parameters and the CP-violating phase  $\delta_{\text{CP}}$  will provide answers on the nature of the mass hierarchy. The latest results from T2K [35] and NOvA [40], another long-baseline neutrino experiment located at Fermilab, slightly favour the normal mass hierarchy. Additionally to those two experiments, a variety of other experiments currently under construction will help to provide answers on the mass hierarchy, such as ORCA [41], PINGU [42], INO [43] and JUNO [44].

## 2.3 Mass Measurements

Neutrino oscillation experiments only provide information on the difference between mass-squares, but not on the absolute values of  $m_i$ . Therefore, methods were developed to determine the absolute scale of the neutrino mass states. The most sensitive measurements were obtained by measurements of the  $\beta$ -decay spectrum of Tritium  ${}^3\text{H}$ , which has a well known nuclear matrix element and a low Q-value. By measuring the endpoint of the  $\beta$ -spectrum and determining the difference to the  $Q$ -value

of the decay, the mass of the electron neutrino can be evaluated. The current best limits from direct mass measurements were set by the Troitsk [45] and Mainz [46] experiments:

$$m_{\nu_e}^{\text{eff}} < 2.05 \text{ eV} \quad (2.12)$$

This value can be related to the mass states  $m_i$  by

$$m_{\nu_e}^{\text{eff}} = \sqrt{\sum_i m_i^2 |U_{ei}|^2} \quad (2.13)$$

The KATRIN experiment, which is currently under construction, will reach a sensitivity of  $m_{\nu_e}^{\text{eff}} < 0.2 \text{ eV}$  [47]. Limits on the masses of the other neutrino flavours could be determined from pion decays ( $\nu_\mu$ ) and tau lepton decays ( $\nu_\tau$ ) [48]

$$\begin{aligned} m_{\nu_\mu}^{\text{eff}} &< 190 \text{ keV} \\ m_{\nu_\tau}^{\text{eff}} &< 18.2 \text{ MeV} \end{aligned} \quad (2.14)$$

Other neutrino mass limits were obtained from cosmological observations. The relic density of neutrinos in the universe is related to the neutrino masses by

$$\Omega_\nu h^2 = \frac{\sum_i m_i}{94 \text{ eV}} \quad (2.15)$$

Thus, a bound on

$$M_\nu = \sum_i m_i \quad (2.16)$$

can be determined by measurements of the relic density. The most recent limits on  $M_\nu$  were provided by Planck [49]:

$$M_\nu < 0.23 \text{ eV} \quad (2.17)$$

## 2.4 Neutrinoless Double Beta Decay

The concept of double beta decay was first introduced by Goeppert-Mayer [50]. Double beta decay occurs in nuclei which are energetically forbidden to decay via single beta decays because the resulting nucleus would be in a higher energy state or in nu-

clei which are forbidden to decay via single beta decay due to the angular momentum of the involved nuclei<sup>2</sup>. However, these isotopes can still achieve a lower energy level by decaying via two instantaneous beta decays [51][52].

As afore mentioned, the Standard Model provides no mass mechanism for neutrinos, but the existence of neutrino oscillations requires at least two of the three known neutrinos to have a mass for the  $\Delta m_{ij}^2$  to be non-zero. To add a mass mechanism for neutrinos to the Standard Model, a sterile right-handed neutrino could be introduced, which would not interact via any of the forces incorporated in the Standard Model. From this, a Dirac mass term would follow, giving the Standard Model neutrinos mass [48].

In 1937 Ettore Majorana suggested the Majorana nature of particles, in which a particle and its anti-particle are identical [53]. Of all Standard Model particles, the neutrino is the only candidate to be a Majorana particle due to its neutral charge. In 1939, Furry suggested the possibility of neutrinoless double beta decay ( $0\nu\beta\beta$ ) based on Majoranas theories. The neutrino of one  $\beta$ -decay mitigates the second  $\beta$ -decay by being absorbed by the W-boson of the second  $\beta$ -decay [54]. In this case, only two electrons with combined energies of the  $Q$ -value of the decay are emitted as shown in Figure 2.2.

The decay rate  $\Gamma_{0\nu}$  of  $0\nu\beta\beta$ -decay can be described using the half-life of the decay  $T_{1/2}^{0\nu}$ , the phase space factor  $G_{0\nu}$ , the nuclear matrix element  $M_\nu$  and the electron mass  $m_e$  [55]:

$$\Gamma_{0\nu} = \frac{1}{T_{1/2}^{0\nu}} = G_{0\nu} |M_\nu|^2 \left| \frac{m_{\beta\beta}}{m_e} \right|^2 \quad (2.18)$$

The decay rate is proportional to the square of the effective Majorana neutrino mass  $\langle m_{\beta\beta} \rangle$ , which can be related to the neutrino mass states  $m_i$  via

$$\langle m_{\beta\beta} \rangle = \sum_i m_i U_{ei}^2 \quad (2.19)$$

The possible limits of  $\langle m_{\beta\beta} \rangle$  are dependent on the nature of the neutrino mass hierarchy [56]. Figure 2.3 shows the allowed values of the effective Majorana neutrino masses for both hierarchies as a function of the lightest neutrino mass  $m_{\text{lightest}}$ , which

---

<sup>2</sup>An example of this is the decay of  $^{48}\text{Ca}$ .

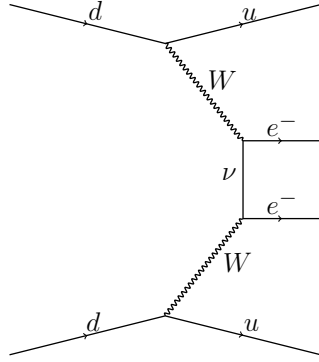


**Figure 2.2:** Feynman diagram for neutrinoless double beta decay. In the presented case the neutrino is a Majorana particle. Adapted from [34].

is equivalent to the lightest neutrino mass eigenstate, i.e.  $m_1$  or  $m_3$ , depending on the mass hierarchy.

The current best limits on  $\langle m_{\beta\beta} \rangle$  at 90 % C.L. are from KamLAND-Zen at

$$\langle m_{\beta\beta} \rangle < (61 - 165) \text{ meV} \quad (2.20)$$

with

$$m_{\text{lightest}} < (180 - 480) \text{ meV} \quad (2.21)$$

KamLAND-Zen use  $^{136}\text{Xe}$  as a double beta decay isotope, which is loaded into liquid scintillator and incorporated into the existing KamLAND structure via a balloon [57]. Over the next run phase KamLAND-Zen is predicted to achieve sensitivities of up to  $\langle m_{\beta\beta} \rangle \approx 40 \text{ meV}$  [58].

The sensitivity to  $\langle m_{\beta\beta} \rangle$  is dependent on the knowledge of the nuclear matrix element of the decay isotope used. Different experiments use different decay isotopes to achieve measurements of  $\langle m_{\beta\beta} \rangle$ . GERDA [59], an experiment located at the Laboratori Nazionali del Gran Sasso investigating the  $0\nu\beta\beta$ -decay of  $^{76}\text{Ge}$  using enriched

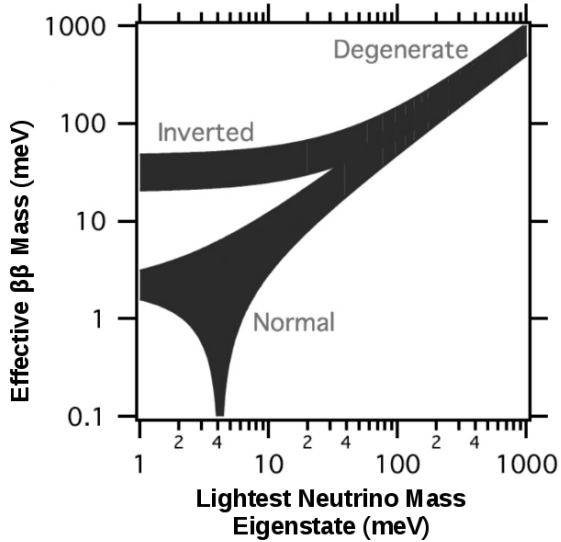


**Figure 2.3:** The effective Majorana neutrino mass  $\langle m_{\beta\beta} \rangle$  versus the mass of the lightest neutrino for the inverted and the normal hierarchy. Taken from [56].

Germanium crystals, have completed their Phase I and reported first results of their Phase II run, offering competitive sensitivity to the current KamLAND-Zen results [60]. The NEMO collaboration have successfully probed the  $0\nu\beta\beta$ -decay of various different isotopes, such as  $^{100}\text{Mo}$ ,  $^{82}\text{Se}$  [61] and  $^{96}\text{Zr}$  [62] (and many more). The isotopes are loaded into the center of the detector by a source foil. The resulting electrons are tracked to give information on the path of each emitted electron and the electron energy is measured by plastic scintillators. Currently, the collaboration is updating their Nemo-3 detector to SuperNemo [63]. CUORE, an experiment using 19  $\text{TeO}_2$  bolometer towers to investigate the double beta decay of  $^{130}\text{Te}$  [64], due to start data taking later this year, is predicted to reach sensitivities of  $\langle m_{\beta\beta} \rangle < (50 - 130)$  meV in five years of running [65]. Also using  $^{130}\text{Te}$  is SNO+, which is described in the following Chapter and which will probe the allowed inverted mass hierarchy region of  $\langle m_{\beta\beta} \rangle$ .

# 3 The SNO+ Detector

SNO+ is a multi-purpose neutrino experiment, located 2 km underground in the Vale Canada Ltd. Creighton Mine [66][67]. Succeeding the SNO (Sudbury Neutrino Observatory) experiment, which finished data taking in 2006 [68], it will use liquid scintillator instead of heavy water as a detection material in order to gain sensitivity at a lower energy threshold [66][69]. The main focus of the experiment will be the search for neutrinoless double beta decay using  $^{130}\text{Te}$  [70]. Additionally to double beta decay measurements, SNO+ provides the sensitivity to study low energy solar neutrinos such as pep and CNO cycle neutrinos, as well as reactor, geo and supernova neutrinos [66]. In this chapter, the main components of the detector are described and the run phases and physics goals outlined, followed by a brief explanation of the trigger system and the SNO+ calibration strategy. Finally, a summary of the expected backgrounds within the detector and the Monte Carlo simulation software used for analysis is given.

## 3.1 The Detector

The SNO+ detector reuses the main components of SNO in order to benefit from the previously built infrastructure [66][67]. Parts of this infrastructure are a transparent acrylic sphere, called the acrylic vessel (AV), with a 12 m diameter and a thickness of 5.5 cm. Installed on top of the AV is the AV neck. The AV is surrounded by a 17.8 m diameter geodesic structure, composed of 270 struts made of stainless steel, called the PMT Support Structure (PSUP). This construction supports  $\approx 9300$  Hamamatsu R1408 photomultiplier tubes (PMT) facing inwards to the centre of the AV. The surrounding cavity, 22 m wide and 34 m high, will store ultra-pure light water for the purpose of supporting the structure and shielding the detector from incoming radiation. The surrounding rock, consisting mainly of norite, provides the equiva-

lent to around 6000 meters of water equivalent (m.w.e) overburden, leading to only approximately 70 muons per day reaching the inside of the PSUP [70][71].

In SNO+, the AV will be filled with 780 tons of Linear Alkyl Benzene (LAB) [69], allowing detection of events with energy  $> 200\text{ keV}$ . Furthermore, fluor 2,5-Diphenyloxazole (PPO) will be added in a concentration of 2 g/L, to optimise the ratio of self absorption and light yield, fixing the light yield to about 10,000 photons/MeV [67]. For the neutrinoless double beta measurements, the LAB-mixture will be loaded with Tellurium, using 1,2 butandiol as a surfactant to dissolve the Tellurium in the scintillator material [70][72].

Due to the change in detection material from heavy water to LAB, slight modifications had to be made to the detector. The density of LAB is lower ( $0.86\text{ g/cm}^3$ ) than the density of the surrounding light water. Therefore, the buoyancy acting on the AV will have a raising effect [67]. Hence, a new hold-down rope-net system has been added to the already existing hold-up ropes from SNO [71].

To achieve the low target levels of  $^{238}\text{U}$  and  $^{232}\text{Th}$  in the detector to control background radiation, the materials used in the scintillator cocktail undergo purification processes underground before being filled into the detector [67]. This is achieved using the scintillator purification plant, which purifies LAB and PPO separately using distillation processes, before the combined LAB-PPO mixture is further purified using a gas stripping process [73][74]. Furthermore, all materials used for the construction of the detector have been assayed to ensure low background rates. A picture of the detector with its major components can be found in Figure 3.1.

## 3.2 The Run Phases and Physics Goals

SNO+ will undergo several run phases which can be used to investigate different physics aspects and detector calibration processes. The first run phase will be the water-fill phase in which the AV is filled with ultra-pure water. This phase will be used to understand the performance of the detector and the response of the PMTs and for optical calibrations of the materials contained within the detector. Main physics goals for this phase are searches for exotic physics such as invisible nucleon decays and solar axion-like particles.

The invisible nucleon decay of  $^{16}\text{O}$  will be investigated by detecting the decay prod-

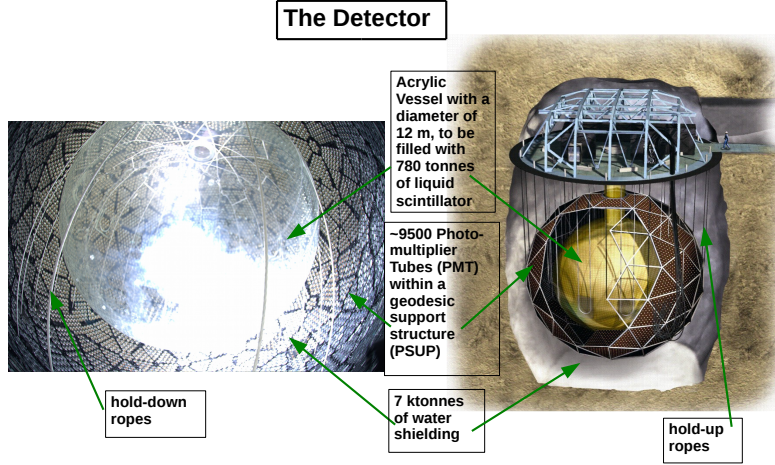


**Figure 3.1:** Presented are a picture of the SNO+ detector (left) taken on the 19/03/2013 with one of the internal cameras which are installed in the PSUP and a schematic of the detector (right). Major detector components are indicated.

ucts of the unstable isotopes created by the invisible nucleon decay. This search is a model-independent search and allows to constrain more exotic models of nucleon decay, such as theories motivated by extra dimensions. A decaying neutron results in unstable  $^{15}\text{O}$ , whilst the remaining unstable nucleus in the case of a invisible proton decay is  $^{15}\text{N}$ . Both isotopes decay by emitting 6.18 MeV and 6.32 MeV gammas respectively. Assuming the expected target levels for all backgrounds, SNO+ can set limits on the decay lifetimes of the invisible neutron ( $\tau_n$ ) and proton ( $\tau_p$ ) decays of

$$\begin{aligned} \tau_n &> 1.25 \times 10^{30} \text{ y} \\ \tau_p &> 1.38 \times 10^{30} \text{ y} \end{aligned} \tag{3.1}$$

at 90 % C.L. in a run time of six months, improving the current KamLAND limit by approximately a factor of 2 [70]. The expected energy spectrum for the water phase is presented in Figure 3.2<sup>3</sup>

For the following run phase of SNO+ the detector will be filled with the pure LAB-

---

<sup>3</sup>A very low detected number of hits per MeV is expected during the water-phase, leading to a large spread in the energy distribution where events with an energy of 3 MeV can reconstruct at 5 MeV.

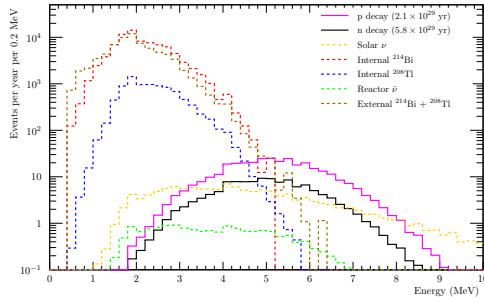


**Figure 3.2:** Physics energy spectra for the SNO+ water phase depicting the invisible nucleon decay and the main backgrounds. Taken from [75].

PPO mixture, referred to in the following as pure scintillator-fill phase. During this phase, internal and external backgrounds will be measured and the optical models and detector responses measured during the water-fill phase will be verified. The main physics goal for this phase is the measurement of low energy solar neutrinos. Assuming background levels similar to those of Borexino phase I [76][77], the uncertainties on the solar fluxes can be reduced to

$$\begin{aligned}
 &\text{pep: } 10\% \\
 &\text{CNO: } 4.5\% \\
 &{}^7\text{Be: } 4\% \\
 &{}^8\text{B: } 8\%
 \end{aligned} \tag{3.2}$$

within a year of data runs. Any measurements on the pp neutrino flux depends on the background levels of  $^{14}\text{C}$  and  $^{85}\text{Kr}$  [70]. The expected solar fluxes are shown in Figure 3.3.

SNO+ is currently undergoing water-fill, which is scheduled to finish in October 2016. The scintillator-fill will start in April 2017, with the loading of the  $0\nu\beta\beta$  isotope starting in late 2017 [79]. In this phase, the detector will be loaded with 0.5% natural Tellurium, which corresponds to approximately 1330 kg of  $^{130}\text{Te}$ , to search for  $0\nu\beta\beta$ -decays of  $^{130}\text{Te}$ , with a  $Q$ -value of 2.53 MeV. The isotope was chosen amongst other reasons due to its large natural abundance and its long half-life. The main backgrounds for this measurement are the solar  ${}^8\text{B}$  neutrinos and the  $2\nu\beta\beta$  decays of the  $^{130}\text{Te}$  itself. All other backgrounds can be reduced by defining a fiducial volume

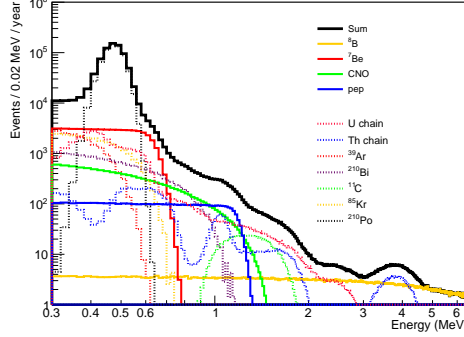


**Figure 3.3:** Physics energy spectra for the SNO+ pure scintillator phase, showing the expected solar event spectrum and the main backgrounds. All presented backgrounds are described in more detail in Section 3.5. Taken from [78].

cut and using coincidence tagging techniques for background decays falling within the region of interest (ROI). At a 0.5 % loading a limit on the half-life of

$$T_{\frac{1}{2}}^{0\nu\beta\beta} > 1.96 \times 10^{26} \text{ y} \quad (3.3)$$

at 90 % C.L. can be achieved within five years of running, corresponding to an effective Majorana neutrino mass of  $\langle m_{\beta\beta} \rangle < (38 - 92) \text{ meV}$ . The approach of loading the isotope within the scintillator allows for increased isotope loads at later run phases for improved sensitivities [70][80]. The energy spectrum of all backgrounds and the anticipated signal can be found in Figure 3.4.

### 3.3 The Electronics System

Photons induced by particles interacting with the detector material are collected by the PMTs surrounding the detector based on the detection efficiency of the PMTs. The readout of these signals has an impact on how well the data can be understood. Thus, the electronics system is briefly described here and the influence on the event timing is discussed.

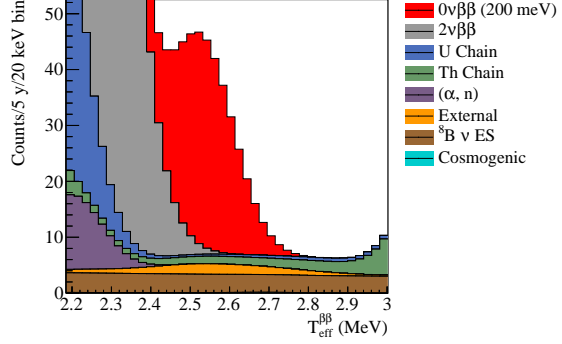


**Figure 3.4:** Physics energy spectra for the SNO+ Tellurium loaded phase, showing the  $0\nu\beta\beta$ -spectrum of  $^{130}\text{Te}$  and the main backgrounds. The plot was made assuming a loading of 0.5 % natural Tellurium, resulting in 1330 kg of  $^{130}\text{Te}$  within the detector over a run time of 5 years. A fiducial volume of 3.5 m and a light yield of 390 hits/MeV was assumed. Taken from [81].

### 3.3.1 Overview

Every time a PMT registers a hit, the signal is send to a PMT Interface Card (PMTIC), each of which samples 32 PMT channels. There the signal is measured by one of four daughter boards connected to the PMTIC. The daughter boards measure the hit threshold and if a certain threshold is crossed, a per channel trigger pulse is generated. A variety of different triggers are available, such as the NHit100 trigger, which consists of a wide square pulse integrated over 100 ns. Additionally to the generation of the trigger pulse, the time to amplitude converter (TAC) starts to ramp and starts integrating over all pulses registered on that channel. The higher the integral on the TAC signal, the earlier the event arrived in that PMT.

The information from the daughter boards is collected and digitised by the Front End Cards (FECs). Each PMT is connected to one FEC and 16 FECs are mounted in one crate, with 19 crates in total. Per crate, the triggers are summed by the Crate Trigger Card (CTC) which sends the signals to the analogue Master Trigger Card (MTC/A+). The MTC/A+ sums over all connected CTC signals and if this sum crosses a threshold a trigger is issued.

That information is passed on to the digital Master Trigger Card (MTC/D). The MTC/D compares the trigger signals to a trigger mask defined by the detector opera-

tor<sup>4</sup>. If the triggers which crossed the threshold are combined in the trigger mask, the MTC/D issues a global trigger (GT), which is send back to the front end of the system [82]. The information of an event is readout from the MTC by the Event Builder. It organises the incoming data into physical events based on the GT information and writes them into zdab files, which can be converted into RAT ROOT files by the user [83].

PMTs can fire without the occurrence of events in the detector. These hits result from electrons released due to thermal excitation and are referred to as “dark current” or noise. To measure the levels of the PMT dark current, the PulseGT trigger is used, which sends a global trigger at user defined time intervals (nominal at 5 Hz) [84].

### 3.3.2 Timing

The initial time from a PMT event crossing the threshold to the signal being received by the MTC/A+ is 110 ns. Furthermore, the time for the GT to arrive back at the front end is 110 ns. Therefore there is a total delay of 220 ns between the event crossing the trigger threshold and the arrival of the GT. This delay is accounted for in the 400 ns trigger gate used by SNO+. All hits arriving 220 ns after, and all hits which arrived 180 ns before the crossing of the threshold, are recorded.

During the sampling of a trigger window no new GT can be issued and any other event occurring within the trigger gate will pile-up with the event which originally issued the trigger. Additionally to the dead time (in which no new trigger can be issued) arising from the electronic properties, a trigger lockout is defined. This results in a 450 ns window during which no other GT pulse can be issued. However, if any event occurring within the lockout window is still above threshold after the lockout time is passed, a new GT can be issued immediately (this is also referred to as re-trigger). Then, all hits occurring within the 180 ns prior to the end of the time lockout are sampled within the new trigger gate [85].

---

<sup>4</sup>Different types of runs require different triggers

## 3.4 The Calibration Setup

The calibration program of the detector is designed to gain an understanding of the optical and energy response of the detector [86]. The parameters measured by the calibration program can be divided into 4 categories: PMT parameters such as channel efficiencies and charge spectrum shapes, electronics parameters for example cable delays and signal delays, optics parameters such as absorption, scattering and re-emission of all detector materials, and detector parameters including PMT and AV positions [87]. The PMT parameters are important to achieve a good energy and position reconstruction of events [66].

To understand the energy response of the detector, a variety of radioactive decay sources will be deployed in the detector. They are designed to cover an energy range of 0.1 MeV – 6 MeV. Amongst the planned sources are AmBe,  $^{60}\text{Co}$ ,  $^{57}\text{Co}$ ,  $^{24}\text{Na}$ ,  $^{48}\text{Sc}$  and  $^{16}\text{N}$ , which will be deployed via an umbilical and which can be moved in the detector using a high purity rope source deployment mechanism [70].

The positions of the calibration sources as well as the positions of detector components such as the AV and the rope net system will be determined using a camera system. Six cameras, installed on the PSUP can determine the position of deployed sources with an accuracy of  $\leq 1\text{ cm}$ . To aid the position measurement of the detector geometry, two underwater lights will be installed on the PSUP [88].

Electronics and optics parameters will be measured using a Laserball source and an in-situ fibre injection system called Embedded LED/Laser Light Injection Entity (ELLIE) [67]. The Laserball emits photons with specific wavelength distributions to both measure the PMT parameters and the absorption properties of the detection material [87]. Like the radioactive sources it will be deployed in dedicated calibration runs [89].

ELLIE was constructed to avoid contamination on the inside of the AV during the calibration. The three ELLIE subsystems are specifically designed to measure different optical properties by injecting a light pulse from the deck area outside of the detector to the inner detector region. An optical fibre transmits the light pulse from the deck to the end of the fibre, which is mounted onto a PMT node in the PSUP [66]. This setup allows ELLIE to perform the following in-situ calibrations: PMT timing calibration, scattering length and attenuation length measurements, response of the

PMT and DAQ and measuring the efficiency of detecting coinciding signals [90].

The 120 optic fibres of ELLIE [67] divide into TELLIE (for the Timing calibration), SMELLIE (for the Scattering Monitoring) and AMELLIE (for the Attenuation Monitoring) [91]. TELLIE will be used to complement the laserball measurements in measuring the PMTs individual timing and gain by using 92 wide-aperture PMMA fibres which are fed by LED drivers [91] [66]. The 8 AMELLIE fibres [91] are made of quartz which will be injected with light from LEDs [66]. The SMELLIE system is described in detail in Chapter 4.

## 3.5 Expected Backgrounds

For any physics analysis it is important to know dominant backgrounds for the processes under investigation. Once identified, analysis techniques can be developed to distinguish background events from physics events of interest. This section outlines all expected backgrounds in SNO+ and their significance, summarising [70] and [92].

### 3.5.1 Internal Backgrounds

All non-signal events which occur within the AV volume are classed as internal backgrounds. One of the naturally occurring radioisotopes found within the scintillator is  $^{238}\text{U}$ , of which the decay scheme is presented on the top in Figure 3.5. For the measurements carried out at SNO+, especially  $^{214}\text{Bi}$ ,  $^{210}\text{Tl}$  and  $^{210}\text{Bi}$  are of concern.

The  $^{214}\text{Bi}$  ( $T_{\frac{1}{2}} = 19.9 \text{ min}$ ) decays to  $^{214}\text{Po}$  via  $\beta$ -decay 99.979 % of the time. The following  $\alpha$ -decay of the  $^{214}\text{Po}$  with a half-life of  $T_{\frac{1}{2}} = 164.3 \mu\text{s}$  can be used to tag and reject these events. For the pure scintillator phase, these decays, which are referred to as  $\beta - \alpha$  coincidences, are used to estimate the Uranium chain events as described in Chapter 7 assuming all isotopes following the  $^{238}\text{U}$  decay are in equilibrium. During the neutrinoless double beta decay measurement, these  $\beta - \alpha$  coincidences can be used to reject decays from  $^{214}\text{Bi}$  that occur within the region-of-interest (ROI). In the remaining cases,  $^{214}\text{Bi}$  decays via an  $\alpha$ -decay into  $^{210}\text{Tl}$  ( $T_{\frac{1}{2}} = 1.3 \text{ min}$ ), which itself decays via a  $\beta$ -decay.

The equilibrium of the Uranium chain content can be broken if the scintillator cocktail is exposed to the surrounding mine air, which contains  $^{222}\text{Rn}$ . This Radon ingress

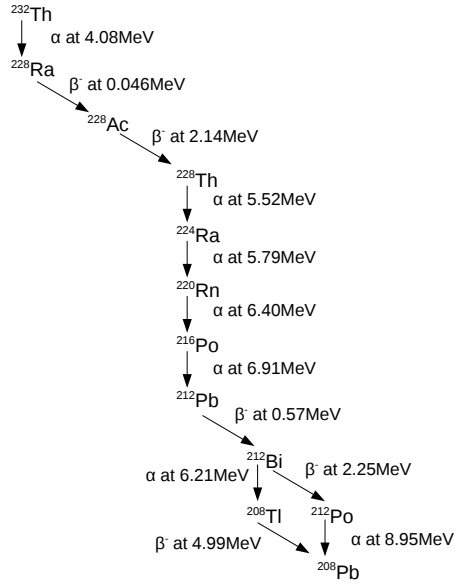
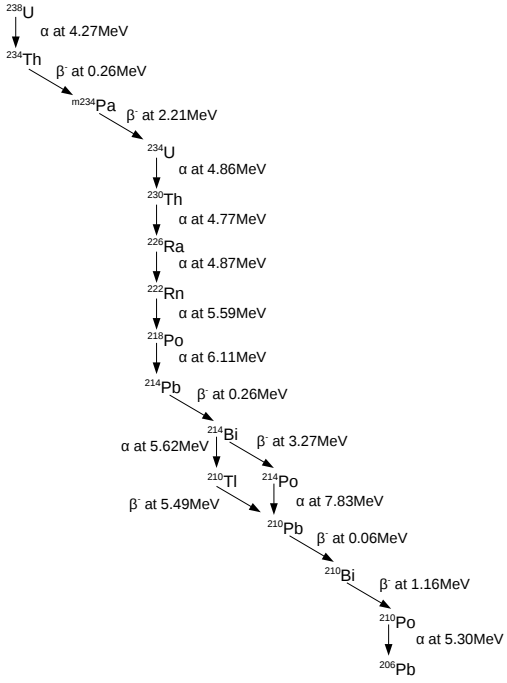


**Figure 3.5:** Uranium (top) and Thorium (bottom) decay chains, adapted from [92]. The presented energies are the energy of the main  $\alpha$ -decay (for  $\alpha$  emitters) and the  $Q$ -value of the  $\beta$ -decay (for  $\beta^-$  emitters).

can occur during the calibration campaigns with radioactive sources as described in Section 3.4. However,  $^{222}\text{Rn}$  is a relatively short lived isotope ( $T_{\frac{1}{2}} = 3.82$  days), followed by a cascade of short-lived daughter nuclei up to  $^{210}\text{Pb}$ . Therefore, equilibrium with  $^{214}\text{Bi}$  can be restored within a small number of weeks. In order to reduce the potential of Radon ingress, a cover gas system containing nitrogen gas in a sealed system to perform as a barrier between detector and mine air is installed. The cover gas is inserted at the top of the AV neck via a bag system which allows to compensate for pressure changes in the mine air, forming a protective layer for the scintillator material below.

Because of the long half-lives of the isotopes at the top of the Uranium chain up to  $^{226}\text{Ra}$  (with  $T_{\frac{1}{2}} = 1599$  y), re-establishing any broken equilibrium between these isotopes would take a long time<sup>5</sup>. Since the  $^{214}\text{Bi}$ - $^{214}\text{Po}$  tagged coincidences measurement concentrates on the bottom of the decay chain, only the level of  $^{226}\text{Ra}$  is a certainty and equilibrium with  $^{238}\text{U}$  and all isotopes up to  $^{226}\text{Ra}$  is simply an assumption. However, all Uranium decay chain elements up to  $^{226}\text{Ra}$  do not provide backgrounds to the physics measurements made at SNO+ due to the low energies of their decays, and thus measuring the Uranium chain levels using the  $^{214}\text{Bi}$ - $^{214}\text{Po}$  coincidence is sufficient for the purposes of SNO+.

Another naturally occurring isotope in the scintillator mixture is  $^{232}\text{Th}$ , the decay scheme of which is found on the bottom in Figure 3.5. For the SNO+ measurements, the isotopes contained in the Thorium chain which are of most concern are  $^{212}\text{Bi}$  and  $^{208}\text{Tl}$ . However the  $^{212}\text{Bi}$  ( $T_{\frac{1}{2}} = 60.6$  min)  $\beta$ -decay into  $^{212}\text{Po}$  ( $T_{\frac{1}{2}} = 300$  ns) can be used to reject  $^{212}\text{Bi}$  events just like for the Uranium chain, using the  $\beta - \alpha$  coincidence.  $^{212}\text{Bi}$  only decays into  $^{212}\text{Po}$  64 % of the time. The remaining 34 % of the cases it decays via an  $\alpha$ -decay into  $^{208}\text{Tl}$  which in return decays via  $\beta$ -decay with a half-life of  $T_{\frac{1}{2}} = 3$  min.

Other internally occurring backgrounds are  $^{40}\text{K}$ ,  $^{39}\text{Ar}$  and  $^{85}\text{Kr}$ .  $^{40}\text{K}$  has a half-life of  $T_{\frac{1}{2}} = 1.248 \times 10^9$  yr which is why it naturally occurs in both the scintillator and the detector materials. The  $^{40}\text{K}$  decays via electron capture 11 % of the time, which is combined with the emission of a gamma at 1.46 MeV and is a background to pep neutrino measurements. However, due to the distinct gamma peak, the  $^{40}\text{K}$  content

---

<sup>5</sup>The equilibrium between any of these isotopes could have been broken long before the oil used for the LAB was transformed into a scintillator.

can be estimated.

$^{39}\text{Ar}$  results from cosmogenic activation of  $^{40}\text{Ar}$  in the atmosphere. The LAB can be contaminated by  $^{39}\text{Ar}$  (as well as  $^{85}\text{Kr}$ ) when it comes into contact with air or the nitrogen used in the purification process of the scintillator or the cover gas system. This Argon isotope decays via  $\beta$ -decay with a Q-value of 0.585 MeV at which it poses no concern to either the double beta or the pep solar neutrino measurements. The isotope  $^{85}\text{Kr}$  is a by-product of nuclear fission and like  $^{39}\text{Ar}$  has such a low Q-value that it only affects CNO and pp measurements. To keep the levels of these isotopes low, the contact of the LAB with air should be kept at a minimum.

### 3.5.2 AV Leaching Backgrounds

As described above, mine air is rich in  $^{222}\text{Rn}$ . It decays through various unstable isotopes into the long-lived  $^{210}\text{Pb}$  ( $T_{\frac{1}{2}} = 22.2 \text{ yr}$ ). Any  $^{222}\text{Rn}$  ingress in the detector will break the  $^{238}\text{U}$  chain equilibrium at this point, resulting in an increased abundance of this isotope. Its daughter  $^{210}\text{Bi}$  is a direct background to the CNO cycle measurement due to its spectral shape. The decay product of  $^{210}\text{Bi}$ ,  $^{210}\text{Po}$  is an  $\alpha$ -emitter which may compromise the  $\alpha - \beta$  and  $\beta - \alpha$  tagged coincidences.

During the construction of SNO+, Radon and its daughters have deposited onto the AV surface. Due to  $\alpha$  recoil, the Radon daughters can be implanted into the AV surface up to a few hundred nm. When the AV comes in contact with the scintillator material or water, these Radon daughters might leach from the AV into the detector material. The rate of leaching of the implanted  $^{210}\text{Pb}$ ,  $^{210}\text{Bi}$  and  $^{210}\text{Po}$  depends on the ambient temperature, the material the AV is in contact with, the depth of the ingress and the initial activity on the surface. The leaching rates were measured for all proposed scintillator cocktails and ultra-pure water in bench top tests at different temperatures. Based on these numbers, predictions were made for the expected  $^{210}\text{Pb}$ ,  $^{210}\text{Bi}$  and  $^{210}\text{Po}$  rates for each detector phase. For the Te-loaded phase, additional amounts of the  $^{210}\text{Po}$  can be introduced alongside the Tellurium itself [93].

### 3.5.3 External Backgrounds

External backgrounds are events occurring inside the AV volume but which originate from decays outside of the AV. These backgrounds come from isotopes on the hold-

down and hold-up ropes, the PMTs and the external water as well as the AV bulk. The main concerns are high energy  $\beta$  and gammas from  $^{214}\text{Bi}$ ,  $^{208}\text{Tl}$  and  $^{40}\text{K}$  decays. Additionally, AV contributions of the Radon daughters  $^{210}\text{Pb}$ ,  $^{210}\text{Bi}$  and  $^{210}\text{Po}$  can add to external background contributions. Introducing a fiducial volume cut, external background events reconstructed inside the AV can be greatly reduced. Using the PMT time distribution, these backgrounds can be constrained even further. For the double beta phase of the experiment, constraints from the water phase and the pure scintillator phase can be used.

### 3.5.4 Cosmogenics

Cosmic particles such as cosmic neutrons, protons and muons can activate radioactive isotopes within the LAB. The highest rate background produced by cosmic rays is  $^7\text{Be}$ , which can be removed by over 99 % by the scintillator purification plant. An isotope which is naturally contained in the scintillator but which can also be produced by cosmogenics is  $^{14}\text{C}$ . It is a background to the measurement of solar pp neutrinos, however, its cosmogenic activation is considered negligible in comparison to the amount naturally contained in the scintillator, which can be concluded from observations made in [94].

Another background induced by interactions with cosmic muons is  $^{11}\text{C}$ , which can be reduced by a coincidence tagging technique. Other muon induced events can be vetoed using a very short time window due to the short half-life of muon induced backgrounds. Other isotopes resulting from cosmogenic activation of Tellurium, such as  $^{124}\text{Sb}$ ,  $^{22}\text{Na}$ ,  $^{60}\text{Co}$ ,  $^{110m}\text{Ag}$  and  $^{88}\text{Y}$  [95] can be reduced by purifying the Tellurium underground [96].

### 3.5.5 ( $\alpha, n$ ) Backgrounds

Neutrons can be produced in the scintillator from  $\alpha$ -particles originating from e.g.  $^{210}\text{Po}$  decays interacting with  $^{13}\text{C}$  which is a component of the scintillator material. When these neutrons are produced, recoils from scattering with protons produce scintillation light, which produces a prompt signal with the energy lost by the initial  $\alpha$ -particles in the scintillator. The neutrons are then captured by hydrogen atoms accompanied with the emission of a specific energy gamma ray. Using the prompt

light from the initial reaction and the signal from the delayed gamma, these events can be rejected using coincidence techniques.

### 3.5.6 Instrumental Backgrounds

Instrumental backgrounds are backgrounds caused by the detector itself, such as electronic noise or flashers. Flashers are events induced by PMTs at high voltage, causing photon emission from the PMTs into the detector. These events can be characterised by the timing profile of the events: a cluster of hits is observed later in time at the opposite side of the detector. Instrumental backgrounds are rejected using data cleaning cuts based on spatial clustering and event timing [97][98].

## 3.6 RAT simulation software

RAT is a simulation package written in C++ using Geant4 libraries. It simulates the detector geometry and physics processes, as well as the electronics system [99]. RAT is under constant development but release tags are issued for stable versions of the code. These stable releases are used to produce high statistics Monte Carlo sets as requested by different analysis groups, which are referred to as production runs.

The ROOT files produced by RAT have different branch types. One branch is the Monte Carlo simulation branch, containing all the truth information of the produced particles. To access this information, one has to loop over all photons created in all PMTs over the entire run. Event information such as triggers are not contained.

The other branch is the so-called event branch. This branch simulates the structure of actual data, ordering all hits produced in the detector by events, including the electronics and DAQ aspects of the detector. Accessing each event returns the information of all hits found within the 400 ns trigger window, trigger type issued and reconstructed variables such as event position and energy.

### 3.6.1 Event generation

Event generators are used to add physics processes or calibration events to the detector simulation. The user can define what type of particle to generate, the position of the

event origin and the rate at which the event occurs. The generators produce events based on look-up tables containing basic properties, e.g. for the decay of an isotope the decay type, the energies released and the daughter isotopes are stored in these tables. To simulate SMELLIE events, the *ellie* generator is used [84]. All properties of the SMELLIE fibres were added to the equivalent look-up table as described in Chapter 5.

### 3.6.2 Event reconstruction

To extract the position and energy of an event occurring in the detector, the event must be reconstructed. The energy reconstruction is based on the number of triggered PMTs, in the following referred to as  $n_{\text{hits}}$ . The detected  $n_{\text{hits}}$  depend on the energy released by the event, the position of the event and the light yield of the detector material [100].

To reconstruct the positions of the event, the timing information of the PMTs is used. Based on the time individual PMTs are hit and the time it takes the photon to travel through the detector material, a position vertex can be reconstructed. The more photons are produced, the more PMTs can be used for reconstruction, therefore the position reconstruction is energy dependent. Events occurring near the edge of the AV can be reflected off the surface, delaying the photons initially produced by the event and therefore leading to higher mis-reconstruction rates for these events [101]. Pre-RAT release 4.6 the energy reconstruction utilises look-up tables, comparing the produced  $n_{\text{hits}}$  to energy values at the equivalent reconstructed detector radius. Post-RAT 4.6, a functional form of the energy reconstruction was introduced, accounting e.g. for detector asymmetries close to the neck [100].

## 3.7 Summary

To achieve the physics goals described in this Chapter, the optical properties of the detection materials need to be understood for each run phase. The Scattering Module of the ELLIE system described in the next Chapter was designed to measure the scattering properties of the detection material throughout all run phases. The analysis for the water run phase is described in the following Chapters. Additionally, the

internal backgrounds of the scintillator cocktail described in this Chapter need to be understood to increase sensitivities of the physics measurements during the pure scintillator and Tellurium-loaded run phases. The strategy for these measurements is also outlined in this document.

## 4 The Scattering Module

The scintillation process in the SNO+ LAB material leads to the emission of photons, the number of which depends on the energy of the interaction which initiated the scintillation. These photons can undergo optical interactions with the detector material following their emission. In order to comprehend the impact of these interactions on the physics results provided by SNO+, their nature needs to be understood and their resulting effects quantified.

The different types of interaction with matter the photons can undergo include Compton scattering, the photoelectric effect, pair production and Rayleigh scattering [52]. The rate and probability of these effects is dependent on the energy of the emitted photons, with Rayleigh scattering and the photoelectric effect being low energy processes, whilst Compton scattering and pair production require higher photon energies. For the LAB used by SNO+, the expected light yield is in the order of  $10^4$  photons per MeV [102], i.e. the average photon emitted by the scintillation process has an energy in the order of 0.1 eV. Pair production can only occur for photons with an energy of at least twice the rest mass of an electron, which would be equivalent to a photon energy of 1 MeV, whilst Compton scattering is a significant effect for photon energies in the order of keV. To free an electron from the atomic shell in the photoelectric effect, the photon has to overcome an energy threshold, which depends on the binding energy of the electron in the shell and is typically at least a few eV. Therefore, at the photon energies expected from the scintillation processes at SNO+, Rayleigh scattering is the expected dominant process.

Any light scattered in the detector arrives later than expected at the PMTs. As described in Section 3.6 the hit timing plays an important role in the position reconstruction of the event. Both position and timing information of a hit are used for multiple background identification and rejection techniques, such as likelihood separation of  $\alpha$  and  $\beta$  particles [103] and coincidence tagging [104][105][106]. For physics

measurements, a fiducial volume cut is required, making a good reconstruction crucial [107].

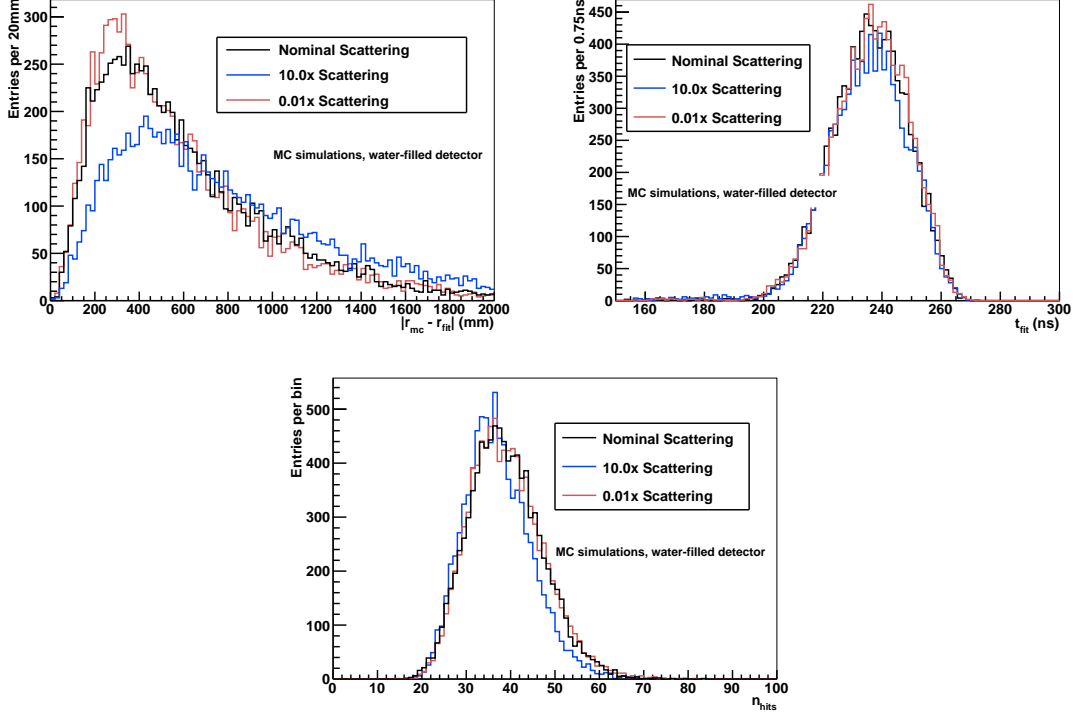
Furthermore, delayed photons might not fall into the selected event window. The more scattering occurs, the more photons are delayed, effecting the number of hits registered for an event. The detector energy resolution depends on the number of hits detected and can be estimated by  $\sigma = \sqrt{n_{\text{hits}}}$  [108]. Overall, the detectors performance and sensitivity to physics measurements depends on good reconstruction techniques, well understood background contributions and the energy resolution, making a good understanding of the scattering properties of the detector material essential.

Figure 4.1 shows invisible proton decay events in a water-filled detector with different amounts of scattering applied. A measure of the amount of scattering occurring in the detector is the scattering length  $l$ . This value describes the mean distance travelled by a photon before it is scattered [109]. Therefore, the longer the scattering length, the less scattering occurs. In RAT, the scattering occurring in each detector medium is defined by  $l$  and to change the scattering in the simulation a scaling factor  $s$  can be applied

$$l_s = \frac{l}{s} \quad (4.1)$$

with  $l_s$  being the new scattering length. If the scattering length is reduced by the factor  $s$ , the amount of scattering occurring is increased by the factor  $s$ .

The scaling factors applied to the simulations to produce the distributions in Figure 4.1 were  $s = 10$  and  $s = 0.01$ . Presented are the registered number of hits (bottom), the reconstructed hit times (top right) and the difference between the true event position and the reconstructed event position (top left). A clear shift can be observed especially for the performance of the position reconstruction. In order to monitor the scattering in the SNO+ detector, the Scattering Module was designed, tailored to monitor the expected effects of scattering in-situ in regular time intervals. This chapter gives a brief overview of the expected scattering and a description of the Scattering Module.



**Figure 4.1:** Invisible proton decay for different reconstruction variables. Shown are the difference between the reconstructed radial position  $r_{\text{fit}}$  and the true radial position  $r_{\text{mc}}$  of the decays  $|r_{\text{mc}} - r_{\text{fit}}|$  (top left), the reconstructed hit time  $t_{\text{fit}}$  (top right) and the  $n_{\text{hits}}$  distribution for the nominal scattering length  $l$  in water, and  $s = 0.01$  and  $s = 10$ .

## 4.1 Rayleigh Scattering

The scattering of an electromagnetic wave on a particle is described by Mie scattering. For particles with sizes much smaller than the wavelength  $\lambda$  of the incoming wave, Mie scattering can be approximated by Rayleigh scattering [110]. In the past it has been shown that the dominant scattering effects in ultra pure water and LAB originate from Rayleigh scattering with negligible contributions from Mie scattering [111][109].

Any incident light on a particle with diameter  $d \ll \lambda$  acts as an electric field  $E_0$  on the particle, causing polarisation and inducing a dipole moment  $p$ , the strength of which is dependent on the polarisation  $\alpha$  of the particle:

$$p = \alpha E_0 \quad (4.2)$$

Since the incident light is a wave and therefore applying an oscillating incident electric field, the dipole moment also oscillates leading to a radiation in all directions. In the most common case, isotropic polarisation, the directions of the incident field and the induced dipole moment coincide. In this case, for a point at distance  $r \gg \lambda$ , the intensity of the scattered light becomes

$$I = \frac{(1 + \cos^2 \theta) k^4 |\alpha|^2}{2r^2} I_0 \quad (4.3)$$

with the scattering angle  $\theta$ , the intensity of the incident wave  $I_0$  and the wavevector  $k$ :

$$k = \frac{2\pi}{\lambda} \quad (4.4)$$

Thus there is a  $\frac{1}{\lambda^4}$ -wavelength dependence of the Rayleigh scattering. Any deviation from that dependence suggests a contamination of the measured medium with particles not fulfilling the  $d \ll \lambda$  criteria. The scattering module has been specifically designed to monitor this wavelength dependence. The distinct angular distribution  $(1 + \cos^2 \theta)$  of the scattered light can also be probed with the scattering module and has been investigated in [112].

## 4.2 The hardware components

This Section describes the main hardware components of the Scattering Module as outlined in the hardware manual [113]. For more detail, please refer to [113].

### 4.2.1 Overview

The Scattering Module of the Embedded LED/Laser Light Injection Entity (SMELLIE) is designed to generate and inject light into the detector via a system of optical fibres. The majority of the hardware components are placed on the deck clean room of the detector in the ELLIE rack. A schematic of the SMELLIE hardware system is presented in Figure 4.2.

To probe the wavelength dependence of the scattering as shown in Equation 4.3, the SMELLIE hardware is based around four pulse-diode laser heads operating at four different wavelengths. These lasers are controlled via the SEPIA II Laser Driver

Unit, which is connected to a specially designed Laser Switch to enable automated laser head switching. From the SEPIA II unit, the light travels to the Fibre Switch, which routes the light into one of the twelve fibres installed in the detector. A part of the light is split and diverted into the Monitoring PMT Unit (MPU), which allows measurement of the performance of the laser heads on a per-pulse basis. The software to control the system is installed on the SNOdrop SMELLIE Control PC, which allows the running of individual components as well as the entire system.

The system can be operated in two different modes: master and slave. For the master mode, the signal which issues the trigger on SMELLIE is provided by the National Instruments DAQ Unit, which is housed in the MPU. This signal is sent to both the SMELLIE system and the SNO+ MTC issuing a global trigger. Hence, the system notifies the detector when a laser pulse is fired and a trigger should be issued. In slave mode, the MTC issues a global trigger and sends a signal to the SMELLIE system to initialise a laser pulse to be fired.

### 4.2.2 The Lasers

For the purposes of SMELLIE, lasers as a light source are preferable over LEDs since they offer coherent light which allows higher intensity light pulses and more efficient beam collimation. Collimated beams are important for the scattering measurement, since a narrow beam simplifies distinction between scattered and direct beam light. Furthermore, a laser offers a narrower wavelength distribution, allowing for easier probing of the wavelength dependence of the scattering. The four laser heads (shown in Figure 4.3) were designed by PicoQuant and are coupled to the fibres using couplings from Schaefter and Kirchhoff.

The wavelengths of the laser heads used for the Scattering Module were chosen according to the photocathode efficiency of the PMTs, as well as the optical properties of the  $0\nu\beta\beta$ -decay isotope proposed for SNO+. The SNO+ PMTs are most efficient in the wavelength window around 400 nm and 450 nm [101][114][115]. Furthermore, at the time SMELLIE was proposed, the  $0\nu\beta\beta$  decay isotope to be loaded into SNO+ was  $^{150}\text{Nd}$ . Loading this isotope into the scintillator mixture results in absorption of light with very specific wavelengths [114]. To avoid these absorption bands, the nominal laser wavelengths were chosen to be 375 nm, 405 nm, 440 nm and 500 nm.

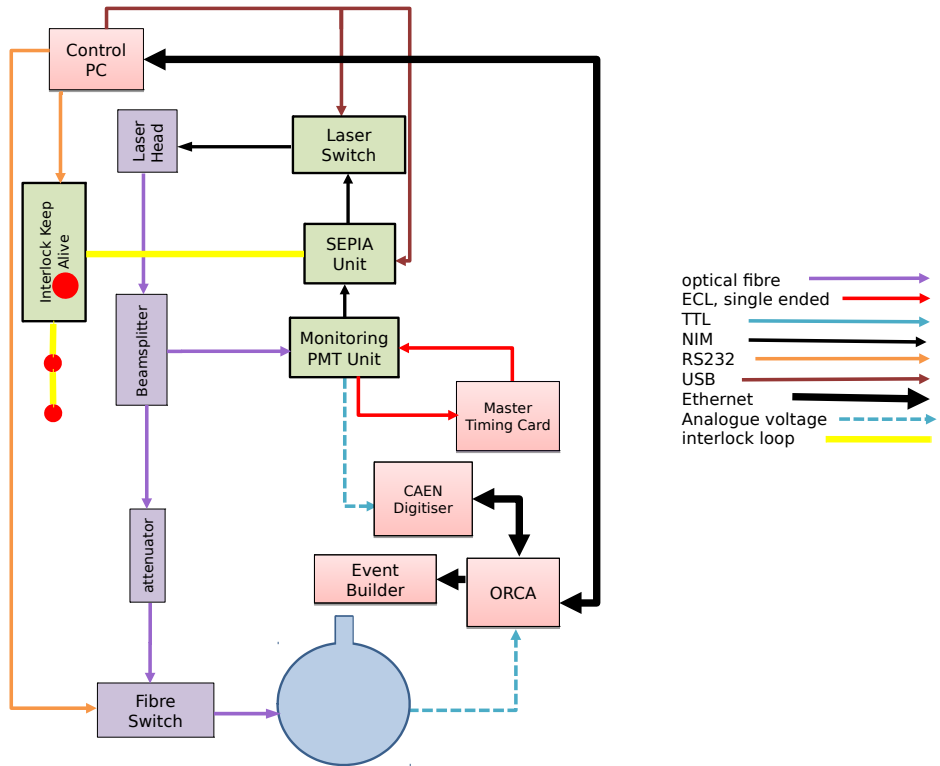


**Figure 4.2:** Schematics of the SMELLIE hardware components. Adapted from [113].

The wavelength distributions of these lasers were measured by the manufacturer and peak at 375 nm, 407 nm, 446 nm and 495 nm. The lasers will be referred to with these wavelengths for the remainder of this document.

It has since been decided that SNO+ will be loaded with  $^{130}\text{Te}$  as  $0\nu\beta\beta$  isotope. There are no absorption peaks for this isotope, but a smooth absorption spectrum [114]. The change means that the opacity of a  $^{130}\text{Te}$  loaded scintillator at wavelengths of 375 nm is increased in comparison to a  $^{150}\text{Nd}$  loading, so a fraction of light emitted by this laser head will be absorbed.

To control the laser heads the SEPIA II Laser Driver is used, which sets the pulse



**Figure 4.3:** The four SMELLIE single-wavelength laser heads.

frequency of the lasers and the intensity setting. The laser intensity can be set as the percentage of the lasers maximum output, with 100 % being the maximum. The intensity can be incremented in 0.1 % steps, but the lower limit a laser can be fired at is limited by the stability of the laser head below a laser specific intensity threshold. An external trigger from the MPU is passed on to SEPIA, the frequency of which can be between 1 kHz – 10 kHz, which determines the pulse frequency of the laser pulses.

Since during detector dark time the SMELLIE hardware is inaccessible, the SEPIA unit passes its signal to a Laser Switch. This laser signal has six output sockets, four of which are connected to one of the laser heads. The choice which output channel is used can be made manually on the Laser Switch or by using the software on the SNOdrop computer. Accidental laser head firing is avoided by three interlocks, two hardware based and one software controlled, which have to all be deactivated at the same time to fire the laser heads.

#### 4.2.3 The Fibres

The optical fibres used have an orange outer sheath to distinguish them from the black TELLIE and AMELLIE fibres and consist of a core with a width of  $50\text{ }\mu\text{m}$ , cladded by glass. The fibres' optimal operating range is 750 nm – 1 450 nm, which is outside of the wavelength range used by the SMELLIE system. Therefore, intensity loss due to attenuation of light is expected. However, these fibres were chosen because of their very low intrinsic radioactivity. Being installed very close to the PMTs in the detector,

low radioactivity is crucial to avoid non-removable background contributions. It has been proven that the radioactivity of the SMELLIE fibres is lower than the background contributions from the PMTs [116]. The SMELLIE fibres can be split into two different types: detector fibres and rack fibres.

### Rack Fibres

The rack fibres are located on deck in the ELLIE rack and connect the laser heads to the Fibre Switch unit. There are in total 12 rack fibres each of which is 1 m long, connecting the four lasers to a beam splitter each, from which the light is routed through an attenuator and then fed into the Fibre Switch. Each beam splitter splits the laser light into two outputs, a low-fraction output and a high-fraction output. Dependent on the laser head power, different beam splitters are connected to each laser: the laser with the highest power is connected to a very asymmetric beam splitter, leading to a huge difference in light intensity passed through the two outputs and the laser with the lowest power is connected to the most symmetric beam splitter, parting the light into more equal intensities.

For each beam splitter, the higher intensity output is fed into the MPU to monitor the lasers on a per pulse basis. The low-fraction light from each beam splitter is passed on to the attenuators. The attenuators allow manual fine adjustment of the light intensities to control the light input into the detector and avoid damage to the PMTs. Output from the attenuators is passed on to one of the 5 inputs at the Fibre Switch. 12 of the 14 outputs of the Fibre Switch are connected to the detector fibres.

### Detector Fibres

Each of the 12 detector fibres is 45 m long and feeds the light from the Fibre Switch on deck into the detector. These fibres are mounted on the PSUP at four different injection points on so-called “S7” node panels, a construction consisting of 7 PMTs, installed on the side of a PMT hex cell [117]. Therefore, each mounting point houses three fibres, which are pointed in three different directions: 10°, 0° and 20°, where 0° points straight to the center of the detector. This allows for the light to cover different path lengths across different detector materials, with the longest path length being covered by a 0° fibre [66][118]. The mounting plates used to fix the fibres on

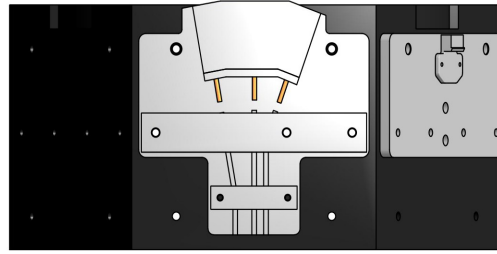


**Figure 4.4:** The SMELLIE mounting plate on the side of a PMT hex cell. The TELLIE plate is included to the right of the SMELLIE plate.

the hex cells is shown in Figure 4.4.

The detector end of the fibres is bonded to collimators, which were designed by Ken Clark at the University of Oxford. The purpose of these collimators is to reduce the emission angle of photons of the SMELLIE beams to provide the necessary narrow beam. To collimate the light, the collimators are designed as a GRIN lens<sup>6</sup>, with the shape of a cylindrical rod made of quartz with varying refractive indices. Because the refractive index on the edges of the rod is smaller than in the center, the light at the edges travels at higher speed, resulting in the same effect which would occur when a convex lens was used. With this method, a beam spread of  $3^\circ$  in air could be achieved for all fibres.

The fibres are referred to according to the PMT “S7” node they are installed on (07, 25, 37, 55) and according to their position on the mounting plate. Therefore, the  $10^\circ$  fibre on node 07 is referred to as FS107 (with FS indicating that the fibre is a SMELLIE fibre). Currently the fibres mounted on nodes 37 and 55 are installed, with the remaining 6 fibres being installed during water-fill [119]. However, during installation the fibres were not mounted in the right slot on the mounting plates according to their name label [120]. Hence, the naming convention for the node 37 and 55 fibres is not enforced. Table 4.1 gives an overview about which fibre label refers to what fibre position hereafter.

---

<sup>6</sup>GRIN – for Graded Refractive Index Lens.

**Table 4.1:** Summary of fibre labels for each node and their pointing angle.

Label	Node	Angle (°)
FS007	07	0
FS107	07	10
FS207	07	20
FS025	25	0
FS125	25	10
FS225	25	20
FS037	37	10
FS137	37	0
FS237	37	20
FS055	55	10
FS155	55	20
FS255	55	0

#### 4.2.4 Hardware Update

A recent upgrade to the SMELLIE system is a super-continuum laser to complement the fixed lasers, allowing for wider measurements of scattering beyond the wavelengths of the existing four lasers. It is a “SuperK Compact” laser manufactured by NKT Photonics. It is basically a “white light” laser source, covering a wavelength range of 400 nm - 2400 nm. A filter module is tuned to operate within 400nm - 700nm, passing a pulse with a variable bandwidth from 10nm - 100nm. It fires pulses at a rate within 1Hz and 24kHz. The filter module allows the user to select a fraction of the spectrum to pass into SNO+. Unlike the existing lasers, the SuperK pulses arrive with large variation in timing due to the non-linear way in which they are generated. Therefore the laser can only be run in master mode to reduce the time variation effect. Additionally to the SuperK laser, the wavelength spectrum must be monitored for each pulse. Therefore each pulse is partially split into an Ocean Optics spectrometer in addition to the monitoring PMT. The SuperK laser and the spectrometer were installed in the ELLIE rack in August 2015. This laser was not used in the analysis presented in the following Chapters.

# 5 Monte Carlo Modeling of the Scattering Module

The measurement of the Rayleigh scattering length in the detector requires the comparison of the real data SMELLIE events with simulated SMELLIE samples. In order to reduce systematic uncertainties on the measurement, the simulation needs to describe the data accurately. Methods were developed to extract the characteristics of each fibre from SMELLIE data to be implemented in the simulation as described in this chapter<sup>7</sup>.

## 5.1 Note on Coordinate Systems

Throughout the SMELLIE analysis two different sets of coordinates were used for both the extraction of the simulation parameters as well as the measurement of the scattering length. Both coordinate systems were used to define cuts on the photons emitted by the SMELLIE pulses and they represented key values in the simulation tuning process. Thus, both coordinate systems are briefly described here.

The detector coordinate system is centered around the PSUP. A Cartesian coordinate system described by  $\{x, y, z\}$  and a polar coordinate system using  $\Theta$  and  $\Phi$  are used to describe points within the detector. The z-axis of the Cartesian coordinate system is pointing from the center of the detector towards the AV neck. The Cartesian

---

<sup>7</sup>All analysis described in this Chapter and Chapter 6 was performed using the "SMELLIE Calibration Utensils for Normal scattering length Calculation" (SCUNC) framework written by the author.

and polar coordinates are linked via these relations:

$$\begin{aligned} x &= r \cdot \sin\Theta \cdot \cos\Phi \\ y &= r \cdot \sin\Theta \cdot \sin\Phi \\ z &= r \cdot \cos\Theta, \end{aligned} \tag{5.1}$$

where  $r$  represents the radius of the PSUP and was set to 8400 mm. The SMELLIE fibre positions were implemented in the simulation using the  $\{x, y, z\}$  detector coordinates.  $\Theta$  and  $\Phi$  distributions of photons emitted by the SMELLIE system represent the position of the PMTs within the detector coordinate system, which were hit by these photons.

The second coordinate used is a coordinate describing the detector with respect to the direction of the investigated SMELLIE fibre. It is referred to in the following as the beam angle  $\alpha$  and is defined as the angle between the fibre direction vector  $\vec{a}$  and the vector  $\vec{b}$  between the fibre position and the position of the PMT which is hit by an emitted photon as presented in Figure 5.1. This coordinate was used to select photons from the SMELLIE beams which have undergone different optical interactions and to extract the angular profiles of the fibres as described in Section 5.3.2.

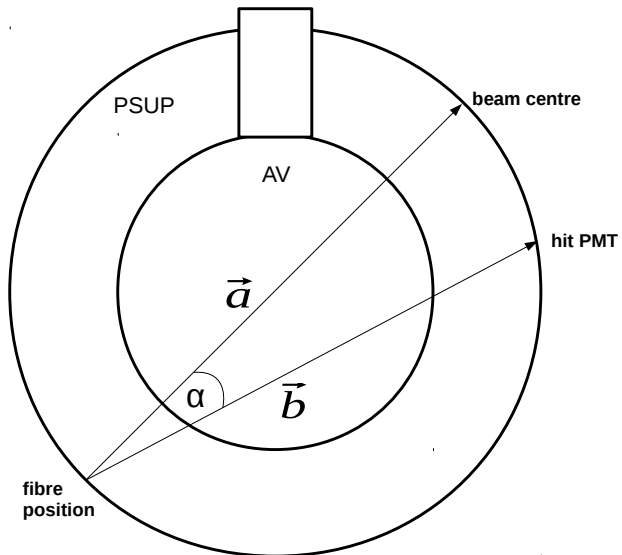


**Figure 5.1:** Definition of the beam angle  $\alpha$ .

## 5.2 Simulation Principles

The simulations are produced as part of the SNO+ simulation package RAT, which is described in more detail in Section 3.6. SMELLIE light pulses are simulated as a specified number of photons which are emitted from a fibre injection point along the pointing direction of the fibre. Properties of the photons, such as wavelength and emission angle are assigned to each emitted photon separately using values from given probability arrays<sup>8</sup>. Each light pulse is defined by a group of properties including system variables like the beam intensity and pulse rate of the beams, laser specific characteristics such as wavelength and intra-pulse timing distributions, and the fibre specifics including the angular distributions of the collimators and the fibre positions and directions. The laser and fibre specific properties of the SMELLIE system were added to RAT as part of the work carried out for this thesis. The methods used to define the laser and fibre properties before the availability of data are described in Appendix A.1 for further reading.

The intensity of the SMELLIE beam pulses is simulated as the number of photons emitted into the detector per pulse. This number is specified by the user when running the simulation. The photons per pulse are then fluctuated according to a Poisson distribution. The intensity selected during a SMELLIE hardware run when taking data denotes the percentage of laser power used during that run. Hence, in order to create simulations with the exact intensity used during a data run, a translation between the hardware laser intensity and the number of photons seen in the detector is necessary. This can be achieved using the Monitoring PMT in the hardware setup described in Chapter 4 [113], as well as a  $n_{\text{hits}}$  based approach as introduced in Section 5.3.3. Furthermore, the pulse rate of the SMELLIE beams is defined in the simulation according to the pulse rates used in the data runs. Noise hits at a constant rate determined from detector measurements as well as the trigger response of the detector (including the trigger generated from the SMELLIE system) can also be implemented in the simulation.

---

<sup>8</sup>For example, the exact wavelength a photon is emitted at is assigned according to the probability a photon is emitted at this wavelength.

## 5.3 Tuning of the Simulations using Commissioning Data

### 5.3.1 Fibre Directions

The fibre positions and directions were initially determined using the installation notes and mounting plate dimensions as described in Appendix A.1<sup>9</sup>. However, comparing simulations of these positions and directions with commissioning data taken in March 2014 of all six installed fibres showed a mis-match in the position of the fibre beam spots. Figure 5.2 shows the  $\Theta$ -coordinates of the PMTs hit by direct beam light for all six currently installed fibres for simulation and the data taken in March 2014. The  $\Phi$ -coordinates of the in-beam light of the same simulations and data samples are shown in Figure 5.3.

The simulations were produced with 2000 photons per beam pulse over 10 000 events in an air-filled detector using RAT 5.0.1. The data displayed was taken on the 20<sup>th</sup> of March 2014 (A summary of the runs investigated in this section is given in Table A.2). A pre-selection was applied to the data, including cuts on the trigger and the  $n_{\text{hits}}$  in the detector (the exact cut value on the  $n_{\text{hits}}$  for each run is also presented in Table A.2), to reject non-SMELLIE events. In the absence of timing calibration a basic cut on the PMT hit time  $> 0$  was employed to remove spurious hits. The direct beam (in-beam) light was then selected for both data and simulation using spatial and timing constraints which are outlined further in Chapter 6.

The discrepancy between data and simulation was more prominent in  $\Theta$  for node 37 whilst a bigger shift in  $\Phi$  was observed for the node 55 fibres. The scale of the deviation appeared larger for the node 37 fibres. Pictures taken during detector shifts showed consistencies with the mounting plate positions recorded during fibre installation [119][121]. Thus, the expected position deviation from the database values must be minimal. Previous studies confirmed that the position of the fibres has little influence on the beam spot position, the defining factor is the fibre direction [122][123]. Therefore, the fibre directions implemented in the simulation were corrected using the commissioning data.

---

<sup>9</sup>These values will be referred to as database values in the following, since they were added to the RAT database to construct MC simulations.

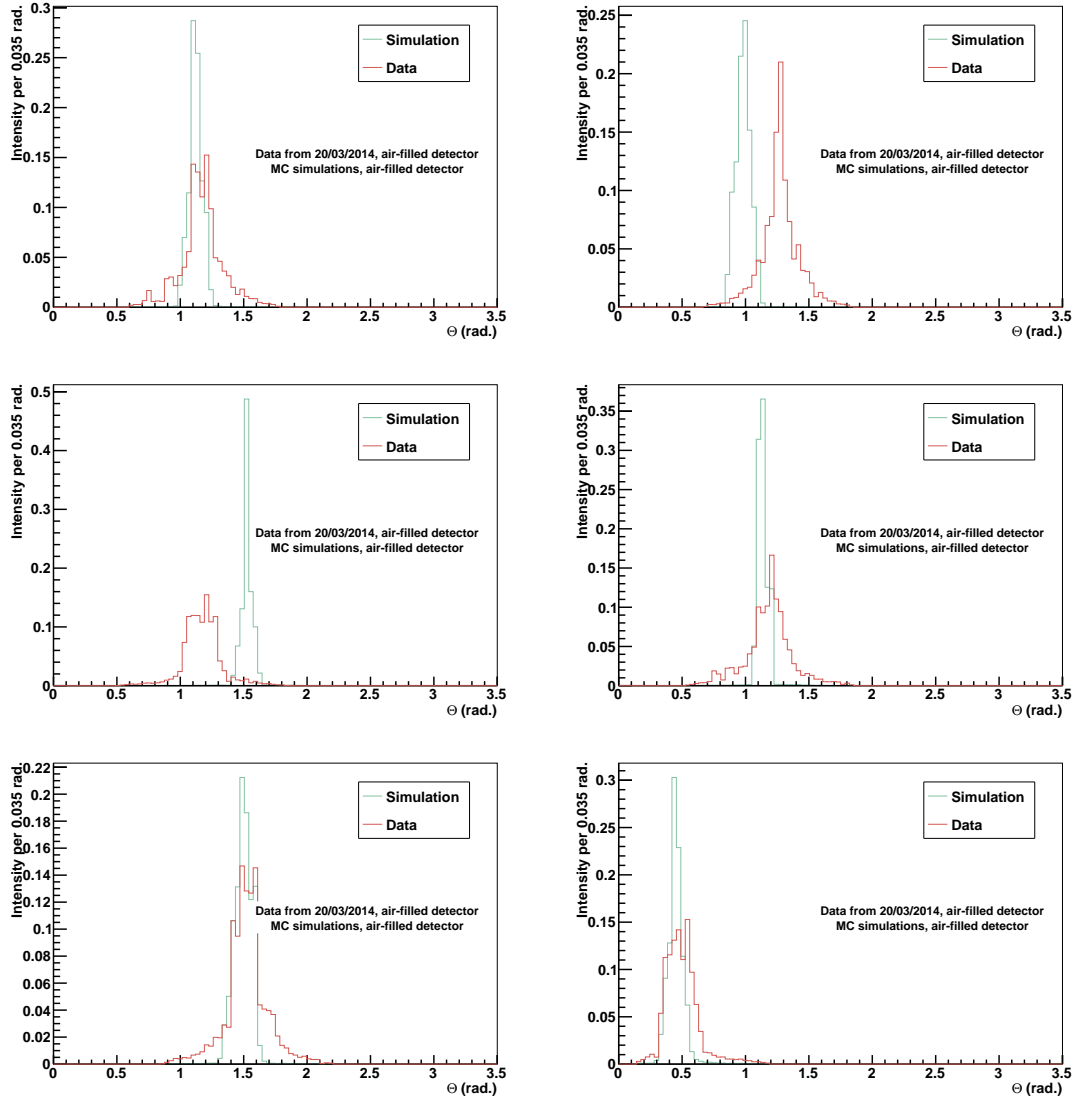


**Figure 5.2:** The  $\Theta$  distributions for all six installed fibres at 495 nm for data and the simulations. The top row shows FS137 (left) and FS037 (right), the middle row shows FS237 (left) and FS255 (right) and the bottom row shows FS055 (left) and FS155 (right). All distributions were scaled to the number of entries in each histogram.

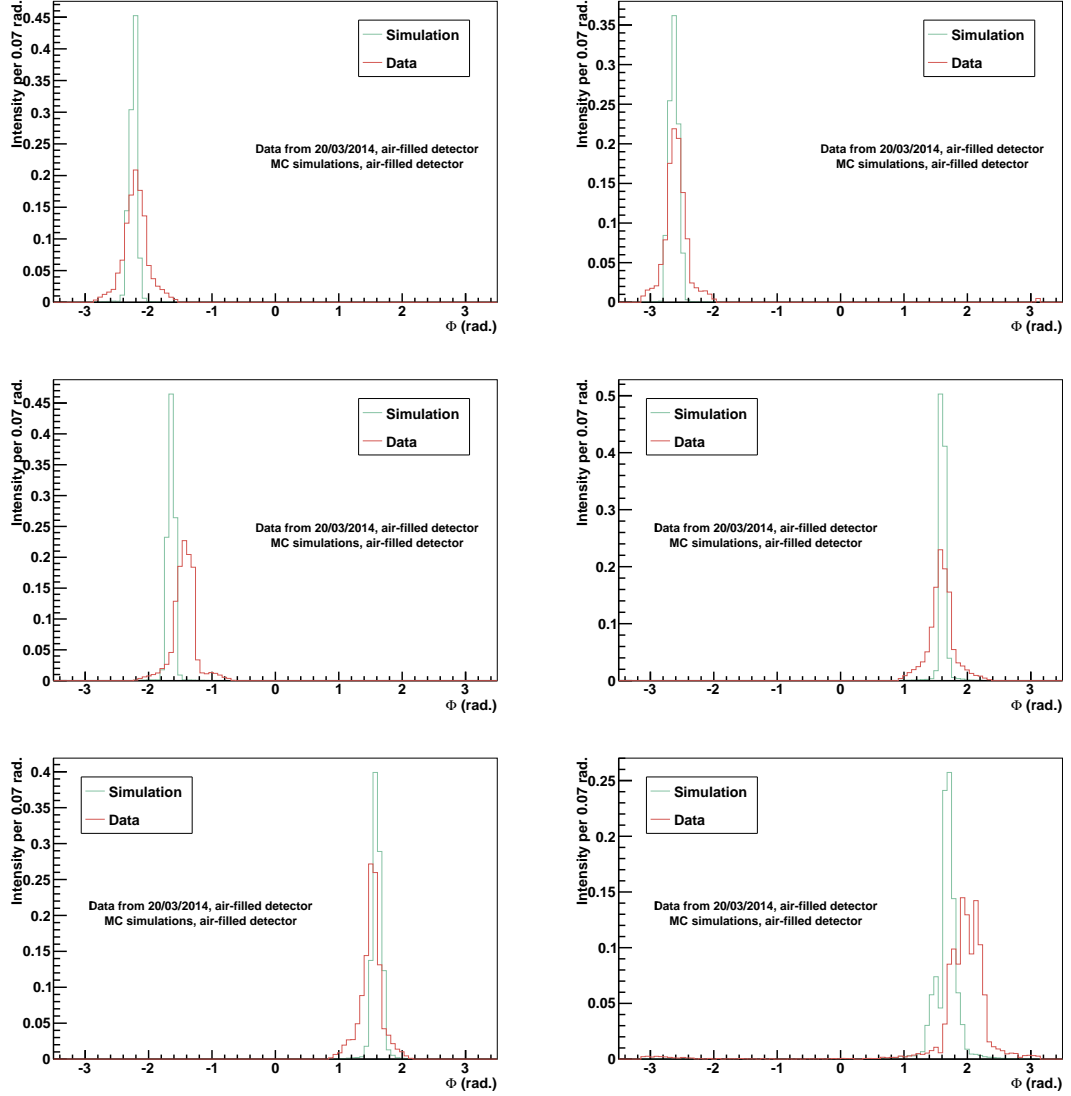


**Figure 5.3:** The  $\Phi$  distributions for all six installed fibres at 495 nm for data and the simulations. The top row shows FS137 (left) and FS037 (right), the middle row shows FS237 (left) and FS255 (right) and the bottom row shows FS055 (left) and FS155 (right). All distributions were scaled to the number of entries in each histogram.

**Table 5.1:** Initial fit results from the  $\Theta$  and  $\Phi$  fits for data and simulation. All shown results are averaged over all available wavelengths for each fibre (for information on the uncertainty evaluation, see Appendix A.4).

Fibre	$\Theta$ (rad.)		$\Phi$ (rad.)	
	Data	Simulation	Data	Simulation
FS137	$1.17 \pm 0.08$	$1.13 \pm 0.08$	$-2.20 \pm 0.11$	$-2.24 \pm 0.09$
FS037	$1.26 \pm 0.07$	$0.99 \pm 0.07$	$-2.60 \pm 0.08$	$-2.63 \pm 0.09$
FS237	$1.17 \pm 0.06$	$1.53 \pm 0.07$	$-1.44 \pm 0.07$	$-1.65 \pm 0.08$
FS255	$1.18 \pm 0.08$	$1.15 \pm 0.08$	$1.59 \pm 0.09$	$1.61 \pm 0.10$
FS055	$1.53 \pm 0.08$	$1.49 \pm 0.08$	$1.51 \pm 0.09$	$1.60 \pm 0.09$
FS155	$0.47 \pm 0.06$	$0.48 \pm 0.08$	$1.99 \pm 0.11$	$1.63 \pm 0.21$

### Direction calculation

The  $\Theta$  and  $\Phi$  distributions of the in-beam light as shown in Figures 5.2 and 5.3 were fitted with a Gaussian function using ROOT for the data obtained for all six installed fibres at 407 nm, 446 nm and 495 nm (data runs 7110 - 7149, Table A.2). The means of these Gaussian fits represent the center of the beam in the  $\Theta$  and  $\Phi$  detector coordinates for each fibre. The resulting Gaussian means in  $\Theta$  and  $\Phi$  were averaged over all wavelengths for each fibre respectively. Additionally, the fits were repeated for simulations for all node 37 and node 55 fibres at 407 nm, 446 nm and 495 nm and their means in  $\Theta$  and  $\Phi$  were averaged accordingly. The mean  $\Theta$  and  $\Phi$  coordinates for data and simulation are presented in Table 5.1 (uncertainties on the fit values followed from the standard deviation as described in Appendix A.4). The observations regarding the shift margins in  $\Theta$  and  $\Phi$  made from Figures 5.2 and 5.3 was confirmed by the results in Table 5.1.

The values in Table 5.1 determined for the data were used to calculate the center of the beam spot in Cartesian coordinates using Equation 5.1. To achieve the fibre directions  $\vec{r}$ , the fibre positions  $\vec{f}$  as implemented in the database were used:

$$\vec{r} = \frac{\vec{p} - \vec{f}}{|\vec{p} - \vec{f}|}, \quad (5.2)$$

where  $\vec{p} = \{x, y, z\}$  is the vector pointing to the center of the beam spot consisting of

**Table 5.2:** Angles between the center fibre and the two angled fibres for both nodes for the directions extracted from data and for the database directions (for information on the uncertainty evaluation, see Appendix A.5).

Directions	Node 37		Node 55	
	10° fibre	20° fibre	10° fibre	20° fibre
Data	$11.0 \pm 2.2^\circ$	$20.0 \pm 2.6^\circ$	$10.0 \pm 2.7^\circ$	$21.8 \pm 2.0^\circ$
Database	$10.0^\circ$	$20.0^\circ$	$10.0^\circ$	$20.0^\circ$

the coordinates determined by Equation 5.1 (the fibre directions are listed in Table A.3).

### Verification of the Directions

**Angle between Fibres** Due to the construction of the mounting plates as shown in Figure 4.4, the angles between the fibres on each plate are fixed to  $10^\circ$  and  $20^\circ$  with respect to the center fibre [117]. Thus, the angles between the different directions should represent  $10^\circ$  and  $20^\circ$ . To determine the angles between the fibres, the geometric definition of the scalar product of two vectors was used. The resulting angles are shown in Table 5.2 for the directions calculated from the data and the directions from the database.

The angles determined from the data matched the nominal values within the uncertainties carried through from the original Gaussian fits (as calculated in Appendix A.5). The largest deviation could be found for the  $20^\circ$  fibre on node 55. This fibre points towards the top edge of the detector near the AV neck, leading to a slightly broader profile in the  $\Phi$ -coordinate which can be seen on the bottom right in Figure 5.3. Due to the detector geometry close to the AV neck, and the asymmetrical nature of the angular profile as discussed in Section 5.3.2, the fit on the fibre direction might have deviated slightly from the center. However, since all calculated angles matched the nominal values within the given uncertainties, the new determined directions do not compromise the integrity of the mounting plate.

**Fibre Directions with respect to the Hex Cell** The obtained fibre directions were used to attempt a conclusion on the cause of the position discrepancies. Since the discrepancies were of different orders of magnitude for the node 37 and node 55 fibres,

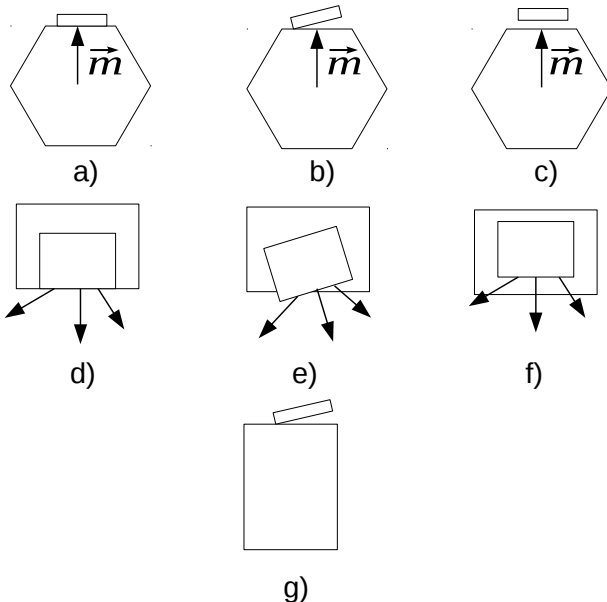


**Figure 5.4:** Possible positions of the mounting plate on top of the PMT hex cell. The top row shows the front face of the PMT with the mounting plate on top as it would be seen from the center of the detector. The middle row gives a top view of the PMT hex cell, with the mounting plate pointing the fibres (shown as arrows) downwards to the center of the detector. The bottom row depicts the side view of the PMT hex cell with the center of the detector being on the right.

the deviations were not a consequence of assumptions made for the initial calculation method. However, the observed discrepancies between simulation and data could be due to a physical misplacement of the mounting plate on the hex cell.

Figure 5.4 shows several possible positions of the mounting plate on the PMT hex cell. Positions a) and d) show the orientation assumed for the initial calculations for the database. All other drawings depict potential shifts in the mounting plate position that could lead to some deviations in the beam spot positions of the fibres. Pictures c) and f) may not lead to any discrepancies, since it has already been proven that pure position divergence does not have a considerable impact on the position of the beam spot [123]. It is more feasible to assume that, additionally to a position variation, the fibre directions are altered as would be the case in sub figures b), e) and g).

The fibre directions were used to determine the angle between the fibre directions

**Table 5.3:** Angles between each fibre direction and the vector  $\vec{m}$  pointing from the center of the PMT to the hex cell face the mounting plate is installed on for all directions listed in Table A.3 (for information on the uncertainty evaluation, see Appendix A.5).

Directions	Node 37		
	0° fibre	10° fibre	20° fibre
Data	$89.3 \pm 2.0^\circ$	$82.5 \pm 1.5^\circ$	$102.0 \pm 1.6^\circ$
Database	$89.999^\circ$	$89.999^\circ$	$89.999^\circ$

Directions	Node 55		
	0° fibre	10° fibre	20° fibre
Data	$89.4 \pm 2.5^\circ$	$87.3 \pm 2.5^\circ$	$94.5 \pm 1.5^\circ$
Database	$89.998^\circ$	$89.998^\circ$	$89.998^\circ$

and the vector pointing from the center of the PMT host hex cell to the hex cell face the plate was installed on (denoted as  $\vec{m}$  in Figure 5.4). If the plate is parallel to the PMT hex cell, this angle should be  $90^\circ$  for all fibres, since the fibres would be aligned with the hex cell face. The resulting angles, evaluated using the definition of the scalar product between two vectors, are presented in Table 5.3.

For both nodes, the angle found for the  $0^\circ$  fibre matched  $90^\circ$  within the given error margins and was very close to the nominal values found for the database. However, the  $10^\circ$  and the  $20^\circ$  fibres showed significant discrepancies for both nodes. On both nodes the angle found for the  $10^\circ$  fibre suggested it is pointing towards the center of the hex cell, since their values are below the expected  $90^\circ$ . Likewise, the increased angle for both  $20^\circ$  fibres suggested these fibres are pointing away from the center of the hex cell. This is consistent with the observations made in [123] for node 37, where the deviations for the two angled fibres occur in opposite directions. Based on these observations, the cause of the direction deviation was considered to be the scenario shown in Sub-figure 5.4 b).

It has been mentioned by the crew who installed the fibres, that the screws securing the mounting plates on the PMT hex cells allowed some movement for the mounting plate once fixed. This could be the potential cause for the observed discrepancies. However, this also leads to the assumption that the changing pressures during the water-fill phase may be strong enough to alter the plate positions, leading to an-

other change in fibre directions. Hence, it is recommended to repeat the direction measurement after water-fill is complete on all 12 then installed fibres.

### 5.3.2 Angular Profiles of Fibre Collimators

The angular profiles of each fibre collimator were implemented in RAT using profiles measured at the University of Oxford and the method described in Section A.1.3. However, by reproducing the  $\Theta$  and  $\Phi$  distributions of the in-beam light using simulations with the corrected fibre directions from Section 5.3.1, more discrepancies between data and simulation could be observed. This can be seen in Figures 5.5 and 5.6, which show the  $\Theta$  and  $\Phi$  distributions of data and simulation at 495 nm for all six fibres respectively. In comparison, the data showed wider profiles than the simulation with more photons emitted at higher angles. Thus, it was decided to use a data driven approach to implement the collimator profiles in the simulation.

Since the angular profile is simulated with respect to the fibre direction, the beam angle  $\alpha$  was used to extract the profile from the data. Due to the circular geometry of the detector, each  $\alpha$  covers a different number of PMTs. In order to achieve a smooth angular distribution, the profile was extracted into histograms with variable angle bins, with each bin covering 5 PMTs in the detector geometry<sup>10</sup>. Each of these bins was subsequently corrected by the number of working PMTs per bin<sup>11</sup>.

All extracted profiles had to be corrected for potential multiple hits, before being translated into the probability array used in the simulation. This correction was necessary to account for secondary or higher order photons hitting a PMT during an event. Each PMT can only fire once per event (as described in Section 3.3.2), however, events with high light yields result in multiple photon hits on one or more PMTs during the event. Correcting for these missed photons was important for the extraction of the angular profiles to avoid distortion of the profile.

The correction was applied using the occupancy of each PMT over the entire run. The occupancy,  $P_i$ , is the probability a PMT  $i$  is hit during an event:

$$P_i = \frac{\text{Number of hits for PMT } i \text{ over entire run}}{\text{Number of events in run}} \quad (5.3)$$

---

<sup>10</sup>A discussion of the optimal number of PMTs per angular bin is given in Appendix A.6.1.

<sup>11</sup>PMTs can be turned off due to electronical issues or physical damage.

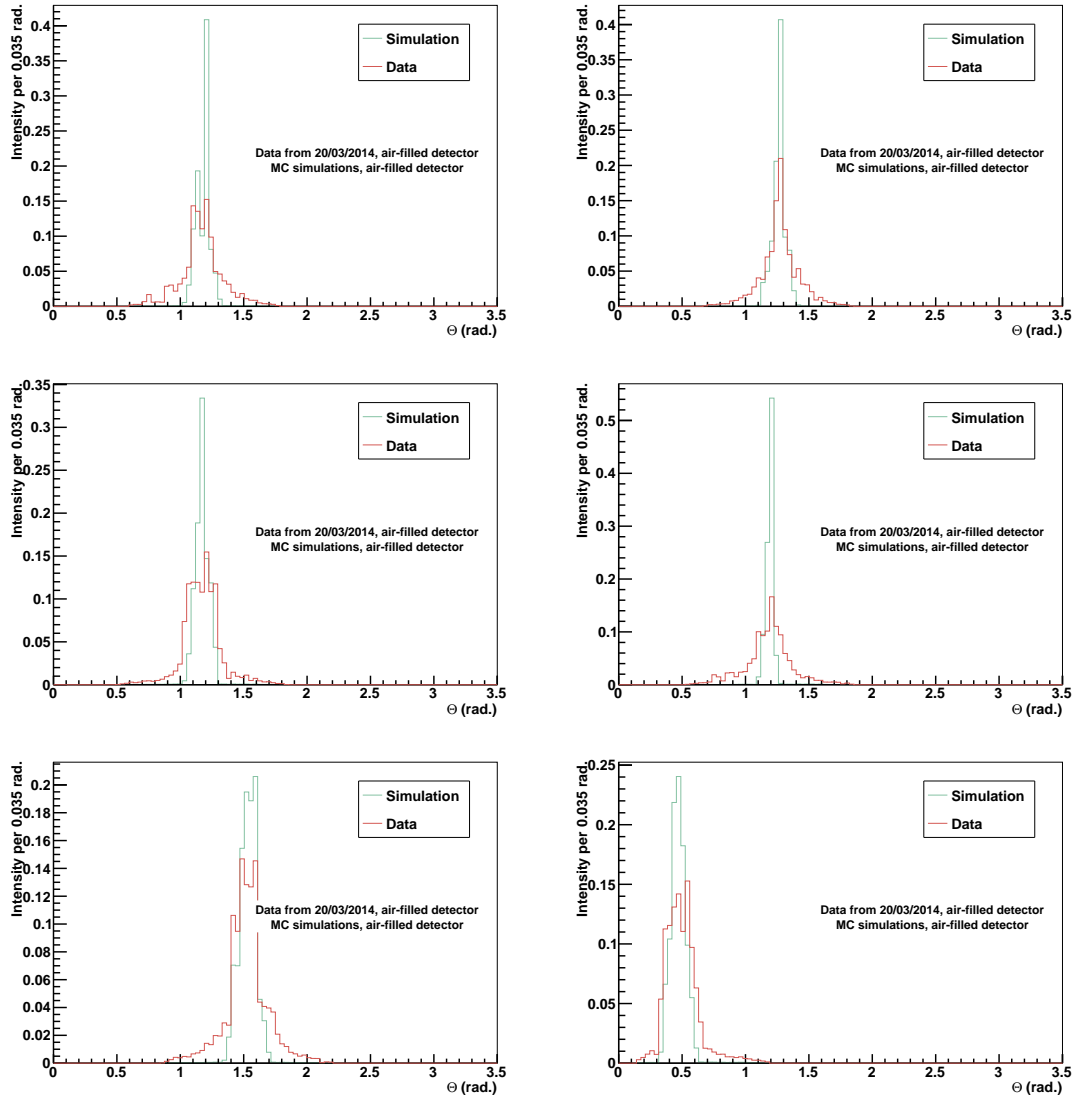


**Figure 5.5:** The  $\Theta$  distributions for all six installed fibres at 495 nm for data and the simulations produced using the directions calculated in Section 5.3.1. The top row shows FS137 (left) and FS037 (right), the middle row shows FS237 (left) and FS255 (right) and the bottom row shows FS055 (left) and FS155 (right). All distributions were scaled to the number of entries in each histogram.

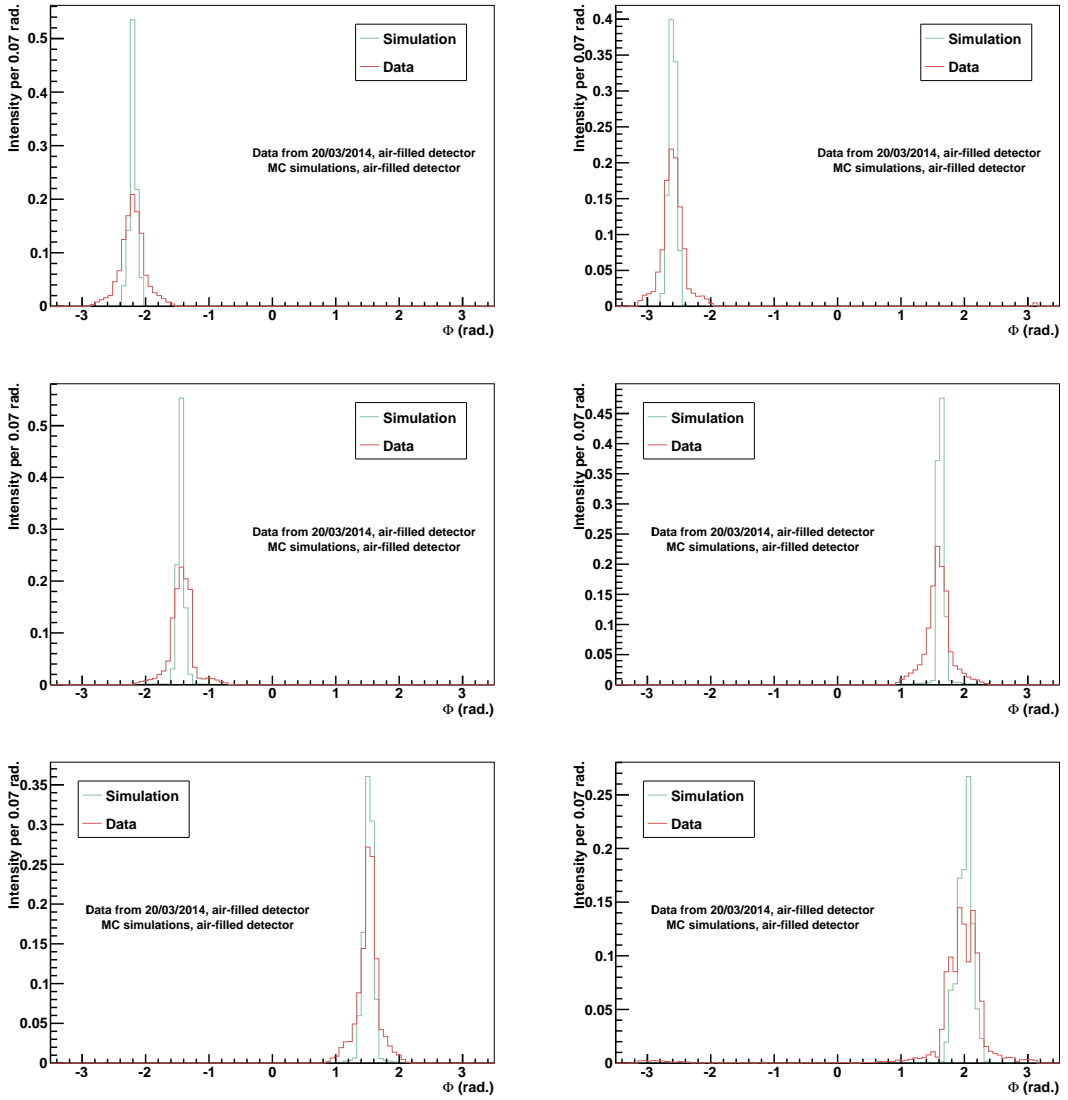


**Figure 5.6:** The  $\Phi$  distributions for all six installed fibres at 495 nm for data and the simulations produced using the directions calculated in Section 5.3.1. The top row shows FS137 (left) and FS037 (right), the middle row shows FS237 (left) and FS255 (right) and the bottom row shows FS055 (left) and FS155 (right). All distributions were scaled to the number of entries in each histogram.

This probability can be expressed using the probability that the PMT does not fire when hit by  $\mu$  amount of photons:

$$P_i = 1 - P(0) = 1 - e^{-\mu_i} \quad (5.4)$$

Hence, the occupancy  $P_i$  could be used to derive the number of photons  $\mu_i$  which hit PMT  $i$ . This assumption breaks down if the occupancy for one or multiple PMTs is equal to 1. In this case, the PMT was hit during every event in the run and all information about multiple photon hits on that PMT was lost. To apply the correction, hits in each PMT were corrected by a factor  $c_i$  containing the number of photons and the hit probability for the given PMT:

$$c_i = 1 + (\mu_i - P_i) \quad (5.5)$$

Only a few runs for fibres FS155, FS037 and FS237 did not reach occupancy values of 1 for any of the PMTs (for further reading, the maximal occupancies for each run are also presented in Table A.2). A comparison between the low intensity run at 28 % laser intensity (with occupancy values below 1) and the high intensity run at 100 % laser intensity (reaching occupancy values of 1) for FS237 is shown in Figure 5.7. This Figure shows the extracted angular profiles in  $\alpha$  normalised to their maximum. As expected, if the intensity is so high that the PMTs at the beam center are hit for every event, the measured intensity impact on these PMTs will not increase with higher photon yields and the tails of the beam distribution appear to have higher relative intensity.

The angular profile extracted from the lowest intensity runs for the fibres FS155, FS037 and FS237 are presented on the left in Figure 5.8, together with the profiles extracted from the Oxford measurements for the respective fibre. On the right of Figure 5.8 are the CCD images taken in Oxford from the position furthest from the fibre for all of the three presented fibres. For all three fibres the Oxford profile dropped in intensity at very small angles in comparison to the data profiles. The data profiles showed details which could also be observed in the CCD images of the fibres. Especially the asymmetrical effects seen in the data profiles for FS237 and FS155 with a less intense center could be seen in the CCD images. Due to the narrow nature of

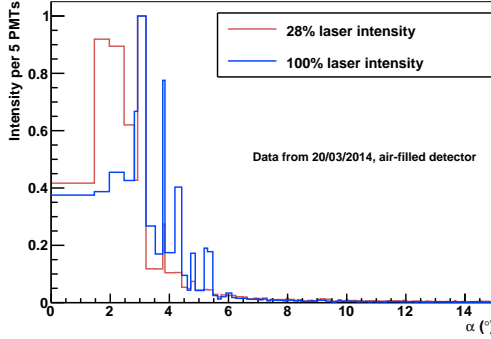


**Figure 5.7:** Angular profiles extracted for FS237 at 446 nm for 20 % and 100 % laser intensity. The angular bins were defined, so that each bin would cover 5 PMTs in the detector geometry, based on the directions of the fibres in the detector.

the Oxford profiles, all these observed details could be lost within the first angular bin<sup>12</sup>.

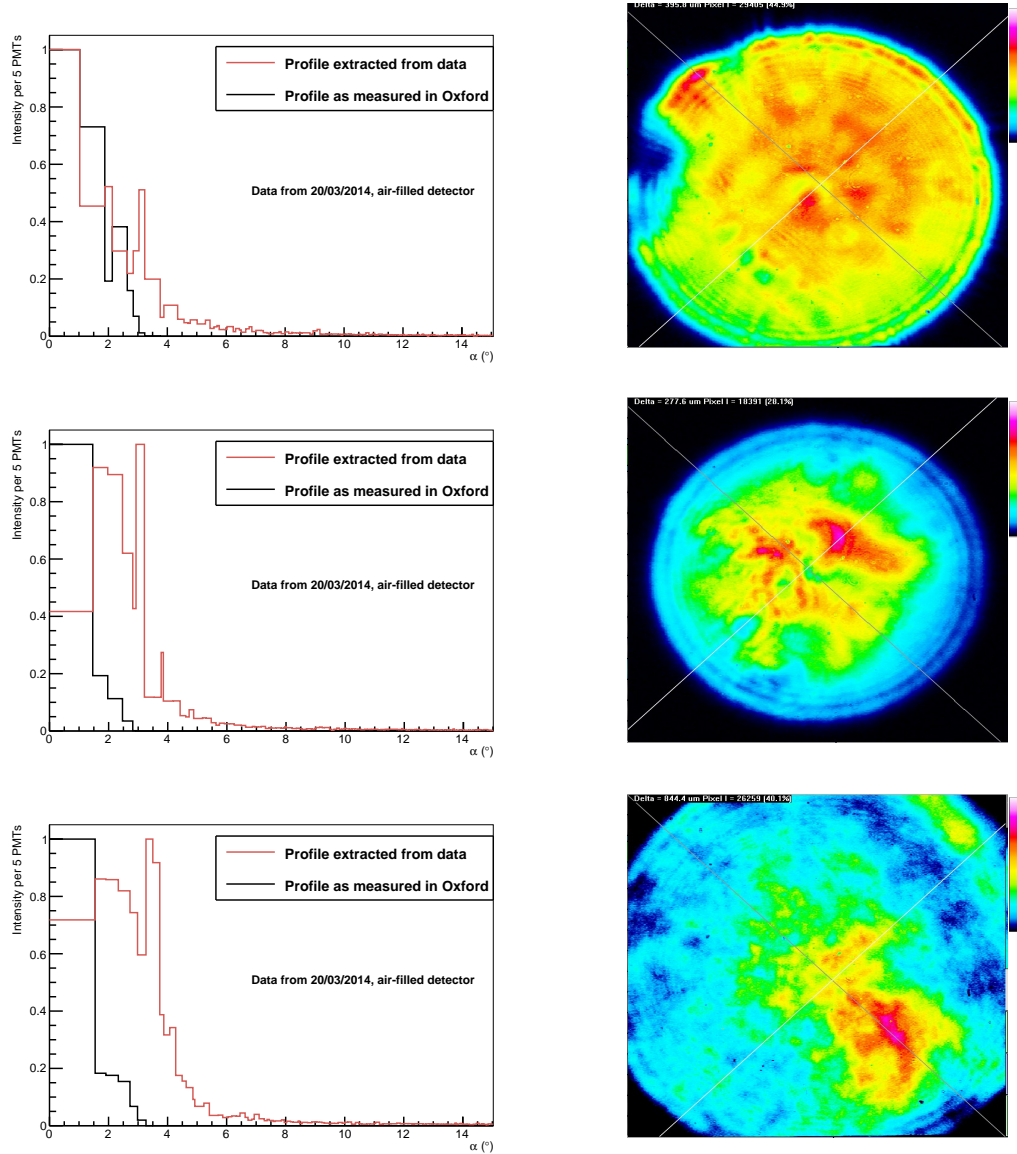
The asymmetrical features of the angular profiles as well as the speckled nature are thought to be results of the collimator construction. Furthermore, an investigation has been carried out to determine the cause of the spread in angular profiles in comparison to the Oxford measurements. For the Oxford measurements the light was passed from the laser through the fibre and then measured with the CCD. In the detector, the light passes more hardware components such as the attenuators, leading to a potential widening of the profiles. Confirmation and further investigations are to follow [124].

Figure 5.9 shows the  $\Theta$  and  $\Phi$  distributions of the direct beam light for FS037, FS237 and FS155 comparing the simulation with the new angular profiles applied to the data for a wavelength of 495 nm. The MC were simulated using the intensities as measured in Section 5.3.3. For all six distributions the simulated beams now covered the same angular range as the respective data profiles, suggesting that the width of the beam profiles agree between data and simulation.

Discrepancies in Figure 5.9 in the observed intensities per bin between data and simulation arose from multiple hits effects. The data runs for both FS037 and FS237 at 495 nm reached occupancy values of  $P_i = 1$  (see Table A.2), leading to a break

---

<sup>12</sup>Compare also Figure A.10 showing the Oxford profiles and CCD images of the three remaining fibres on nodes 37 and 55. Especially for fibre FS255 the entire profile seems to be condensed to the first two angular bins.



**Figure 5.8:** The angular profiles for FS037 (top), FS237 (middle) and FS155 (bottom). Presented on the left are the converted profiles from the Oxford measurements compared to the profiles extracted from the data. Each angular bin covers 5 PMTs with respect to the fibre directions. The right shows the CCD images recorded in Oxford for the measurement point furthest away from the fibre. The colour scale represents how much light was exposed on each point of the CCD. Areas in red were hit by the most photons, whilst areas in blue were hit by very few photons.

down of the multiple hits correction as described above. As observed for the high intensity angular profile in Figure 5.7, the tail of the distributions appeared more intense, whilst the intensity of the central beam region was lower in comparison to the simulation. FS155 did not reach occupancy values of  $P_i = 1$  for the 495 nm data run, yielding a valid multiple hits correction for each PMT and therefore matching the data well to the simulation.

In order to achieve profiles for all fibres, low intensity data runs are necessary. The next data taking period will be during the water phase, altering the already measured profiles of fibres FS037, FS237 and FS155 due to the different refractive index of water. Thus, the profile measurements will have to be repeated for all six fibres. The shape of the angular profiles should be considered as a systematic on the scattering length measurement due to uncertainties arising from the measurement procedure.

### 5.3.3 Intensity Measurement

To replicate the SMELLIE data in the simulation, the laser power used during a run needs to be translated to the number of photons emitted into the detector per beam pulse (nppb). A measurement strategy was developed as described in this section to use SMELLIE intensity scan runs to acquire a mapping of laser intensity to nppb for each fibre-wavelength combination. These nppb values can then be used to replicate any SMELLIE data at a given laser intensity in the simulation.

#### Basic Principle

The measurement was based on the mean total number of hits,  $n_{\text{hits}}^{\text{meas}}$ , emitted into the detector during a run. A range of MC simulations with different intensities between 100 nppb and 10 000 nppb, simulated with 10 000 events each, was used as reference. For each of these samples the mean number of hits  $n_{\text{hits}}^{\text{mean, sim}}$  was extracted and plotted against the nppb that the respective sample was produced with. The resulting distribution was fitted to a logarithmic function:

$$f(x) = p_0 \cdot \log(p_1 + p_2 \cdot x), \quad (5.6)$$

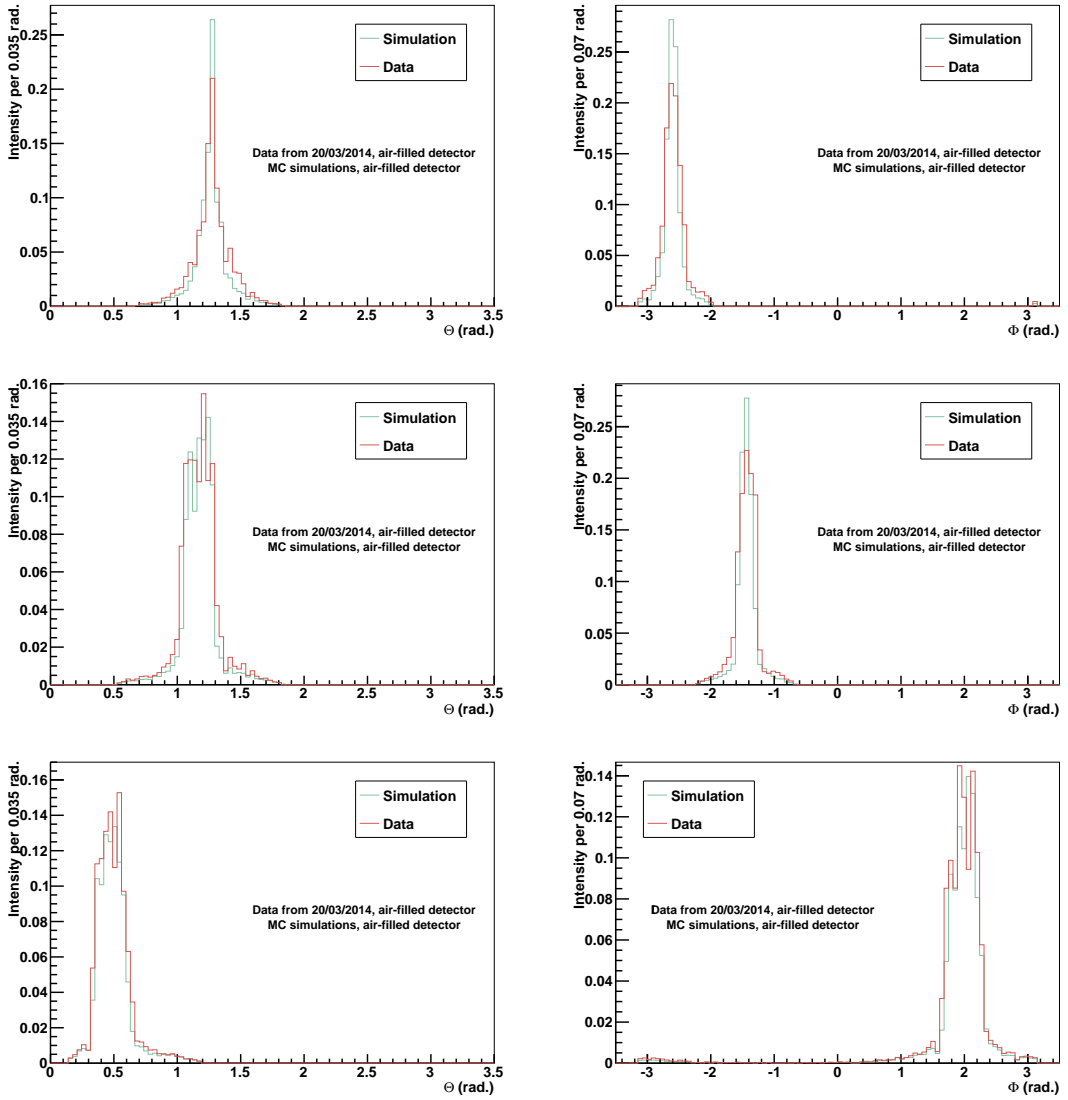


**Figure 5.9:** The  $\Theta$  (left) and  $\Phi$  (right) distributions for FS037 (top), FS237 (middle) and FS155 (bottom) at 495 nm for data and the simulations. The angular profiles measured from runs 7112, 7116 and 7179 as presented in Figure 5.8 were applied to the simulation. The simulation was produced with intensities measured from data as described in Section 5.3.3. All distributions were scaled to the number of entries in each histogram.

with the fit parameters p0, p1 and p2. This was repeated for each fibre-wavelength combination.

Subsequently, the mean number of hits  $n_{\text{hits}}^{\text{mean, data}}$  was obtained from the data samples. The value of  $x$  for which

$$n_{\text{hits}}^{\text{mean, data}} = f(x) \quad (5.7)$$

represented the equivalent nppb with which the data was produced. This method was tested for both an air-filled and a water-filled detector, for which the results are discussed below. In both cases, fake data sets with random intensities chosen at 845 nppb (data set 1), 1 765 nppb (data set 2) and 3 589 nppb (data set 3) were used to verify the method.

To evaluate the uncertainty on  $x$ , the standard deviation of the number of hits distributions was used:

$$\sigma = \sqrt{\sum_i^N (n_{\text{hits}}^i - n_{\text{hits}}^{\text{mean}})^2 / N}, \quad (5.8)$$

with the index  $i$  running over all  $N$  bins of the number of hits distributions [125]. Figure 5.10 shows the distributions obtained from the MC control samples for

$$\{n_{\text{hits}}^{\text{mean, sim}}, n_{\text{hits}}^{\text{mean, sim}} + \sigma^{\text{sim}}, n_{\text{hits}}^{\text{mean, sim}} - \sigma^{\text{sim}}\}$$

for FS237 at 446 nm in an air-filled detector. Using the fit function defined in Equation 5.6, the functions  $f(x)_{\text{up, down}}$  were obtained for the  $n_{\text{hits}}^{\text{mean, sim}} \pm \sigma^{\text{sim}}$  distributions. The uncertainty on the measurement of  $x$  was then determined by comparing

$$\begin{aligned} n_{\text{hits}}^{\text{mean, data}} &= f(x)_{\text{up, down}} \\ \text{and} \\ n_{\text{hits}}^{\text{mean, data}} \pm \sigma^{\text{data}} &= f(x) \end{aligned} \quad (5.9)$$

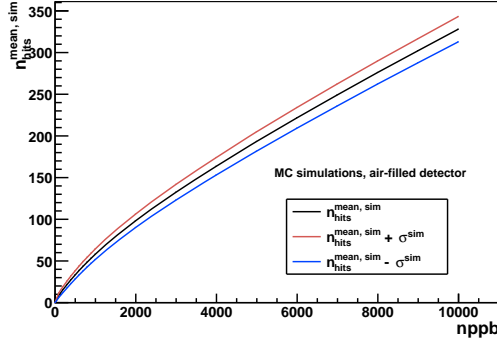


**Figure 5.10:** Mean number of hits versus number of photons simulated per beam pulse for FS237 at 446 nm in an air-filled detector. Shown are the curve resulting from the mean number of hits  $n_{\text{hits}}$  and the modified distributions used to evaluate the uncertainty on the measurement using the standard deviation  $\sigma$  of the  $n_{\text{hits}}$  distributions.

### Measurement in an air-filled detector

The angular profiles of the fibres have an impact on the  $n_{\text{hits}}$  distributions observed for each fibre. Thus, only FS037, FS237 and FS155<sup>13</sup> were considered for the intensity measurement. In order to demonstrate the measurement principle, the measurement was carried out on the air-fill commissioning runs taken in March 2014. First, possible limitations of the measurement are discussed and the method is verified using the fake data sets mentioned above.

**Limits in air-fill** The number of hits registered in the detector depends on a number of factors, one of which is the amount of scattering occurring within the detector. The scattering length in air (as presented in Table A.8 for several wavelengths close to the SMELLIE laser wavelengths) is in the order of  $10^{15}$  mm and so very little scattering is expected within the AV volume. Even halving or doubling these scattering length values has no impact on the amount of scattering that occurs across the AV with a diameter in the order of  $10^4$  mm and therefore the intensity measurement in air is not expected to be dependent on the scattering.

One interesting aspect of the intensity measurement is to find the nppb value, for which the occupancy reaches  $P_i = 1$ , since this limits the multiple hits corrections for the data and therefore the measurements carried out with the system. Thus, the

---

<sup>13</sup>The three fibres for which an angular profile could be extracted from the data, see Section 5.3.2.

**Table 5.4:** Maximum expected occupancy values  $P_i^{\max}$  in an air-filled detector for a range of intensities.

Simulated intensity (nppb)	FS037	FS237	FS155
1 100	$0.91 \pm 0.04$	$0.90 \pm 0.04$	$0.77 \pm 0.04$
1 200	$0.95 \pm 0.04$	$0.91 \pm 0.04$	$0.80 \pm 0.04$
1 300	$0.96 \pm 0.04$	$0.93 \pm 0.04$	$0.83 \pm 0.04$
1 400	$0.97 \pm 0.04$	$0.95 \pm 0.04$	$0.85 \pm 0.04$
1 500	$0.97 \pm 0.04$	$0.95 \pm 0.04$	$0.86 \pm 0.04$
1 600	$0.98 \pm 0.04$	$0.97 \pm 0.04$	$0.87 \pm 0.04$
1 700	$0.98 \pm 0.04$	$0.98 \pm 0.04$	$0.90 \pm 0.04$
1 800	$0.99 \pm 0.04$	$0.98 \pm 0.04$	$0.91 \pm 0.04$
1 900	$0.98 \pm 0.04$	$0.98 \pm 0.04$	$0.92 \pm 0.04$
2 000	$0.99 \pm 0.04$	$0.99 \pm 0.04$	$0.93 \pm 0.04$
2 100	$0.99 \pm 0.04$	$0.99 \pm 0.04$	$0.94 \pm 0.04$
2 200	$1.00 \pm 0.04$	$0.99 \pm 0.04$	$0.94 \pm 0.04$
2 300	$0.99 \pm 0.04$	$0.99 \pm 0.04$	$0.95 \pm 0.04$
2 400	$1.00 \pm 0.04$	$1.00 \pm 0.04$	$0.95 \pm 0.04$
2 500	$1.00 \pm 0.04$	$1.00 \pm 0.04$	$0.96 \pm 0.01$
2 600	$1.00 \pm 0.04$	$1.00 \pm 0.04$	$0.97 \pm 0.04$
2 700	$1.00 \pm 0.04$	$1.00 \pm 0.04$	$0.98 \pm 0.04$
2 800	$1.00 \pm 0.04$	$1.00 \pm 0.04$	$0.98 \pm 0.04$
2 900	$1.00 \pm 0.04$	$1.00 \pm 0.04$	$0.98 \pm 0.04$
3 000	$1.00 \pm 0.04$	$1.00 \pm 0.04$	$0.99 \pm 0.04$

maximum occupancy  $P_i^{\max}$  was calculated at each simulated nppb intensity using the PMT which has registered the most hits. The results for each fibre are listed in Table 5.4 for a selected range of simulated intensities.

Both node 37 fibres achieved high occupancy values at intensities above 2 000 nppb. Accounting for statistical uncertainties, data runs should not exceed 1 700 nppb for either fibre if the multiple hits corrections are applied. On the contrary, FS155 is a very low intensity fibre, reaching high occupancies around (2 700 – 3 000) nppb. This is a result of the low intensity, off-center angular profile extracted for this fibre in Section 5.3.2.

**Table 5.5:** Standard deviation  $\sigma$ , the bias  $b$  and the uncertainty  $u$  on the measured number of photons for the fake data sets for FS037, FS237 and FS155 in air-fill. All four simulated wavelengths, 375 nm, 407 nm, 446 nm and 495 nm, are presented.

Fibre	Wavelength (nm)	data set 1			data set 2			data set 3		
		$\sigma$	$b$	$u$	$\sigma$	$b$	$u$	$\sigma$	$b$	$u$
FS037	495	2.2	-32.2	133.2	2.5	-11.5	201.6	3.0	97.8	322.6
	446	1.9	-38.5	121.1	2.4	-13.3	182.5	3.6	107	293.5
	407	2.2	-35.8	122.9	2.1	-3.7	185.9	3.3	124.2	301.2
	375	1.8	-34.3	130.1	2.0	-7.3	196.5	2.6	113.8	317.9
FS237	495	1.9	-39.2	135.2	1.9	-4.3	204.2	4.4	137.6	333.1
	446	1.8	-51.1	125.0	2.0	-13.3	187.5	2.8	134.9	307.5
	407	1.7	-45.0	125.7	2.8	4.2	190.3	3.0	163.3	314.3
	375	1.3	-41.2	132.4	3.0	0.5	201.2	3.1	155.7	331.8
FS155	495	1.8	-31.1	129.6	2.6	-15.8	198.7	2.7	98.3	325.7
	446	1.3	-41.2	120.5	1.7	-25.0	184.7	5.3	86.0	306.8
	407	1.9	-35.2	120.5	1.8	-4.9	185.2	2.5	142.0	307.3
	375	2.2	-32.2	127.5	2.1	-8.4	196.0	2.2	125.0	324.9

**Verification using fake data sets** For each of the three fibres considered the fake data sets 1, 2 and 3 at the above mentioned nppb were produced for all four wavelengths used by the SMELLIE system. Each data set contained 10 000 events and for a statistical analysis of the intensity measurements,  $M = 20$  samples were generated for each fake data set. The fit values for  $f(x)$  and  $f(x)_{\text{up}, \text{down}}$  for each fibre-wavelength combination can be found in Tables A.4 - A.6.

The standard deviation  $\sigma$  and the bias  $b$  of the measurements were determined by plotting  $(x_{\text{sim}} - x_{\text{meas}})$  for all 20 data samples at each intensity. Here,  $x_{\text{sim}}$  is the intensity the fake data was simulated with and  $x_{\text{meas}}$  the measured value determined using the described method. The resulting distributions were fitted with a Gaussian, with the mean of the fit being equivalent to the bias  $b$  of the measurement and the standard deviation of the fit being equivalent to  $\sigma$ . All values of  $\sigma$  and  $b$  can be found in Table 5.5, alongside the average uncertainty  $u$  on the measurement.

Negative bias values indicate that the measurement approach overestimated the nppb, which was the case for low intensities (data set 1). On the contrary, a positive bias suggests an underestimation of the nppb as was the case for high intensities (data set 3). The closest results could be achieved with the medium intensity data set. The

**Table 5.6:** Measured number of photons per beam pulse for March 2014 air-fill data for fibres FS037, FS237 and FS155. Listed here are the resulting nppb values for the highest intensity runs available for each wavelength. The measured intensities for runs 7151 - 7179 are presented in Table A.9.

Fibre	407 nm	446 nm	495 nm
FS037	(1 221 $\pm$ 160) nppb	(3 884 $\pm$ 343) nppb	(3 281 $\pm$ 333) nppb
FS237	(1 482 $\pm$ 181) nppb	(4 650 $\pm$ 415) nppb	(3 928 $\pm$ 393) nppb
FS155	(666 $\pm$ 115) nppb	(2 293 $\pm$ 233) nppb	(2 335 $\pm$ 257) nppb

fluctuation in bias over different intensities was a result of the large fit range used, covering 0 nppb - 10 000 nppb. This large range sacrifices the measurement accuracy at low and high intensities. However, the measured bias was negligible in comparison to the uncertainties on the measurement.

**Measurements on the March 2014 data** The intensity measurement was carried out on the March 2014 data for FS155, FS037 and FS237. The resulting nppb for the intensity scan runs for fibre FS237 are shown in Table A.9 for further information. For all other runs of these fibres, the concluding intensities are presented in Table 5.6.

As expected from Section 5.3.2 and Table 5.4 FS155 emitted very little light. The light yields of FS037 and FS237 were similar, with FS237 emitting marginally more photons for each wavelength. The measured intensities for FS155 for all wavelengths suggested that  $P_i^{\max} < 1$  for all three runs based on Table 5.4. This agrees with the judgment made in Section 5.3.2 based on Table A.2. The predicted occupancy values for 2 300 nppb for FS155 in Table 5.4 were consistent with the values found for runs 7128 and 7141 within the statistical limits of the measurement. The same conclusion could be made comparing the 1 200 nppb value for FS037 to run 7116 and the 1 500 nppb value for FS237 to run 7120. Overall it could be confirmed that the intensity measurement yielded conclusive results.

### Water-filled detector scenario

The next SMELLIE data and the first scattering length measurements using the system will be carried out in a water-filled detector. Having shown the principle on simulations and data in air-fill, the limits of the measurements in water-fill and

potential differences are discussed.

**Adjusting the angular profiles** The fibre emission angles for each photon are expected to be smaller in water compared to air due to the difference in refractive indices. Thus, the angular profiles in water are expected to be narrower. To account for this effect, the measured profiles for FS037, FS237 and FS155 were re-calculated using Snell's law [126]:

$$\frac{n_2}{n_1} = \frac{\sin\Theta_1}{\sin\Theta_2} \quad (5.10)$$

In this case,  $\Theta_2$  is the emission angle of the photons in air<sup>14</sup>. The refractive indices  $n_2$  and  $n_1$  represent the optical properties of air and the quartz of the fibre collimator respectively. Rearranging Equation 5.10, the incident angle  $\Theta_1$  of the photons emitted by the laser on the quartz-air interface could be determined using the measured angular profiles. Knowing  $\Theta_1$ , Equation 5.10 could be utilised again to determine the emission angle  $\Theta_2^{\text{water}}$  in water by replacing  $n_2$  with the refractive index in water  $n_2^{\text{water}}$ .

Figure 5.11 shows the expected change in refractive index for water and air for different wavelengths. Based on this Figure the refractive indices used for the calculation were set to

$$n_{\text{air}} = 1.0003$$

$$n_{\text{water}} = 1.34$$

The quartz used for the fibre collimators has a varying refractive index [113]. No information on the wavelength dependence or the precise value at the collimator edge of the quartz was available. Therefore, a refractive index of  $n_{\text{quartz}} = 1.46$  [127] was assumed.

The resulting profiles for all three fibres compared to the air-fill profiles extracted from data are shown in Figure 5.12. The significant features observed for fibres FS237 and FS155 resulting in a lower intensity central beam were not apparent in water-fill. Due to the smaller emission angles, all these features were shifted to lower bins of the profile. Since the most intense part of the beam for fibre FS037 was found within the beam center, the differences in the two angular profiles were not as dominant.

---

<sup>14</sup>Thus equivalent to the beam angle  $\alpha$  describing the angular profiles

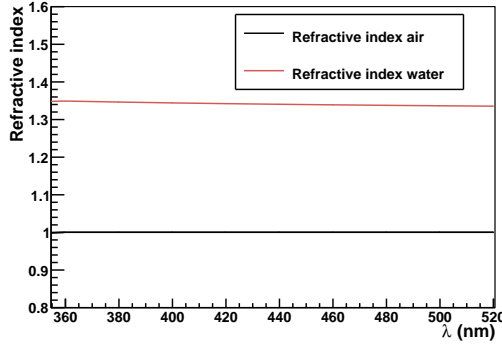


**Figure 5.11:** Refractive index in air and water over the wavelength range covered by the SMELLIE lasers. This plot is based on [128].

**Limits in water-fill** As for the study in air-fill, the impact of the scattering length on the intensity measurement was considered. In order to evaluate the sensitivity of the measurement on the scattering length of the detector medium, the nominal values  $l$  for the scattering length used in RAT were varied using the scaling factor  $s$  as defined in Equation 4.1. The estimated scattering length in water currently implemented in RAT for selected wavelengths is presented in Table A.8. A scaling factor of  $s = 2.0$  and  $s = 0.4$  was applied to a set of MC control samples simulated with intensities ranging from 100 nppb to 10 000 nppb. The resulting  $n_{\text{hits}}^{\text{mean, sim}}$  vs. nppb distributions are shown in Figure 5.13 for all simulated intensities (left) and for a subset with intensities up to 1 000 nppb (right).

Unlike for air, changing the scattering length in water had a significant impact on the distribution. The effect on the observed  $n_{\text{hits}}^{\text{mean, sim}}$  increased with simulated intensity. If more photons are emitted per beam pulse, more photons are likely to scatter leading to more registered hits in the detector. However, the distributions only separated at intensities around and above 1 000 nppb (see the left plot in Figure 5.13). Therefore, the intensity measurement could be accomplished at low intensities without having to account for uncertainties arising from the amount of scattering in the water. Subsequently, low intensity data which does not exceed 1 000 nppb is required for the scattering length measurement described in Chapter 6.

Since it is not advised to carry out the scattering length measurement with data exceeding 1 000 nppb, only occupancy values up to this intensity are of concern. Table 5.7 shows the maximal expected occupancy values  $P_i^{\max}$  for all three considered fibres

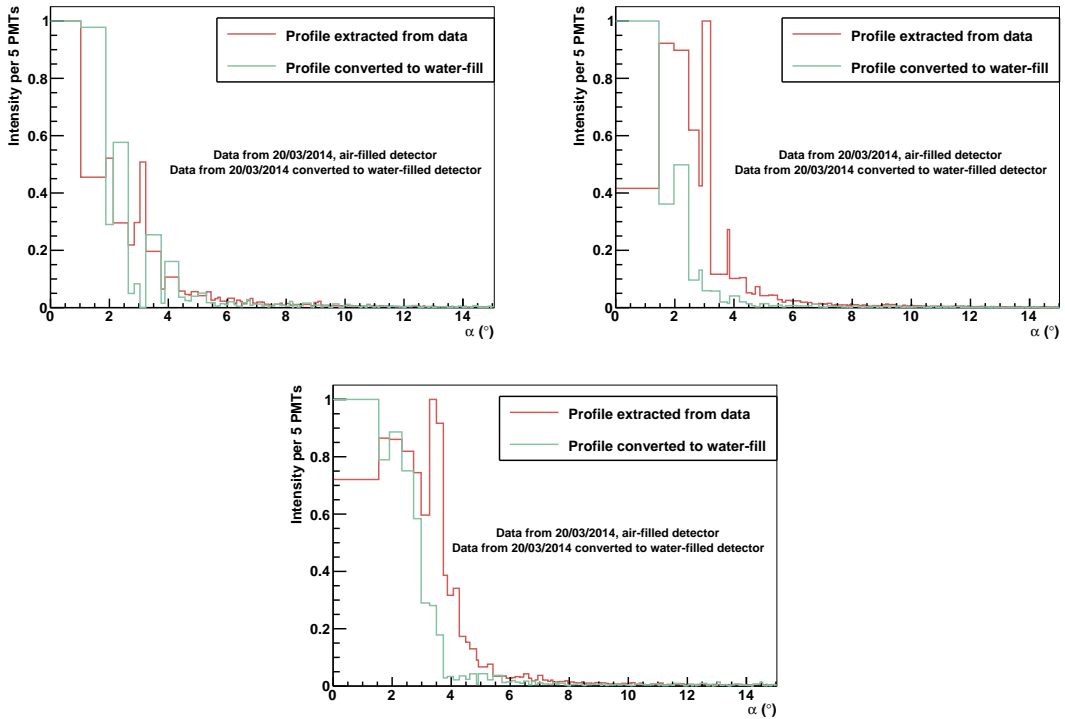


**Figure 5.12:** Comparison between the angular profiles in air and the estimated profiles in water for FS037, FS237 and FS155. The angular profiles for water-fill were estimated from the air-fill profiles measured as described in Section 5.3.2 using Equation 5.10.

at 1 000 nppb, none of which reached  $P_i^{\max} = 1$ . It can be observed that the occupancy levels for FS237 and FS155 were higher than the observed occupancy levels for similar intensities in air-fill (compare Table 5.4). This is a direct result of the shift in the angular profile to the center of the profile for both fibres, which means that more light was emitted at lower angles.

**Verification using fake data sets** The intensity measurement was carried out as described for air-fill. However, since the measurement principles for a fit range of up to 10 000 nppb have already been presented and the scattering length measurement is restricted to intensities below 1 000 nppb, the fit range of the function in Equation 5.6 was restricted to 0 nppb - 1 000 nppb (the resulting fit parameters are listed in Tables A.4 - A.6).

Due to the reduced fit range the measurement was only carried out for the low

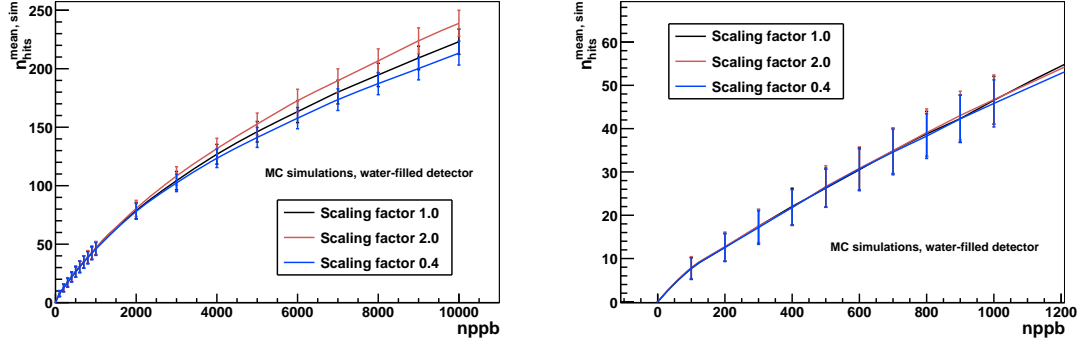


**Figure 5.13:** Mean number of hits versus number of photons simulated per beam pulse for FS237 at 446 nm in a water-filled detector. Depicted are the resulting distributions for the nominal scattering length of water used in RAT, as well as the distributions for a scaling factor of  $s = 2.0$  and a scaling factor of  $s = 0.4$ . The plot on the left shows the development of the distributions for all simulations from 100 nppb to 10 000 nppb. The right plot shows the same distributions for the simulations ranging from 100 nppb to 1 000 nppb.

**Table 5.7:** Maximum expected occupancy values  $P_i^{\max}$  in a water-filled detector for 1 000 nppb.

Fibre	$P_i^{\max}$
FS037	$0.91 \pm 0.01$
FS237	$0.97 \pm 0.01$
FS155	$0.83 \pm 0.01$

intensity fake data set at 845 nppb. As for air-fill, the standard deviation  $\sigma$  and the bias  $b$  were determined and are presented alongside the measurement uncertainty  $u$  in Table 5.8. A slight over-estimation of the nppb values was observed, however the reduced fit range also reduced the bias of the measurement. The uncertainty of the measurement did not change significantly from the values found for air-fill. Improving the measurement by reducing the fit range gives confidence for the scattering length measurement described in Chapter 6.

**Table 5.8:** Standard deviation  $\sigma$ , bias  $b$  and the uncertainty  $u$  on the measured number of photons for the low intensity fake data set at 845 nppb for FS037, FS237 and FS155. All four simulated wavelengths, 375 nm, 407 nm, 446 nm and 495 nm, are presented. The simulations were produced using a water-filled detector geometry.

Fibre	Wavelength (nm)	$\sigma$	$b$	$u$
FS037	495	2.1	-2.2	191.3
	446	2.2	0.0	165.3
	407	2.0	-2.7	157.6
	375	2.2	-0.2	160.3
FS237	495	2.8	0.2	213.1
	446	3.2	-3.1	189.1
	407	2.2	-3.8	180.3
	375	2.1	-1.8	182.0
FS155	495	2.4	-1.4	188.4
	446	2.2	0.0	163.7
	407	2.2	-0.2	156.5
	375	1.4	-3.0	160.5

## 5.4 Summary

The SMELLIE system was successfully incorporated into the RAT simulation software. Wavelength and timing distributions were added based on information provided by the manufacturer of the SMELLIE lasers PicoQuant. Using SMELLIE air-fill data from the March 2014 commissioning runs, the fibre directions for the simulation were calculated based on fits extracted from data. The calculated fibre positions were found to be a good approximation to the actual data and the direction discrepancies were attributed to a shift in the mounting plate position.

The angular profiles originally converted from the Oxford measurements were found to result in a simulated beam far narrower than observed from the data. A new approach to determine the angular profiles of the collimators was introduced, using the data. However, due to restrictions arising from the high intensity nature of the data, profiles of only three fibres could be measured. Applying the measured profiles to the simulation and comparing the in-beam light to the data yielded a good match.

A conversion method of the data intensity to the number of photons emitted per

beam pulse was introduced. The validity of the method was tested for an air-filled and a water-filled detector scenario. Applying the method to air-fill data led to comprehensive results. Restrictions for the scattering length measurement in a water-filled detector as presented in Chapter 6 were found. All described simulation aspects should be considered as systematic uncertainties for the scattering length measurement described in Chapter 6.

During the scintillator phase increased scattering is expected and absorption and re-emission effects need to be considered. It is therefore advised to re-validate the intensity measurement for this run phase to find the intensity limits for any scattering measurements. Significant shifts in angular profiles and fibre directions in comparison to the water-fill phase are not expected.

# 6 Measurement of the Rayleigh Scattering Length during the Water Phase

The analysis technique described in this Chapter has been especially tuned for the first run phase of SNO+ with a water-filled detector (see Section 3.2). Understanding the optical properties of the water is important for the physics measurements during this phase, e.g. limits on nucleon decay. Additionally, the analysis described here is limited to the four single wavelength SMELLIE lasers, since at the time the analysis was developed the hardware upgrade had not been added to the simulation. However, the described methods can be easily adjusted for later run phases as well as the new hardware setup.

## 6.1 Note on Angular Profiles

Since the interactions of photons depend on the angle at which they encounter different detector geometries and materials, using the right emission profile for the fibres is crucial. As described in Section 5.3.2, only three profiles could be extracted from the data by the time of writing. To demonstrate the measurement for all fibres, it was decided to use a generic averaged profile from these three fibres. The profiles were converted to a water profile as described in Section 5.3.3 and re-binned to  $0.2^\circ$  wide angular bins. The re-binning was necessary because the original profiles covering 5 PMTs per bin yielded different bin edges for each fibre. The re-binned profiles were then averaged and smoothed to remove fibre specific fluctuations. The resulting profile, as shown in Figure 6.1 was then applied as a generic water profile to all 12 fibres of the SMELLIE system.

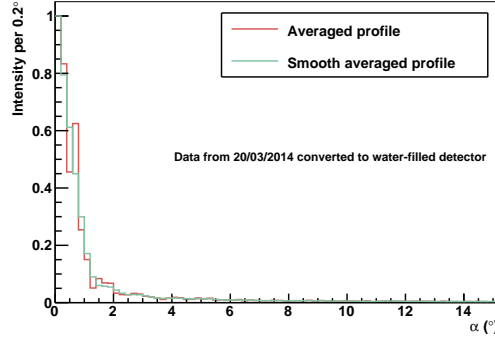


**Figure 6.1:** Average angular profile of SMELLIE fibres in a water-filled detector. The profiles from the air-fill commissioning data for fibres FS037, FS237 and FS155 were converted to a water-profile, averaged and smoothed to be applied as a generic water-profile to all 12 SMELLIE fibres.

## 6.2 Measurement Principles

The photons emitted by the SMELLIE fibres can undergo different optical interactions in the water-filled detector, which are depicted in Figure 6.2. Photons scattered in the detector and in-beam photons are the event topologies most sensitive to the scattering length of the detector medium. Hence, a cut selection was developed to separate scattered and in-beam photons from other photon types. The cut strategy is described in this section, followed by an illustration of the measurement procedure on a fake data set.

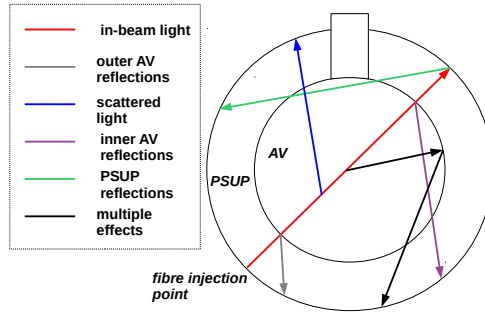


**Figure 6.2:** Optical interactions a photon can undergo in the detector.

### 6.2.1 Cut Selection

#### Cut Definition

The photons were split into the different cut regions shown in Figure 6.2 by applying timing and spatial constraints. First the crossing points of direct photons with the AV and the PSUP were determined<sup>15</sup>. With these crossing points, the distances a photon travels in the detector between each crossing point could be determined:

$$\begin{aligned}
 a &= |\vec{r}_{\text{pmtpos}} - \vec{r}_{\text{AVnear}}| \\
 b &= |\vec{r}_{\text{AVnear}} - \vec{r}_{\text{fibrepos}}| \\
 c &= |\vec{r}_{\text{pmtpos}} - \vec{r}_{\text{AVfar}}| \\
 d &= |\vec{r}_{\text{AVfar}} - \vec{r}_{\text{fibrepos}}| \\
 e &= |\vec{r}_{\text{PSUP}} - \vec{r}_{\text{AVfar}}| \\
 f &= |\vec{r}_{\text{pmtpos}} - \vec{r}_{\text{PSUP}}| \\
 g &= |\vec{r}_{\text{AVfar}} - \vec{r}_{\text{AVnear}}|
 \end{aligned} \tag{6.1}$$

Here, the indices AVnear and AVfar denote near and far side crossing points with the AV with respect to the fibre position. All vector  $\vec{r}_i$  represent the positions in detector coordinates of the investigated fibre ( $i = \text{fibrepos}$ ), the PMT hit by the photon ( $i = \text{pmtpos}$ ), the AV crossing points ( $i = \text{AVnear}, \text{AVfar}$ ) and the crossing point with the PSUP ( $i = \text{PSUP}$ ). The distances  $a - g$  are also shown in Figure 6.3. Using these distances the time a photon travels from the fibre to the detecting PMT in case the photon is reflected off each respective crossing point could be determined:

$$\begin{aligned}
 t_{\text{AVnear}} &= t_{\text{off}} + (a + b) \cdot n_{\text{water}} / \mathbf{c} \\
 t_{\text{AVfar}} &= t_{\text{off}} + (c + d - b - e) \cdot n_{\text{scint}} / \mathbf{c} + (b + e) \cdot n_{\text{water}} / \mathbf{c} \\
 t_{\text{PSUP}} &= t_{\text{off}} + (f + g - b - e) \cdot n_{\text{scint}} / \mathbf{c} + 2 \cdot (b + e) \cdot n_{\text{water}} / \mathbf{c}.
 \end{aligned} \tag{6.2}$$

Similarly, the travel time of the photon directly from fibre to the hit PMT follows:

$$t_{\text{beam}} = t_{\text{off}} + g \cdot n_{\text{scint}} / \mathbf{c} + (b + e) \cdot n_{\text{water}} / \mathbf{c} \tag{6.3}$$

---

<sup>15</sup>As described in Appendix B.1.

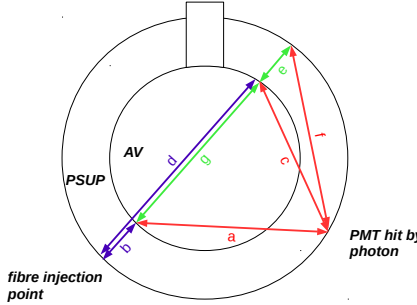


**Figure 6.3:** Distances between crossing points as defined in Equation 6.1. Depicted in blue are the distances between the fibre and different crossing points, green are the distances between crossing points and red are the distances from the crossing points to the PMT which registered the photon hit.

The variable  $t_{\text{off}}$  describes the time offset following from the trigger delay. It was defined for each run by performing a Gaussian fit on the timing of all light which spatially covers all PMTs hit by direct beam light. The speed of light  $c$  and the refractive indices  $n_{\text{scint}}, n_{\text{water}}$  were used to convert the distances into time traveled. These times were used as benchmark values to define the timing cuts on the SMELLIE beams by comparing them to the time the photon triggered the PMT. Since the analysis was carried out in a water-filled detector, the refractive indices  $n_{\text{scint}} = n_{\text{water}}$ .

Spatial cuts on the positions of the hit PMT were applied to further constrain photons originating from direct beam light and both types of AV reflections. In-beam photons and outer AV reflections, i.e. reflections off the first crossing point with the AV, are confined to small areas in the detector which depend on the fibre direction and the angular profile of the fibre. For both cut regions a cut on the beam angle  $\alpha$  and on the position  $z$  of the hit PMTs were made. The second, inner AV, reflections were selected by a variety of beam angle  $\alpha$  and timing cut combinations.

Figure 6.4 shows the different selected regions for all three fibres on node 07 at 407 nm. The plots on the left show the beam angle  $\alpha$  vs. the time residual  $t_{\text{res}}$ . The time residual is defined using the time the PMT registers a hit  $t_{\text{PMT}}$ , the time it would take the photon to travel directly from the fibre to the hit PMT,  $t_{\text{Path}}$ , and the trigger offset  $t_{\text{off}}$ :

$$t_{\text{res}} = t_{\text{PMT}} - t_{\text{Path}} - t_{\text{off}} \quad (6.4)$$

The plots were made simulating 10 000 SMELLIE pulses at an intensity of 900 nppb. Equivalent plots for the remaining SMELLIE fibres are presented in Figures B.1 – B.3.

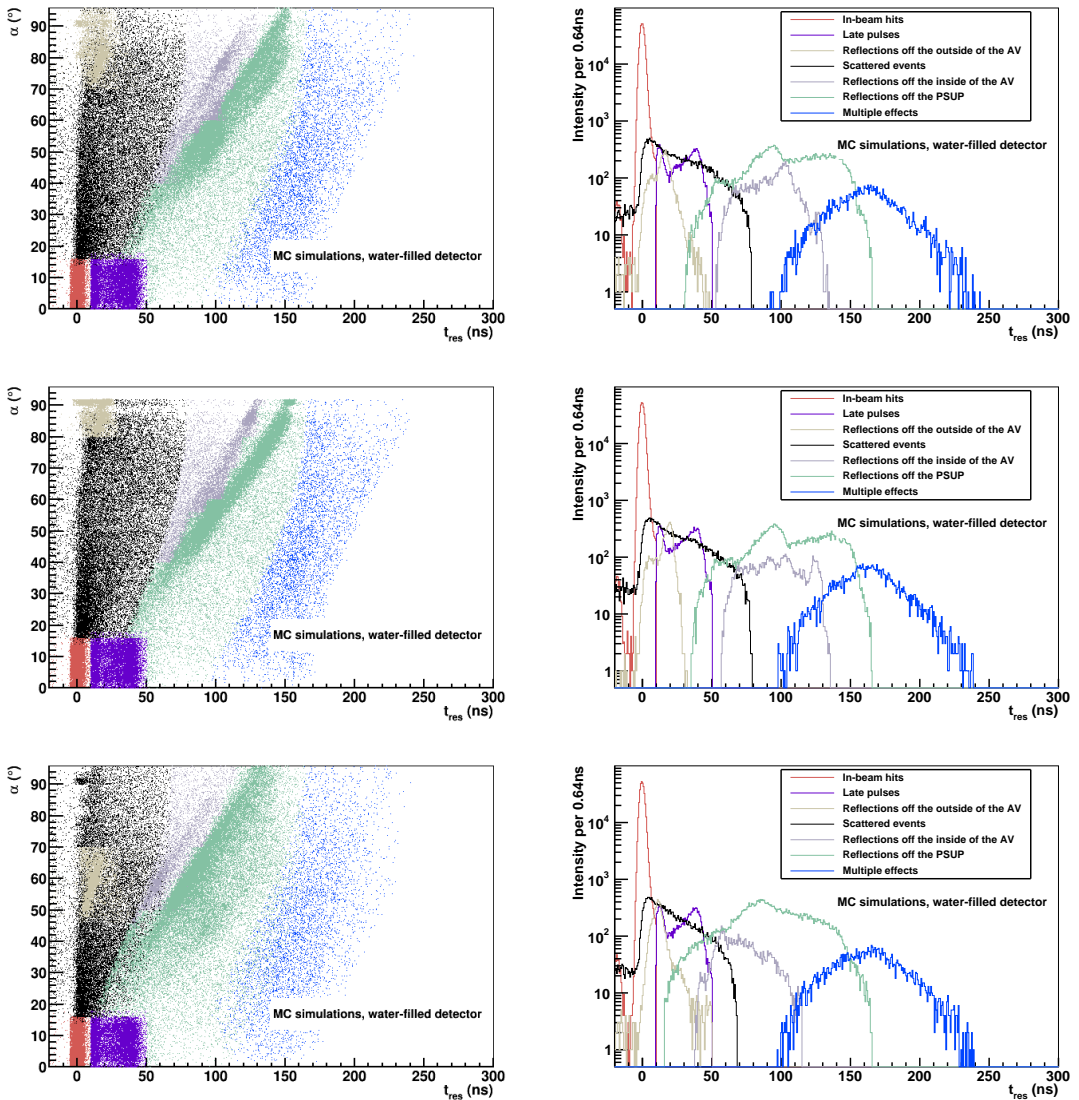
Additionally to the cuts on the optical interactions shown in Figure 6.2, another cut was applied to the SMELLIE runs labeled “Late pulses” in Figure 6.4. These are events which are registered in PMTs passing the spatial in-beam cuts but fire the PMT up to around 40 ns later than expected for direct beam photons. This is a known response of the PMTs to pulsed light sources and caused by photons triggering a second cascade in the PMTs after the initial arrival of the direct beam light [129]. Late pulses are also expected due to ionisation effects in ageing tubes with degrading vacuum. From Figure 6.4 it can also be observed that the location of the AV reflected light changes for each angled fibre, making it necessary to tune the angular cuts on these regions separately.

Table 6.1 shows the cuts applied for each cut region. A photon hit had to pass all cut values for a particular region to be selected for that region, except for the inside AV reflection region. To be able to distinguish between the inside AV reflected photons and photons reflected off the PSUP, the spatial cut was split into segments, each of which being paired with a different timing cut. The cut values  $\alpha_i^k$ ,  $z_i^k$ ,  $t_{\text{AVfar}}^{\text{cut}}$  and  $t_{\text{PSUP}}^{\text{cut}}$  shown in Table 6.1 (with  $i$  denoting the cut region and  $k$  if it is the lower or upper cut boundary) are fibre specific and listed in Table 6.2.

## Cut Verification

The cut selection was tuned and tested using three control samples for each fibre-wavelength combination simulated using a detector without the AV, a detector with the scattering turned off and a detector with both the AV removed and no scattering. An average noise rate of 500 Hz per PMT was simulated for each sample. The cuts were applied to each of these samples and adjusted according to the observations. Figure 6.5 shows the cuts presented in Tables 6.1 and 6.2 applied to the control samples for FS025 at 375 nm.

The events selected by the direct beam cut do not seem to be affected by the alterations in the simulations, suggesting there is very little contamination of non-direct beam events. On the contrary few hits that do not originate from scattering or PMT



**Figure 6.4:** Cut selection for the node 07 fibres at 407 nm. Shown are the  $\alpha$  vs  $t_{\text{res}}$  (left) and the  $t_{\text{res}}$  distributions (right) as defined in Equation 6.4 for FS107 (top), FS007 (middle) and FS207 (bottom).

**Table 6.1:** SMELLIE cut selection to define the different cut regions according to the optical interactions. A photon hit had to pass each requirement for a certain region to be classed in this cut region, except for the inner AV reflections. For this cut region, each angular cut is paired with a specific timing window.

Cut region Cut region	Spatial cuts		Timing cuts (ns)	
	lower	upper	lower	upper
In-beam	— $z_{\text{beam}}^{\min}$ (mm)	$\alpha_{\text{beam}}$ ( $^{\circ}$ ) $z_{\text{beam}}^{\max}$ (mm)	— —	$t_{\text{beam}} + 5 \text{ ns}$ —
Late Pulses	— $z_{\text{beam}}^{\min}$ (mm)	$\alpha_{\text{beam}}$ ( $^{\circ}$ ) $z_{\text{beam}}^{\max}$ (mm)	— —	$t_{\text{beam}} + 5 \text{ ns}$ —
outer AV reflections	$\alpha_{\text{AVnear}}^{\min}$ ( $^{\circ}$ ) $z_{\text{AVnear}}^{\min}$ (mm)	$\alpha_{\text{AVnear}}^{\max}$ ( $^{\circ}$ ) $z_{\text{AVnear}}^{\max}$ (mm)	—	$t_{\text{AVnear}} + 5 \text{ ns}$ —
Scattered events	—	—	—	$t_{\text{AVfar}} - t_{\text{AVfar}}^{\text{cut}}$
inside AV reflections	For this cut there is an “or” between each of the following lines			
	$\alpha_{\text{AVfar}} ({}^{\circ})$ $(\alpha_{\text{AVfar}} ({}^{\circ}) + 15 {}^{\circ})$ $(\alpha_{\text{AVfar}} ({}^{\circ}) + 20 {}^{\circ})$ $(\alpha_{\text{AVfar}} ({}^{\circ}) + 20 {}^{\circ})$ $(\alpha_{\text{AVfar}} ({}^{\circ}) + 30 {}^{\circ})$ $(\alpha_{\text{AVfar}} ({}^{\circ}) + 30 {}^{\circ})$ $(\alpha_{\text{AVfar}} ({}^{\circ}) + 40 {}^{\circ})$ $(\alpha_{\text{AVfar}} ({}^{\circ}) + 40 {}^{\circ})$ $(\alpha_{\text{AVfar}} ({}^{\circ}) + 50 {}^{\circ})$ $(\alpha_{\text{AVfar}} ({}^{\circ}) + 50 {}^{\circ})$ $(\alpha_{\text{AVfar}} ({}^{\circ}) + 60 {}^{\circ})$ $(\alpha_{\text{AVfar}} ({}^{\circ}) + 60 {}^{\circ})$	$(\alpha_{\text{AVfar}} ({}^{\circ}) + 15 {}^{\circ})$ $(\alpha_{\text{AVfar}} ({}^{\circ}) + 20 {}^{\circ})$ $(\alpha_{\text{AVfar}} ({}^{\circ}) + 30 {}^{\circ})$ $(\alpha_{\text{AVfar}} ({}^{\circ}) + 40 {}^{\circ})$ $(\alpha_{\text{AVfar}} ({}^{\circ}) + 50 {}^{\circ})$ $(\alpha_{\text{AVfar}} ({}^{\circ}) + 60 {}^{\circ})$	$(t_{\text{AVfar}} - t_{\text{AVfar}}^{\text{cut}})$ $(t_{\text{AVfar}} - t_{\text{AVfar}}^{\text{cut}})$	$(t_{\text{PSUP}} - t_{\text{PSUP}}^{\text{cut}})$ $(t_{\text{PSUP}} - t_{\text{PSUP}}^{\text{cut}} + 10 \text{ ns})$ $(t_{\text{PSUP}} - t_{\text{PSUP}}^{\text{cut}} + 20 \text{ ns})$ $(t_{\text{PSUP}} - t_{\text{PSUP}}^{\text{cut}} + 25 \text{ ns})$ $(t_{\text{PSUP}} - t_{\text{PSUP}}^{\text{cut}} + 35 \text{ ns})$ $(t_{\text{PSUP}} - t_{\text{PSUP}}^{\text{cut}} + 40 \text{ ns})$ $(t_{\text{PSUP}} - t_{\text{PSUP}}^{\text{cut}} + 45 \text{ ns})$
PSUP reflections	—	—	$t_{\text{AVfar}} - t_{\text{AVfar}}^{\text{cut}}$	$t_{\text{PSUP}} + 15 \text{ ns}$
Multiple effects	—	—	$t_{\text{PSUP}} + 15 \text{ ns}$	—

noise appear to be selected by the scattering region cut. A significant contamination of scattered events is observed in the outer AV reflection cut as well as the inner AV reflections. Some PSUP reflections are selected by the AV reflection cut and vice versa. The higher the angle of the fibre, the more of these reflections are selected by the respective other cut (compare also Figure 6.4).

Additionally to the visual inspection of these simulations (including the simulations using the full detector geometry), the history of each created photon was checked for noise and scattering flags, which were implemented in the Monte Carlo information of the RAT simulation by the author. These flags are part of the RAT Monte Carlo branch as described in Section 3.6, for which the photons in each cut region were counted and the relative content of scattered and noise photons was evaluated. These values were then averaged over all four SMELLIE nodes for each type of angled fibre. The resulting numbers are presented in Table 6.3 for all wavelengths.

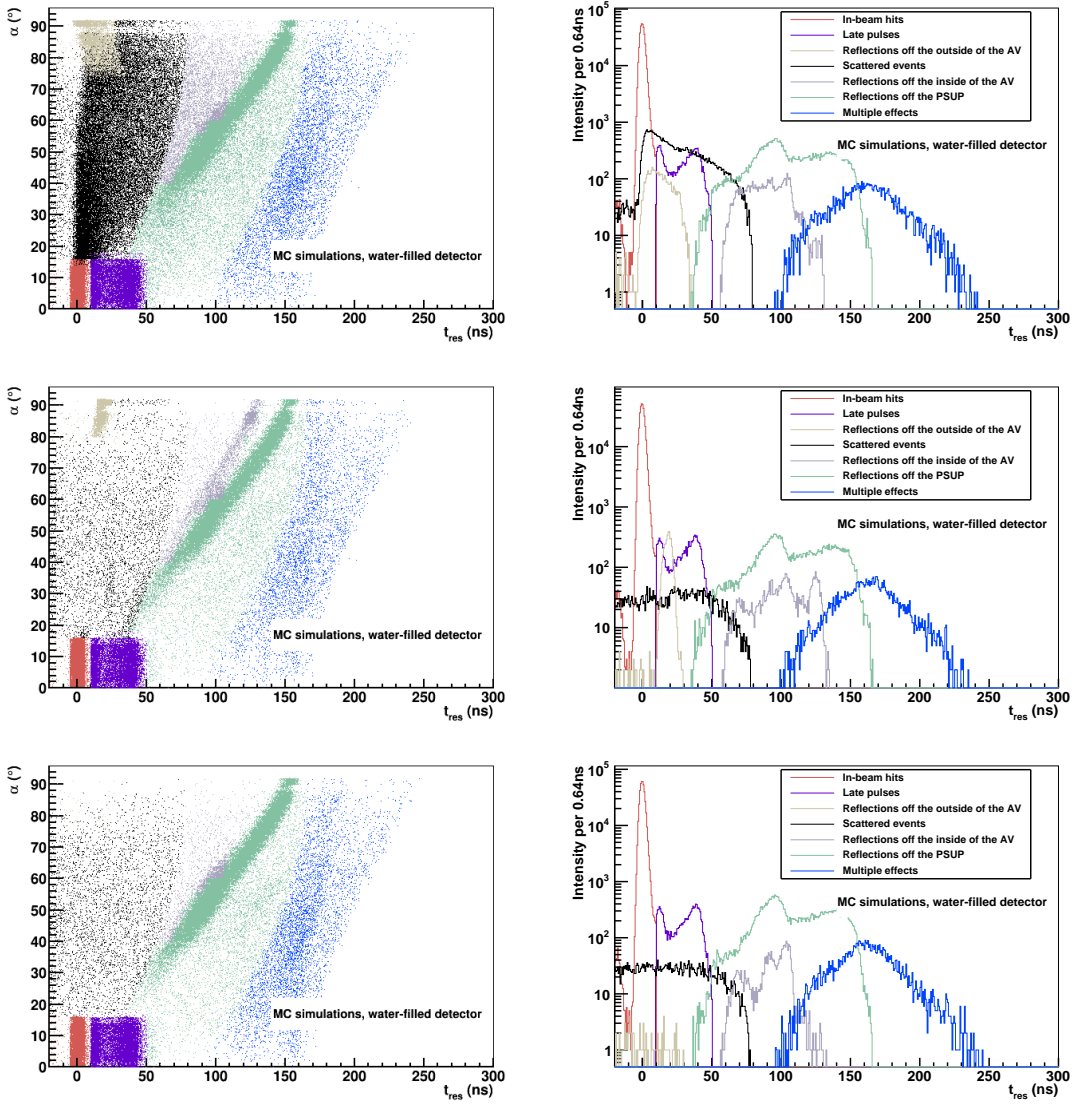


**Figure 6.5:** The different detector control samples for FS025 at 375 nm for a detector simulated without the AV (top), a detector simulated with no scattering (middle) and a detector simulated without the AV and scattering (bottom). Shown are the  $\alpha$  vs  $t_{\text{res}}$  (left) and the  $t_{\text{res}}$  distributions (right) as defined in Equation 6.4

**Table 6.2:** The SMELLIE cut values for each fibre for the fibre dependent variables shown in Table 6.1.

Fibre	$\alpha_{\text{beam}}$ ( $^{\circ}$ )	$z_{\text{beam}}^{\min}$ (mm)	$z_{\text{beam}}^{\max}$ (mm)	$\alpha_{\text{AVnear}}^{\min}$ ( $^{\circ}$ )	$\alpha_{\text{AVnear}}^{\max}$ ( $^{\circ}$ )	$z_{\text{AVnear}}^{\min}$ (mm)	$z_{\text{AVnear}}^{\max}$ (mm)	$\alpha_{\text{AVfar}}$ ( $^{\circ}$ )	$t_{\text{AVfar}}^{\text{cut}}$ (ns)	$t_{\text{PSUP}}^{\text{cut}}$ (ns)
FS007	17	-7000	1000	80	120	2800	6000	40	50	55
FS107	17	-7500	-500	70	95	2000	5400	40	50	55
FS207	17	-4200	4000	47	70	3700	7000	30	60	80
FS025	17	-7000	1000	75	120	2500	6000	40	50	55
FS125	17	-7500	0	70	110	2000	5500	40	50	55
FS225	17	-4200	4000	48	80	4000	7000	20	60	80
FS037	19	-2500	7500	65	98	-5800	-2500	40	50	55
FS137	21	-2000	7500	70	120	-5600	-2500	40	50	55
FS237	17	-1000	7000	50	80	-5500	-1800	20	60	80
FS055	17	-4000	5000	60	90	-7000	-3500	40	50	55
FS155	17	4500	8500	53	75	-3600	1000	20	60	80
FS255	21	-1400	7000	70	120	-6000	2200	40	50	55

Both the late pulse region and the multiple effect region were not considered for this verification step. The late pulses are a PMT effect which is not reflected in the Monte Carlo information when looping through all created photons. As discussed in Section 3.6, the Monte Carlo branch has no trigger window information, all created photons are counted, leaving a lot of PMT noise hits to be selected by the multiple effects cut due to its missing upper timing cut boundary. Therefore, this region is dominated by noise hits when applying this cut verification method and was not considered in this analysis step.

Overall the observations made for Figure 6.5 were confirmed by the numbers in Table 6.3. The scattering contamination of the AV reflection cuts varied with fibre angle due to the directionality of these events, whilst the contamination of the in-beam region with scattered events did not exceed 2.0 %. The scattering cut region contains predominantly scattered and noise photons, the ratio of which changed with wavelength due to the wavelength dependence of Rayleigh scattering. Concluding the cut verification process, very pure in-beam and scattering regions could be achieved with very little contributions from photons originating from other optical interactions in the detector. The high contamination of noise hits in the scattering region especially for the higher wavelength runs was considered as a systematic on the scattering length measurement.

**Table 6.3:** The relative content of scattered and noise hits in several cut regions averaged over all fibres for the four different wavelengths.

Wavelength (nm)	Cut	10°		0°		20°	
		scattered (%)	noise (%)	scattered (%)	noise (%)	scattered (%)	noise (%)
375	in-beam	1.55	0.28	1.75	0.33	1.58	0.27
	outside AV reflections	54.38	7.52	52.44	5.75	40.31	10.89
	inside AV reflections	52.40	9.26	58.80	10.98	60.06	10.34
	Scattered events	68.24	30.07	68.28	30.37	67.62	31.40
	PSUP reflections	16.36	10.32	19.21	10.51	16.60	10.94
407	in-beam	1.12	0.23	1.31	0.29	1.16	0.24
	outside AV reflections	46.74	8.45	44.17	6.20	33.84	11.55
	inside AV reflections	42.04	8.82	49.78	10.69	50.65	10.75
	Scattered events	63.16	34.54	63.26	34.93	62.91	35.84
	PSUP reflections	11.75	9.11	13.73	9.50	11.93	9.79
446	in-beam	0.79	0.26	0.90	0.31	0.81	0.26
	outside AV reflections	37.73	10.09	35.27	7.43	25.72	13.70
	inside AV reflections	31.07	11.17	38.97	14.44	39.75	13.68
	Scattered events	53.16	44.05	52.72	45.07	52.42	45.86
	PSUP reflections	7.85	10.03	9.00	10.51	8.00	10.43
495	in-beam	0.54	0.36	0.61	0.45	0.54	0.37
	outside AV reflections	28.58	13.97	26.73	10.26	18.24	18.03
	inside AV reflections	18.11	15.50	25.61	22.22	24.18	20.91
	Scattered events	35.22	61.48	35.03	62.36	35.16	63.00
	PSUP reflections	4.50	15.33	5.28	15.60	4.59	15.52

## 6.2.2 Measurement Strategy

For the scattering length measurement, all hits selected by the in-beam cut ( $N_{\text{in-beam}}$ ) and the scattering cut ( $N_{\text{scatt}}$ ) were counted over an entire SMELLIE run for each fibre-wavelength combination<sup>16</sup>. The higher the scattering, the less direct beam light is detected. On each data sample, the ratio of  $N_{\text{in-beam}}$  and  $N_{\text{scatt}}$  with respect to the total number of hits in the entire run  $N_{\text{total}}$  was evaluated:

$$\begin{aligned} c_{\text{scatt}}^{\text{data}} &= \frac{N_{\text{scatt}}}{N_{\text{total}}} \\ c_{\text{in-beam}}^{\text{data}} &= \frac{N_{\text{in-beam}}}{N_{\text{total}}} \end{aligned} \quad (6.5)$$

A set of simulations was then produced with different scaling factors  $s$  as defined in Equation 4.1 applied to the water to achieve samples with different scattering rates (in the following referred to as control samples). Since the scattering length in the detector is not expected to be much different to the one currently used in the

<sup>16</sup>Note that the multiple hits correction described in Section 5.3.2 was applied.

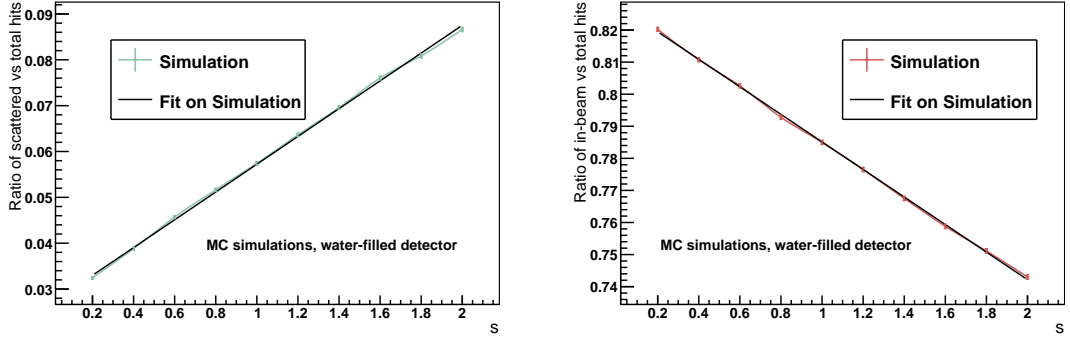


**Figure 6.6:** The  $c^{\text{sim}}$  vs.  $s^{\text{sim}}$  for the scattering region (left) including the linear fit with  $\chi^2 = 19.1$  and the direct beam region (right) including the linear fit with  $\chi^2 = 6.4$  for FS155 at 446 nm. Presented are both the distributions and the fits on the distributions used to determine  $s^{\text{data}}$ .

simulation, i.e. not have a scaling factor hugely different from  $s = 1$ , a scaling factor range between 0.2 and 2.0 was considered for the water-phase measurements. In case the scattering length does differ significantly, the measurement can be easily adapted.

As for the data,  $c_{\text{scatt}}^{\text{sim}}$  and  $c_{\text{in-beam}}^{\text{sim}}$  were determined for each of the produced simulations. For each fibre-wavelength combination, the extracted  $c_i$  were plotted versus the respective scaling factor,  $s$ , applied to that simulation as presented in Figure 6.6 for FS155 at 446 nm (The uncertainties on the  $c_i$  were determined as described in Appendix B.2). These distributions were fitted using a linear function

$$f_1(s) = p0 \cdot s + p1 \quad (6.6)$$

with  $p0$  and  $p1$  being the fit parameters. The corresponding scaling factor for the data can be evaluated by finding the intersection of  $c^{\text{data}}$  with  $f_1(s)$  and re-arranging the resulting equation:

$$s^{\text{data}} = \frac{c^{\text{data}} - p1}{p0} \quad (6.7)$$

The uncertainty  $\Delta s^{\text{data}}$  follows from the uncertainty propagation using the uncertainties of the fit parameters and the statistical uncertainty on  $c^{\text{data}}$ . Carrying out the measurement for each fibre-wavelength combination produced 96 values<sup>17</sup> for  $s^{\text{data}}$ , the average of which represented the final measured value. Using Equation 4.1, the

<sup>17</sup>48 from the scattering region and 48 from the direct beam region

measured scaling factor can be converted back to a value for the scattering length of the water present in the detector at each wavelength.

A significant variation in measured scaling factor for different fibres could indicate a spatial variation in scattering length within the detection material. Thus, a contamination with e.g. crystals sinking to the bottom of the detector (variation in  $z$ -direction) could be observed using the SMELLIE system. Equivalently, a deviation of scaling factor values at different wavelengths can indicate a contamination of the detection material showing a divergence from the expected Rayleigh scattering distribution.

### 6.2.3 Bias of the Measurement

To determine the bias of the measurement  $M = 20$  SMELLIE simulations were produced for each fibre-wavelength combination at the nominal scattering length of the water volume, resulting in a simulated scaling factor of  $s_{\text{sim}} = 1.0$ . The scaling factor measurement was carried out for each of these samples and for each determined  $s_{\text{meas}}^{ij}$  the value

$$f^{ij} = s_{\text{sim}} - s_{\text{meas}}^{ij} \quad (6.8)$$

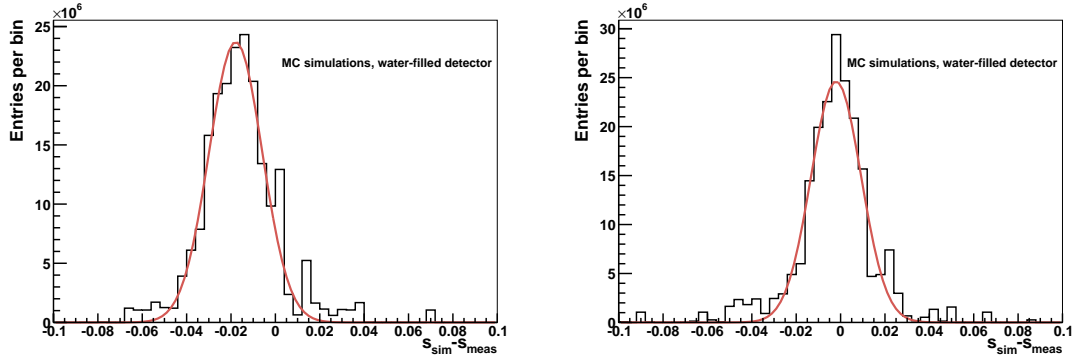
was calculated for each fibre  $i$  and wavelength  $j$ .

Figure 6.7 shows the resulting  $f^{ij}$  distribution using two different sets of Monte Carlo control samples. The distribution on the left was measured using simulations with scaling factors ranging from  $s = 0.2$  to  $s = 2.0$  in 0.2 steps. For the distribution on the right, control samples with applied scaling factors between  $s = 0.8$  and  $s = 1.2$  with steps of 0.1 were used. To determine the bias  $b_s$  of the measurements, both distributions were fitted with a Gaussian function, the mean of which is equivalent to  $b_s$ . For the measurement using a broader range of control samples

$$b_s = -0.018 \quad (6.9)$$

whilst for the second measurement using the shorter range of control samples

$$b_s = -0.002. \quad (6.10)$$



**Figure 6.7:** Measurement bias for the scaling factor measurement. Shown on the left is the measurements of  $s_{\text{meas}}$  carried out with control samples ranging from  $s = 0.2$  to  $s = 2.0$  in 0.2 steps. Shown on the right is the measurements of  $s_{\text{meas}}$  carried out with control samples ranging from  $s = 0.8$  to  $s = 1.2$  in 0.1 steps.

A negative bias means the measured scaling factor was over-estimated, which was the case in both measurements. Reducing the range of scaling factors used for the simulated control samples and adding a few more steps between the simulated scaling factors can reduce the measurement bias significantly. However, reducing the range of used scaling factors in the control samples is only possible once one has determined an approximate value of the data scaling factor to be measured. Therefore, any first iteration of the scaling factor measurement will introduce a slight bias leading to a marginal over-estimation of the scaling factor.

The bias is caused by the non-linear dependence between beam intensity, detected number of hits and the scattering length present in the detector, which was previously discussed in Section 5.3.3 when studying the intensity measurement procedure. As previously stated the simulations were produced at 900 nppb, at which a slight scattering length dependence could be observed for the detected number of hits (see Figure 5.13). Since the scaling factor measurement uses the principle of counting the number of hits in different cut regions and overall, a non-linear dependence over larger scattering length ranges is therefore to be expected. This is affecting the accuracy of the scaling factor measurement. However, the effect is only very slight at the used intensity and thus the bias can be reduced by decreasing the control sample range to smaller scattering length variations.

**Table 6.4:** The measured intensities for the fake data sets averaged over all fibres for the four different wavelengths. The uncertainty on the average followed using the uncertainty propagation from the uncertainties on the single measurements.

Wavelength (nm)	Intensity (nppb)
375	$941 \pm 46$
407	$940 \pm 44$
446	$938 \pm 47$
495	$935 \pm 56$

### 6.3 Measurement on a fake data set

Since at the time of writing no data was available to apply the strategy, fake data was produced by a third party with the intensity and the scaling factor  $s^{\text{data}}$  unknown to the author. For each fibre-wavelength combination the intensity measurement as described in Section 5.3.3 was carried out. Based on the findings in Section 5.3.3 it was agreed with the third party to produce fake data with intensities below 1 000 nppb. The average values over all fibres for each wavelength are presented in Table 6.4. For more detailed information, all measured values for all fibre-wavelength combinations can be found in Appendix Table B.1.

The fake data sets were each simulated with the same intensity. From Section 5.3.3 it is expected that intensities below 1 000 nppb are slightly overestimated by the measurement method. Additionally, from Table 6.4, a wavelength-dependent trend can be observed on the average values, the higher the wavelength, the lower the measured values. This follows from the scattering in the samples, the higher the wavelength, the lower the scattering. As observed in Figure 5.13 at intensities between 900 nppb and 1 000 nppb a slight scattering dependence on the intensity measurement appears. However, the effect is small and therefore the measured intensities were expected to be a good estimation of the actual values within the given uncertainties.

For a real data scenario, the intensities of none of the fibre-wavelength combinations should be the same, since the angular profiles vary for each fibre and each laser has different light output. Therefore, to proceed with the scattering length measurement, the control samples with scaling factors between 0.2 and 2.0 were simulated with the actual intensity measured for the respective fibre-wavelength combination. For

**Table 6.5:** The scattering length for different wavelengths as determined for the fake data sets using the measured scaling factor  $s^{\text{data}}$ .

Wavelength (nm)	Scattering Length (mm)
380	$110\,406 \pm 412$
400	$135\,550 \pm 505$
440	$198\,459 \pm 740$
500	$330\,933 \pm 1\,234$

completeness, the resulting fit parameters  $p_0$  and  $p_1$  and the measured  $c_{\text{scatt/in-beam}}^{\text{data}}$  and scaling factors  $s_{\text{scatt/in-beam}}^{\text{data}}$  are presented in Tables B.2 and B.2.

The average scaling factor of the data is

$$s^{\text{data}} = 1.341 \pm (0.005)_{\text{stat.}} \quad (6.11)$$

A scaling factor larger than  $s^{\text{data}} = 1$  means a shorter scattering length of the water than expected, therefore more scattering occurs. No wavelength dependence of the measured scaling factors could be observed. The resulting scattering length of the water following from this scaling factor for wavelengths close to the wavelengths of the SMELLIE lasers<sup>18</sup> are listed in Table 6.5. The scaling factor the fake data was simulated at is  $s^{\text{data}} = 1.325$ . Any discrepancies to the measured value stated above are discussed in Section 6.5.

## 6.4 Systematic Uncertainties

Additionally to the statistical uncertainty on the measurement, discrepancies between simulation and reality can cause uncertainties on the measurement. In this section, these are investigated and their impact on the scattering length measurement is determined. The systematics were evaluated by re-simulating the Monte Carlo control samples at the different scattering lengths with the described alterations applied. The measurement was then repeated using these altered samples and the systematic uncertainty was evaluated by determining the standard deviation with the originally

---

<sup>18</sup>The scattering length values were taken from the arrays implemented in RAT, which only provides scattering length values in 20 nm steps.

measured values:

$$\sigma = \sqrt{\frac{\sum_k^L \sum_i^N \sum_j^M (s_{\text{meas}}^{\text{data}} - s_{\text{sys}}^{\text{data}})_{ijk}^2}{N \cdot M \cdot L}} \quad (6.12)$$

Here,  $N$  is the number of fibres,  $M$  the four wavelengths and  $L$  represents the scattering and in-beam measurement regions.

All considered uncertainties may lead to a misidentification of events when applying the cut selection described in Section 6.2.1. Any deviation in number of events selected by the in-beam and the scattering cut ( $N_{\text{in-beam}}$  and  $N_{\text{scatt}}$ ) can lead to an over- or underestimation of the scaling factor  $s^{\text{data}}$ . The systematic uncertainty evaluation was carried out using a conservative approach assuming no correlation between any of the systematics considered.

#### 6.4.1 AV position and scattering

In the simulation the AV is centered exactly around the origin of the detector coordinate system. However, changing the tensions on the rope net designed to stop the AV from rising during scintillator-fill can alter the position of the AV in  $z$ -direction. A shift in the AV position can cause a shift in the PMTs hit by the AV reflected photons, consequently contaminating the scattering cut region. The TELLIE system can determine the AV position within 30 mm [130]. Therefore, the control samples were simulated moving the AV up and down by this margin. The uncertainty from this effect was evaluated to be

$$\Delta s_{\text{sys}}^{\text{AVpos}} = 0.055 \quad (6.13)$$

Furthermore, the scattering within the AV itself might lead to photons mistakenly selected as being scattered in the detector volume. The impact of this effect was tested by doubling and halving the scattering occurring in the AV by applying the equivalent scaling factors. Applying these changed values to the control samples leads to

$$\Delta s_{\text{sys}}^{\text{AVscatt}} = 0.012 \quad (6.14)$$

## 6.4.2 Intensity

The scaling factor measurement depends on the number of photons emitted into the detector. The more photons are emitted, the more photons are selected for each cut region. To avoid large discrepancies between data and simulation, the intensity measurement described in Section 5.3.3 was developed. For an estimate of the systematic uncertainty following from the intensity measurement, the control samples were re-simulated after applying the uncertainties of the intensity measurement for each fibre-wavelength combination. The resulting systematic is

$$\Delta s_{\text{sys}}^{\text{int}} = 0.174 \quad (6.15)$$

## 6.4.3 Angular Profiles

Evaluating the systematic uncertainties arising from the angular profiles of the fibres is more challenging, since the measurement described in Section 5.3.2 yields no natural uncertainty on the profile. Two aspects of the profile can lead to discrepancies between data and simulation: a varying width and higher or lower tail contributions. To follow the conservative approach of the uncertainty estimation, both aspects of the angular profiles were considered independently.

The generic angular profile was fitted using a Gaussian over a fit range of  $0^\circ - 1.5^\circ$ :

$$f_1(\alpha) = p0 \cdot \exp\left(-\frac{1}{2} \left(\frac{\alpha - p1}{p2}\right)^2\right) \quad (6.16)$$

with the three fit parameters  $p0$ ,  $p1$  and  $p2$ . The tail of the profile was fitted over a range of  $1.0^\circ - 10^\circ$  with an exponential function:

$$f_2(\alpha) = \exp(p3 + p4 \cdot \alpha) \quad (6.17)$$

with the fit parameters  $p3$  and  $p4$ . Both resulting functions were combined in order to find a function which describes the angular profile:

$$f_3(\alpha) = f_1(\alpha) + f_2(\alpha). \quad (6.18)$$

Figure 6.8 shows the two fits on the generic angular profile (left) and the combined

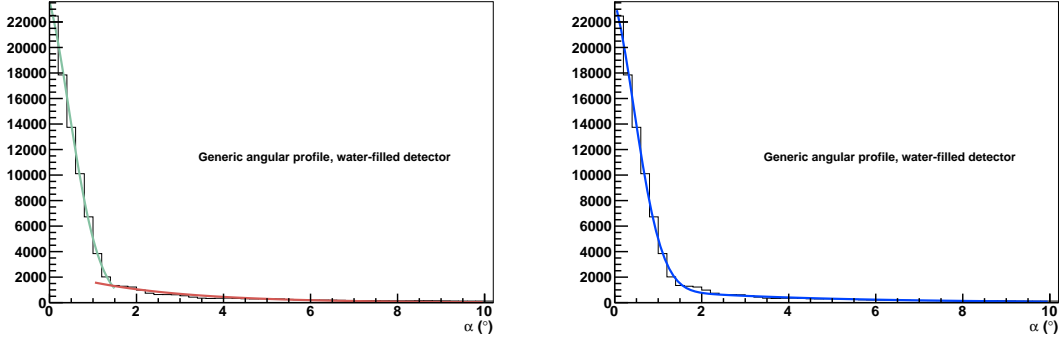


**Figure 6.8:** The fits  $f_1(\alpha)$  and  $f_2(\alpha)$  on the generic water profile (left) and the combined function  $f_3(\alpha)$  in comparison to the generic water profile (right).

**Table 6.6:** The fit values used to define  $f_3(\alpha)$  describing the generic angular water profile.

Fit parameter	Value
$p_0$	$2.36 \times 10^4$
$p_1$	-0.21
$p_2$	0.65
$p_3$	7.10
$p_4$	-0.272

function  $f_3(\alpha)$  (right) in comparison to the generic profile. The fit parameters are listed in Table 6.6.

As shown in Appendix A.6.1, the width of the measured profile depends on the choice of number of PMTs covered by each bin. For each of the three fibres used for the profile measurements, the profile contributions below  $\alpha = 6^\circ$  were compared for the different scenarios considered in Appendix A.6.1. A factor was determined which describes the change in width relative to the measured profiles using 5 PMTs per angular bin. Additionally, the profiles were measured for the available 495 nm and 446 nm runs for FS155 as described in Section 5.3.2<sup>19</sup>. These additional profiles were compared to the FS155 profile measured from 407 nm below  $\alpha = 6^\circ$  to account for

---

<sup>19</sup>As described before, all of these FS155 runs could be used to extract the angular profile, however the angular profile shown in Section 5.3.2 which was applied to the simulation was measured using the 407 nm run only.

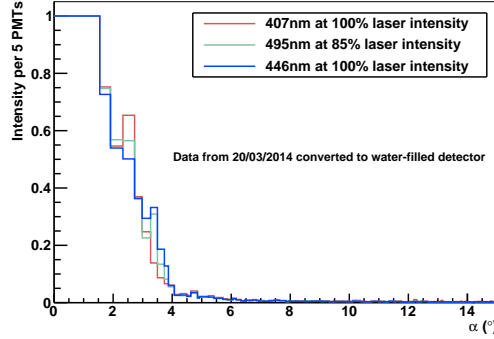


**Figure 6.9:** Angular profiles of FS155 extracted from the 407 nm, 446 nm and 495 nm runs listed in Table A.2 as described in Section 5.3.2. The profiles were converted to the water profiles using the method described in Section 5.3.3.

potential fluctuations over different runs. All three profiles are shown in Figure 6.9.

It was found that the width of the profile determined for the three runs of FS155 does not vary significantly. Averaging the fluctuation factors determined by comparing the different binned profiles over all three fibres yields a fluctuation factor of

$$f_{\text{width}} = 2.0 \quad (6.19)$$

To determine the fluctuation in the tail, the process was repeated considering profile contributions above  $\alpha = 4^\circ$ . For the tail contributions, it was found that the fluctuations between different runs for the same fibre are larger than the fluctuations achieved by varying the bin sizes. The resulting factor was determined to be

$$f_{\text{tail}} = 1.3 \quad (6.20)$$

To study the effects of changing the width of the profile,  $p2$ , the standard deviation of the Gaussian fit, was changed by  $p2 \cdot f_{\text{width}}$  and  $p2/f_{\text{width}}$ . The tail was altered by applying  $f_{\text{tail}}$  to  $p4$  in the same fashion. The resulting profiles are shown in Figure 6.10. For the scaling measurement follows

$$\begin{aligned} \Delta s_{\text{sys}}^{\text{width}} &= 0.145 \\ \Delta s_{\text{sys}}^{\text{tail}} &= 0.135 \end{aligned} \quad (6.21)$$

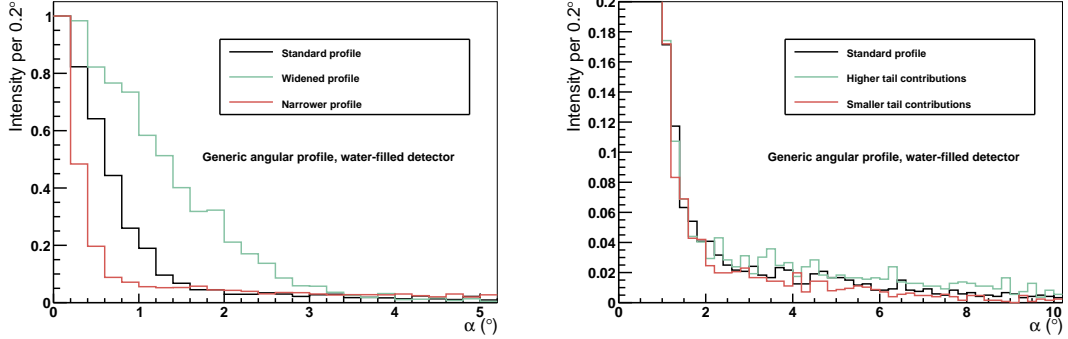


**Figure 6.10:** Generic angular profile with altered width (left) and altered tail (right) using  $f_{\text{width}} = 2.0$  and  $f_{\text{tail}} = 1.3$ .

#### 6.4.4 Fibre Direction

Alterations in the fibre directions may lead to misidentification of events by the applied spatial cuts. The fibre directions for the node 37 and node 55 fibres were measured as described in Section 5.3.1, generating uncertainties on the fibre directions following from the procedure. To achieve uncertainties on the fibre directions for the remaining fibres, the direction measurement was carried out on the fake data sets for the node 07 and node 25 fibres (see Appendix Table B.4).

Each direction vector has three components with accompanying uncertainties. These uncertainties can be applied in a variety of combinations as is illustrated in Figure 6.11 for a 2-dimensional case. Given sufficient amount of time, all these possibilities should be studied by considering a cone around the direction vector covering all possibilities. However, this work concentrates more on a qualitative measure of the uncertainties. Therefore two cases were picked to be studied for this document.

The SNO+ geometry is based around the  $z$ -axis. Even though this geometry is broken by the fibre positions it was decided to study direction alterations within the  $x$ - $y$ -plane (case 1) and along the  $z$ -axis (case 2) separately. Hence, in case 1 no uncertainties were applied to the  $z$ -components of the direction vector, whilst in case 2 uncertainties were applied to the  $z$ -components only. The sign each coordinate was altered with was determined by a generator which randomly returned True (+) and False (-). The resulting signs are listed in Table 6.7 for each fibre. The determined

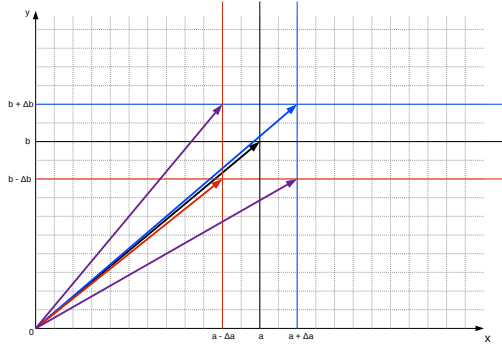


**Figure 6.11:** Schematic of 2-dimensional vector  $\vec{v} = \begin{pmatrix} a \pm \Delta a \\ b \pm \Delta b \end{pmatrix}$  and the possible uncertainty combinations and the resulting vectors.  $\vec{v}$  is depicted in black, whilst a symmetric application of the uncertainties are shown in blue  $\begin{pmatrix} a + \Delta a \\ b + \Delta b \end{pmatrix}$  and red  $\begin{pmatrix} a - \Delta a \\ b - \Delta b \end{pmatrix}$ . Asymmetric application of the uncertainties are depicted in purple.

uncertainty on the scaling factor is:

$$\Delta s_{\text{sys}}^{\text{direction}} = 0.253 \quad (6.22)$$

### 6.4.5 Noise

The noise rates in the detector are measured using the PulseGT trigger. Any uncertainty on this measurement is considered small and of statistical nature. Currently, the noise rate in RAT is simulated at 500 Hz for each PMT. A full SMELLIE scan is expected to take 1 day. The noise hits expected for all PMTs within the trigger window of 400 ns are:

$$N = 500 \text{ Hz} \cdot (400 \times 10^{-9}) \text{ s} \cdot 9300 \quad (6.23)$$

The PulseGT trigger measures the noise rate at 5 Hz, therefore leading to a total number of measured noise hits of

$$N_{\text{tot}} = N \cdot 5 \text{ Hz} \cdot 3600 \text{ s} \cdot 24 = 803\,520 \pm 896, \quad (6.24)$$

**Table 6.7:** The signs of the applied direction uncertainties for each fibre as returned by the random generator.

Fibre	<i>x-y</i> -plane		<i>z</i> -axis
	<i>x</i>	<i>y</i>	
FS007	-	-	-
FS107	+	+	+
FS207	-	-	+
FS025	-	-	-
FS125	+	-	+
FS225	+	-	-
FS037	-	-	-
FS137	+	-	+
FS237	+	-	-
FS055	+	-	+
FS155	+	+	-
FS255	-	-	+

an uncertainty of approximately 0.1 %. Thus, the uncertainty on the noise rate for a SMELLIE run is

$$\Delta r = 0.5 \text{ Hz}. \quad (6.25)$$

Re-simulating the control samples with the altered noise rate yields

$$\Delta s_{\text{sys}}^{\text{noise}} = 0.007 \quad (6.26)$$

## 6.5 Summary and Discussion

A cut selection was developed to split photon hits from the SMELLIE beams according to their optical interactions inside the detector. The cut selection was verified using different detector geometries and the photon history in the Monte Carlo simulations. A measurement strategy was established to measure the scattering occurring in the detector medium using data. The bias on the measurement was found to be dependent on the range and number of control samples used to measure the scaling factor.

To test the measurement strategy, it was applied to a fake data set. The intensity of the fake data set was measured using the method described in Section 5.3.3 and was found to be on average

$$I = (938 \pm 24) \text{ nppb.} \quad (6.27)$$

A marginal overestimation of the intensity was expected from the bias considerations on the measurement. Furthermore, given the measured scaling factor value an increased amount of scattering for the fake data set is predicted, leading to a potential minimal increase in the measured intensity value following Figure 5.13. The scaling factor was measured to be

$$s^{\text{data}} = 1.34 \pm (0.01)_{\text{stat.}} \pm (0.37)_{\text{sys.}} . \quad (6.28)$$

Considering the findings in Section 6.2.3, this value is expected to over-estimate the actual scaling factor of the data set by approximately  $\Delta s = 0.02$ .

Figure 6.12 shows the relative contribution of each systematic uncertainty on the scaling factor measurement. Major contributions on the systematic uncertainty originated from the uncertainties on the direction measurement. This is an effect of the applied spatial cuts to separate the different measurement cut regions. Repeating the direction measurements in a water-filled detector with a narrower beam profile and increased statistics (i.e. more data samples) may improve the uncertainty on the fibre directions. Additionally, only a random set of altered fibre directions was used for this measurement. To achieve a better representation of the systematic uncertainties arising from the direction measurements, an iteration over all possible directions contained within a cone around the fibre direction should be considered.

Other considerable contributions to the uncertainty on the measurement followed from the intensity measurement and the angular profiles of the fibres. The uncertainty on the intensity measurement for each fibre-wavelength combination is of statistical nature. Reiterating the intensity measurement over a number of different data sets at the same intensity for each fibre-wavelength combination could improve these uncertainties. Additionally, combining the intensity measurement described in this thesis with the intensity measurement proposed in [113] may yield a more precise value.

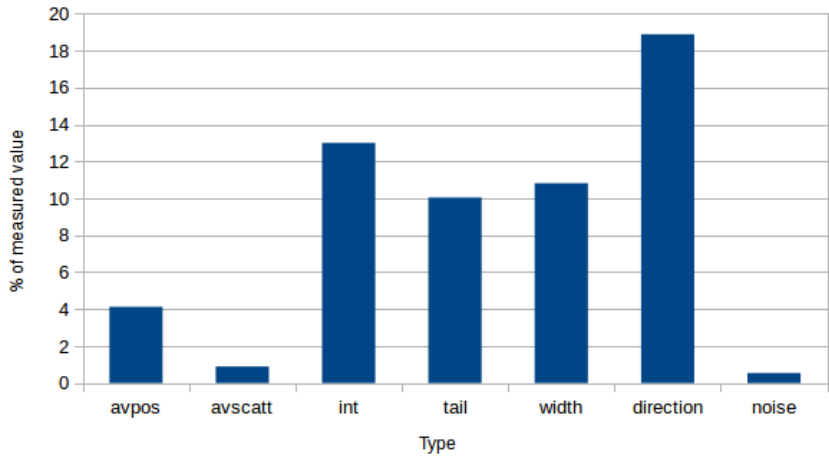


**Figure 6.12:** Relative contributions of the systematic uncertainties on the scaling factor measurement.

**Table 6.8:** The scattering length for different wavelengths as determined for the fake data sets using the measured scaling factor  $s^{\text{data}}$  including the systematic uncertainties on the measurement.

Wavelength (nm)	Scattering Length (mm)
380	$110\,489 \pm 30\,508$
400	$135\,651 \pm 37\,455$
440	$198\,606 \pm 54\,839$
500	$331\,180 \pm 91\,445$

Also, both the tail and the width of the angular profile were considered separately, but in reality they are correlated to each other. If a good understanding of the angular profiles and the interaction between the profile width and the profile tail can be achieved, the uncertainty on the scaling factor measurement arising from this aspect will be reduced. The impact on the scattering length  $l$  for different wavelengths is shown in Table 6.8 including the systematic uncertainties.

Figure 6.13 shows the registered number of hits (bottom), the reconstructed hit times (top right) and the difference between the true event position and the reconstructed event position (top left) for invisible proton-decay events in a water-filled detector similar to Figure 4.1. Presented are the different distributions with the measured scaling factor from the fake data set  $s^{\text{data}}$  applied to the water, as well as the

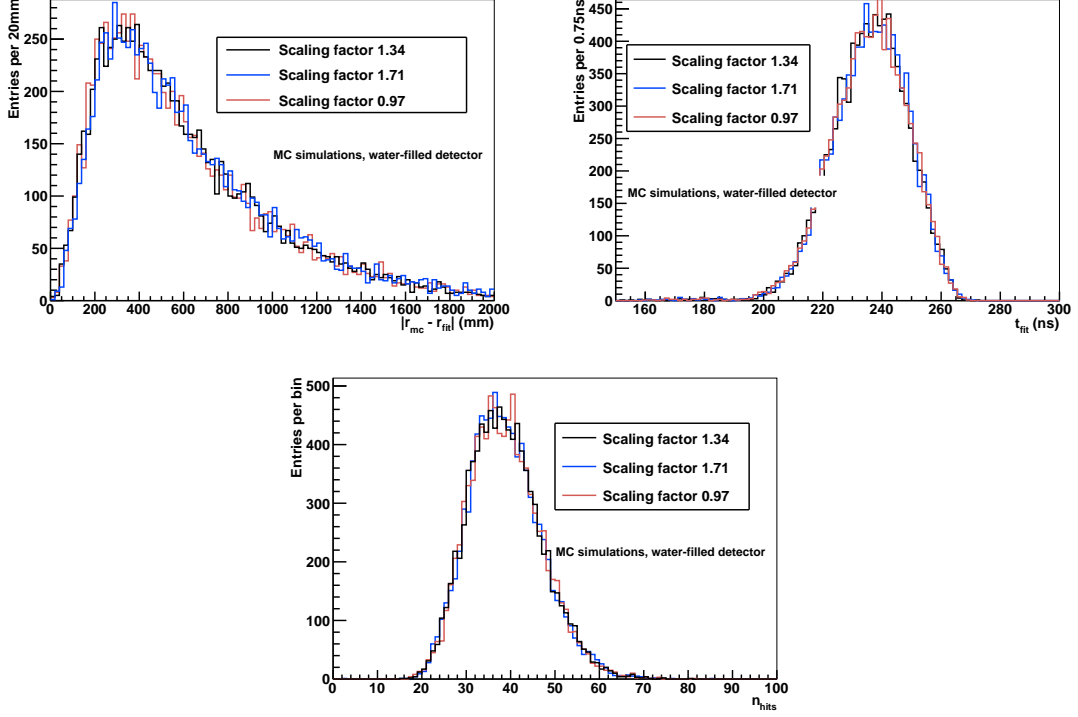


**Figure 6.13:** Invisible proton decay for different reconstruction variables. Shown are the difference between reconstructed and true position  $|r_{mc} - r_{fit}|$  (top left), the reconstructed hit time  $t_{fit}$  (top right) and the  $n_{hits}$  distribution for the in this Chapter measured scattering length  $l$  in water and  $s = 0.97$  and  $s = 1.71$ , covering the uncertainty on the measurement.

upper uncertainty boundary  $s_{upper}^{data} = 1.34 + \sqrt{0.01^2 + 0.37^2}$  and the lower uncertainty boundary  $s_{lower}^{data} = 1.34 - \sqrt{0.01^2 + 0.37^2}$ . It can be observed that none of the distributions varies significantly with the given measurement uncertainties of the scattering in the water volume.

After the blind analysis on the fake data set was finalised, the intensity parameter and the scaling factor used to produce the fake data set were revealed by the third party:

$$I^{data} = 930 \text{ nppb} \quad (6.29)$$

$$s^{data} = 1.325$$

Comparing these values to the values measured by the work presented in this docu-

ment a good match can be observed. The discrepancies between the measured and the simulated scaling factor can be retraced to the bias of the measurement and can be eliminated by choosing a set of control samples simulated with values closer to the measured value. The slight overestimation of the measured intensity was expected as discussed above.

The presented measurement can be easily adapted for the scintillator phase. Additionally to the optical effects described in this Chapter, absorption and re-emission effects have to be considered for the scintillator cocktail. Therefore, a separate fit on the re-emission properties of the scintillator material similar to the scattering length measurement will have to be carried out. Preliminary studies on the measurement in scintillator have been done [131].

# 7 Internal Background Estimation during the Pure Scintillator Phase

## 7.1 Measurement of Uranium and Thorium chain Backgrounds in Pure Scintillator

The levels of all Uranium and Thorium chain isotopes in the scintillator volume can be determined using the respective Bismuth-Polonium (Bi-Po) coincidences within the decay chains, provided all isotopes within the decay chain are in equilibrium. Due to the short half-lives of  $^{212}\text{Po}$  ( $T_{\frac{1}{2}} = 0.30\ \mu\text{s}$ ) and  $^{214}\text{Po}$  ( $T_{\frac{1}{2}} = 164\ \mu\text{s}$ ) these isotopes decay shortly after the decay of the Bismuth isotopes into Polonium, allowing the Bismuth decay to be tagged [70]. Thus, a cut selection was developed to select pure  $^{212}\text{Bi}^{212}\text{Po}$  and  $^{214}\text{Bi}^{214}\text{Po}$  samples, containing as little of other event types as possible. This Chapter discusses the applied cut selection and the resulting measurement uncertainty for Uranium and Thorium chain backgrounds during the pure scintillator phase and for a one month merged data set simulated for a Tellurium-loaded cocktail.

### 7.1.1 Cut Selection for $^{212}\text{Bi}^{212}\text{Po}$ and $^{214}\text{Bi}^{214}\text{Po}$ Measurements

The cut strategy, as depicted in Figure 7.1, was developed to focus on the selection of the Po candidate in either measurement, and to then look back in time at the previous events to find the Bi candidate. The  $^{212}\text{Po}$  and  $^{214}\text{Po}$  decay by emitting  $\alpha$  particles at specific energy values, providing a narrow, distinct energy and  $n_{\text{hits}}$  spectrum. On the contrary, the Bismuth isotopes decay emitting  $\beta$ -particles, which can have energies

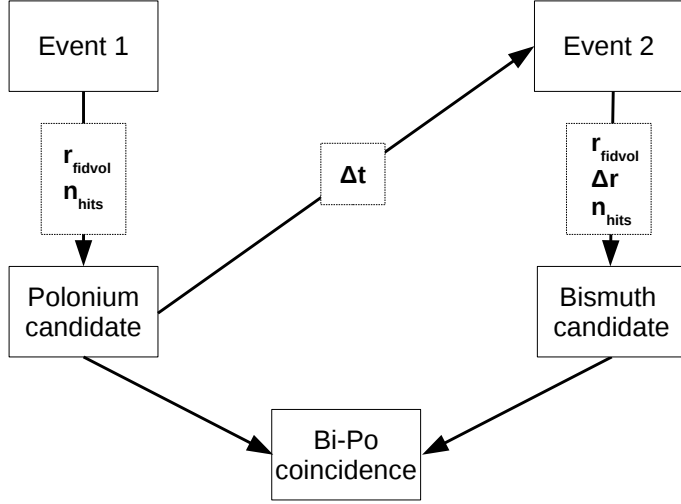


**Figure 7.1:** Cut flow scheme for Bismuth-Polonium (Bi-Po) coincidence measurements. The Polonium selection criteria  $r_{\text{fidvol}}$  and  $n_{\text{hits}}^{\text{Po}}$  are applied to an event 1. If this event passes both cuts, it is selected as a Polonium candidate. Subsequently, a previous event 2 is looked for within a time interval  $\Delta t$ . If event 2 passes the Bismuth selection cuts  $r_{\text{fidvol}}$ ,  $\Delta r$  and  $n_{\text{hits}}^{\text{Bi}}$ , it is selected as a Bismuth candidate and a Bi-Po coincidence event is tagged.

ranging over a broad spectrum up to the  $Q$ -value of the decay, due to the three-body nature of the decay. Therefore, it would prove challenging to select a Bismuth sample with low background contamination using cuts on the  $n_{\text{hits}}$  spectra alone.

### Selection of the Polonium candidate

First, a fiducial volume cut was applied. The cut was chosen to reject backgrounds from external sources (see Section 3.5), but to keep as many Bi-Po events as possible. This is especially important for the  $^{212}\text{Bi}$ - $^{212}\text{Po}$  decays, which are expected to occur at very low rates. Thus, the fiducial volume was chosen to be equivalent of a cut on the reconstructed event radius at  $r_{\text{fidvol}} < 4\,000 \text{ mm}$  based on [132].

Assuming all background isotopes are distributed isotropically within the AV, the

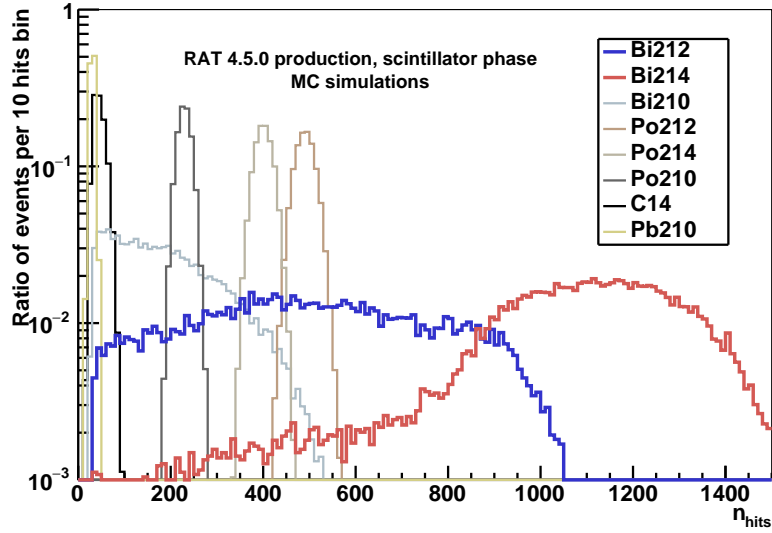


**Figure 7.2:** The  $n_{\text{hits}}$  spectra of the four high rate backgrounds  $^{14}\text{C}$ ,  $^{210}\text{Pb}$ ,  $^{210}\text{Bi}$  and  $^{210}\text{Po}$  and the individual Bi-Po coincidence isotopes  $^{212}\text{Bi}$ ,  $^{212}\text{Po}$ ,  $^{214}\text{Bi}$  and  $^{214}\text{Po}$ . Each distribution was scaled by a factor of (1 / Number of entries in the histogram) for convenience. To each distribution a fiducial volume cut of  $r_{\text{fidvol}} < 4\,000 \text{ mm}$  was applied and re-triggered events were rejected. The plot was produced using RAT 4.5.0 production files.

number of decays found within a certain volume  $V(r_{\text{fidvol}})$  is:

$$N_{r_{\text{fidvol}}} = N_{\text{all}} \cdot \frac{V(r_{\text{fidvol}})}{V(r_{AV})} = N_{\text{all}} \cdot \left( \frac{r_{\text{fidvol}}}{r_{AV}} \right)^3, \quad (7.1)$$

with  $N_{\text{all}}$  being all events found within the AV,  $V(r_{AV})$  being the volume of the AV with a radius  $r_{AV}$  and  $r_{\text{fidvol}}$  being the radius of the chosen fiducial volume. Thus, the abundance of all background isotopes, including the  $^{212}\text{Po}$  and  $^{214}\text{Po}$  isotopes, was reduced by a factor of  $\left( \frac{r_{\text{fidvol}}}{r_{AV}} \right)^3$ .

An  $n_{\text{hits}}$  cut was applied to select  $^{212}\text{Po}$  and  $^{214}\text{Po}$  events based on the spectra shown in Figure 7.2. The  $n_{\text{hits}}$  cuts on the  $^{212}\text{Po}$  and  $^{214}\text{Po}$  were tuned especially to reject the other respective Polonium isotope and  $^{210}\text{Po}$  from the leaching backgrounds. Some of the cut efficiency was sacrificed in order to be able to reach a higher purity in the  $^{212}\text{Po}$  and  $^{214}\text{Po}$  selection. The  $n_{\text{hits}}$  cut efficiency was determined by considering only events occurring within the fiducial radius of  $r_{\text{fidvol}} < 4\,000 \text{ mm}$  which do not contain

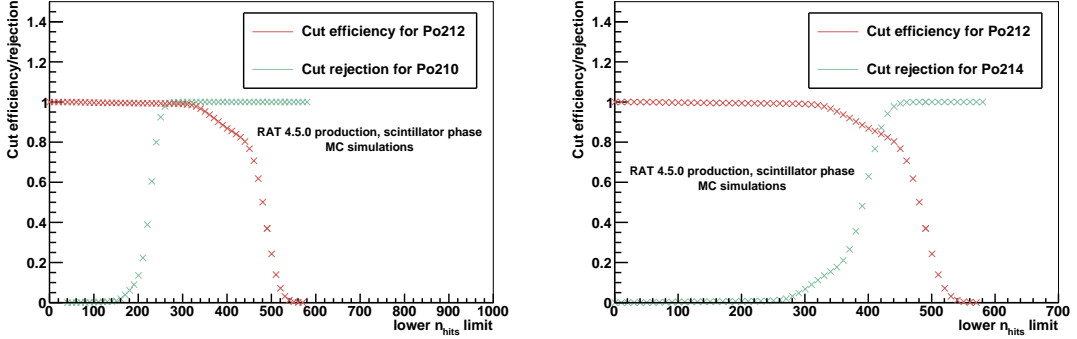


**Figure 7.3:** Development of the cut efficiencies for the  $^{212}\text{Po}$   $n_{\text{hits}}$  cut with a fixed upper limit of  $n_{\text{hits}} = 580$  and a variable lower limit ranging from  $n_{\text{hits}} = 0$  to  $n_{\text{hits}} = 580$  in steps of 10. On the left, the  $^{212}\text{Po}$  cut efficiency is compared to the rejection of  $^{210}\text{Po}$  events, the right shows the rejection of  $^{214}\text{Po}$  events at each cut value. The plots were produced using RAT 4.5.0 production files.

hits from re-triggered events<sup>20</sup>. The cuts were applied to RAT 4.5.0 MC production samples and the cut efficiency  $\epsilon^{\text{Po}21x}(n_{\text{hits}})$  was extracted:

$$\epsilon^{\text{Po}21x}(n_{\text{hits}}) = \frac{N_{\text{events}}^{n_{\text{hits}}}}{N_{\text{events}}^{r_{\text{fidvol}}}} \quad (7.2)$$

The cut rejection follows from that as  $r^{\text{Po}21x}(n_{\text{hits}}) = 1 - \epsilon^{\text{Po}21x}(n_{\text{hits}})$ . Figure 7.3 shows the efficiency plots for the  $^{212}\text{Po}$  selection alongside the rejection of the cut values on both  $^{214}\text{Po}$  and  $^{210}\text{Po}$ . The efficiency plot for the  $^{214}\text{Po}$  selection is presented in Figure 7.4, including the rejection progress for  $^{212}\text{Po}$  and  $^{210}\text{Po}$ . Having a narrow energy spectrum made it necessary to apply a lower and an upper hit boundary on the spectrum to avoid misidentification of events. The energies emitted by the  $^{210}\text{Po}$  decay and the  $^{214}\text{Po}$  decay are lower than the energy of the  $^{212}\text{Po}$  decay, hence only a fine tuning of the lower  $n_{\text{hits}}$  cut value was required for the  $^{212}\text{Po}$  selection, as shown in Figure 7.3. For the tuning of the  $n_{\text{hits}}$  cut values for the  $^{214}\text{Po}$  selection, the upper boundary was determined with respect to the rejection of  $^{212}\text{Po}$ , whilst the lower boundary depended on the rejection potential of  $^{210}\text{Po}$  as depicted in Figure 7.4. The values were chosen to be  $450 \leq n_{\text{hits}} \leq 580$  for  $^{212}\text{Po}$  and  $290 \leq n_{\text{hits}} \leq 450$  for  $^{214}\text{Po}$ .

---

<sup>20</sup>See Section 3.3.2 for a definition of re-triggered events.

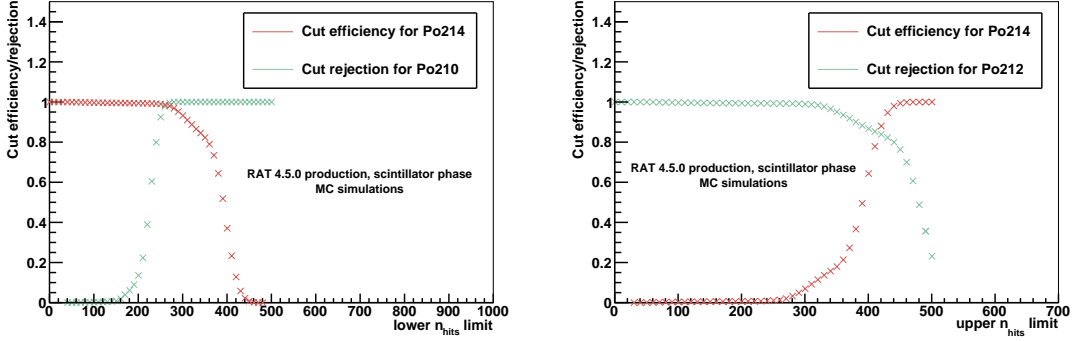


**Figure 7.4:** Development of the cut efficiencies for the  $^{214}\text{Po}$   $n_{\text{hits}}$  cut. The left plot shows the  $^{214}\text{Po}$  cut efficiency compared to the  $^{210}\text{Po}$  cut rejection. Here, the upper cut value was fixed to  $n_{\text{hits}} = 500$ , whilst the lower limit was increased from  $n_{\text{hits}} = 0$  to  $n_{\text{hits}} = 500$  in steps of 10. The right plot compares the  $^{214}\text{Po}$  cut efficiency to the  $^{212}\text{Po}$  rejection. Due to the higher energy emitted by the  $^{212}\text{Po}$  decay, the lower cut value was set to  $n_{\text{hits}} = 0$ , whilst the upper limit was varied from  $n_{\text{hits}} = 500$  to  $n_{\text{hits}} = 0$  in steps of 10. The plots were produced using RAT 4.5.0 production files.

### Inter-event timing cut

A cut on the inter-event timing was applied based on the half-life  $T_{\frac{1}{2}}$  of the Polonium decay, which is the defining factor of the decay time between the Bismuth and the Polonium candidate. The number of isotopes remaining after a certain amount of time  $t$  is described by the exponential decay law

$$N(t) = N_0 \cdot \exp\left(\frac{-\ln 2 \cdot t}{T_{\frac{1}{2}}}\right) \quad (7.3)$$

where  $N_0$  is the amount of isotopes found at  $t = 0$ . Integrating this exponential function within a time interval  $\Delta t$  yields the number of decays which have occurred within this time  $\Delta t$ . Hence, the cut efficiency on an inter-event timing cut between the Polonium and the Bismuth candidate is [106]:

$$\epsilon(\Delta t) = \frac{N_{\text{events}}^{\Delta t}}{N_{\text{events}}^{n_{\text{hits}}}} = \frac{\int_{0_{ns}}^{\Delta t} \exp\left(\frac{-\ln 2 \cdot t}{T_{\frac{1}{2}}}\right) dt}{\int_{0_{ns}}^{\infty} \exp\left(\frac{-\ln 2 \cdot t}{T_{\frac{1}{2}}}\right) dt}. \quad (7.4)$$

To achieve a selection efficiency of  $\epsilon(\Delta t) = 99.95\%$ , an inter-event time window  $\Delta t$

of  $1.799 \times 10^6$  ns was chosen for the  $^{214}\text{Bi}^{214}\text{Po}$  coincidence, equating to approximately  $11 T_{\frac{1}{2}}$ . For the same cut efficiency, an inter-event time window  $\Delta t$  of  $3.69 \times 10^3$  ns was sufficient to select  $^{212}\text{Bi}^{212}\text{Po}$  coincidences, relating to approximately  $12 T_{\frac{1}{2}}$ . In order to reject  $^{212}\text{Bi}^{212}\text{Po}$  events from the  $^{214}\text{Bi}^{214}\text{Po}$  selection,  $\Delta t$  was required to be larger than 3 690 ns, which reduces the potential mistagging of  $^{212}\text{Bi}^{212}\text{Po}$  events by 99.95 %. From Equation 7.4 follows an efficiency loss of 1.38 % on the  $^{214}\text{Bi}^{214}\text{Po}$  selection due to the lower timing boundary.

A lower limit on  $\Delta t$  had to be considered for the  $^{212}\text{Bi}^{212}\text{Po}$  coincidences. The selection only considers coincidences in which both isotopes are triggered as separate events. If the Bismuth and Polonium fall within the same trigger window, they were not considered for the selection, since such an event would yield a higher  $n_{\text{hits}}$  count than expected from the Polonium decay. As described in Section 3.3.2, the trigger window contains all events following within 220 ns of the Bismuth events. Therefore, if the  $^{212}\text{Po}$  decays within 220 ns of the  $^{212}\text{Bi}$ , both decays are seen as one event [85]. From Equation 7.4 follows an efficiency loss of 51.6 %. It should be noted that this is only an approximation, i.e it is assumed that any Polonium decay occurring 220 ns after the Bismuth decay still crosses the required threshold when the time-lock window is reset (see Section 3.3.2). The influence of the trigger on the event selection is very complex and the available statistics were not sufficient to undergo a comprehensive study of this effect, which has been carried out in [133].

### Selection of the Bismuth candidate

The position of the Bismuth candidate depends on the position of the Polonium decay. The mixing of isotopes due to circulations in the scintillator cocktail is expected to be negligible over very short time frames, thus within the short timing interval in which the Bi-Po coincidences occur, no movement in the decay positions of the two isotopes is predicted [134]. Thus, the factor  $\left(\frac{r_{\text{fidvol}}}{r_{AV}}\right)^3$  does not represent the efficiency of a fiducial volume cut on the Bismuth, since this factor is only valid for a random isotropic distribution of isotopes.

A fiducial volume cut on the Bismuth was necessary, since some Bismuth candidates can be reconstructed outside of the fiducial volume up to the boundary of the AV, as Figure 7.5 shows. To avoid misidentifying backgrounds from external sources as

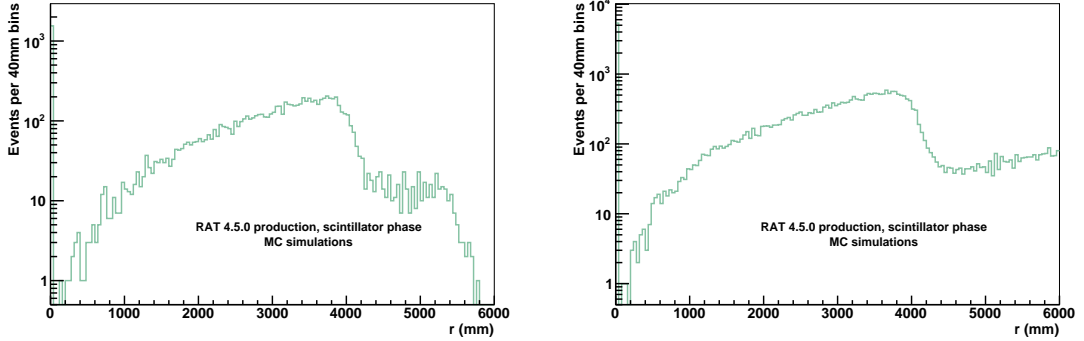


**Figure 7.5:** The reconstructed position of the  $^{212}\text{Bi}$  (left) and  $^{214}\text{Bi}$  (right) candidates within the AV volume. All cuts on the Polonium candidate as shown in Figure 7.1 have been applied. These were plotted using the RAT 4.5.0 production files for the  $^{212}\text{Bi}^{212}\text{Po}$  and  $^{214}\text{Bi}^{214}\text{Po}$  coincidences.

Bismuth candidates, the fiducial volume cut was chosen to be  $r_{\text{fidvol}}^{\text{Bi}21x} < 4000 \text{ mm}$ . The efficiency  $\epsilon(r_{\text{fidvol}}^{\text{Bi}21x})$  of this cut could only be determined from the simulation using the relation shown in Equation 7.5. Using the production samples<sup>21</sup> the efficiency was found to be 91.1 % for the  $^{212}\text{Bi}^{212}\text{Po}$  coincidence and 87.6 % for the  $^{214}\text{Bi}^{214}\text{Po}$  selection. These values are dependent on the reconstruction resolution and are likely to change as the reconstruction processes are refined for later RAT releases.

$$\epsilon(r_{\text{fidvol}}^{\text{Bi}21x}) = \frac{N_{\text{events}}^{r_{\text{fidvol}}(Bi)}}{N_{\text{events}}^{\Delta t}}, \quad (7.5)$$

with  $N_{\text{events}}^{r_{\text{fidvol}}(Bi)}$  being the number of events passing the fiducial volume cut on the Bismuth candidate and  $N_{\text{events}}^{\Delta t}$  is the number of events left after applying the inter-event timing cut.

A cut on the distance  $\Delta r$  between the two selected isotopes was applied (since their decay positions should be equal, see above). Equivalent to Equation 7.1, the cut efficiency on isotropically distributed events follows from

$$N_{\Delta r} = N_{\text{all}} \cdot \frac{V(r_{\Delta r})}{V(r_{\text{fidvol}})} = N_{\text{all}} \cdot \left( \frac{\Delta r}{r_{\text{fidvol}}} \right)^3, \quad (7.6)$$

---

<sup>21</sup>listed in Table C.3

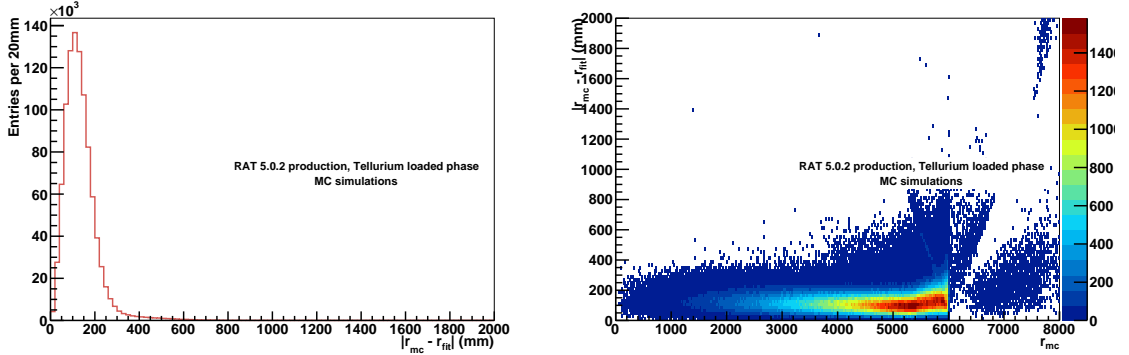


**Figure 7.6:** SNO+ position reconstruction resolution demonstrated on  $^{130}\text{Te}$   $0\nu\beta\beta$  decays. Shown on the left are the difference between the reconstructed radial position  $r_{\text{fit}}$  and the true radial position  $r_{\text{mc}}$  of the decays  $|r_{\text{mc}} - r_{\text{fit}}|$ . The right plot shows the same variable vs  $r_{\text{mc}}$ . The plots were made using RAT 5.0 production files with the same detector configurations as described in Section 7.3.

with

$$\Delta r = \sqrt{(x_1 - x_2)^2 + (y_1 - y_2)^2 + (z_1 - z_2)^2}. \quad (7.7)$$

Here,  $\{x_i, y_i, z_i\}$  describe the reconstructed position coordinates of two isotopes  $i = 1, 2$ .

The difference between the positions of the two coincidence decays depends solely on the expected reconstruction resolution (see Section 3.6), which is presented in Figure 7.6 using a sample of  $^{130}\text{Te}$   $0\nu\beta\beta$  decays from the RAT 5.0 production. Figure 7.7 shows  $\Delta r$  between the Bi-Po coincidence decays after the previously mentioned cuts have been applied. Based on these plots and the study in [106] on position reconstruction, cut values of  $\Delta r > 0$  mm<sup>22</sup> and  $\Delta r \leq 2000$  mm were applied. The cut efficiency  $\epsilon(\Delta r)$  can be determined using the RAT 4.5.0 production samples from

$$\epsilon(\Delta r) = \frac{N_{\text{events}}^{\Delta r}}{N_{\text{events}}^{r_{\text{fidvol}}(Bi)}}, \quad (7.8)$$

where  $N_{\text{events}}^{\Delta r}$  is the number of events left after applying the selection criterion on the positions of the two decays.

Finally, a cut on the deposited  $n_{\text{hits}}$  of the Bismuth candidates was considered. Several high rate backgrounds are expected in the scintillator volume, including  $^{14}\text{C}$ ,

<sup>22</sup>to reject events with invalid reconstruction

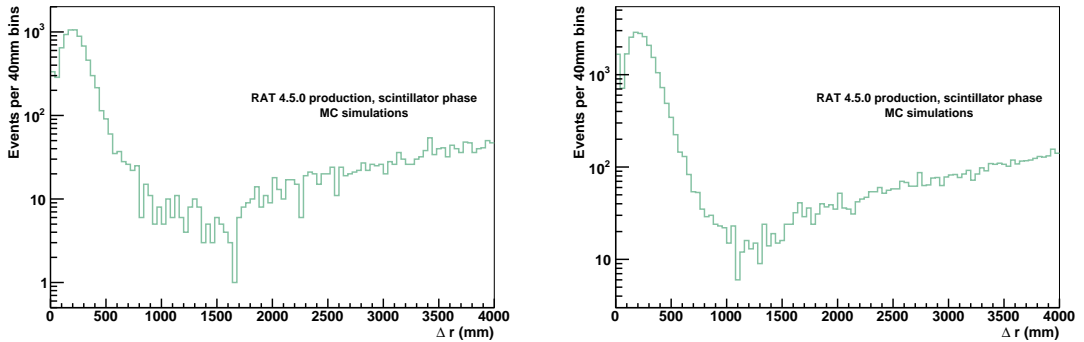


**Figure 7.7:** Reconstructed inter-event distance  $\Delta r$  between the Bismuth and Polonium decays for the  $^{212}\text{Bi}^{212}\text{Po}$  (left) and  $^{214}\text{Bi}^{214}\text{Po}$  (right) coincidences. The Polonium cut selection and the fiducial volume cut on the Bismuth candidate was applied. The inter-event distance  $\Delta r$  of all Bismuth and Polonium candidates was calculated using Equation 7.7. The plots were made using the RAT 4.5.0 production files for the  $^{212}\text{Bi}^{212}\text{Po}$  and  $^{214}\text{Bi}^{214}\text{Po}$  coincidences. The rise in the distributions for  $\Delta r > 2000\text{ mm}$  is due to a potential poor reconstruction of these events. For RAT 4.5.0 production ntuples, the validity of the fitted values was not stored. In later RAT productions a validity flag was added to each event, so poorly reconstructed events can be vetoed.

which naturally occurs in the scintillator cocktail, and the isotopes entering the inner volume from the AV surface via leaching,  $^{210}\text{Pb}$ ,  $^{210}\text{Bi}$  and  $^{210}\text{Po}$  [70]. The energy spectra especially from  $^{210}\text{Bi}$  and  $^{210}\text{Po}$  overlap with the energy spectra of  $^{214}\text{Bi}$  and  $^{212}\text{Bi}$ , as is shown in Figure 7.2. The majority of  $^{214}\text{Bi}$  events emit an energy which yields  $n_{\text{hits}} \geq 600$  at which value all potentially problematic high rate backgrounds are mostly rejected.

The  $^{212}\text{Bi}$  spectrum overlaps significantly with the spectra from the other isotopes (see Figure 7.2). A cut on  $n_{\text{hits}} \geq 100$  was applied to reduce the misidentification of  $^{14}\text{C}$  and  $^{210}\text{Pb}$  without sacrificing the  $^{212}\text{Bi}$  selection. The cut values as well as the cut efficiencies for both selections are summarised in Table 7.1 together with the total selection efficiency on each coincidence. Part of this study was to compare the measurement capabilities with and without an  $n_{\text{hits}}$  cut on the Bismuth candidate, hence the efficiencies for both cases are presented.

### Selection efficiencies of $^{212}\text{Bi}^{212}\text{Po}$ and $^{214}\text{Bi}^{214}\text{Po}$ coincidences

The total efficiency  $\epsilon$  presented in Table 7.1 for the cut selections could be determined by multiplying the individual efficiencies for each cut. Here, events occurring in the

**Table 7.1:** Cuts and cut efficiencies for each cut parameter for the  $^{212}\text{Bi}^{212}\text{Po}$  and  $^{214}\text{Bi}^{214}\text{Po}$  coincidence selection. The cut efficiencies were determined as described in Equations 7.1–7.8. The total efficiency  $\epsilon$  on each selection follows from Equation 7.9.

	$^{212}\text{Bi}^{212}\text{Po}$			$^{214}\text{Bi}^{214}\text{Po}$		
	Cut value lower	Cut value upper	efficiency	Cut value lower	Cut value upper	efficiency
$r_{\text{fidvol}}$	-	4 000 mm	$\left(\frac{r_{\text{fidvol}}}{r_{AV}}\right)^3$	-	4 000 mm	$\left(\frac{r_{\text{fidvol}}}{r_{AV}}\right)^3$
$n_{\text{hits}}^{\text{Po}}$	450	580	0.767	290	450	0.946
$\Delta t$	400 ns	3 690 ns	0.484	3 690 ns	1 798 788 ns	0.9857
$r_{\text{fidvol}}$ on Bi	-	4 000 mm	0.911	-	4 000 mm	0.876
$\Delta r$	0 mm	2 000 mm	0.81	0 mm	2 000 mm	0.786
Combined efficiency	8.1 %			19.0 %		
$n_{\text{hits}}^{\text{Bi}}$	100	-	0.93	600	-	0.869
Total efficiency $\epsilon$	7.5 %			16.5 %		

neck were not considered due to irregularities in reconstruction involving these events (compare Section 3.6). Hence, the cut efficiency  $\epsilon$  was evaluated only analysing events reconstructed within the AV volume with  $r_{AV} = 6\,000\,\text{mm}$ :

$$\epsilon = \left(\frac{r_{\text{fidvol}}}{r_{AV}}\right)^3 \cdot \epsilon^{\text{Po}21x}(n_{\text{hits}}) \cdot \epsilon(\Delta t) \cdot \epsilon(r_{\text{fidvol}}^{\text{Bi}21x}) \cdot \epsilon(\Delta r) \cdot \epsilon^{\text{Bi}21x}(n_{\text{hits}}) \quad (7.9)$$

The efficiencies for the  $n_{\text{hits}}$  cuts, the fiducial volume cut  $r_{\text{fidvol}}^{\text{Bi}21x}$  on the Bismuth candidate and the  $\Delta r$  cut were taken from the Rat 4.5.0 MC production samples presented in Table C.3.

### Measurement of $^{214}\text{Bi}^{214}\text{Po}$ coincidences

The number of the remaining  $^{214}\text{Bi}^{214}\text{Po}$  coincidences after applying the cuts,  $N_{\text{Bi}214\text{Po}214}^{\text{allcuts}}$ , was determined. Knowing the cut efficiency  $\epsilon$ , the number of  $^{214}\text{Bi}^{214}\text{Po}$  coincidences occurring within the AV volume  $N_{\text{Bi}214\text{Po}214}$  could be calculated by

$$N_{\text{Bi}214\text{Po}214} = \frac{N_{\text{Bi}214\text{Po}214}^{\text{allcuts}}}{\epsilon}. \quad (7.10)$$

Table 7.2 shows the number of expected Bismuth decays  $N_{\text{Bi}214}$  in 181 days at the rate presented in Table C.1, as well as for the cases that the rate is double or half the

**Table 7.2:** Expected event yields and measurement uncertainties for the Uranium and Thorium chain measurements for a run period of 181 days. The expected rates for each coincidence were taken from Table C.1 and correspond to the expected background concentrations as presented in Table 7.3. The development of the uncertainties for double and half the expected event rates are also presented. The displayed uncertainties do not include potential mistagged coincidence events.  $N_{\text{Bi}21x}$  is the number of expected  $^{21x}\text{Bi}$  decays in 181 days.  $N_{\text{Po}21x}$  is the expected number of  $^{21x}\text{Po}$  decays when accounting for branching ratios of the Bismuth decays, which is equivalent to the number of expected coincidences  $N_{\text{Bi}21x\text{Po}21x}$ .

	$^{212}\text{Bi}^{212}\text{Po}$			$^{214}\text{Bi}^{214}\text{Po}$		
	expected rate	$2 \times$ rate	$\frac{1}{2} \times$ rate	expected rate	$2 \times$ rate	$\frac{1}{2} \times$ rate
$N_{\text{Bi}21x}$	338	676	169	2429	4858	1214
$N_{\text{Po}21x}$	216	433	108	2428	4857	1214
$N_{\text{Bi}21x\text{Po}21x}^{\text{all cuts}}$	$16 \pm 4$	$32 \pm 6$	$8 \pm 3$	$401 \pm 20$	$801 \pm 28$	$200 \pm 14$
$N_{\text{Bi}21x\text{Po}21x} \pm \Delta N_{\text{Bi}21x\text{Po}21x}$	$213 \pm 53$	$427 \pm 80$	$107 \pm 40$	$2430 \pm 126$	$4855 \pm 184$	$1212 \pm 87$
$\frac{\Delta N_{\text{Bi}21x\text{Po}21x}}{N_{\text{Bi}21x\text{Po}21x}}$	24.88 %	18.74 %	37.38 %	5.18 %	3.79 %	7.18 %

**Table 7.3:** Expected Uranium and Thorium chain concentrations in gram of isotope per gram of LAB in the pure scintillator phase. The concentrations of all isotopes contained in Uranium and Thorium chain not listed in this table are the same as the stated  $^{238}\text{U}$  or  $^{232}\text{Th}$  level, respectively. The values for  $^{210}\text{Pb}$ ,  $^{210}\text{Bi}$  and  $^{210}\text{Po}$  are based on Borexino results and do not include the leaching case.

Isotope	Concentration (g/g)
$^{238}\text{U}$	$1.6 \times 10^{-17}$
$^{214}\text{Po}$	$1.6 \times 10^{-17}$
$^{210}\text{Tl}$	$3.4 \times 10^{-21}$
$^{210}\text{Pb}$	$6.1 \times 10^{-25}$
$^{210}\text{Bi}$	$3.8 \times 10^{-28}$
$^{210}\text{Po}$	$4.2 \times 10^{-24}$
$^{232}\text{Th}$	$6.8 \times 10^{-18}$
$^{212}\text{Po}$	$4.4 \times 10^{-18}$
$^{208}\text{Tl}$	$2.4 \times 10^{-18}$

currently expected values. The rates in Table C.1 are based on the target concentration levels presented in Table 7.3.  $^{214}\text{Bi}$  decays 99.979 % of the time into  $^{214}\text{Po}$  [92], leading to the assumed abundance of  $^{214}\text{Po}$  decays  $N_{\text{Po}214}$  introduced in Table 7.2.

A coincidence event can only be tagged if a  $^{214}\text{Po}$  and a  $^{214}\text{Bi}$  decay are selected by the cuts. Thus, the number of coincidence events  $N_{\text{Bi}214\text{Po}214}$  depends on the number

of  $^{214}\text{Po}$  decays. The measurement uncertainty on  $N_{\text{Bi}^{214}\text{Po}^{214}}$  was calculated (see the last row in Table 7.2) using the uncertainty  $\Delta N_{\text{Bi}^{214}\text{Po}^{214}}$  which depended on  $\Delta\epsilon = 2.25 \times 10^{-3}$  and the statistic uncertainty on  $N_{\text{Bi}^{214}\text{Po}^{214}}^{\text{allcuts}}$ . For further information on the uncertainty evaluation see Appendix C.2. Due to the high statistics predicted from the Uranium chain decays, even at half the expected rates a very low uncertainty measurement on the  $^{214}\text{Bi}^{214}\text{Po}$  coincidences could be made within a pure scintillator phase of 181 days (A development of the measurement accuracy following from the statistical uncertainty on the selected  $^{214}\text{Bi}^{214}\text{Po}$  coincidences can be found in C.4).

### Measurement of $^{212}\text{Bi}^{212}\text{Po}$ coincidences

The values presented in Table 7.2 for the  $^{212}\text{Bi}^{212}\text{Po}$  coincidence were determined equivalently. The predicted rates for the Thorium chain decays are much lower than for Uranium chain decays. Additionally, only 64 % of all  $^{212}\text{Bi}$  isotopes decay into  $^{212}\text{Po}$ , reducing the number of events even further. Over half of the measurement efficiency was lost due to the short half-life of  $^{212}\text{Po}$  and the resulting low efficiency on the inter-event timing cut. The predicted number of events  $N_{\text{Bi}^{212}\text{Po}^{212}}^{\text{allcuts}}$  left after all cuts was very small. With an uncertainty on the cut efficiency of  $\Delta\epsilon = 0.98 \times 10^{-3}$ , this lead to a comparably low measurement accuracy even at increased rates on the  $^{212}\text{Bi}^{212}\text{Po}$  coincidence measurements (as for the  $^{214}\text{Bi}^{214}\text{Po}$  coincidences, the measurement accuracy following from the statistical uncertainty on the selected  $^{212}\text{Bi}^{212}\text{Po}$  coincidences can be found in C.4).

#### 7.1.2 Misidentification of other Backgrounds

The developed cuts have the potential to select events which are not real Bi-Po coincidences. Ideally, a fake data set containing decays of all isotopes present in the scintillator is needed to study the behaviour of all backgrounds under the cut conditions. However, for the pure scintillator run phase, only separate MC samples were available for each isotope. Hence, the expected mistagged Bi-Po events were calculated using the expected rates for each background isotope as described in this section. Since two events were considered, a Polonium and a Bismuth candidate, the number of mistagged events results from a combination of the amount of false Polonium candidates selected and the probability of a false Bismuth candidate occurring within

the considered event timing. External backgrounds were not considered, since it was found they are negligible for a Bi-Po selection within the chosen fiducial volume cut [132].

### Polonium selection cuts

The Polonium selection cuts for  $^{212}\text{Po}$  and  $^{214}\text{Po}$  as shown in Figure 7.1 were applied to the RAT 4.5.0 MC production samples listed in Table C.2 to extract the cut efficiency on each isotope using Equation 7.2. The resulting decays expected within 181 days for each non-leaching background are listed in Table 7.4 for both cut selections. More energy spectra from other isotopes overlap with the quenched energy emitted by the  $^{214}\text{Po}$   $\alpha$  particle than for the  $^{212}\text{Po}$  decay, leading to more isotopes contributing to the misidentification rate for this cut.

Additionally to the isotopes listed in Table 7.4,  $^{210}\text{Pb}$ ,  $^{210}\text{Bi}$  and  $^{210}\text{Po}$  isotopes can enter the scintillator volume by leaching off the inner AV surface as described in Section 3.5. Their decay rate expected within the scintillator depends on the leaching rate and on how many isotopes are being distributed within the fiducial volume. Table 7.5 presents the decays selected by the  $^{212}\text{Po}$  and  $^{214}\text{Po}$  cuts for two different leaching scenarios. On the right, the remaining events are listed in the case no leaching events occur within the fiducial volume and only the internal background contributions of  $^{210}\text{Pb}$ ,  $^{210}\text{Bi}$  and  $^{210}\text{Po}$  are considered. The left side of Table 7.5 shows the maximum leaching case assuming isotropic distribution of the leaching backgrounds within the scintillator volume (see Chapter 8 for more information on the leaching background calculation).

Since the decay rate of  $^{214}\text{Po}$  is relatively high, it dominated the  $^{214}\text{Po}$  cut selection over all other backgrounds in the no leaching case. If the leaching content is distributed isotropically in the scintillator mix, the  $^{210}\text{Bi}$  decays provided the largest contribution of misidentified events. Regardless of the leaching scenario, the  $^{212}\text{Po}$  selection was dominated by backgrounds for this measurement. As a result of its low decay rate very few events were selected within the fiducial volume although very few backgrounds passed the cuts due to the relatively high energy emitted by  $^{212}\text{Po}$  decays. However, except for  $^{210}\text{Po}$  and  $^{214}\text{Po}$ , all events passing the cuts were  $\beta$ -emitters or electrons produced by solar signals. Thus, applying a classifier which can distinguish between

**Table 7.4:** Events selected in 181 days by the  $^{212}\text{Po}$  and  $^{214}\text{Po}$  cuts including all non-leaching backgrounds and the solar signals available from the RAT 4.5.0 production. All numbers were evaluated by determining the cut efficiencies as shown in Table C.5 from applying the Polonium selection cuts on the RAT 4.5.0 production ntuples listed in Table C.2. Re-triggered events were rejected.

Isotope	$^{212}\text{Po}$	$^{214}\text{Po}$
$^{39}\text{Ar}$	0	20
$^{14}\text{C}$	0	0
$^{40}\text{K}$	169	340
$^{232}\text{Th}$	0	0
$^{228}\text{Ra}$	0	0
$^{228}\text{Ac}$	17	10
$^{228}\text{Th}$	0	2
$^{224}\text{Ra}$	0	5
$^{220}\text{Rn}$	0	47
$^{216}\text{Po}$	0	82
$^{212}\text{Pb}$	0	0
$^{212}\text{Bi}$	9	30
$^{212}\text{Po}$	49	15
$^{208}\text{Tl}$	0	0
$^{238}\text{U}$	0	0
$^{234}\text{Th}$	0	0
$^{234m}\text{Pa}$	104	161
$^{234}\text{U}$	0	0
$^{230}\text{Th}$	0	0
$^{226}\text{Ra}$	0	6
$^{222}\text{Rn}$	0	1
$^{218}\text{Po}$	0	109
$^{214}\text{Pb}$	15	198
$^{214}\text{Bi}$	24	27
$^{214}\text{Po}$	5	681
$^{210}\text{Tl}$	0	0
Solar		
$^8\text{B}$	20	29
$^7\text{Be}$	0	379
CNO	12	335
PEP	303	481
Total	727	2958

**Table 7.5:** Events selected in 181 days by the  $^{212}\text{Po}$  and  $^{214}\text{Po}$  cuts for all leaching backgrounds. All numbers were evaluated by determining the cut efficiencies as shown in Table C.5 from applying the Polonium selection cuts on the RAT 4.5.0 production ntuples listed in Table C.2. Re-triggered events were rejected. In the non-leaching case the rates from the expected internal Uranium chain contents as shown in Table C.1. In the leaching case the rates were added on a daily basis over 181 days assuming a 9 months phase of water-fill and 3 months of partial fill as described in Chapter 8.

Isotope	Events with leaching		Events without leaching	
	$^{212}\text{Po}$	$^{214}\text{Po}$	$^{212}\text{Po}$	$^{214}\text{Po}$
$^{210}\text{Bi}$	1 856 877	15 125 338	104	847
$^{210}\text{Pb}$	0	0	0	0
$^{210}\text{Po}$	344	7 918	7	169
Total	1 857 221	15 133 256	111	1016

events originating from  $\alpha$ -decays and events originating from  $\beta$ -decays might reduce the misidentification of the Polonium events. Such a classifier was not available for RAT 4.5.0 production files but is available in later versions of RAT. Applying this cut might also improve the signal to background ratio in the worst case leaching scenario for the  $^{214}\text{Po}$  selection by rejecting the dominant  $^{210}\text{Bi}$  contributions.

### Bismuth selection cuts

To determine the events passing the Bismuth cut selection, the cut efficiencies on each isotope had to be applied to the number of events  $x$  falling within the time window  $\Delta t$  based on the rate  $R$  (as presented in Table C.1) for each isotope :

$$x = R \cdot \Delta t, \quad (7.11)$$

Assuming an isotropic distribution of the background isotopes, the effects of the fiducial volume and  $\Delta r$  cuts followed from Equations 7.1 and 7.6. Thus, the number of events being misidentified as a Bismuth decay originating from isotope  $i$  is:

$$N_{\text{mis}}^i = N_{\text{all}}^i \cdot \left( \frac{r_{\text{fidvol}}}{r_{AV}} \right)^3 \cdot x^i \cdot \left( \frac{\Delta r}{r_{\text{fidvol}}} \right)^3 \cdot \epsilon^i (n_{\text{hits}}) = N_{\text{all}}^i \cdot \left( \frac{\Delta r}{r_{AV}} \right)^3 \cdot x^i \cdot \epsilon^i (n_{\text{hits}}), \quad (7.12)$$

Tables 7.6 and 7.7 show all non-leaching events predicted to pass these cuts in a run

**Table 7.6:** Events selected in 181 days by the  $^{212}\text{Bi}$  and  $^{214}\text{Bi}$  cuts including all non-leaching backgrounds and the solar signals available from the RAT 4.5.0 production. All numbers were determined using Equation 7.12. The  $n_{\text{hits}}$  cut efficiencies were determined by applying the respective cuts within a fiducial volume to the RAT 4.5.0 production files listed in Table C.2. Re-triggered events have been rejected. The cut efficiencies for each isotope are listed in Table C.6.

Isotope	$^{212}\text{Bi}$		$^{214}\text{Bi}$	
	before $n_{\text{hits}}^{\text{Bi}}$	after $n_{\text{hits}}^{\text{Bi}}$	before $n_{\text{hits}}^{\text{Bi}}$	after $n_{\text{hits}}^{\text{Bi}}$
$^{39}\text{Ar}$	0	0	0	0
$^{14}\text{C}$	33 683	2	17 472 527	0
$^{40}\text{K}$	0	0	0	0
Th chain	0	0	0	0
U chain	0	0	0	0
Solar	0	0	0	0
Total	33 683	2	17 472 527	0

period of 181 days. The events listed in Table 7.7 represent the two leaching scenarios as described above. For each isotope, the event yields with and without applying a separate  $n_{\text{hits}}$  cut on the Bismuth candidate are presented. In both cut selections, the additional  $n_{\text{hits}}$  cut reduced the amount of misidentified events significantly. Due to the low time window and the event position restriction, only the high rate backgrounds  $^{210}\text{Pb}$ ,  $^{210}\text{Bi}$  and  $^{210}\text{Po}$  contributed to the misidentification rate.

### Mistagging probabilities and expected backgrounds

Tables 7.4 - 7.7 show the events passing the Polonium and Bismuth cuts separately. To get an estimate of how many events are falsely tagged (mistagged) as a Bi-Po coincidence, the two separate selections had to be combined. There are three different scenarios which can lead to mistagging: pairing a true Polonium with a misidentified Bismuth candidate, pairing a misidentified Polonium candidate with a true Bismuth or misidentifying both the Polonium and Bismuth candidate.

Once a Polonium candidate was found the probability to find a Bismuth event within a given time window  $\Delta t$  was applied. This probability was calculated using

**Table 7.7:** Events selected in 181 days by the  $^{212}\text{Bi}$  and  $^{214}\text{Bi}$  cuts for all leaching backgrounds. All numbers were determined using Equation 7.12. The  $n_{\text{hits}}$  cut efficiencies were determined by applying the respective cuts within a fiducial volume to the RAT 4.5.0 production files listed in Table C.2. Re-triggered events have been rejected. The resulting efficiencies are listed in Table C.6. In the leaching case, the rates were scaled and summed over 181 days assuming a 9 month water-fill period and a 3 month partial-fill as described in Chapter 8.

Isotope	Events with leaching				Events without leaching			
	$^{212}\text{Bi}$		$^{214}\text{Bi}$		$^{212}\text{Bi}$		$^{214}\text{Bi}$	
	before $n_{\text{hits}}^{\text{Bi}}$	after $n_{\text{hits}}^{\text{Bi}}$						
$^{210}\text{Bi}$	1 175	803	609 729	70	0	0	0	0
$^{210}\text{Pb}$	1 174	0	608 976	0	0	0	0	0
$^{210}\text{Po}$	1 281	1 277	664 243	0	1	1	303	0
Total	3 630	2 080	1 882 948	70	1	1	303	0

the probability that no events occur during  $\Delta t$ , given by the Poissonian distribution

$$P(0) = e^{-\lambda} \quad (7.13)$$

with

$$\lambda = R_{\text{bckg}} \cdot \Delta t \cdot \left( \frac{\Delta r}{r_{AV}} \right)^3, \quad (7.14)$$

where  $R_{\text{bckg}}$  is the sum of the background rates for each isotope  $i$  multiplied by the respective  $n_{\text{hits}}$  cut efficiency on the Bismuth candidate:

$$R_{\text{bckg}} = \sum_i^{\text{all isotopes}} R^i \cdot \epsilon^i(n_{\text{hits}}) \quad (7.15)$$

The probability of finding a non-Bismuth event within the given cuts is

$$P_{\text{mis}}^{\text{Bi}} = 1 - P(0). \quad (7.16)$$

If a false Polonium  $N_{\text{mis}}^{\text{Po}}$  was tagged, the probability of subsequently selecting a true Bismuth event  $P_{\text{true}}^{\text{Bi}}$  also followed from Equation 7.16 by replacing  $R_{\text{bckg}}$  with the respective rate  $R^{\text{Bi}}$  and cut efficiency  $\epsilon^{\text{Bi}}(n_{\text{hits}})$ .

Tables 7.8 and 7.9 show the mistagging probabilities  $P_{\text{true}}^{\text{Bi}}$  and  $P_{\text{mis}}^{\text{Bi}}$  for different

**Table 7.8:** Mistagging probabilities of the Bismuth candidate and number of true ( $N_{\text{true}}^{\text{Po}}$ ) and misidentified ( $N_{\text{mis}}^{\text{Po}}$ ) Polonium candidates expected in 181 days for the  $^{212}\text{Bi}^{212}\text{Po}$  coincidence measurement.  $N_{\text{mis}}^{\text{Po}}$  is the sum of all non- $^{212}\text{Po}$  events for this selection from Tables 7.4 and 7.5.  $P_{\text{true}}^{\text{Bi}}$  represent the probability to tag a true  $^{212}\text{Bi}$  event within  $\Delta t = 3\,690\,\text{ns}$  after selecting a false  $^{212}\text{Po}$  event, whilst  $P_{\text{mis}}^{\text{Bi}}$  is the probability to tag a non- $^{212}\text{Bi}$  event within the given time window. Both  $P_{\text{true}}^{\text{Bi}}$  and  $P_{\text{mis}}^{\text{Bi}}$  followed from Equation 7.16.

	with leaching		without leaching	
	before $n_{\text{hits}}^{\text{Bi}}$	after $n_{\text{hits}}^{\text{Bi}}$	before $n_{\text{hits}}^{\text{Bi}}$	after $n_{\text{hits}}^{\text{Bi}}$
$N_{\text{true}}^{\text{Po}}$			49	
$N_{\text{mis}}^{\text{Po}}$	1\,857\,899		789	
$P_{\text{true}}^{\text{Bi}}$	$2.78 \times 10^{-12}$	$2.66 \times 10^{-12}$	$2.78 \times 10^{-12}$	$2.66 \times 10^{-12}$
$P_{\text{mis}}^{\text{Bi}}$	$2.61 \times 10^{-5}$	$5.36 \times 10^{-6}$	$1.67 \times 10^{-5}$	$7.07 \times 10^{-8}$

leaching scenarios before and after the  $n_{\text{hits}}$  cuts on the Bismuth candidates have been applied. Since  $P_{\text{true}}^{\text{Bi}}$  only represented the probability of finding a random Bismuth event within a time  $\Delta t$ , its value did not depend on the leaching scenario. The values for the Polonium candidate selection  $N_{\text{true}}^{\text{Po}}$  (number of  $^{212}\text{Po}$  or  $^{214}\text{Po}$  selected) and  $N_{\text{mis}}^{\text{Po}}$  (number of misidentified Polonium candidates) were taken from Tables 7.4 and 7.5. As for the Bismuth mistagging probability,  $N_{\text{true}}^{\text{Po}}$  did not depend on the leaching scenario and none of the Polonium tags depended on the  $n_{\text{hits}}$  cut on the Bismuth candidate.

The number of mistagged coincidences  $N_{\text{mis}}^{\text{coinc}}$  were determined using the values in Tables 7.8 and 7.9:

$$N_{\text{mis}}^{\text{coinc}} = N_{\text{true}}^{\text{Po}} \cdot P_{\text{mis}}^{\text{Bi}} + N_{\text{mis}}^{\text{Po}} \cdot P_{\text{true}}^{\text{Bi}} + N_{\text{mis}}^{\text{Po}} \cdot P_{\text{mis}}^{\text{Bi}}. \quad (7.17)$$

The mistagged coincidences are presented in Table 7.10 for the  $^{212}\text{Bi}^{212}\text{Po}$  selection and in Table 7.11 for the  $^{214}\text{Bi}^{214}\text{Po}$  selection. All previously discussed leaching scenarios and the different Bismuth  $n_{\text{hits}}$  cut options are shown. For the full uncertainty calculation see Appendix C.3. In all scenarios, the largest mistagging contribution originated from the case in which a false Polonium and a false Bismuth were selected. Very rarely was a true Polonium matched with a misidentified Bismuth candidate. Tagging a true Bismuth candidate with a false Polonium candidate occurred in even less cases for most scenarios.

**Table 7.9:** Mistagging probabilities of the Bismuth candidate and number of true ( $N_{\text{true}}^{\text{Po}}$ ) and misidentified ( $N_{\text{mis}}^{\text{Po}}$ ) Polonium candidates expected in 181 days for the  $^{214}\text{Bi}^{214}\text{Po}$  coincidence measurement.  $N_{\text{mis}}^{\text{Po}}$  is the sum of all non- $^{214}\text{Po}$  events for this selection from Tables 7.4 and 7.5.  $P_{\text{true}}^{\text{Bi}}$  represent the probability to tag a true  $^{214}\text{Bi}$  event within  $\Delta t = 1\,798\,788\,\text{ns}$  after selecting a false  $^{214}\text{Po}$  event, whilst  $P_{\text{mis}}^{\text{Bi}}$  is the probability to tag a non- $^{214}\text{Bi}$  event within the given time window. Both  $P_{\text{true}}^{\text{Bi}}$  and  $P_{\text{mis}}^{\text{Bi}}$  followed from Equation 7.16.

	with leaching		without leaching	
	before $n_{\text{hits}}^{\text{Bi}}$	after $n_{\text{hits}}^{\text{Bi}}$	before $n_{\text{hits}}^{\text{Bi}}$	after $n_{\text{hits}}^{\text{Bi}}$
$N_{\text{true}}^{\text{Po}}$			681	
$N_{\text{mis}}^{\text{Po}}$	15 135 526		3 286	
$P_{\text{true}}^{\text{Bi}}$	$1.04 \times 10^{-8}$	$9 \times 10^{-9}$	$1.04 \times 10^{-8}$	$9 \times 10^{-9}$
$P_{\text{mis}}^{\text{Bi}}$	$1.34 \times 10^{-2}$	$1.96 \times 10^{-7}$	$8.62 \times 10^{-3}$	$1.13 \times 10^{-8}$

**Table 7.10:** Estimated event contributions from mistagging for the  $^{212}\text{Bi}^{212}\text{Po}$  selection in 181 days. All three possible combinations are presented, as well as their sum. The leaching and non-leaching case is considered before and after the  $n_{\text{hits}}$  cut on the Bismuth candidate is applied.

	before $n_{\text{hits}}^{\text{Bi}}$		after $n_{\text{hits}}^{\text{Bi}}$	
	With leaching	Without leaching	With leaching	Without leaching
$N_{\text{Bi}^{212}\text{Po}212}^{\text{all cuts}}$	$18 \pm 4$		$16 \pm 4$	
$N_{\text{true}}^{\text{Po}} \cdot P_{\text{mis}}^{\text{Bi}}$	$(1.3 \pm 0.2) \times 10^{-3}$	$(0.8 \pm 0.1) \times 10^{-3}$	$(2.6 \pm 0.3) \times 10^{-4}$	$(3.5 \pm 0.4) \times 10^{-6}$
$N_{\text{mis}}^{\text{Po}} \cdot P_{\text{true}}^{\text{Bi}}$	$(5.2 \pm 0.2) \times 10^{-6}$	$(2.20 \pm 0.04) \times 10^{-9}$	$(4.9 \pm 0.4) \times 10^{-6}$	$(2.10 \pm 0.04) \times 10^{-9}$
$N_{\text{mis}}^{\text{Po}} \cdot P_{\text{mis}}^{\text{Bi}}$	$48 \pm 2$	$(1.32 \pm 0.02) \times 10^{-2}$	$10.0 \pm 0.4$	$(5.59 \pm 0.09) \times 10^{-5}$
$N_{\text{mis}}^{\text{coinc}}$	$48 \pm 2$	$0.0140 \pm 0.0002$	$10.0 \pm 0.4$	$(5.9 \pm 0.1) \times 10^{-5}$

Applying the  $n_{\text{hits}}$  cut on the Bismuth candidate for the  $^{214}\text{Bi}^{214}\text{Po}$  measurement reduced the mistagged coincidences by 99.9985 %, providing an almost pure  $^{214}\text{Bi}^{214}\text{Po}$  event selection with an expected background contamination in the full leaching case of only 0.7 %. The timing between the  $^{212}\text{Bi}$  decay and the  $^{212}\text{Po}$  decay is shorter than for the  $^{214}\text{Bi}^{214}\text{Po}$  coincidence, which led to lower mistagged backgrounds in the full leaching case than for the Uranium chain measurement before the  $n_{\text{hits}}^{\text{Bi}}$  cut was

**Table 7.11:** Estimated event contributions from mistagging for the  $^{214}\text{Bi}^{214}\text{Po}$  selection in 181 days. All three possible combinations are presented, as well as their sum. The leaching and non-leaching case is considered before and after the  $n_{\text{hits}}$  cut on the Bismuth candidate is applied.

	before $n_{\text{hits}}^{\text{Bi}}$		after $n_{\text{hits}}^{\text{Bi}}$	
	With leaching	Without leaching	With leaching	Without leaching
$N_{\text{Bi}^{214}\text{Po}^{214}}^{\text{allcuts}}$	$461 \pm 22$		$401 \pm 20$	
$N_{\text{true}}^{\text{Po}} \cdot P_{\text{mis}}^{\text{Bi}}$	$9.2 \pm 0.7$	$5.9 \pm 0.4$	$1.3 \pm 0.6 \times 10^{-4}$	$(7.7 \pm 0.6) \times 10^{-6}$
$N_{\text{mis}}^{\text{Po}} \cdot P_{\text{true}}^{\text{Bi}}$	$0.157 \pm 0.008$	$(3.4 \pm 0.1) \times 10^{-5}$	$0.136 \pm 0.007$	$(3.0 \pm 0.1) \times 10^{-5}$
$N_{\text{mis}}^{\text{Po}} \cdot P_{\text{mis}}^{\text{Bi}}$	$203\,387 \pm 10\,646$	$28 \pm 1$	$3 \pm 2$	$(3.7 \pm 0.1) \times 10^{-5}$
$N_{\text{mis}}^{\text{coinc}}$	$203\,396 \pm 10\,646$	$34 \pm 1$	$3 \pm 1$	$(7.4 \pm 0.2) \times 10^{-5}$

applied<sup>23</sup>. However, the  $n_{\text{hits}}^{\text{Bi}}$  cut was developed to only reject  $^{14}\text{C}$  and  $^{210}\text{Pb}$ , leaving high  $^{210}\text{Po}$  and  $^{210}\text{Bi}$  rates. At the expected rates, a sample purity of only 63 % could be achieved. Therefore it is important for this measurement to understand the nature of the leaching backgrounds at a high level.

### 7.1.3 Influence of Mistagged events on the Measurement Accuracy

When applying this cut selection to a data run, the selected events are a sum of the measured Bi-Po coincidence and the mistagged coincidences:

$$N_{\text{allcuts}}^{\text{data}} = N_{\text{Bi}^{21x}\text{Po}^{21x}}^{\text{allcuts}} + N_{\text{mis}}^{\text{coinc}} \quad (7.18)$$

The statistical uncertainty of the value follows from  $\Delta N_{\text{allcuts}}^{\text{data}} = \sqrt{N_{\text{allcuts}}^{\text{data}}}$ . Figure 7.8 shows the development of the uncertainty on the Bi-Po coincidence measurements over a period of 181 days. For both, the  $^{212}\text{Bi}^{212}\text{Po}$  and  $^{214}\text{Bi}^{214}\text{Po}$  coincidences, a range of scenarios is presented considering different rates for the Bi-Po coincidences and the leaching backgrounds which dominated the mistagged events. Increasing the rate of the Bi-Po coincidences (labelled as signal in Figure 7.8) improved the measurement

<sup>23</sup>Assuming the no leaching case, no mistagged events were expected once the  $n_{\text{hits}}$  cuts on the Bismuth candidates were applied. In order to confirm that the number of mistags is purely dependent on the leaching rate, the expected  $N_{\text{mis}}^{\text{coinc}}$  at increased rates for all backgrounds is listed in Table C.7. Increasing the rates of any of the backgrounds other than the leaching isotopes had no effect on the mistagged events.

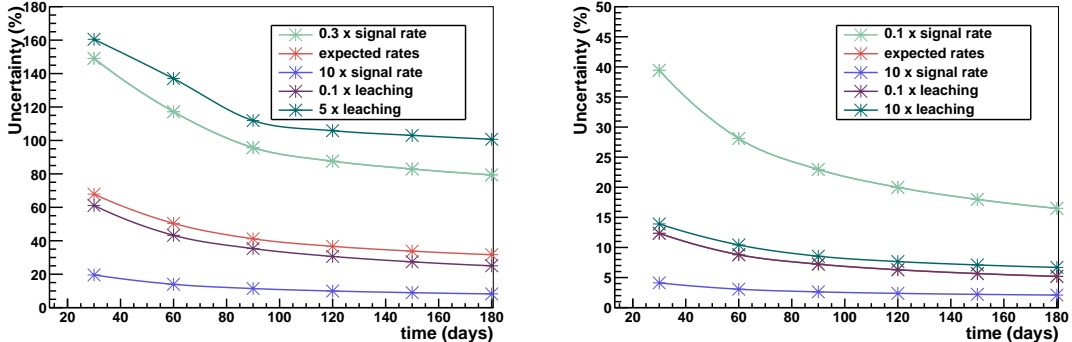


**Figure 7.8:** Development of the Uncertainties on the  $^{212}\text{Bi}^{212}\text{Po}$  (left) and  $^{214}\text{Bi}^{214}\text{Po}$  (right) measurements for different leaching and Bi-Po coincidence rates over 181 days. Each marker emphasises a 30 day period.

uncertainty for both cases significantly. Due to the low selection efficiency of the  $^{212}\text{Bi}^{212}\text{Po}$  coincidence and the initial low expected rate (as shown in Table C.1), a decrease in rate had a large effect on the measurement. The leaching rate had very little impact on the  $^{214}\text{Bi}^{214}\text{Po}$  measurement resulting from the good background rejection, especially of the leaching backgrounds on the Bismuth candidate selection. Thus, for the Uranium chain, the measurement uncertainty predominantly depended on the rate of the  $^{214}\text{Bi}^{214}\text{Po}$  decays in the scintillator volume.

## 7.2 Alternative Measurement of the Thorium chain

In comparison to the Uranium chain measurement, very low accuracy could be achieved on the Thorium chain measurement. This was a result of both the low expected occurrence of  $^{212}\text{Bi}^{212}\text{Po}$  decays, as well as the small efficiency on the inter-event timing cut as shown in Table 7.1. However, there are two other fast decay steps in the Thorium chain with the potential to provide a measurement on the Thorium chain contents. Both decays are investigated in this Section.

### 7.2.1 The $^{212}\text{Bi}^{208}\text{Tl}$ coincidence

The first investigated coincidence is the other  $^{212}\text{Bi}$  decay to  $^{208}\text{Tl}$  with a half-life of  $T_{\frac{1}{2}} = 3.05\text{ min}$  and a branching ratio of 36 %. In comparison to the  $^{212}\text{Bi}^{212}\text{Po}$

coincidence, the expected total number of coincidences is smaller due to the smaller branching ratio. However, the efficiency loss due to in-window coincidences is negligible for the  $^{212}\text{Bi}^{208}\text{Tl}$  selection, since the half-life of  $^{208}\text{Tl}$  is significantly longer.

Unlike for the  $^{212}\text{Bi}^{212}\text{Po}$  coincidences, no production files containing the  $^{212}\text{Bi}^{208}\text{Tl}$  coincidences were available at the time this document is written. Thus, the effects of a  $\Delta r$  cut on the distances between the two isotopes and the efficiencies of a fiducial volume cut on  $^{212}\text{Bi}$  could not be studied thoroughly. Since the efficiencies of these cuts mainly depended on the reconstruction accuracy, generic efficiency values for both cuts were assumed based on the values listed in Table 7.1. The efficiencies were set to  $\epsilon(r_{\text{fidvol}}^{\text{Bi}212}) = 0.90$  and  $\epsilon(\Delta r^{\text{Bi}212}) = 0.80$ . The remaining cut selection comprised of a combination of  $n_{\text{hits}}$  and  $\Delta t$  selection criteria, combined with a fiducial volume cut on  $^{208}\text{Tl}$ .

Contrary to the  $^{212}\text{Po}$  decays, the  $Q$ -value of the  $^{208}\text{Tl}$   $\beta$ -decay is so high, that rejecting the high rate backgrounds  $^{14}\text{C}$ ,  $^{210}\text{Pb}$ ,  $^{210}\text{Bi}$  and  $^{210}\text{Po}$  by applying an  $n_{\text{hits}}$  cut on the  $^{208}\text{Tl}$  decay was no problem. The only backgrounds, which cannot be rejected 100 % without sacrificing the efficiency on the coincidence selection are the solar signal  $^8\text{B}$ ,  $^{214}\text{Bi}$  and  $^{210}\text{Tl}$ . Decays of  $^{214}\text{Bi}$  to  $^{210}\text{Tl}$  are extremely rare, so that only one  $^{210}\text{Tl}$  event was expected over a running period of a year. Therefore, the  $n_{\text{hits}}$  cut on  $^{208}\text{Tl}$  was tuned to reject as many  $^{214}\text{Bi}$  and  $^8\text{B}$  events as possible. A different  $n_{\text{hits}}$  cut was also required on the Bismuth candidate, since the underlying  $^{212}\text{Bi}$  decay is an  $\alpha$ -decay with  $E = 6.21 \text{ MeV}$ . The resulting  $n_{\text{hits}}$  spectrum yielded a much narrower peak, which required the application of a lower and an upper limit on the  $n_{\text{hits}}$  values of an event.

The final cut values for this coincidence selection are presented in Table 7.12. To determine the limits of the inter-event time window  $\Delta t$ , Equation 7.4 was used with a selection efficiency of  $\epsilon(\Delta t) = 0.9995$ . The number of mistagged coincidences can be calculated utilising Equation 7.17. Each component of this equation are listed in Equation 7.19 and Table 7.13. Since the high rate backgrounds were rejected by the  $n_{\text{hits}}^{\text{Ti}208}$  cut and  $P_{\text{mis}}^{\text{Bi}} = 1$  for both the leaching and the non-leaching case due to the large time window, no distinction was made between the full leaching and the non-leaching case.

**Table 7.12:** Cuts and cut efficiencies for each cut parameter for the  $^{212}\text{Bi}^{208}\text{Tl}$  coincidence selection. The cut efficiencies were determined as described in Equations 7.2 and 7.4. The total efficiency  $\epsilon$  on each selection followed from multiplying all determined efficiencies, equivalent to Equation 7.9.

	Cut value		efficiency
	lower	upper	
$r_{\text{fidvol}}$	-	4 000 mm	$\left(\frac{r_{\text{fidvol}}}{r_{AV}}\right)^3$
$n_{\text{hits}}^{\text{Tl}208}$	1 600	-	0.794
$\Delta t$	400 ns	2 010 s	0.9995
$r_{\text{fidvol}}^{\text{Bi}212}$	-	4 000 mm	0.90
$\Delta r^{\text{Bi}212}$	0 mm	2 000 mm	0.80
$n_{\text{hits}}^{\text{Bi}212}$	220	370	0.956
Total efficiency $\epsilon$	16.2 %		

$$\begin{aligned}
 N_{\text{true}}^{\text{Tl}} &= 29 \\
 N_{\text{mis}}^{\text{Tl}} &= 179 \\
 P_{\text{true}}^{\text{Bi}} &= 0.0015 \\
 P_{\text{mis}}^{\text{Bi}} &= 1.00
 \end{aligned} \tag{7.19}$$

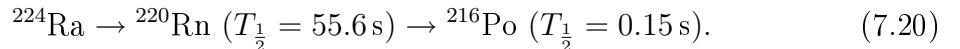
At the expected rates, the only non-Thallium events selected by the cuts applied to the  $^{208}\text{Tl}$  candidate were  $^8\text{B}$  events from the sun. Since both the  $^{208}\text{Tl}$  and the  $^8\text{B}$  are detected via electrons, no further cut could be applied to reject the  $^8\text{B}$  without a considerable loss of selected  $^{208}\text{Tl}$ . The high mistagging probability of the Bismuth candidate selection is due to the large inter-event time window. Thus, not only will all misidentified  $^{208}\text{Tl}$  events lead to a mistag, following from the  $N_{\text{true}}^{\text{Tl}} \cdot P_{\text{mis}}^{\text{Bi}}$  term presented in Table 7.13, it appears likely that all selected  $^{208}\text{Tl}$  will be paired with a false Bismuth candidate. A discussion of reducing the selection time window for the  $^{224}\text{Ra}^{220}\text{Rn}^{216}\text{Po}$ , decays with shorter half-lives than  $^{208}\text{Tl}$ , is given in the next Section. With the measurement yielding a higher amount of mistagged coincidences than the selection on  $^{212}\text{Bi}^{212}\text{Po}$  coincidences, the measurement uncertainty on the Thorium chain could not be improved using the  $^{212}\text{Bi}^{208}\text{Tl}$  coincidences.

**Table 7.13:** Estimated event contributions from mistagging for the  $^{212}\text{Bi}^{208}\text{Tl}$  selection in 181 days. All possible combinations are presented, as well as their sum.

$N_{\text{Bi}^{212}\text{Tl}208}^{\text{allcuts}}$	$19 \pm 4$
$N_{\text{mis}}^{\text{Tl}} \cdot P_{\text{mis}}^{\text{Bi}}$	179
$N_{\text{mis}}^{\text{Tl}} \cdot P_{\text{true}}^{\text{Bi}}$	0
$N_{\text{true}}^{\text{Tl}} \cdot P_{\text{mis}}^{\text{Bi}}$	29
$N_{\text{mis}}^{\text{coinc}}$	208
Measurement uncertainty	79.3 %

## 7.2.2 The triple $\alpha$ -coincidence $^{224}\text{Ra}^{220}\text{Rn}^{216}\text{Po}$

Another short-lived coincidence decay occurring within the Thorium decay chain is the triple  $\alpha$ -decay



The half-lives of these decays are such that a cut efficiency loss due to in-window coincidences is negligible, yet they are shorter than the half-life of  $^{208}\text{Tl}$ . Furthermore, the branching ratios of all these decays are 100 % each, thus no statistics are lost throughout the decay. This may lead to an improvement of the uncertainties on the measurement. Hence, using these decays for a potential alternative measurement of the Thorium chain is investigated in this Section.

As above, no production files with the  $^{224}\text{Ra}^{220}\text{Rn}^{216}\text{Po}$  coincidences were available at the time of writing. Therefore, similar to the  $^{212}\text{Bi}^{208}\text{Tl}$  coincidence selection the efficiencies of the  $\Delta r$  and  $r_{\text{fidvol}}$  requirements on the coincidence decays were estimated based on the values in Table 7.1. Therefore,  $\epsilon(r_{\text{fidvol}}^{\text{Rn}220}) = \epsilon(r_{\text{fidvol}}^{\text{Po}216}) = 0.90$  and  $\epsilon(\Delta r^{\text{Rn}220}) = \epsilon(\Delta r^{\text{Po}216}) = 0.80$ . The remaining cut selection comprised of a combination of  $n_{\text{hits}}$  and  $\Delta t$  selection criteria, combined with a fiducial volume cut on  $^{224}\text{Ra}$ .

The  $n_{\text{hits}}$  cuts on the isotopes were chosen using the same method as for the Polonium candidate selection described in Section 7.1.1. The main focus was to reject the high-rate  $^{210}\text{Po}$  background. All chosen  $n_{\text{hits}}$  cut values and the resulting efficiencies are presented in Table 7.14. As for the  $^{212}\text{Bi}^{212}\text{Po}$  cut selection, the values of the

**Table 7.14:** Cuts and cut efficiencies for each cut parameter for the  $^{214}\text{Ra}^{220}\text{Rn}^{216}\text{Po}$  triple  $\alpha$ -coincidence selection. The cut efficiencies were determined as described in Equations 7.2 and 7.4. The total efficiency  $\epsilon$  on each selection followed from multiplying all determined efficiencies, equivalent to Equation 7.9.

	Cut value		efficiency
	lower	upper	
$r_{\text{fidvol}}$	-	4 000 mm	$\left(\frac{r_{\text{fidvol}}}{r_{AV}}\right)^3$
$n_{\text{hits}}^{\text{Ra}224}$	210	300	0.8422
$\Delta t^{\text{Rn}220}$	400 ns	609.7 s	0.9995
$r_{\text{fidvol}}^{\text{Rn}220}$	-	4 000 mm	0.90
$\Delta r^{\text{Rn}220}$	0 mm	2 000 mm	0.80
$n_{\text{hits}}^{\text{Rn}220}$	260	340	0.8068
$\Delta t^{\text{Po}216}$	400 ns	1.6 s	0.9995
$r_{\text{fidvol}}^{\text{Po}216}$	-	4 000 mm	0.90
$\Delta r^{\text{Po}216}$	0 mm	2 000 mm	0.80
$n_{\text{hits}}^{\text{Po}216}$	290	400	0.8161
Total efficiency $\epsilon$	8.5 %		

inter-event timing cut  $\Delta t$  were determined using Equation 7.4 with a required cut efficiency  $\epsilon(\Delta t) = 0.9995$ . The derived values are also listed in Table 7.14. With these efficiencies,  $N_{\text{Ra}224\text{Rn}220\text{Po}216}^{\text{allcuts}} = 29$  out of  $N_{\text{Ra}224\text{Rn}220\text{Po}216} = 338$  coincidence events were expected to be selected in 181 days.

To estimate the mistagged coincidences  $N_{\text{mis}}^{\text{coinc}}$ , the equation used to determine the mistags for the  $^{212}\text{Bi}^{212}\text{Po}$  selection (Equation 7.17) had to be expanded to account for the third involved isotope. Thus, the mistags follow from the number of mistagged and true  $^{224}\text{Ra}$  decays  $N_{\text{mis/true}}^{\text{Ra}}$ , the probability  $P_{\text{mis/true}}^{\text{Rn}}$  to find a mistagged or true  $^{220}\text{Rn}$  candidate within the given cut values and the probability  $P_{\text{mis/true}}^{\text{Po}}$  to find a mistagged or true  $^{216}\text{Po}$  candidate within the given cut values:

$$\begin{aligned}
 N_{\text{mis}}^{\text{coinc}} = & N_{\text{mis}}^{\text{Ra}} \cdot P_{\text{mis}}^{\text{Rn}} \cdot P_{\text{mis}}^{\text{Po}} + N_{\text{mis}}^{\text{Ra}} \cdot P_{\text{true}}^{\text{Rn}} \cdot P_{\text{mis}}^{\text{Po}} + N_{\text{mis}}^{\text{Ra}} \cdot P_{\text{true}}^{\text{Rn}} \cdot P_{\text{true}}^{\text{Po}} + N_{\text{mis}}^{\text{Ra}} \cdot P_{\text{mis}}^{\text{Rn}} \cdot P_{\text{true}}^{\text{Po}} \\
 & + N_{\text{true}}^{\text{Ra}} \cdot P_{\text{mis}}^{\text{Rn}} \cdot P_{\text{mis}}^{\text{Po}} + N_{\text{true}}^{\text{Ra}} \cdot P_{\text{true}}^{\text{Rn}} \cdot P_{\text{mis}}^{\text{Po}} + N_{\text{true}}^{\text{Ra}} \cdot P_{\text{mis}}^{\text{Rn}} \cdot P_{\text{true}}^{\text{Po}}
 \end{aligned} \tag{7.21}$$

**Table 7.15:** Mistagging probabilities of the Radon and Polonium candidates and number of true and misidentified Radium candidates expected in 181 days for the  $^{224}\text{Ra}/^{220}\text{Rn}/^{216}\text{Po}$  coincidence measurement.  $P_{\text{true}}^{\text{Rn}, \text{Po}}$  represent the probability to tag a true  $^{220}\text{Rn}$  or  $^{216}\text{Po}$  event within the given  $\Delta t$  cuts after selecting false  $^{224}\text{Ra}/^{220}\text{Rn}$  events. Both  $P_{\text{true}}^{\text{Rn}, \text{Po}}$  and  $P_{\text{mis}}^{\text{Rn}, \text{Po}}$  followed from Equation 7.16.  $N_{\text{true}}^{\text{Ra}}$  are the true number of  $^{224}\text{Ra}$  events selected by the fiducial volume cut and  $n_{\text{hits}}^{\text{Ra}}$  cut from Table 7.14 and  $N_{\text{mis}}^{\text{Ra}}$  are all non- $^{224}\text{Ra}$  events selected by these cuts.

	with leaching	without leaching
$N_{\text{true}}^{\text{Ra}}$	85	
$N_{\text{mis}}^{\text{Ra}}$	108 278 508	1 926 831
$P_{\text{true}}^{\text{Rn}}$	0.00039	
$P_{\text{mis}}^{\text{Rn}}$	1.00	0.238
$P_{\text{true}}^{\text{Po}}$	$1.08 \times 10^{-6}$	
$P_{\text{mis}}^{\text{Po}}$	0.15	$4.08 \times 10^{-5}$

$P_{\text{mis/true}}^{\text{Rn}, \text{Po}}$  were determined as described in Equation 7.16. The values for the cuts described above are presented in Table 7.15. Both, the full leaching case as well as the no leaching case as discussed in Section 7.1.2 were considered. Due to the large timing cut on the  $^{220}\text{Rn}$  candidate, the mistagging probability reached  $P_{\text{mis}}^{\text{Rn}} = 1.00$  in the full leaching case.

The contributions of each term in Equation 7.21, the total number of mistagged coincidences  $N_{\text{mis}}^{\text{coinc}}$  and the number of true triple- $\alpha$  coincidences  $N_{\text{Ra}224\text{Rn}220\text{Po}216}^{\text{allcuts}}$  selected by the cuts are presented in Table 7.16. Using this cut selection, more coincidences were selected than when applying the  $^{212}\text{Bi}/^{212}\text{Po}$  cut selection described in Section 7.1.1. However, in both leaching scenarios more mistagged coincidences were selected than in the Bi-Po measurement, leading to a higher overall measurement uncertainty in both cases than found in Section 7.1.3. This was mainly due to the high mistagging probability on  $^{220}\text{Rn}$ . In order to reduce the mistagged coincidences, different cuts would need to be applied.

The key to lowering the number of mistagged coincidences is to lower the mistagging probability of the cut selection on  $^{220}\text{Rn}$ . Thus, it was investigated which  $\Delta r^{\text{Rn}220}$  and  $\Delta t^{\text{Rn}220}$  values have to be applied to drop the mistagging probability by only 0.0001 to  $P_{\text{mis}}^{\text{Rn}} = 0.9999$  in the full leaching case in order to verify if it was possible to reduce the mistagging probability. Therefore, Equation 7.16 (combined with Equation 7.14)

**Table 7.16:** Estimated event contributions from mistagging for the  $^{224}\text{Ra}^{220}\text{Rn}^{216}\text{Po}$  selection in 181 days. All seven possible combinations are presented, as well as their sum. The leaching and non-leaching case was considered.

	With leaching	Without leaching
$N_{\text{Ra224Rn220Po216}}^{\text{allcuts}}$	$29 \pm 5$	
$N_{\text{mis}}^{\text{Ra}} \cdot P_{\text{mis}}^{\text{Rn}} \cdot P_{\text{mis}}^{\text{Po}}$	16 241 776	19
$N_{\text{mis}}^{\text{Ra}} \cdot P_{\text{true}}^{\text{Rn}} \cdot P_{\text{mis}}^{\text{Po}}$	6 334	0.0
$N_{\text{mis}}^{\text{Ra}} \cdot P_{\text{true}}^{\text{Rn}} \cdot P_{\text{true}}^{\text{Po}}$	0.0	0.0
$N_{\text{mis}}^{\text{Ra}} \cdot P_{\text{mis}}^{\text{Rn}} \cdot P_{\text{true}}^{\text{Po}}$	117	1
$N_{\text{true}}^{\text{Ra}} \cdot P_{\text{mis}}^{\text{Rn}} \cdot P_{\text{mis}}^{\text{Po}}$	13	0.0
$N_{\text{true}}^{\text{Ra}} \cdot P_{\text{true}}^{\text{Rn}} \cdot P_{\text{mis}}^{\text{Po}}$	0.0	0.0
$N_{\text{true}}^{\text{Ra}} \cdot P_{\text{mis}}^{\text{Rn}} \cdot P_{\text{true}}^{\text{Po}}$	0.0	0.0
$N_{\text{mis}}^{\text{coinc}}$	16 248 240	20
Measurement uncertainty	13 899.7 %	35 %

was re-arranged for each variable with setting  $P_{\text{mis}}^{\text{Rn}} = 0.9999$  and the resulting cut values are:

$$\Delta r^{\text{Rn}220} = (4.8 \times 10^{-3}) \text{ mm}$$

$$\Delta t^{\text{Rn}220} = 9.89 \text{ s}$$

The original cut value on  $\Delta r^{\text{Rn}220}$  was chosen due to the accuracy of the event reconstruction and it is not considered feasible for this value to be orders of magnitude lower than  $\Delta r^{\text{Rn}220} = 2000 \text{ mm}$ . Therefore, adjusting the cut on the event distance is not an option. Setting the upper limit of the inter-event timing cut to the value stated above, reduces the selection efficiency of this cut on  $^{220}\text{Rn}$  to  $\epsilon(\Delta t^{\text{Rn}220}) = 0.116$ . This would decrease the selected coincidences over a run period of 181 days to  $N_{\text{Ra224Rn220Po216}}^{\text{allcuts}} = 3$  without providing a noteworthy reduction of mistagged coincidences. Defining tighter selection criteria on the given cuts did not supply an improved measurement on the Thorium chain content.

## 7.3 Testing the Bi-Po selection on the Te-loaded one Month Merged Data Set

All predictions of mistagged coincidences described in Sections 7.1.1 and 7.2 were purely based on theoretical predictions, since only separate data sets for each background decay were available. To truly understand the mistagging of the coincidence measurements, a data set is needed with all backgrounds combined. As part of the study to reject backgrounds for the  $0\nu\beta\beta$ -measurements, a merged data set was produced for a data taking period of one month using a scintillator cocktail with 0.3 % Te loading and a bisMSB wavelength shifter.

The data set was produced to explicitly study the rejection of coincidence decays in the region of interest and therefore contains both  $^{212}\text{Bi}^{212}\text{Po}$  and  $^{214}\text{Bi}^{214}\text{Po}$  decays. Other signals contained in the data set are the high rate backgrounds  $^{14}\text{C}$ ,  $^{210}\text{Bi}$  and  $^{210}\text{Po}$ , as well as the two-neutrino and neutrinoless double beta decay signals. Additionally,  $(\alpha, n)$ -decay coincidences and some external backgrounds were added to the data set. A comprehensive list and more information on how the data set was produced can be found in [135].

### 7.3.1 Adjusting the Cut Selection

The same cut flow as presented in Figure 7.1 was applied to measure the Thorium and Uranium chain contents. However, different light yields are expected for different phases of data taking, depending on the components of the scintillator cocktail and their emission spectrum. The expected light yield in pure scintillator is 520 Nhits/MeV, whilst adding bisMSB as wavelength shifter in a 0.3 %Te loaded cocktail shifts the light yield to 200 Nhits/MeV<sup>24</sup> [70]. Therefore, the  $n_{\text{hits}}$  cuts as defined in Section 7.1.1 had to be adjusted.

The  $n_{\text{hits}}$  cuts on the Polonium candidates were tuned as described in Section 7.1.1, with focus on rejecting  $^{210}\text{Po}$  events as well as events from the other respective Polonium decay. The equivalent efficiency/rejection plots are presented in Figures 7.9 and 7.10. For the  $n_{\text{hits}}$  selection on the Bismuth candidate, the aim was to reject the high

---

<sup>24</sup>This is a conservative calculation. Cocktail R&D has resulted in improvements since and is still undergoing.

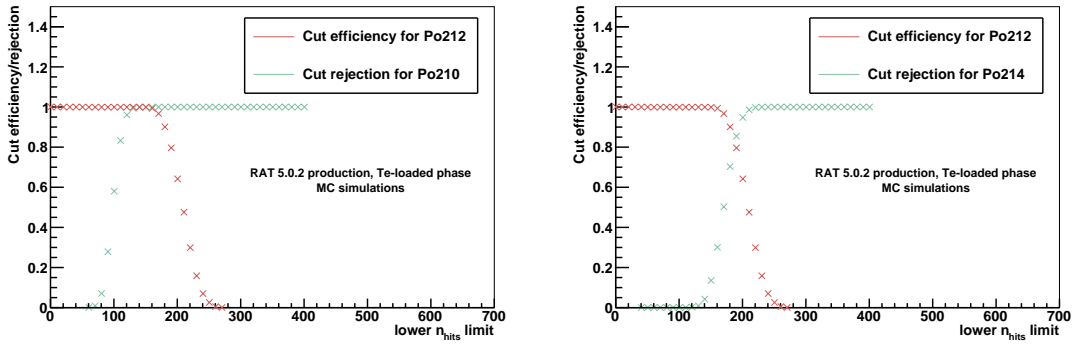


**Figure 7.9:** Development of the cut efficiencies for the  $^{212}\text{Po}$   $n_{\text{hits}}$  cut for Tellurium loaded scintillator, with a fixed upper limit of  $n_{\text{hits}} = 400$  and a variable lower limit ranging from  $n_{\text{hits}} = 0$  to  $n_{\text{hits}} = 400$  in steps of 10. On the left, the  $^{212}\text{Po}$  cut efficiency is compared to the rejection of  $^{210}\text{Po}$  events, the right shows the rejection of  $^{214}\text{Po}$  events at each cut value. The plots were produced using RAT 5.0.2 production files.

rate backgrounds without sacrificing too much signal. Due to the higher expected rates for each background in the Tellurium phase [92], an upper limit was introduced to the  $^{212}\text{Bi}$  selection to additionally reduce the mistagging of  $^{214}\text{Bi}$ .

The efficiencies of the  $\Delta r$  cut and the fiducial cut on the Bismuth candidate were determined using the RAT 5.0.2 production ntuples as shown in Table C.9. Based on the distributions in Figure 7.11, the distance cut could be reduced to  $\Delta r = 1\,500\,\text{mm}$  without a significant efficiency loss. It is worth noting that in Figure 7.11 very little event contributions could be observed above 2000 mm. This is a direct result of applying a cut on the fit validity which could not be applied to the RAT 4.5.0 production files used to produce Figure 7.7. The fit validity is a boolean variable added to later versions of RAT, returning TRUE when the fit of an event was successful and FALSE if the fit algorithm did not provide a reasonable result. The final cut values and the corresponding efficiencies for both coincidence selections are listed in Table 7.17.

### 7.3.2 Applying the Cuts

In order to verify the validity of the assumptions made for the mistagging estimations in Section 7.1.2, the mistagged backgrounds were determined for the equivalent Tellurium loading for all the backgrounds contained in the merged data set. However, the number of triggered events in the merged data set did not correlate to the number

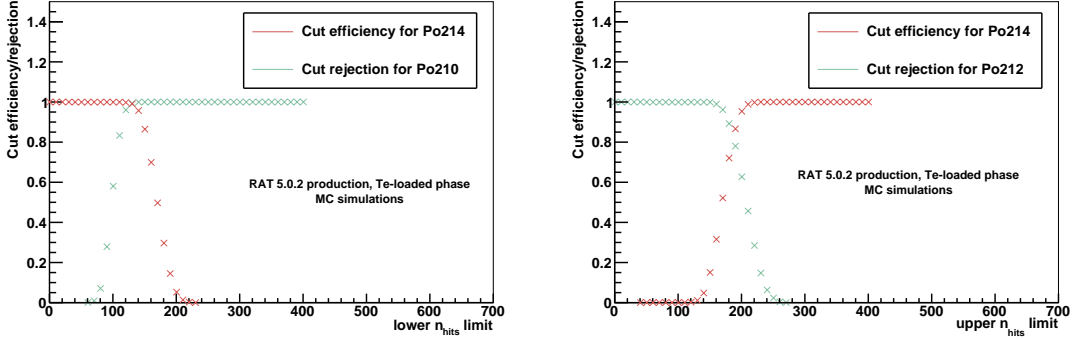


**Figure 7.10:** Development of the cut efficiencies for the  $^{214}\text{Po}$   $n_{\text{hits}}$  cut for Tellurium loaded scintillator. The left plot shows the  $^{214}\text{Po}$  cut efficiency compared to the  $^{210}\text{Po}$  cut rejection. Here, the upper cut value was fixed to  $n_{\text{hits}} = 400$ , whilst the lower limit was increased from  $n_{\text{hits}} = 0$  to  $n_{\text{hits}} = 400$  in steps of 10. The right plot compares the  $^{214}\text{Po}$  cut efficiency to the  $^{212}\text{Po}$  rejection. Due to the higher energy emitted by the  $^{212}\text{Po}$  decay, the lower cut value was set to  $n_{\text{hits}} = 0$ , whilst the upper limit was varied from  $n_{\text{hits}} = 400$  to  $n_{\text{hits}} = 0$  in steps of 10. The plots were produced using RAT 5.0.2 production files.

of expected events for one month for this cocktail mixture [135]. Thus, the resulting rates for each background were different to the rates expected for this detector setup. Additionally, the efficiency of the fiducial volume cut was not proportional to the factor  $\left(\frac{r_{\text{fid vol}}}{r_{AV}}\right)^3$  for any backgrounds originating from external sources. Finally, only events with a valid reconstruction were considered for the analysis on the merged data set. Whether a reconstructed fit is valid depends highly on the position and energy reconstruction. The smaller the energy of the reconstructed particle, the more likely it will be misreconstructed (compare Section 3.6). No study had been done on the reconstruction efficiency per isotope or energy by the time this document was written. Hence, it was decided to perform the mistagging calculation based on the number of events found in the fiducial volume in the merged data set.

The rates  $R^i$  for each background, as used in Equation 7.16, were determined using the number of events found in the fiducial volume and the duration of the run. The efficiencies of the  $n_{\text{hits}}$  cuts on all considered isotopes were evaluated using the RAT 5.0.2 production files (The files are presented in Table C.8, the  $n_{\text{hits}}$  cut efficiencies are shown in Tables C.10 and C.11). Using Equation 7.17, the number of expected mistagged events was calculated. However, some of the files used to compile the merged data set had identical number seeds, meaning that the events in files with two

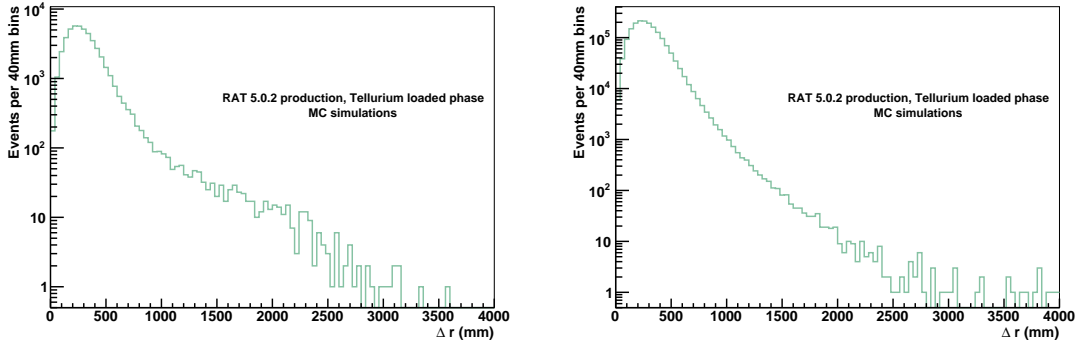


**Figure 7.11:** Reconstructed inter-event distance  $\Delta r$  between the Bismuth and Polonium candidates for the  $^{212}\text{Bi}^{212}\text{Po}$  (left) and  $^{214}\text{Bi}^{214}\text{Po}$  (right) coincidences in Tellurium loaded scintillator. The Polonium cut selection and the fiducial volume cut on the Bismuth candidate have been applied.  $\Delta r$  between the Bismuth and Polonium candidates was calculated using Equation 7.7. The plots were made using the one month merged data set, selecting only  $^{212}\text{Bi}^{212}\text{Po}$  and  $^{214}\text{Bi}^{214}\text{Po}$  events respectively. All selected Bismuth and Polonium candidates were required to pass a fit validity flag.

identical seeds had the exact same timing and position properties. These files were mostly  $^{210}\text{Po}$  and  $^{210}\text{Bi}$  files [135], to account for this a factor of 0.942 was applied to both isotopes in the calculation of mistagged coincidences.

Additionally to the considerations made in Section 7.1.2, the contributions from the respective other Bi-Po coincidence to the mistagging had to be accounted for. This was not an issue for the pure scintillator phase, since the expected rates in pure scintillator are so low that within the timing cuts no  $^{214}\text{Bi}^{214}\text{Po}$  coincidence would be selected as  $^{212}\text{Bi}^{212}\text{Po}$  coincidence and vice versa. In the Tellurium loaded phase the rates of the Thorium and Uranium chain events are so high that there is a possibility of mistagging Bi-Po coincidences. In order to determine the mistagging, the timing cut efficiencies of the Bi-Po cuts on the other coincidence were evaluated. The resulting values are

$$\begin{aligned}\epsilon(\Delta t) &= 0.0005 \text{ for the } ^{214}\text{Bi}^{214}\text{Po} \text{ inter-event timing on } ^{212}\text{Bi}^{212}\text{Po} \\ \epsilon(\Delta t) &= 0.0093 \text{ for the } ^{212}\text{Bi}^{212}\text{Po} \text{ inter-event timing on } ^{214}\text{Bi}^{214}\text{Po}\end{aligned}\quad (7.22)$$

The efficiencies for both, the fiducial volume cut on the Bismuth and the distance between the Polonium candidate event and the Bismuth candidate event, were taken from Table 7.17. The efficiencies of the  $n_{\text{hits}}$  cuts were taken from Tables C.10 and

**Table 7.17:** Cuts and cut efficiencies for each cut parameter for the  $^{212}\text{Bi}^{212}\text{Po}$  and  $^{214}\text{Bi}^{214}\text{Po}$  coincidence selection for Tellurium loaded scintillator. The cut efficiencies were determined as described in Equations 7.1–7.8. The total efficiency  $\epsilon$  on each selection followed from Equation 7.9.

	$^{212}\text{Bi}^{212}\text{Po}$			$^{214}\text{Bi}^{214}\text{Po}$		
	Cut value		efficiency	Cut value		efficiency
	lower	upper		lower	upper	
$r_{\text{fidvol}}$	-	4 000 mm	$\left(\frac{r_{\text{fidvol}}}{r_{AV}}\right)^3$	-	4 000 mm	$\left(\frac{r_{\text{fidvol}}}{r_{AV}}\right)^3$
$n_{\text{hits}}^{\text{Po}}$	180	330	0.907	140	280	0.9552
$\Delta t$	220 ns	3 690 ns	0.484	3 690 ns	1 798 788 ns	0.9857
$r_{\text{fidvol}}$ on Bi	-	4 000 mm	0.902	-	4 000 mm	0.939
$\Delta r$	0 mm	1 500 mm	0.992	0 mm	1 500 mm	0.9996
$n_{\text{hits}}^{\text{Bi}}$	10	300	0.924	300	680	0.8282
Total efficiency $\epsilon$	10.8 %			21.7 %		

**Table 7.18:** Estimated mistagged events for the Bi-Po coincidences in the Tellurium phase for 1 month.

	$^{212}\text{Bi}^{212}\text{Po}$	$^{214}\text{Bi}^{214}\text{Po}$
$N_{\text{Bi}21x\text{Po}21x}^{\text{allcuts}}$	$202 \pm 14$	$13\,230 \pm 115$
$N_{\text{mis}}^{\text{coinc, other}}$	$11.7 \pm 0.1(\text{sys.}) \pm 3(\text{stat.})$	$6 \pm 0.1(\text{sys.}) \pm 2(\text{stat.})$
$N_{\text{mis}}^{\text{coinc, Bi-Po}}$	$12 \pm 3(\text{stat.})$	0
Total $N_{\text{mis}}^{\text{coinc}}$	$24 \pm 4$	$6 \pm 2$

C.11. The expected number of mistags for each selection, alongside the expected number of selected Bi-Po coincidences are presented in Table 7.18. As for the pure scintillator phase, more mistagged coincidences were found for the  $^{212}\text{Bi}^{212}\text{Po}$  selection. However, the impact on the measurement was not as significant as it was for the pure scintillator phase, since more  $^{212}\text{Bi}^{212}\text{Po}$  events were selected by the cuts. A very pure  $^{214}\text{Bi}^{214}\text{Po}$  sample was predicted.

Tables 7.19 and 7.20 show the event yields resulting from applying the cuts to the merged data set. In real data two succeeding events do not have to originate from the two coincidence decays, it is possible that other events are recorded between the Bismuth and the Polonium decay. Therefore, once the Polonium candidate was selected, the Bismuth candidate selection was applied to multiple events preceding the

**Table 7.19:** Resulting event yield after applying the  $^{212}\text{Bi}^{212}\text{Po}$  cut selection to the Mixed data set. All cuts listed in Table 7.17 were applied. Once Polonium candidate was selected, the Bismuth selection was applied to two preceding events. If the first preceding event passed the cut both candidates were selected as a coincidence. If the first preceding event did not pass the Bismuth selection cuts the cuts were applied to the second preceding event. If this event passed the cuts, both candidates were selected as a coincidence event.

Isotope	Fiducial volume cut	$^{212}\text{Po}$ candidate	1 <sup>st</sup> $^{212}\text{Bi}$ candidate	2 <sup>nd</sup> $^{212}\text{Bi}$ candidate
$^{14}\text{C}$	495 824	0	0	0
$0\nu\beta\beta$	16 754	0	0	0
$2\nu\beta\beta$	74 472	1	0	0
( $\alpha, n$ )	25	0	0	0
$^{212}\text{Bi}^{212}\text{Po}$	556	163	163	0
$^{214}\text{Bi}^{214}\text{Po}$	18 075	15	15	0
$^{210}\text{Bi}$	476 138 528	6	2	0
$^{210}\text{Po}$	187 498 528	0	4	1
External	2 187	0	0	0
Total	264 263 578	185	184	1

Polonium candidate within the respective time window. If the first preceding event (i.e. the event with the shortest  $\Delta t$  to the Polonium candidate) passes the Bismuth selection cuts, the coincidence was selected and the selection of a new Polonium candidate was started. In case the first preceding event did not pass the Bismuth selection, the next preceding event was considered. Due to the short time window, only two preceding events were considered for the  $^{212}\text{Bi}^{212}\text{Po}$  selection, whilst for the  $^{214}\text{Bi}^{214}\text{Po}$  selection three preceding events were investigated.

The selected  $^{212}\text{Bi}^{212}\text{Po}$  coincidences in Table 7.19 seemed less than predicted from the calculation in Table 7.18. This is due to uncertainties in the time window from trigger effects as described in Section 7.1.1. Due to the longer half-life of the  $^{214}\text{Po}$ , this effect had no impact when applying the  $^{212}\text{Po}^{212}\text{Bi}$  selection to the  $^{214}\text{Bi}^{214}\text{Po}$  coincidence, leading to a good match between predicted and selected numbers. The random mistagged coincidences  $N_{\text{mis}}^{\text{coinc}}$  selected from the data set were less than predicted, which might be caused by stopping the selection after two Bismuth candidates and not looping over all events found within the time window.

The events selected by the  $^{214}\text{Bi}^{214}\text{Po}$  selection in Table 7.20 matched the predicted values well within the statistical uncertainties. Looking at the different terms in the

**Table 7.20:** Resulting event yield after applying the  $^{214}\text{Bi}^{214}\text{Po}$  cut selection to the Mixed data set. All cuts listed in Table 7.17 were applied. Once Polonium candidate was selected, the Bismuth selection was applied to two preceding events. If the first preceding event passed the cut both candidates were selected as a coincidence. If the first preceding event did not pass the Bismuth selection cuts the cuts were applied to the second preceding event. If this event passed the cuts, both candidates were selected as a coincidence event.

Isotope	Fiducial volume cut	$^{214}\text{Po}$ candidate	$1^{st} \text{ }^{214}\text{Bi}$ candidate	$2^{nd} \text{ }^{214}\text{Bi}$ candidate	$3^{rd} \text{ }^{214}\text{Bi}$ candidate
$^{14}\text{C}$	495 824	0	0	0	0
$0\nu\beta\beta$	16 754	0	3	0	0
$2\nu\beta\beta$	74 472	0	1	0	0
$(\alpha, n)$	25	0	0	0	0
$^{212}\text{Bi}^{212}\text{Po}$	556	0	0	0	0
$^{214}\text{Bi}^{214}\text{Po}$	18 075	13 266	12 302	895	70
$^{210}\text{Bi}$	76 138 528	5	0	0	0
$^{210}\text{Po}$	187 498 528	0	0	0	0
External	2 187	0	0	0	0
Total	264 263 578	13 271	12 306	895	70

$N_{\text{mis}}^{\text{coinc}}$  calculation for this selection, there were some contributions from true  $^{214}\text{Bi}$  events:

$$\begin{aligned} N_{\text{true}}^{\text{Po}} \cdot P_{\text{mis}}^{\text{Bi}} &= 0.01 \\ N_{\text{mis}}^{\text{Po}} \cdot P_{\text{true}}^{\text{Bi}} &= 2.3 \\ N_{\text{mis}}^{\text{Po}} \cdot P_{\text{mis}}^{\text{Bi}} &= 3.2 \end{aligned} \quad (7.23)$$

Adding up the numbers from Table 7.20, one  $^{214}\text{Bi}$  is mistagged with one of the selected  $^{210}\text{Bi}$  events, matching the expectations from Equation 7.23.

The purity and uncertainty on the measurement are shown in Table 7.21 for both the predictions from the calculation and the numbers from the Merged Data Set. As for the pure scintillator phase, a very good Uranium chain measurement could be achieved with a pure  $^{214}\text{Bi}^{214}\text{Po}$  sample. The higher statistics of Thorium chain events improved the measurement of these contents.

## 7.4 Summary

A cut selection was developed to select pure samples of  $^{212}\text{Bi}^{212}\text{Po}$  and  $^{214}\text{Bi}^{214}\text{Po}$  coincidences to measure the internal Uranium and Thorium chain contributions of

**Table 7.21:** Purities and measurement uncertainties for the Bi-Po coincidence selection for a one month Tellurium loaded phase. Both the values for predictions from calculation and the event yields from the merged data set are presented. The uncertainties on the purities were calculated as described in Appendix B.2 for values where the numerator is a subset of the denominator.

		$^{212}\text{Bi}^{212}\text{Po}$	$^{214}\text{Bi}^{214}\text{Po}$
Purity	Calculation	$0.89 \pm 0.02$	$0.9995 \pm 0.0002$
	Merged Data Set	$0.88 \pm 0.02$	$0.9996 \pm 0.0002$
Uncertainty	Calculation	7.4 %	0.9 %
	Merged Data Set	8.3 %	0.9 %

the scintillator cocktail during the pure scintillator-fill run phase. A number of cuts was applied to determine a Polonium candidate and a Bismuth candidate within a time window  $\Delta t$  determined by the half-life of the Polonium decay. Furthermore, the number of mistagged coincidences was evaluated using the number of events selected by the Polonium cuts and the probability to find a random background decay within the given time windows which passes the Bismuth cuts. For this analysis, all expected backgrounds internal to the scintillator cocktail as well as solar neutrino events were considered.

For both coincidence selections it was found that an additional  $n_{\text{hits}}^{\text{Bi}}$  cut on the Bismuth candidate reduced the mistagged coincidences significantly. Comparing the worst-case leaching scenario and the no-leaching case scenario it was found that the leaching backgrounds have no critical impact on the measurement of the Uranium chain contents. Due to the expected low rates of the Thorium chain events and low cut efficiencies arising from the short half-life of the  $^{212}\text{Po}$ , the Thorium chain extraction yielded a higher measurement uncertainty. In the worst-case leaching scenario, i.e. full isotropic leaching, the main backgrounds for both measurements were found to be decays originating from the leaching backgrounds  $^{210}\text{Bi}$  and  $^{210}\text{Po}$ . The measurement of the Thorium chain could not be improved by considering other fast decays.

The cut selection was applied to a one month Tellurium loaded merged data set. The calculation method to determine the mistagged coincidences was verified with the backgrounds contained within the data set. Due to the added Uranium and Thorium chain contents introduced by the loading of the Tellurium isotope both decay chains

could be constrained very well. The improved reconstruction algorithms for the later version of RAT used for the merged data set allowed for a tighter  $\Delta r$  cut, improving the rejection of mistagged coincidences especially for the Thorium chain measurement.

# 8 Evaluation of the Uranium and Thorium chain Backgrounds in Partial-Fill

During the transition period from the water phase to the scintillator phase, the water will be drained from the bottom of the AV, whilst the equivalent volume is replaced by the scintillator cocktail via the top. This phase is referred to in the following as the partial-fill phase. In an attempt to improve the measurement uncertainty of the Thorium chain contents, an analysis was developed using the partial-fill phase to measure the internal background contributions in the scintillator volume.

This Chapter explains how the rates of the background contributions in the scintillator cocktail were adjusted to the partial-fill scenario. Furthermore, the changes in cut efficiencies and cut application were investigated. Finally, the results are discussed and the effect on the pure scintillator phase measurement described in Chapter 7 is studied. Throughout this Chapter, a full isotropic leaching case was assumed and for both the  $^{212}\text{Bi}^{212}\text{Po}$  and  $^{214}\text{Bi}^{214}\text{Po}$  selections the  $n_{\text{hits}}^{\text{Bi}}$  cuts were applied on the Bismuth candidate. Neck events were not considered during the calculation of the rates as well as the Bi-Po measurement.

## 8.1 Calculating the Background Rates in a Partial-filled Detector

### 8.1.1 Internal Backgrounds in the Scintillator Volume

The background rates used for the analysis in Chapter 7 are the target background rates  $R_{\text{full}}^i$  for each isotope  $i$  in a fully filled AV. Since these rates originate from isotope decays internal to the scintillator cocktail, they are directly proportional to the scintillator volume contained within the AV.

The partial-fill period is estimated to take 91 days. Thus, with a full scintillator volume of  $V_{\text{full}} = 904.8 \text{ m}^3$ , the scintillator volume will increase by  $V_{\text{part}} = 9.93 \text{ m}^3$  per day. From this, the background rates  $R_k^i$  for each day  $k$  of the partial-fill phase can be estimated by

$$R_k^i = R_{\text{full}}^i \cdot \frac{V_k}{V_{\text{full}}} \quad (8.1)$$

with  $V_k$  being the scintillator volume at day  $k$

$$V_k = V_{k-1} + V_{\text{part}} \quad (8.2)$$

and  $V_0 = 0$ .

### 8.1.2 Leaching Backgrounds in the Scintillator Volume

As described in Section 3.5, the leaching backgrounds  $^{210}\text{Pb}$ ,  $^{210}\text{Bi}$  and  $^{210}\text{Po}$  originate from the AV surface. Therefore, the leaching rates depend on the AV surface area covered by the scintillator volume. The surface area of a sphere cap is

$$A_k = 2\pi r h_k \quad (8.3)$$

with  $r = 6\,000 \text{ mm}$  and  $h_k$  as shown in the schematic of a partial-filled detector in Figure 8.1. To determine the parameter  $h_k$  for each day of filling, the equation for the volume of a spherical cap was used:

$$V_k = \frac{\pi}{3} h_k^2 (3 \cdot r - h_k) \quad (8.4)$$

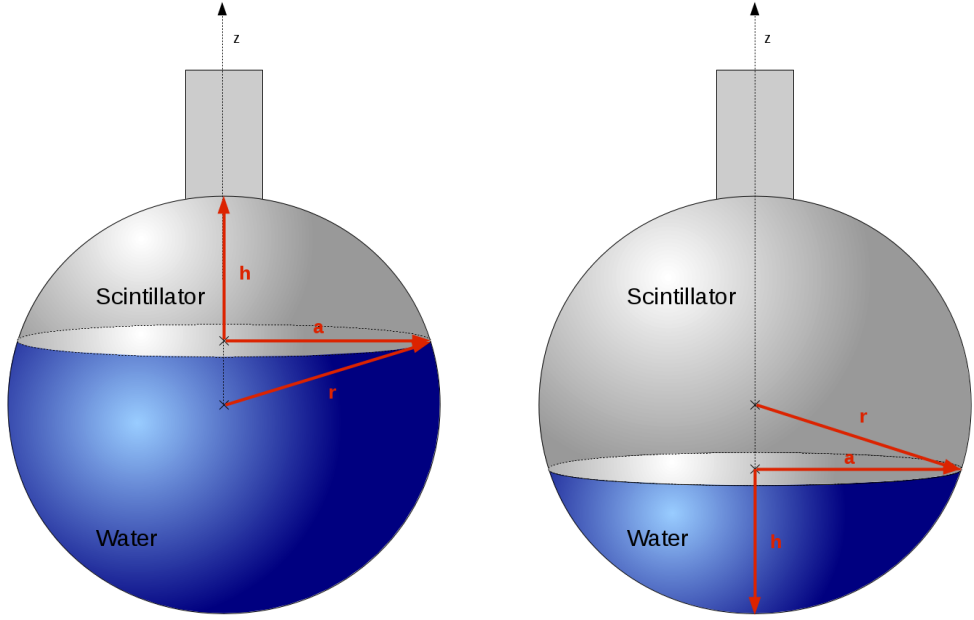


**Figure 8.1:** Schematic of a partial-filled detector. The scenario on the left shows the detector and all variables used to calculate the rates for the time the scintillator volume is confined to the area above the equator (i.e. the fill level  $z_k \geq 0$ ). The right shows the detector for and all used variables for the time the scintillator volume reaches below the equator (with  $z_k < 0$ ).

An additional constraint was applied to the calculated  $h_k$  to ensure the integrity of the detector geometry:

$$r = \frac{1}{2}h_k \left( \left( \frac{a_k}{h_k} \right)^2 + 1 \right) \quad (8.5)$$

with all parameters as depicted in Figure 8.1. The calculated  $A_k$  and expected  $V_k$  for the first 45 fill days are listed in Table D.1 for further information.

Knowing  $A_k$ , the daily leaching rates  $R_{\text{leach}, k}^i$  could be determined<sup>25</sup>

$$R_{\text{leach}, k}^i = R_{\text{leach, full, } k}^i \cdot \frac{A_k}{A_{\text{full}}} \quad (8.6)$$

---

<sup>25</sup>Even for a full scintillator volume the leaching rates  $R_{\text{leach, full, } k}^i$  change daily dependent on the time the AV surface has been submerged in the scintillator cocktail. The numbers for the full scintillator leaching rates were provided to the author by the head of the Backgrounds working group. Considering a 91 day partial-fill, the values for  $R_{\text{leach, full, } k}^i$  with  $k > 91$  were used to determine the full leaching case for the analysis in Chapter 7.

with  $A_{\text{full}} = 452.39 \text{ m}^2$ , the surface area of the AV sphere. For each of the three leaching isotopes, the rates  $R_{\text{leach}, k}^i$  were added to the internal rates  $R_k^i$  of these isotopes. The expected events in a 91 day partial-fill phase are presented in Table 8.1. Thus, 55  $^{212}\text{Bi}^{212}\text{Po}$  coincidences and 616  $^{214}\text{Bi}^{214}\text{Po}$  coincidences are expected to occur in the scintillator volume during the partial-fill phase.

### 8.1.3 Backgrounds in the Water Volume

During the water-phase,  $\alpha$ -decays are not expected to leave a detectable signature in the detector [92] (all expected backgrounds and their rates in a water-filled detector are listed in the Appendix in Table D.3). As for the scintillator volume, these rates had to be adjusted for the partial-fill phase. Since the water volume takes up the volume of the AV sphere not filled by the scintillator (compare Figure 8.1), the internal background rates  $R_k^{i, \text{water}}$  and leaching rates  $R_{\text{leach}, k}^{i, \text{water}}$  could be estimated by

$$\begin{aligned} R_k^{i, \text{water}} &= R^{i, \text{water}} \cdot \frac{V_{\text{full}} - V_k}{V_{\text{full}}} \\ R_{\text{leach}, k}^{i, \text{water}} &= R_{\text{leach}, \text{full}, k}^{i, \text{water}} \cdot \frac{A_{\text{full}} - A_k}{A_{\text{full}}} \end{aligned} \quad (8.7)$$

## 8.2 Cut Selection on Scintillator Volume Events

The overall cut strategy was the same as the one presented in Figure 7.1. However, due to the daily changing detector setup, the behaviour of the cuts over the fill period had to be investigated. Furthermore, the misreconstruction of water volume events in the scintillator volume had to be considered as well as potential effects on the scintillator-water interface.

These studies were carried out using RAT 5.3.1 partial-fill production files. For this production, each expected isotope decay was simulated at 90 different fill levels over 90 days<sup>26</sup> in both the water volume and the scintillator volume. The calculated rates from Section 8.1 were adjusted to ensure at least 100 events were simulated for each isotope at each fill level. The files used are listed in Appendix Tables D.4 and D.5 for further information.

---

<sup>26</sup>The 91st day is the day the full scintillator volume is achieved.

**Table 8.1:** Expected event contributions for all internal and leaching backgrounds in the scintillator volume in the 91 day partial-fill period.

Isotope	Expected events
$^{228}\text{Ac}$	86
$^{39}\text{Ar}$	10 759
$^{210}\text{Bi}$	31 231 389
$^{212}\text{Bi}$	86
$^{214}\text{Bi}$	616
$^{14}\text{C}$	513 526 878
$^{40}\text{K}$	1 067
$^{85}\text{Kr}$	10 801
$^{234m}\text{Pa}$	616
$^{210}\text{Pb}$	31 212 113
$^{212}\text{Pb}$	86
$^{214}\text{Pb}$	616
$^{210}\text{Po}$	34 147 121
$^{212}\text{Po}$	55
$^{214}\text{Po}$	616
$^{216}\text{Po}$	86
$^{218}\text{Po}$	616
$^{224}\text{Ra}$	86
$^{226}\text{Ra}$	616
$^{228}\text{Ra}$	86
$^{220}\text{Rn}$	86
$^{222}\text{Rn}$	616
$^{228}\text{Th}$	86
$^{230}\text{Th}$	616
$^{232}\text{Th}$	86
$^{234}\text{Th}$	616
$^{208}\text{Tl}$	31
$^{210}\text{Tl}$	0.13
$^{234}\text{U}$	616
$^{238}\text{U}$	616

The fill level  $z_k$  could be related to the variable  $h_k$  shown in Figure 8.1 via

$$\begin{aligned} z_k &= 6000 - h_k \text{ for } z_k \geq 0 \\ z_k &= -6000 + h_k \text{ for } z_k < 0 \end{aligned} \quad (8.8)$$

Please note that the value of  $h_k$  is always positive. The variable  $z_k$  is equivalent to the detector  $z$ -coordinate, i.e. at  $z_k = 0$  the scintillator-water interface is located at the detector equator. All fill levels used for the partial-fill production are listed in Table D.2 in the Appendix.

### 8.2.1 Fiducial Volume Cut

For this analysis, only events reconstructing in the scintillator volume were of interest. Due to the geometry of the scintillator volume, the fiducial volume considered depended on both the radius  $r_{\text{fidvol}}$  and  $h_k$ <sup>27</sup>:

$$\begin{aligned} \epsilon(r_{\text{fidvol}}) &= \frac{h_{\text{fidvol},k}^2 (3r_{\text{fidvol}} - h_{\text{fidvol},k})}{h_k^2 (3r - h_k)} \text{ for } z_k \geq 0 \\ \epsilon(r_{\text{fidvol}}) &= \frac{h_{\text{fidvol},k}^2 (3r_{\text{fidvol}} - h_{\text{fidvol},k})}{4 \cdot r^3 - h_k^2 (3r - h_k)} \text{ for } z_k < 0 \text{ and } z_{\text{fidvol},k} \geq 0 \\ \epsilon(r_{\text{fidvol}}) &= \frac{4 \cdot r_{\text{fidvol}}^3 - h_{\text{fidvol},k}^2 (3r_{\text{fidvol}} - h_{\text{fidvol},k})}{4 \cdot r^3 - h_k^2 (3r - h_k)} \text{ for } z_k < 0 \text{ and } z_{\text{fidvol},k} < 0 \end{aligned} \quad (8.9)$$

The change in efficiency once the scintillator volume reaches below the equator is a result of Equation 8.4 only being valid for volumes up to half of the sphere volume. Any volumes beyond the half-sphere had to be calculated using the volume of a full sphere.

#### Determining $h_{\text{fidvol},k}$

The chosen value of  $h_{\text{fidvol},k}$  depended on the behaviour of both scintillator volume and water volume events around the scintillator water interface. The left plot in Figure 8.2 shows the reconstructed  $z$ -position of scintillator volume events of  $^{210}\text{Bi}$  vs all days of filling. The start day 1642 is equivalent to the 1st of July 2014. During the production,

---

<sup>27</sup>for the definition of  $z_{\text{fidvol},k}$  see Equation 8.10

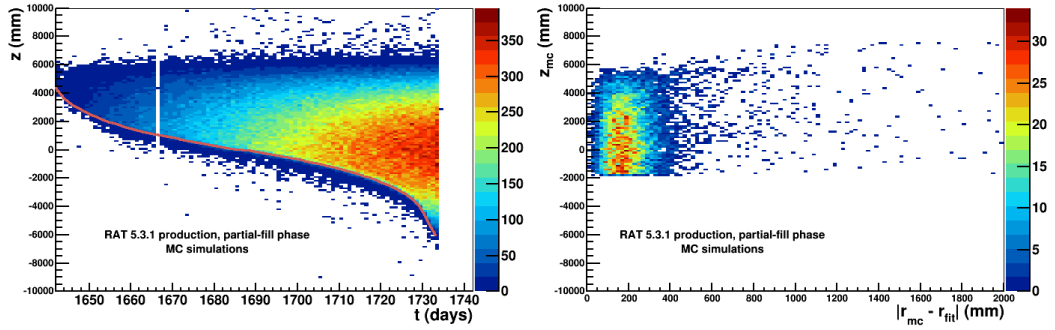


**Figure 8.2:** Left: Progression of the reconstructed z-coordinate over time for  $^{210}\text{Bi}$  scintillator volume events. All days of the partial-fill period are shown. The red line shows the fill level for each day. Right: True z-position of  $^{210}\text{Po}$  events in the scintillator volume vs the difference between the true radial position and the reconstructed radial position. This plot was created using the RAT 5.3.1 production sample for day 1715.

day 1666 was accidentally skipped and the supposed fill level  $z_{1666}$  was incremented on day 1667. Therefore, day 1666 was ignored for the remaining analysis<sup>28</sup>. It could be observed that some events according to Figure 8.2 are misreconstructed in the water volume, however, no unusual effects were observed on the scintillator water interface.

A comparison of the true  $z$ -coordinate  $z_{\text{mc}}$  the event was simulated at vs the difference between the true radial position  $r_{\text{mc}}$  and the reconstructed radial position  $r_{\text{fit}}$  for  $^{210}\text{Po}$  scintillator volume events for day 1715 is presented on the right in Figure 8.2. The larger the value of  $|r_{\text{mc}} - r_{\text{fit}}|$ , the worse the reconstruction performance. No increase in misreconstructed events could be observed around the scintillator water interface. Hence, no constraints on  $h_{\text{fidvol},k}$  could be determined from the scintillator events only.

Since some scintillator volume events were misreconstructed below  $z_k$ , it was expected that some water volume events misreconstruct above  $z_k$ . To determine how far above  $z_k$  these events were reconstructed, the value  $z - z_k$  was evaluated for all water volume events with  $z > z_k$ . The resulting  $z - z_k$  distribution for  $^{212}\text{Bi}$  water volume events is shown on the left in Figure 8.3. The bulk of events, which originate from  $\gamma$  events penetrating into the scintillator volume similar to events from external backgrounds, are reconstructed within 500 mm above the fill level.

---

<sup>28</sup>This is equivalent to not filling and turning the detector off on day 1666 and continuing data taking and filling on day 1667.

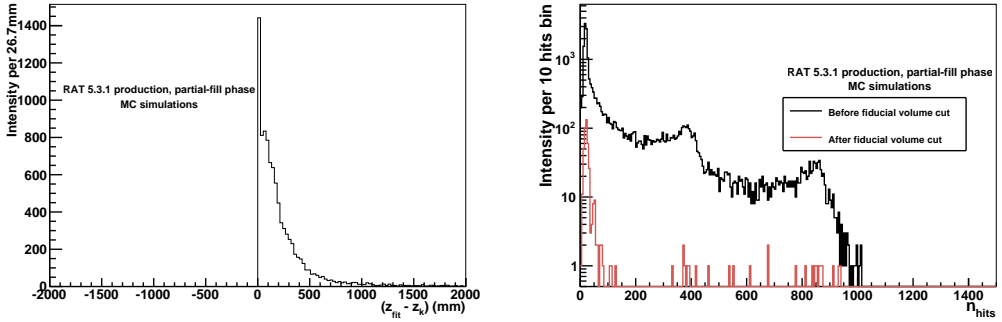


**Figure 8.3:** Left: The  $z - z_k$  for all events with  $z > z_k$  for  $^{212}\text{Bi}$  water volume events, summed over all 91 partial-fill days. Right: The  $n_{\text{hits}}$  spectrum of  $^{212}\text{Bi}$  water volume events, summed over all 91 partial-fill days.

For the chosen

$$z_{\text{fidvol},k} = z_k + 653 \text{ mm} \quad (8.10)$$

95 % of all misreconstructed water volume events were rejected. This value was converted to  $h_{\text{fidvol},k}$  using Equation 8.8. Rejecting water-volume events is important since they have non-negligible energy contributions leading to a possible selection of Polonium or Bismuth coincidence candidates, as the  $n_{\text{hits}}$  spectrum of  $^{212}\text{Bi}$  water volume events on the right in Figure 8.3 shows.

### Determining $r_{\text{fidvol}}$

Especially for the first days of partial-fill, very little scintillator volume will be available for analysis purposes. However, it is important to get an early look at data to understand the scintillator cocktail and monitor a potential change in internal background rates over time. Therefore, for these early fill stages it was decided to extend the fiducial volume cut of  $r_{\text{fidvol}} = 4\,000 \text{ mm}$  used for the full scintillator phase. The choice of  $r_{\text{fidvol}}$  depended on the reconstruction performance at radii close to the AV and the rejection power of external backgrounds.

Figure 8.4 shows on the left the true radial position  $r_{\text{mc}}$  vs the reconstruction value  $|r_{\text{mc}} - r_{\text{fit}}|$  for scintillator  $^{210}\text{Po}$  events on day 1715. A clear increase in misreconstructed events could be observed around the AV at  $r_{\text{mc}} = 5\,500 \text{ mm}$ . Below  $r_{\text{mc}} = 5\,000 \text{ mm}$  the misreconstruction rate was stable.

On the right of Figure 8.4 the reconstructed radial position of external backgrounds

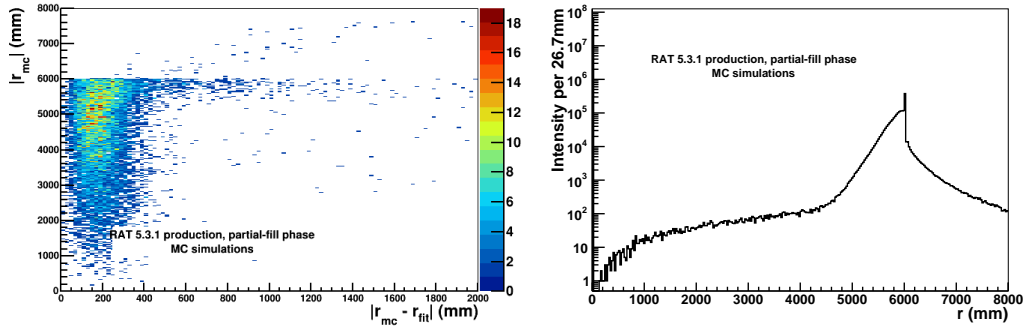


**Figure 8.4:** Left: True radial position  $r_{mc}$  of  $^{210}\text{Po}$  events in the scintillator volume vs the difference between the true radial position and the reconstructed radial position. This plot was created using the RAT 5.3.1 production sample for day 1715. Right: Reconstructed event radius of external background events, summed over all 91 partial-fill days.

for the partial-fill phase is shown. Most of the events which reconstructed inside of the AV were reconstructed above  $r = 4\,500\,\text{mm}$ . Based on both plots in Figure 8.4, the fiducial radius cut was chosen to be

$$r_{\text{fidvol}} < 5\,000\,\text{mm} \quad (8.11)$$

### Efficiency progression of the fiducial volume cut

Using the determined values of  $h_{\text{fidvol},k}$  and  $r_{\text{fidvol}}$ , the efficiency progression vs fill level  $z_k$  was calculated with Equation 8.9. The resulting distribution is presented in Figure 8.5 (note that here  $z_{\text{fill}} = z_k$ ).

### 8.2.2 Cut on the Number of Hits

The left of Figure 8.6 shows the  $n_{\text{hits}}$  spectrum for different fill days for  $^{210}\text{Bi}$  scintillator volume events. It could be observed that the  $n_{\text{hits}}$  spectrum does not change over the fill period. Therefore, to select the Bi-Po coincidences in the partial-fill phase, the same  $n_{\text{hits}}$  cuts for the Polonium and Bismuth candidates were used as listed in Table 7.1 for the full scintillator period.

The development of the cut efficiencies was studied for each fill level and each isotope. The cut efficiency of the  $n_{\text{hits}}^{\text{Po}}$  cut on  $^{210}\text{Bi}$  scintillator volume events vs fill

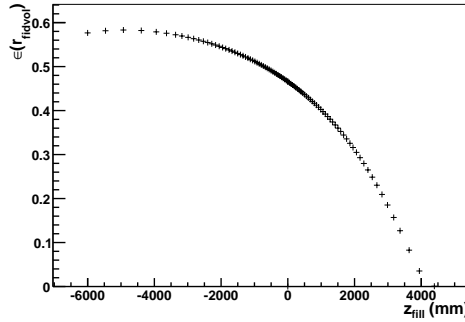


**Figure 8.5:** Efficiency progression of fiducial volume cut vs fill level for all fill levels simulated for the RAT 5.3.1 partial-fill production. The values were calculated using Equation 8.9.

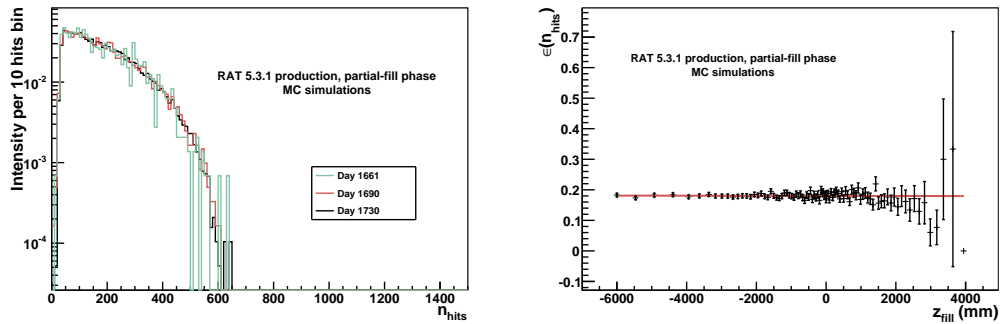


**Figure 8.6:** Left: The  $n_{\text{hits}}$  spectrum for different days of filling for  $^{210}\text{Bi}$  scintillator volume events. Each spectrum was normalised to the number of events which occurred at that fill level. Right:  $\epsilon(n_{\text{hits}})$  progression for all fill levels of the partial fill period for the  $^{214}\text{Po}$   $n_{\text{hits}}$  cut applied to  $^{210}\text{Bi}$  scintillator volume events.

level is presented on the right in Figure 8.6. It was found that within the statistical uncertainties the cut efficiencies do not change with fill level.

For each isotope decay expected in the scintillator volume, the  $\epsilon(n_{\text{hits}})$  vs fill level distributions were fitted using a linear function

$$f(z_k) = p0 \cdot z_k + p1 \quad (8.12)$$

with the fit parameters  $p0$  and  $p1$ . None of the fits yielded a  $p0$  which exceeded values in the order of  $10^{-5}$ . This resulted in an efficiency variation over the entire partial-fill of around 10 %, which was considered negligible. Thus, the cut efficiencies

were set to  $p1$  for each isotope. The uncertainties of the cut efficiencies followed from the uncertainties on the fit. For further information, all efficiency values can be found in the Appendix in Tables D.8 and D.9

### 8.2.3 Other Cuts

#### Bi-Po coincidences

Apart from the fiducial volume cuts on the Polonium and Bismuth candidates and the  $\Delta r$  cut, all cuts to select the Bi-Po coincidences in partial-fill were kept the same as listed in Table 7.1 for the pure scintillator fill. Based on the improved reconstruction performance observed for the 5.0.2 production on Section 7.3, the upper limit of the distance cut was changed to  $\Delta r < 1500\text{ mm}$ . The efficiencies of the time window cut  $\Delta t$ , the fiducial volume cut on the Bismuth candidate and the distance cut  $\Delta r$  between the Polonium and Bismuth candidates were studied for each fill level. The resulting distributions are presented in Figure 8.7 for  $^{212}\text{Bi}^{212}\text{Po}$  coincidences on the left and  $^{214}\text{Bi}^{214}\text{Po}$  coincidences on the right.

No change in cut efficiency could be observed over the fill period for  $\epsilon(\Delta t)$  and  $\epsilon(\Delta r)$ . However, a change over time especially for the first fill days was found for  $\epsilon(r_{\text{fidvol}}^{\text{Bi}})$ . As for the  $n_{\text{hits}}$  cuts, the efficiency  $\epsilon(\Delta r)$  was determined using the fit parameter  $p1$  (which is equivalent to the respective cut efficiencies in Table 8.2) of the linear fits. For  $\epsilon(r_{\text{fidvol}}^{\text{Bi}})$  the value determined for each fill level as shown in Figure 8.7 was applied. For the time window cut, the calculated efficiencies listed in Table 7.1 were used.

The resulting cut efficiencies found for the partial-fill analysis on both  $^{212}\text{Bi}^{212}\text{Po}$  and  $^{214}\text{Bi}^{214}\text{Po}$  coincidences are presented in Table 8.2. The selection efficiencies differ from the efficiencies found for the pure scintillator-fill, which was a result of the later version of RAT used for this analysis leading to improved reconstruction efficiencies. Furthermore, to deal with the different detector scenario during partial-fill, a different fitter was applied to reconstruct events during the production of the files. A lowest and highest total cut efficiency are presented in Table 8.2. Due to the changing fiducial volume cut efficiency, a different Bi-Po selection efficiency is achieved for each partial-fill day. Comparing the efficiencies shown in Figure 8.5, the highest selection efficiency was reached towards the end of partial-fill and the lowest selection efficiency

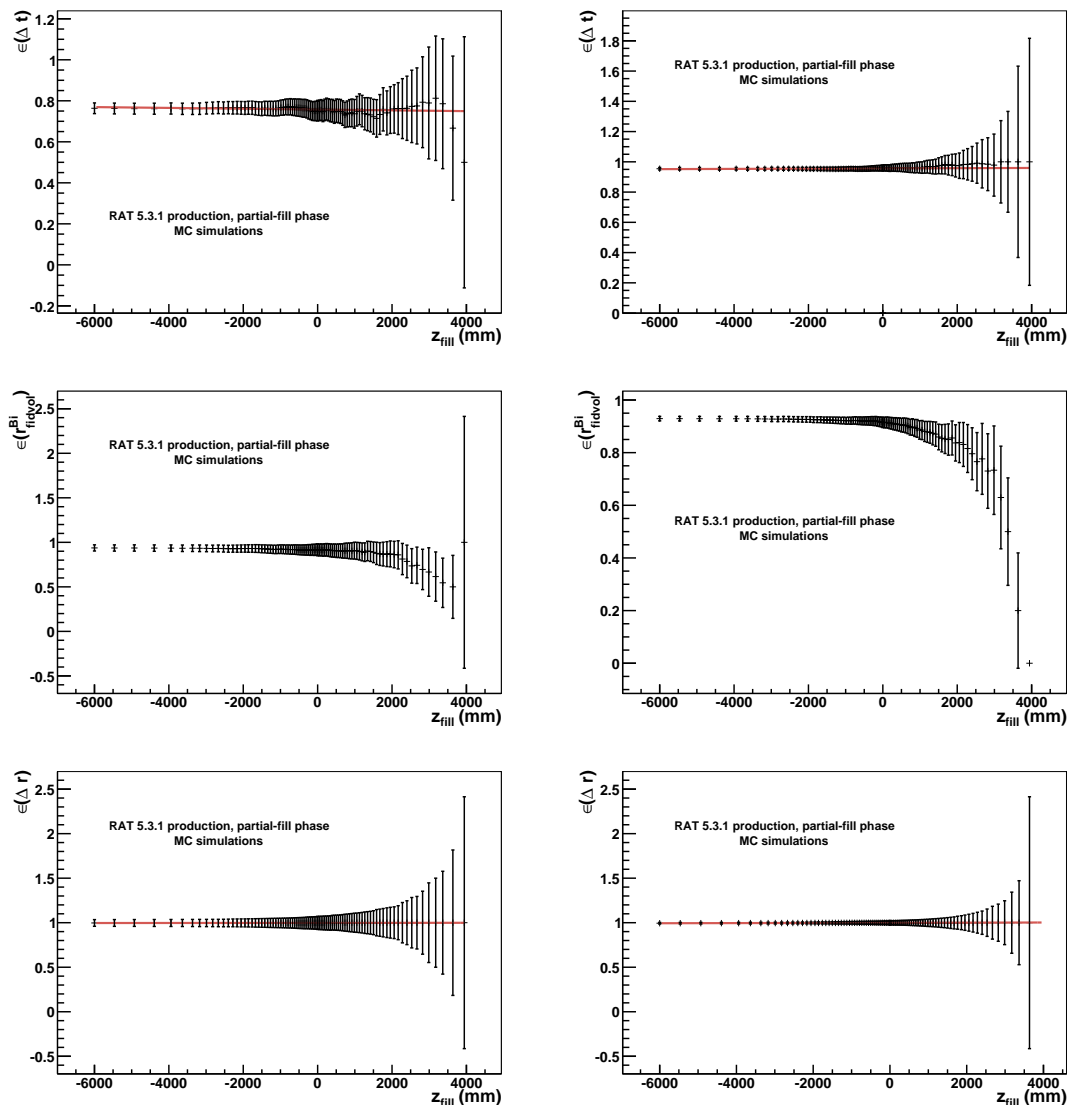


**Figure 8.7:** The development of the  $\Delta t$  (top),  $r_{\text{fidvol}}^{\text{Bi}}$  (middle) and  $\Delta r$  (bottom) cut efficiencies vs fill level for all fill levels of the partial-fill period for the  $^{212}\text{Bi}^{212}\text{Po}$  (left) and  $^{214}\text{Bi}^{214}\text{Po}$  (right) coincidences.

**Table 8.2:** Cut efficiencies for each cut parameter for the  $^{212}\text{Bi}^{212}\text{Po}$  and  $^{214}\text{Bi}^{214}\text{Po}$  coincidence selection in partial-fill. The cut efficiencies were determined as described in this Chapter. The total efficiency  $\epsilon$  on each selection follows from Equation 7.9.

	$^{212}\text{Bi}^{212}\text{Po}$	$^{214}\text{Bi}^{214}\text{Po}$
$r_{fidvol}$	see Equation 8.9/Figure 8.5	
$n_{\text{hits}}^{\text{Po}}$	0.097	0.82
$\Delta t$	0.484	0.9857
$r_{fidvol}$ on Bi	see Figure 8.7	
$\Delta r$	0.998	0.999
$n_{\text{hits}}^{\text{Bi}}$	0.928	0.907
Lowest total efficiency $\epsilon_{\text{low}}$	$(2 \pm 2)\%$	$(1 \pm 1)\%$
Highest total efficiency $\epsilon_{\text{high}}$	$(24 \pm 1)\%$	$(39.7 \pm 0.8)\%$

was achieved on the first day.

### Mistagged coincidences

The mistagged coincidences in the scintillator volume during the partial-fill phase were estimated using the same method as described in Section 7.1.2. Hence, the efficiencies of the fiducial volume cuts and the  $n_{\text{hits}}$  cuts on both Polonium and Bismuth candidates needed to be known as well as the effects of applying the time window  $\Delta t$  and the distance cut  $\Delta r$ . The efficiency progression of the fiducial volume cut of a mistagged Bismuth candidate follows the distribution in Figure 8.5. Since the time window  $\Delta t$  is constant for all fill levels, the number of mistagged events selected within  $\Delta t$  depended solely on the decay rates of the background isotopes as calculated in Section 8.1.

However, the efficiency of the  $\Delta r$  cut on random isotope decays depended on the fiducial volume, resulting in a changing cut impact with fill level. The cut was constructed to consider a sphere around any selected Polonium candidate, therefore its efficiency to select mistagged Bismuth candidates is

$$\begin{aligned} \epsilon(\Delta r) &= \frac{4 \cdot \Delta r^3}{h_k^2 \cdot (3r_{\text{fidvol}} - h_k)} \text{ for } z_k > 0 \\ \epsilon(\Delta r) &= \frac{4 \cdot \Delta r^3}{4 \cdot r_{\text{fidvol}}^3 - h_k^2 \cdot (3r_{\text{fidvol}} - h_k)} \text{ for } z_k < 0 \end{aligned} \quad (8.13)$$

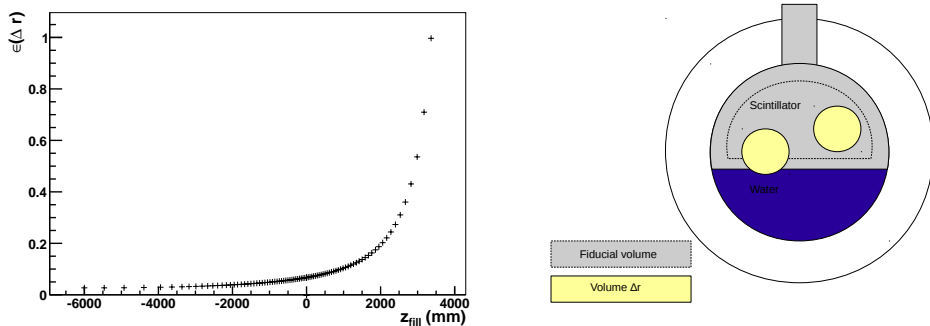


**Figure 8.8:** Left: Progression of the cut efficiency of the  $\Delta r$  of events isotropically distributed within the fiducial volume as determined using Equation 8.13. Right: Schematic of a partial-filled detector with a fiducial volume applied to the scintillator. Depicted in yellow is the sphere covered by the  $\Delta r$  cut with a Polonium candidate positioned within the fiducial volume (right yellow sphere) and a Polonium candidate positioned at the edge of the fiducial volume.

The resulting distribution vs fill level is presented on the left in Figure 8.8. This estimate is a conservative approach, since it also considers events outside of the fiducial volume if the Polonium candidate was selected towards the edge, as the schematic on the right of Figure 8.8 shows. Therefore, the resulting mistags might be slightly over-estimated.

Additionally to the isotopes considered for the mistagging study in Chapter 7, external backgrounds were considered in this study. In Chapter 7 they were considered negligible within the chosen fiducial volume based on the study in [132], however, the expanded fiducial radius cut used for the partial-fill analysis had not been previously considered. External events from  $^{214}\text{Bi}$  and  $^{40}\text{K}$  originating from the hold-down ropes, the AV and the outer water volume were included, as well as  $^{210}\text{Pb}$ ,  $^{210}\text{Bi}$  and  $^{210}\text{Po}$  AV contributions.

The resulting mistagged coincidences for both coincidence selections are presented in Table 8.3. Like for scintillator-fill more mistagged events were observed for the  $^{212}\text{Bi}^{212}\text{Po}$  selection. Unlike for scintillator-fill these originated from external events rather than the leaching backgrounds. This is a result of the low expected leaching rates during the partial-fill phase.

**Table 8.3:** Estimated event contributions from mistagging in the scintillator volume during the 91 day partial-fill phase as determined using Equation 7.17.

	$^{212}\text{Bi}^{212}\text{Po}$	$^{214}\text{Bi}^{214}\text{Po}$
$N_{\text{true}}^{\text{Po}} \cdot P_{\text{mis}}^{\text{Bi}}$	$(5.1 \pm 0.2) \times 10^{-5}$	$(3.6 \pm 0.2) \times 10^{-5}$
$N_{\text{mis}}^{\text{Po}} \cdot P_{\text{true}}^{\text{Bi}}$	$(8.6 \pm 0.02) \times 10^{-6}$	$0.0267 \pm 0.0004$
$N_{\text{mis}}^{\text{Po}} \cdot P_{\text{mis}}^{\text{Bi}}$	$19.4190 \pm 0.0005$	$0.87 \pm 0.04$
$N_{\text{mis}}^{\text{coinc}}$	$19.4191 \pm 0.0005$	$0.90 \pm 0.04$

## 8.3 Effect of the Cut Selection on Water Volume events

As previously discussed, events occurring in the water volume could be selected as Polonium and Bismuth candidates. A separate study of these events is necessary because of the different background rates expected in the water volume. To determine the expected mistagged water volume events, the same strategy as for scintillator mistags was used. However, the effect of the  $\Delta r$  was not considered on these events due to the geometric characteristics of the partial-fill detector. Therefore, the determined numbers only reflect an upper limit of expected mistags.

To determine the event rates of water volume events passing the fiducial volume cut, the number of events being reconstructed above  $z_k$  was determined for each expected isotope  $i$  using the partial-fill production files. Since the fiducial volume cut was designed to reject 95 % of all water volume events reconstructing above the scintillator water interface, the efficiency of the fiducial volume cut then followed from

$$\epsilon^i(r_{\text{fidvol}}) = \frac{N_{z>z_k}^i}{N_{\text{all}}^i} \cdot 0.05 \quad (8.14)$$

with  $N_{\text{all}}^i$  being all events simulated and  $N_{z>z_k}^i$  being all events reconstructed above  $z_k$  for isotope  $i$  over the entire partial-fill period.

The efficiencies of the applied  $n_{\text{hits}}$  cuts were determined by considering all water volume events within  $r = 5\,000\,\text{mm}$ . This approach was chosen since the analysis of scintillator volume events yielded no change in  $n_{\text{hits}}$  cut efficiencies for different fill levels. For further information, Appendix Tables D.10, D.11 and D.12 present the

**Table 8.4:** Estimated event contributions from mistagging in the water volume during the 91 day partial-fill phase. All shown values represent an upper limit of the expected event contributions, since the effect of the  $\Delta r$  cut on the Bismuth candidate selection probability was not considered.

	$^{212}\text{Bi}^{212}\text{Po}$	$^{214}\text{Bi}^{214}\text{Po}$
$N_{\text{mis}}^{\text{Po}} \cdot P_{\text{true}}^{\text{Bi}}$	$< (1 \pm 2) \times 10^{-10}$	$< (2.4 \pm 0.2) \times 10^{-5}$
$N_{\text{mis}}^{\text{Po}} \cdot P_{\text{mis}}^{\text{Bi}}$	$< (8 \pm 21) \times 10^{-8}$	$< (1.9 \pm 0.1) \times 10^{-6}$
$N_{\text{mis, water}}^{\text{coinc}}$	$< (8 \pm 21) \times 10^{-8}$	$< (2.6 \pm 0.2) \times 10^{-5}$

evaluated efficiencies for the fiducial volume cut and the  $n_{\text{hits}}$  cuts.

Since no  $\alpha$  events are expected to be visible in the water volume (and therefore no true Polonium events could be selected), Equation 7.17 could be altered to

$$N_{\text{mis, water}}^{\text{coinc}} = N_{\text{mis}}^{\text{Po}} \cdot P_{\text{true}}^{\text{Bi}} + N_{\text{mis}}^{\text{Po}} \cdot P_{\text{mis}}^{\text{Bi}} \quad (8.15)$$

Table 8.4 shows the expected upper limits for water volume mistags. Even without considering the  $\Delta r$  cut, the number of mistags from the water volume was found to be negligible.

## 8.4 Mistagging of Scintillator Volume Events with Water Volume Events

Another potential source for mistagged coincidences is pairing a scintillator volume Polonium candidate with a water volume Bismuth candidate and vice versa. To evaluate the number of these occurrences, Equation 7.17 was modified to

$$\begin{aligned} N_{\text{mis, mix}}^{\text{coinc}} &= N_{\text{true, scint}}^{\text{Po}} \cdot P_{\text{mis, water}}^{\text{Bi}} + N_{\text{true, scint}}^{\text{Po}} \cdot P_{\text{true, water}}^{\text{Bi}} \\ &\quad + N_{\text{mis, scint}}^{\text{Po}} \cdot P_{\text{mis, water}}^{\text{Bi}} + N_{\text{mis, scint}}^{\text{Po}} \cdot P_{\text{true, water}}^{\text{Bi}} \\ &\quad + N_{\text{mis, water}}^{\text{Po}} \cdot P_{\text{mis, scint}}^{\text{Bi}} + N_{\text{mis, water}}^{\text{Po}} \cdot P_{\text{true, scint}}^{\text{Bi}} \end{aligned} \quad (8.16)$$

with  $N_{x, \text{scint/water}}^{\text{Po}}$  the Polonium candidate selected by the cuts in the scintillator/water volume and  $P_{x, \text{scint/water}}^{\text{Bi}}$  the probability to tag a Bismuth candidate in the scintillator/water volume. For all variables in Equation 8.16 the same considerations were

**Table 8.5:** Estimated event contributions from mistagging of scintillator volume events with water volume events during the 91 day partial-fill phase. All terms including the selection probability of Bismuth candidates from the water volume represent upper limits, since the effect of the  $\Delta r$  cut on the Bismuth candidate selection probability was not considered.

	$^{212}\text{Bi}^{212}\text{Po}$	$^{214}\text{Bi}^{214}\text{Po}$
$N_{\text{true, scint}}^{\text{Po}} \cdot P_{\text{mis, water}}^{\text{Bi}}$	$< (1 \pm 3) \times 10^{-8}$	$< (8.2 \pm 0.6) \times 10^{-7}$
$N_{\text{true, scint}}^{\text{Po}} \cdot P_{\text{true, water}}^{\text{Bi}}$	$< (1 \pm 2) \times 10^{-11}$	$< (1.00 \pm 0.07) \times 10^{-5}$
$N_{\text{mis, scint}}^{\text{Po}} \cdot P_{\text{mis, water}}^{\text{Bi}}$	$< (5 \pm 11) \times 10^{-3}$	$< (2.561 \pm 0.006) \times 10^{-2}$
$N_{\text{mis, scint}}^{\text{Po}} \cdot P_{\text{true, water}}^{\text{Bi}}$	$< (6 \pm 9) \times 10^{-6}$	$< 0.3145 \pm 0.0004$
$N_{\text{mis, water}}^{\text{Po}} \cdot P_{\text{mis, scint}}^{\text{Bi}}$	$(2.2 \pm 0.4) \times 10^{-4}$	$(1.9 \pm 0.2) \times 10^{-5}$
$N_{\text{mis, water}}^{\text{Po}} \cdot P_{\text{true, scint}}^{\text{Bi}}$	$(7 \pm 1) \times 10^{-11}$	$(8.2 \pm 0.5) \times 10^{-7}$
$N_{\text{mis, mix}}^{\text{coinc}}$	$< (5 \pm 12) \times 10^{-3}$	$< 0.3401 \pm 0.0004$

made as for the calculation of mistagged coincidences in the scintillator and water volumes only as described in Sections 8.2 and 8.3. The resulting event yields for the  $^{212}\text{Bi}^{212}\text{Po}$  and  $^{214}\text{Bi}^{214}\text{Po}$  selections are listed in Table 8.5.

As for the water volume mistags, all terms including  $P_{\text{true/mis, water}}^{\text{Bi}}$  represent an upper limit, since the  $\Delta r$  cut was not considered. The main contributions to  $N_{\text{mis, mix}}^{\text{coinc}}$  arose from terms including misidentified Polonium scintillator volume candidates. The mistagged coincidences for the  $^{212}\text{Bi}^{212}\text{Po}$  coincidence selection were dominated by statistical uncertainties.

## 8.5 Measurement Uncertainty

The uncertainty on the Bi-Po coincidence measurements followed from the number of true selected Bi-Po coincidences  $N_{\text{Bi21xPo21x}}^{\text{allcuts}}$  and all events  $N_{\text{allcuts}}^{\text{data}}$  selected by the cuts in a given data sample

$$u = \frac{\sqrt{N_{\text{allcuts}}^{\text{data}}}}{N_{\text{Bi21xPo21x}}^{\text{allcuts}}} \quad (8.17)$$

with

$$N_{\text{allcuts}}^{\text{data}} = N_{\text{Bi21xPo21x}}^{\text{allcuts}} + N_{\text{mis, scint}}^{\text{coinc}} + N_{\text{mis, water}}^{\text{coinc}} + N_{\text{mis, mix}}^{\text{coinc}} \quad (8.18)$$

**Table 8.6:** Event yields for true Bi-Po coincidence events and mistagged events and measurement uncertainty for the  $^{212}\text{Bi}^{212}\text{Po}$  and  $^{214}\text{Bi}^{214}\text{Po}$  coincidence selections for the 91 day partial-fill phase.

	$^{212}\text{Bi}^{212}\text{Po}$	$^{214}\text{Bi}^{214}\text{Po}$
expected $N_{\text{Bi}21x}$	86	616
expected $N_{\text{Po}21x}$	55	616
$N_{\text{Bi}21x\text{Po}21x}^{\text{allcuts}}$	11	208
$N_{\text{mis, scint}}^{\text{coinc}}$	19.419	0.90
$N_{\text{mis, water}}^{\text{coinc}}$	$8 \times 10^{-8}$	$2.6 \times 10^{-5}$
$N_{\text{mis, mix}}^{\text{coinc}}$	0.005	0.34
Measurement uncertainty	50.1 %	7.0 %

The expected event yields for the  $^{212}\text{Bi}^{212}\text{Po}$  and  $^{214}\text{Bi}^{214}\text{Po}$  coincidences and the respective measurement uncertainties for a 91 day partial-fill phase are shown Table 8.6. The high cut efficiencies for the  $r_{\text{fidvol}}^{\text{Bi}}$  and  $\Delta r$  cuts for the true Bi-Po coincidence selections and the very low expected background rates as a result of the detection volume led to very low measurement uncertainties considering the short measurement period.

The impact of applying the partial-fill measurement results on the Uranium and Thorium chain measurements is shown in Figure 8.9. This Figure presents the development of the measurement uncertainty during the pure scintillator-fill phase over a measurement period of 181 days considering the pure scintillator-fill measurement only and adding the partial-fill measurement. For both internal background chains the measurement uncertainty could be lowered significantly by considering a partial-fill measurement. The statistical limits of the measurement were reached quicker with a partial-fill measurement, however, over a 181 day pure scintillator-fill run the measurement accuracy could still be improved. Combining the 91 day partial-fill analysis with a 181 day pure scintillator run, the uncertainties on the measurement were found to be:

$$\begin{aligned} & ^{212}\text{Bi}^{212}\text{Po}: 27.6 \% \\ & ^{214}\text{Bi}^{214}\text{Po}: 4.1 \% \end{aligned} \tag{8.19}$$

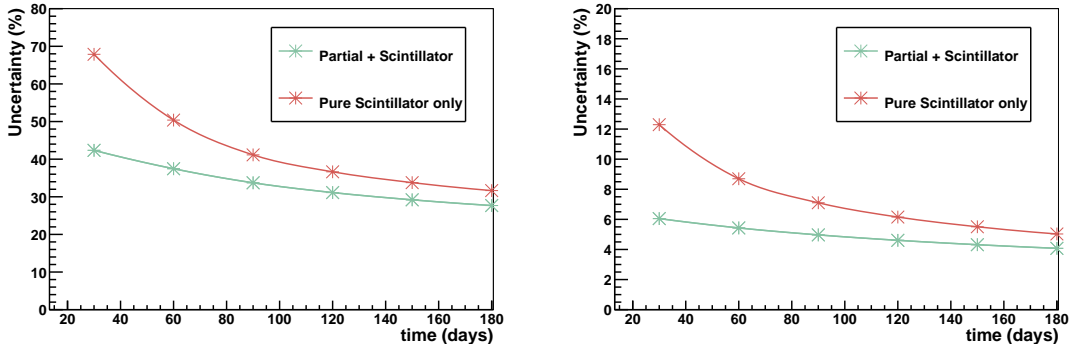


**Figure 8.9:** Development of the uncertainties on the  $^{212}\text{Bi}^{212}\text{Po}$  (left) and  $^{214}\text{Bi}^{214}\text{Po}$  (right) measurements over 181 days of pure scintillator-fill. Compared are the progressions considering a pure scintillator-fill analysis as described in Chapter 7 only and the resulting progression when combining the partial-fill analysis with the pure scintillator analysis. Each marker emphasises a 30 day period.

## 8.6 Summary

The measurement strategy for determining the Uranium and Thorium chain contents within the scintillator cocktail was applied to the partial-fill detector phase. This intermediate phase between the water-fill and the scintillator-fill yields a constantly changing detector scenario. It was shown that by some geometric considerations the internal background and leaching background rates could be adjusted to the new detector scenario.

The cuts developed in Chapter 7 could be used for this analysis. Due to the changing detector scenario some cut efficiencies were found to change considerably with fill level. The different fitter applied for partial-fill simulations and the improved reconstruction algorithms for the RAT 5.3.1 production led to higher cut efficiencies for the  $r_{\text{fidvol}}^{\text{Bi}}$  and  $\Delta r$  cuts on the true Bi-Po coincidences. The main mistagging contributions originated from scintillator volume events.

Combining the partial-fill analysis with the pure scintillator-fill measurements the measurement uncertainties could be improved significantly during the first months of scintillator-fill. Since the main goal of SNO+ is the measurement of  $0\nu\beta\beta$ -decay, which is why only a short pure scintillator phase is anticipated, understanding the backgrounds internal to the scintillator cocktail quickly is important. Achieving an early understanding of the internal backgrounds will also improve our capabilities to

measure solar fluxes during the pure scintillator phase.

The assumed background target rates can change due to re-circulation of the scintillator cocktail and improvements in the scintillator purification process. The partial-fill analysis was carried out considering separate rates for each day and summed over the entire filling period. Considering changing target rates over time, this can also be applied to the full scintillator analysis. Lower background rates, especially of the leaching backgrounds will result in lower mistags, which will especially affect the Thorium chain measurement. However, lower background events also leads to lower amounts of Bi-Po coincidences. Any improvement on the measurement is therefore dependent on the development of the ratio of leaching rate vs internal rate over time.

The different fiducial radius used for the partial-fill study may give confidence that the radial cut for the pure scintillator-fill can be expanded. However, since the leaching is going to affect the scintillator measurement more than the partial-fill measurement due to increased rates, and a radial dependence of the leaching contributions is expected (unlike the isotropic assumptions made in this study), a fiducial cut might be used to reject the leaching backgrounds additionally to the external backgrounds. A study looking into a radial fit on the background contributions is planned [136]. Based on the results of this, an extensive study on the fiducial volume cut for the partial-fill and the scintillator-fill analysis is necessary.

## 9 Conclusion

SNO+ has the potential to probe the inverse mass hierarchy and the majorana nature of neutrinos through the double beta decay program. Furthermore it has the sensitivity to measure solar neutrino fluxes at low energies and improve current limits on invisible nucleon decays. The work presented in this document will contribute to achieving these goals by providing tools to understand the intrinsic detector properties over different run phases.

Air-fill commissioning data was used to define the simulation of the Scattering Module. The direction and angular profiles were extracted and a method to measure the intensity of the data was developed. Cross-checks with the data yielded conclusive results. However, due to physical change in the detector setup, the presented work will be repeated once water-fill is complete.

The strategy to measure the scattering length during the water phase physics run was presented and applied to a fake data set. It was shown that the measurement estimates the detector properties well and that any arising discrepancies are understood. The main uncertainties originated from the system itself, indicating that more work to define the Scattering Module needs to be carried out once more data is available. It was proven that the current uncertainties will not affect the water phase measurements. The presented work can be adapted for the scintillator-fill phase.

Understanding the backgrounds in the scintillator during the partial-fill phase is important for several reasons: it will give an early insight if at the given background rates a solar measurement is feasible and it will provide information on the efficiency of the scintillator purification process. Methods to measure the internal Uranium and Thorium chain contents during the pure scintillator phase were described. It was found that the measurement of the Thorium chain was limited by the leaching backgrounds and the expected decay rates of the chain isotopes themselves. Applying the measurement to different fast decays occurring in the chain yielded no improvement on

the measurement. The Uranium chain measurements were much better constrained and shown to be statistics limited. The measurement method was confirmed using a merged data set for the Tellurium phase. Coupling a partial-fill and scintillator-fill background measurement leads to an understanding of the internal background contributions within the statistical limits over a few months of run time. The developed method will provide a tool to measure the background rates over time to help achieve an accurate background model of the scintillator cocktail before the loading of Tellurium. Constraining the background contributions will help improve the sensitivities of any physics measurement carried out during the pure scintillator phase.

# A Appendix - Scattering Module

## A.1 Initial definition of the Simulation Parameters

### A.1.1 Extracting the Wavelength and Timing distributions

Both the wavelength distributions and intra-pulse timings were extracted from measured distributions provided by the manufacturer for each laser as shown in Figures A.1 and A.2. These distributions were translated into probability arrays by extracting the values from these plots using a plot-to-table converter called PlotDigitizer [137]. Once the distributions were extracted, they were normalised to their maximum to convert the values into probabilities. The wavelength and timing (with respect to the trigger time) of each simulated beam photon is then randomly selected from these probability arrays. Due to dispersion effects in the detector material the intra-pulse timing distribution is expected to broaden. However, this effect is predicted to be too small to be resolved with the time resolution achieved by the SNO+ PMTs. Its significance will be investigated in detail during the SNO+ water-fill phase.

### A.1.2 Calculating Fibre Directions and Positions

The fibre positions were determined by adapting a script which was used to calculate the TELLIE positions and directions as listed in [119]. This script uses the position of the PMT the fibres are installed on (host) and the nearest neighbouring PMT in detector coordinates, as well as the position of the central PMT on the node panel. Figure A.3 shows a schematic of the three PMTs involved and the fibre mounting plate. Knowing the coordinates of the neighbouring PMT is important to understand which of the six hex cell faces of the host PMT the mounting plate is installed on.

To determine the positions of the fibres, first the position of the mounting plate

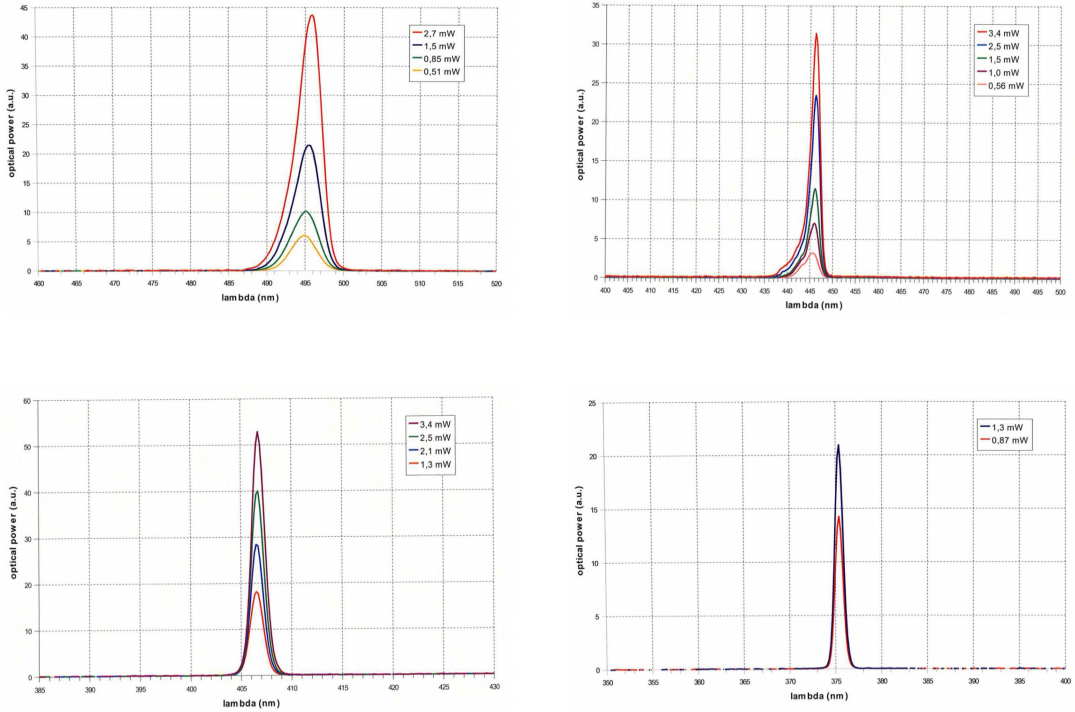


**Figure A.1:** Wavelength distributions for the four SMELLIE lasers at 495 nm (top left), 446 nm (top right), 407 nm (bottom left) and 375 nm (bottom right) as provided by the manufacturer PicoQuant. For each laser, the wavelength was monitored at different laser powers. When normalised to their maximum, the distributions for each laser power describe the same shape. For the simulation, the distribution at the highest power was extracted using a plot-to-table converter.

must be determined. Using the detector coordinates of the PMTs, a unit vector  $\vec{k}$  pointing towards the mounting plate can be defined as follows:

$$\vec{k} = \frac{\vec{n} - \vec{c}}{|\vec{n} - \vec{c}|}, \quad (\text{A.1})$$

with  $\vec{n}$  and  $\vec{c}$  as defined in Figure A.3. Multiplying this vector by the sum of the hex cell radius  $r$  and the width of the mounting plate  $w$  and adding the resulting vector to the vector pointing to the center of the host PMT  $\vec{h}$ , yields the position  $\vec{p}$  of the

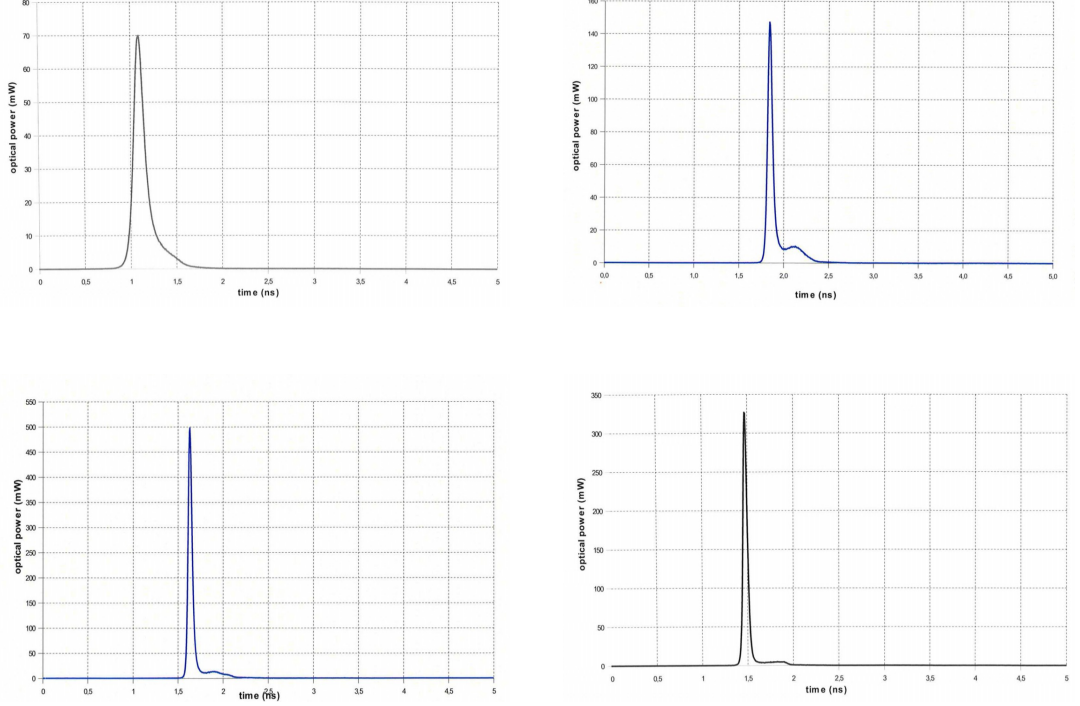


**Figure A.2:** Intra-pulse timing distributions for the four SMELLIE lasers at 495 nm (top left), 446 nm (top right), 407 nm (bottom left) and 375 nm (bottom right) as provided by the manufacturer PicoQuant. For the simulation, the distributions were extracted using a plot-to-table converter.

fibre in alignment with the PMT face:

$$\vec{p} = \vec{k} \cdot (r + w) + \vec{h}. \quad (\text{A.2})$$

The mounting plate drawings are presented in Figure A.4. Due to its design, the mounting plate protrudes marginally over the edge of the PMT face. Hence, the position  $\vec{p}$  of the center fibre was corrected to account for the resulting shift of the fibre tip. The direction  $\vec{d}$  of the center fibre follows from the position of the host PMT:

$$\vec{d} = -1 \cdot \frac{\vec{h}}{|\vec{h}|} \quad (\text{A.3})$$

The positions of the two angled fibres on the plate are determined with respect to

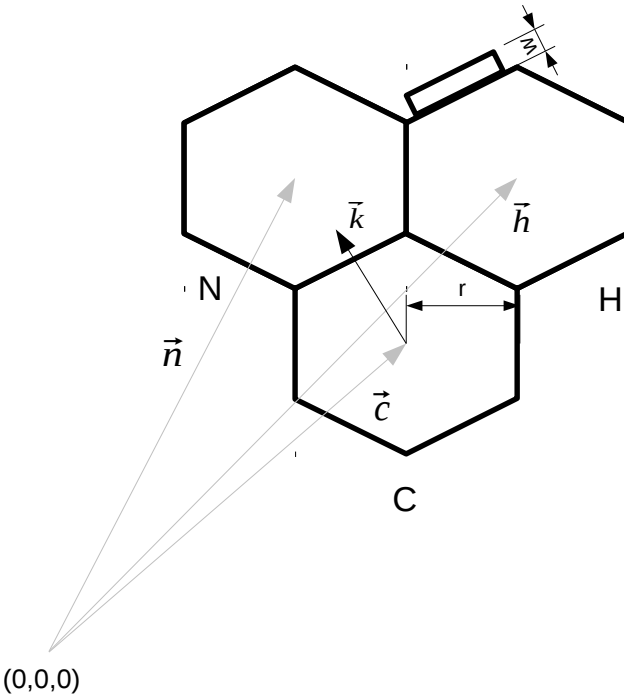


**Figure A.3:** Geometric considerations used to calculate the fibre positions, showing the host PMT (H) of the mounting plate, its neighbouring PMT (N) and the center PMT (C) of the node panel. The position  $(0,0,0)$  is the center of the Cartesian detector coordinate system and  $\vec{h}$ ,  $\vec{n}$  and  $\vec{c}$  are the vectors pointing to the center of the host, neighbouring and center PMTs respectively. The mounting plate width  $w$  and the radius of the hex cell  $r$  are also depicted

the position of the center fibre. Using the cross product between the vector  $\vec{f} = \vec{p} - \vec{h}$  pointing from the host PMT to the position of the central fibre and the direction vector of the center fibre  $\vec{d}$ , yields a vector pointing towards the right to the  $20^\circ$  fibre. This direction vector can then be used to determine the positions of the angled fibres by using the distances between the fibres, the position of the center fibre and the magnitude of the protrusion of the fibres. The directions of the angled fibres are determined by rotating the direction vector of the center fibre counterclockwise by  $10^\circ$  or clockwise by  $20^\circ$  respectively.

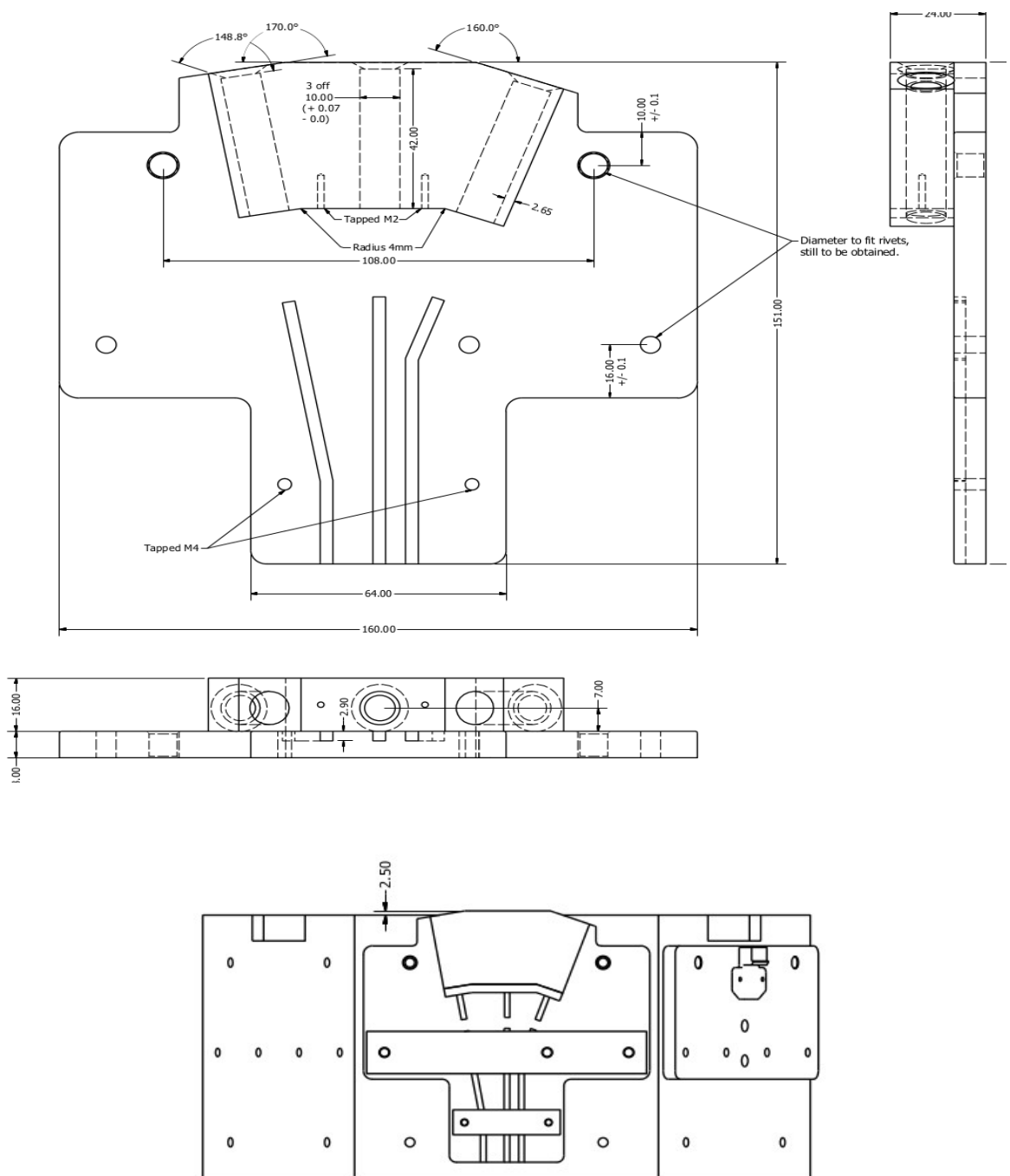


**Figure A.4:** Dimensions of the SMELLIE mounting plates. Presented on the top are the internal dimensions of the mounting plate. The bottom drawing shows the mounting plate with respect to the PMT hex cell.

### A.1.3 Implementing the Angular Profiles

The angular distributions of the collimators for each fibre have been measured offline at the University of Oxford using a charged-coupled device (CCD) positioned at three distances with respect to the fibre. The separation between each distance was 25 mm. The measured profiles were saved as ADC value vs. position on screen in  $41.4124 \mu\text{m}$  steps in 2 dimensions, denoted as v profile and u profile (see Figure A.5). Subsequently, the profiles were provided to the author to be implemented into the simulation.

These profiles were not centered around 0, in fact the 0 point of the measurements is equivalent to the edges of the screen. However, for the simulation a centered profile is needed, since the simulation assumes a circular symmetry and assigns the emission angles of the photons with respect to the fibre direction. Hence, to convert the measurements into angular profiles which can be used in the simulation, the provided profiles had to be centered first. In order to reject noise hits, all positions with a measured ADC intensity  $< 100$  were removed from the profiles<sup>29</sup>. Then the width  $w$  of the profile was determined using the first value  $x_1$  and the last value  $x_2$  of the distribution:

$$w = x_2 - x_1. \quad (\text{A.4})$$

The center  $m$  of the distribution is found by adding the half-width to the first point of the profile:

$$m = x_1 + \frac{w}{2} \quad (\text{A.5})$$

To achieve a distribution which is centered around 0,  $m$  is subtracted from each point of the profile.

Once all profiles were centered, the measured values were converted from the distance  $c$  measured in  $\mu\text{m}$  to angles. Figure A.6 shows a sketch of the experimental setup used for the measurements. The distances  $c$  were converted into angles  $\beta$  using the trigonometric identities, using the distance  $b$  from fibre to camera position. Both  $c$  and  $b$  are indicated in Figure A.6. However, the distance  $b$  from the fibre to each measurement point is unknown. Thus, the opening angle of the beam,  $\alpha$ , needed to be determined first in order to calculate  $b$ . The opening angle  $\alpha$  defines the angle between the center of the beam at  $m$  and the outer-most points  $e_i$  of the profiles

---

<sup>29</sup>The profiles were assumed to be top hat profiles

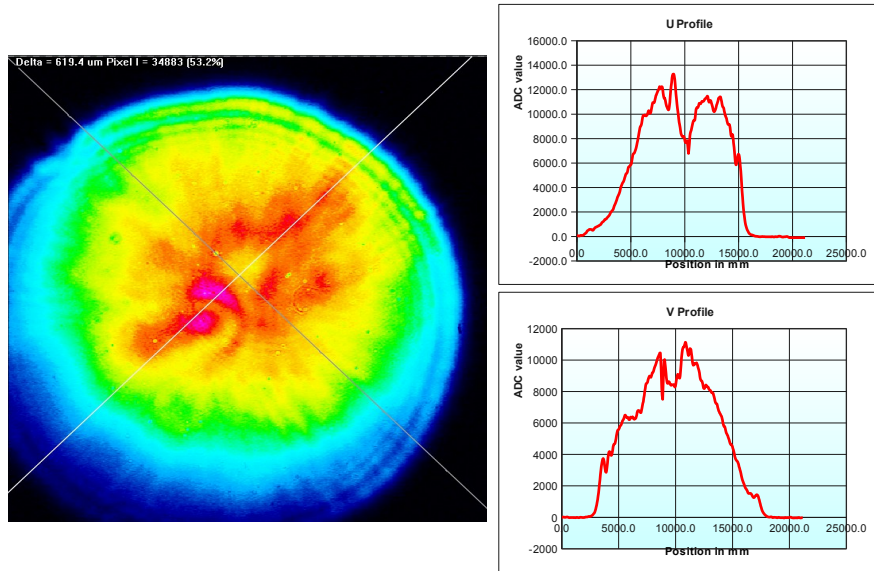


**Figure A.5:** Example of the angular profile measurements carried out at the University of Oxford. Depicted is the far profile for fibre FS137. An image of the beam was taken using a CCD (left side). The colour scale represents how much light was exposed on each point of the CCD. Areas in red were hit by the most photons, whilst areas in blue were hit by very few photons. Based on that colour scheme, the angular profile was extracted in two planes, the v and the u profile (right). These values were provided by Oxford University for all 12 fibres and all three measurement positions to be translated to the simulation as described here.

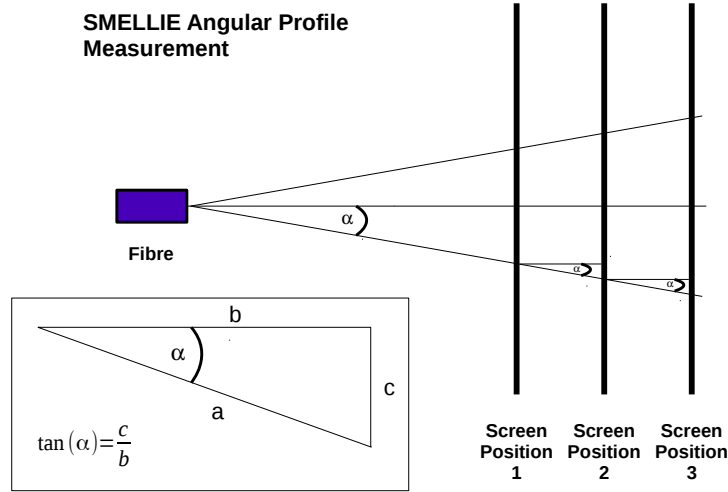


**Figure A.6:** Sketch of the angular profile measurements as carried out at the University of Oxford.

defined by

$$e_1 = x_1 - m \text{ and } e_2 = x_2 - m \quad (\text{A.6})$$

Due to the geometry of the experimental setup, this angle  $\alpha$  can also be found between the endpoints  $e_i$  at two different camera positions as shown in Figure A.6. Hence, the trigonometric identity could be used to evaluate  $\alpha$  at each measurement intersection by replacing the distance  $c$  with the difference between the edge points  $e_i$  at two measurement positions and setting  $b$  to a multiple of the 25 mm separation between each measurement point<sup>30</sup>. Since there were two profiles ( $u$  and  $v$ ) at each of the three measurement points, 6 estimations of  $\alpha$  could be extracted for each fibre using this method. To achieve a consistent measurement, these values were averaged for each fibre and the resulting angles are listed in Table A.1.

These opening angles were then used to calculate the distance  $b$  from the fibre to each measurement point for all fibres. Using trigonometric identities, these distances

---

<sup>30</sup>A measurement of  $\alpha$  is possible between the nearest (from the fibre) and medium screen positions and the medium and furthest (from the fibre) screen positions as well as between the nearest and the furthest screen position. Therefore,  $b$  can be replaced by 25 mm or 50 mm dependent on the screen configuration investigated.

**Table A.1:** Opening angles of the fibre collimators as measured at the University of Oxford.

Node	FS1xx	FS0xx	FS2xx
07	2.12	4.27	2.76
25	3.21	3.48	2.39
37	3.25	3.31	2.88
55	3.21	4.01	1.98

$b$  were then used to convert the measured profiles into angular distributions. As mentioned before, the simulation assumes a circular symmetry of the profiles, hence only the magnitudes of the calculated angles  $\beta$  were considered, essentially doubling the profile contributions from the measurements. Including both u and v profiles from each of the three measurement points left 6 angular profiles for each fibre. These profiles were averaged for each fibre and normalised to their maximum before they were added as probability arrays to the simulation. Each simulated photon is emitted at an angle picked from these arrays.

## A.2 Commissioning run information

**Table A.2:** Summary of the SMELLIE runs used for this study. Presented are the run number, the fibre, wavelength and laser intensity used for this run, the number of SMELLIE events contained in each run, the  $n_{\text{hits}}$  cut value used to veto re-triggers and non-SMELLIE events and the maximal occupancy values  $P_i^{\max}$  as calculated in Equation 5.3. To calculate  $P_i^{\max}$ , the PMT  $i$  with the most hits was used. The uncertainty on the occupancy was determined using the statistical uncertainties  $\sqrt{N}$  on each, the number of events per run and the number of hits for the most hit PMT.

Run number	Fibre	Wavelength	Laser intensity (%)	Number of events	$n_{\text{hits}}$ cut	$P_i^{\max}$
7110	FS055	407 nm	100	17 145	80	$1.00 \pm 0.01$
7112	FS155	407 nm	100	24 757	20	$0.57 \pm 0.01$
7114	FS137	407 nm	100	25 789	80	$1.00 \pm 0.01$
7116	FS037	407 nm	100	17 307	40	$0.94 \pm 0.01$
7118	FS255	407 nm	100	14 417	100	$1.00 \pm 0.01$
7120	FS237	407 nm	100	32 956	50	$0.98 \pm 0.01$
7124	FS055	495 nm	85	302 874	150	$1.000 \pm 0.003$
7128	FS155	495 nm	85	24 120	70	$0.98 \pm 0.01$
7130	FS137	495 nm	85	32 525	120	$1.00 \pm 0.01$
7132	FS037	495 nm	85	47 120	100	$1.00 \pm 0.01$
7134	FS255	495 nm	85	40 546	190	$1.00 \pm 0.01$
7136	FS237	495 nm	85	24 064	110	$1.00 \pm 0.01$
7139	FS055	446 nm	100	30 002	220	$1.00 \pm 0.01$
7141	FS155	446 nm	100	23 573	90	$0.99 \pm 0.01$
7143	FS137	446 nm	100	15 546	200	$1.00 \pm 0.01$
7145	FS037	446 nm	100	21 257	140	$1.00 \pm 0.01$
7147	FS255	446 nm	100	26 634	250	$1.00 \pm 0.01$
7149	FS237	446 nm	100	58 280	140	$1.00 \pm 0.01$
7151	FS237	446 nm	95	21 459	140	$1.00 \pm 0.01$
7153	FS237	446 nm	90	24 052	140	$1.00 \pm 0.01$
7155	FS237	446 nm	85	10 280	140	$1.00 \pm 0.01$
7157	FS237	446 nm	80	8 138	140	$1.00 \pm 0.02$
7159	FS237	446 nm	75	9 021	130	$1.00 \pm 0.01$
7161	FS237	446 nm	70	12 232	130	$1.00 \pm 0.01$
7163	FS237	446 nm	65	14 432	130	$1.00 \pm 0.01$
7165	FS237	446 nm	60	11 946	120	$1.00 \pm 0.01$
7167	FS237	446 nm	55	24 638	120	$1.00 \pm 0.01$
7169	FS237	446 nm	50	6 424	120	$1.00 \pm 0.02$
7171	FS237	446 nm	45	5 428	110	$1.00 \pm 0.02$
7173	FS237	446 nm	40	6 864	110	$1.00 \pm 0.02$
7175	FS237	446 nm	35	6 574	85	$1.00 \pm 0.02$
7177	FS237	446 nm	30	7 947	24	$0.89 \pm 0.01$
7179	FS237	446 nm	28	6 058	16	$0.57 \pm 0.01$

## A.3 Direction Measurement

**Table A.3:** Calculated directions from this study and the RAT database for all six installed fibres. The uncertainties on the direction measurement follow from the standard deviation of the fit on  $\Theta$  and  $\Phi$  as described in Section A.4.

Fibre	$\vec{r}$ from Data	$\vec{r}$ from Database
FS137	$(-0.5156 \pm 0.0339)$	$(-0.5257)$
	$(-0.7446 \pm 0.0247)$	$(-0.7236)$
	$(0.4238 \pm 0.0347)$	$(0.4472)$
FS037	$(-0.6676 \pm 0.0198)$	$(-0.6166)$
	$(-0.6323 \pm 0.0227)$	$(-0.5928)$
	$(0.3930 \pm 0.0292)$	$(0.5180)$
FS237	$(-0.1940 \pm 0.0334)$	$(-0.2993)$
	$(-0.8723 \pm 0.0130)$	$(-0.9159)$
	$(0.4488 \pm 0.0235)$	$(0.2673)$
FS255	$(0.0103 \pm 0.0435)$	$(0.000)$
	$(0.9045 \pm 0.0147)$	$(0.8944)$
	$(0.4263 \pm 0.0312)$	$(0.4472)$
FS055	$(0.0475 \pm 0.0436)$	$(0.000)$
	$(0.9627 \pm 0.0107)$	$(0.9585)$
	$(0.2665 \pm 0.0381)$	$(0.2851)$
FS155	$(-0.0791 \pm 0.0271)$	$(-0.0001)$
	$(0.6869 \pm 0.0170)$	$(0.6875)$
	$(0.7225 \pm 0.0312)$	$(0.7262)$

## A.4 Uncertainties on the Fibre Direction Measurements

The directions of the SMELLIE fibres were calculated using data runs 7110 – 7149 by fitting the  $\Theta$  and  $\Phi$  coordinates of the direct beam light with a Gaussian function.

The resulting values were averaged over all three available wavelengths for each fibre:

$$\begin{aligned}\Theta &= \left( \sum_i^{\text{all wavelengths}} \Theta(i) \right) / 3 \\ \Phi &= \left( \sum_i^{\text{all wavelengths}} \Phi(i) \right) / 3\end{aligned}\quad (\text{A.7})$$

The uncertainty on the measurement followed from the standard deviations of the Gaussian fits, which were combined for each fibre using the Gaussian uncertainty propagation:

$$\begin{aligned}\sigma_\Theta &= \sqrt{\left( \sum_i^{\text{all wavelengths}} \sigma_\Theta(i)^2 \right)} / 3 \\ \sigma_\Phi &= \sqrt{\left( \sum_i^{\text{all wavelengths}} \sigma_\Phi(i)^2 \right)} / 3\end{aligned}\quad (\text{A.8})$$

The measured  $\Theta$  and  $\Phi$  were converted into Cartesian coordinates using Equation 5.1. The uncertainties of these values were therefore determined by:

$$\begin{aligned}\Delta x &= \sqrt{(r \cdot \cos\Theta \cdot \cos\Phi \cdot \sigma_\Theta)^2 + (r \cdot \sin\Theta \cdot \sin\Phi \cdot \sigma_\Phi)^2} \\ \Delta y &= \sqrt{(r \cdot \cos\Theta \cdot \sin\Phi \cdot \sigma_\Theta)^2 + (r \cdot \sin\Theta \cdot \cos\Phi \cdot \sigma_\Phi)^2} \\ \Delta z &= r \cdot \sin\Theta \cdot \sigma_\Theta.\end{aligned}\quad (\text{A.9})$$

Each component of the direction vector  $\vec{r}$  as defined by Equation 5.2 can be written as

$$\begin{aligned}\hat{r}_x &= \frac{r_x}{\sqrt{r_x^2 + r_y^2 + r_z^2}} = \frac{p_x - f_x}{\sqrt{(p_x - f_x)^2 + (p_y - f_y)^2 + (p_z - f_z)^2}} \\ \hat{r}_y &= \frac{r_y}{\sqrt{r_x^2 + r_y^2 + r_z^2}} = \frac{p_y - f_y}{\sqrt{(p_x - f_x)^2 + (p_y - f_y)^2 + (p_z - f_z)^2}} \\ \hat{r}_z &= \frac{r_z}{\sqrt{r_x^2 + r_y^2 + r_z^2}} = \frac{p_z - f_z}{\sqrt{(p_x - f_x)^2 + (p_y - f_y)^2 + (p_z - f_z)^2}}.\end{aligned}\quad (\text{A.10})$$

For the uncertainty on the fibre direction followed

$$\begin{aligned}\Delta\hat{r}_x &= \sqrt{\left(\frac{\delta\hat{r}_x}{\delta r_x} \cdot \Delta x\right)^2 + \left(\frac{\delta\hat{r}_x}{\delta r_y} \cdot \Delta y\right)^2 + \left(\frac{\delta\hat{r}_x}{\delta r_z} \cdot \Delta z\right)^2} \\ \Delta\hat{r}_y &= \sqrt{\left(\frac{\delta\hat{r}_y}{\delta r_x} \cdot \Delta x\right)^2 + \left(\frac{\delta\hat{r}_y}{\delta r_y} \cdot \Delta y\right)^2 + \left(\frac{\delta\hat{r}_y}{\delta r_z} \cdot \Delta z\right)^2} \\ \Delta\hat{r}_z &= \sqrt{\left(\frac{\delta\hat{r}_z}{\delta r_x} \cdot \Delta x\right)^2 + \left(\frac{\delta\hat{r}_z}{\delta r_y} \cdot \Delta y\right)^2 + \left(\frac{\delta\hat{r}_z}{\delta r_z} \cdot \Delta z\right)^2},\end{aligned}\quad (\text{A.11})$$

where

$$\begin{aligned}\frac{\delta\hat{r}_i}{\delta r_i} &= \frac{\sqrt{r_x^2 + r_y^2 + r_z^2} - r_i \cdot (r_x^2 + r_y^2 + r_z^2)^{-\frac{1}{2}}}{r_x^2 + r_y^2 + r_z^2} \\ \frac{\delta\hat{r}_i}{\delta r_j} &= r_i \cdot r_j \cdot (r_x^2 + r_y^2 + r_z^2)^{-\frac{3}{2}}\end{aligned}\quad (\text{A.12})$$

with  $i \neq j$  and  $i, j = x, y, z$ .

## A.5 Uncertainty on the Angle between Fibres

The angle between two fibres was calculated using the fibre directions. Thus, the uncertainty of the angle between two fibres depended on the uncertainty on their directions. The angle between two fibres is

$$\beta = \cos^{-1}x \quad (\text{A.13})$$

with

$$x = \frac{\vec{a} \cdot \vec{b}}{|\vec{a}| |\vec{b}|} = \frac{a_x b_x + a_y b_y + a_z b_z}{\sqrt{a_x^2 + a_y^2 + a_z^2} \cdot \sqrt{b_x^2 + b_y^2 + b_z^2}}, \quad (\text{A.14})$$

where  $\vec{a}, \vec{b}$  represent the fibre directions. The uncertainty on  $\beta$  followed from differentiating Equation A.13 by each component  $k_i$ , where  $k = a, b$  and  $i = x, y, z$ :

$$\frac{\delta \cos^{-1}x}{\delta k_i} = \frac{\delta \cos^{-1}}{\delta x} \cdot \frac{\delta x}{\delta k_i} \quad (\text{A.15})$$

with

$$\frac{\delta \cos^{-1}}{\delta x} = -\frac{1}{1-x^2} \quad (\text{A.16})$$

and

$$\frac{\delta x}{\delta k_i} = \frac{l_i \cdot \sqrt{a_x^2 + a_y^2 + a_z^2} \sqrt{b_x^2 + b_y^2 + b_z^2} - k_i \cdot (a_x b_x + a_y b_y + a_z b_z) \cdot \frac{\sqrt{l_x^2 + l_y^2 + l_z^2}}{\sqrt{k_x^2 + k_y^2 + k_z^2}}}{(a_x^2 + a_y^2 + a_z^2) \cdot (b_x^2 + b_y^2 + b_z^2)}. \quad (\text{A.17})$$

Here,  $l = a, b$  and  $l \neq k$ . The uncertainty on  $\beta$  was determined with the Gaussian uncertainty propagation:

$$\Delta\beta = \sqrt{\left(\frac{\delta \cos^{-1}}{\delta a_x} \cdot \Delta a_x\right)^2 + \left(\frac{\delta \cos^{-1}}{\delta a_y} \cdot \Delta a_y\right)^2 + \left(\frac{\delta \cos^{-1}}{\delta a_z} \cdot \Delta a_z\right)^2 + \left(\frac{\delta \cos^{-1}}{\delta b_x} \cdot \Delta b_x\right)^2 + \left(\frac{\delta \cos^{-1}}{\delta b_y} \cdot \Delta b_y\right)^2 + \left(\frac{\delta \cos^{-1}}{\delta b_z} \cdot \Delta b_z\right)^2} \quad (\text{A.18})$$

This equation is also valid for the uncertainty on the angle between the fibre and the PMT hex cell if  $\Delta b_x = \Delta b_y = \Delta b_z = 0$ .

## A.6 Angular Profile Measurement

### A.6.1 Binning of the Angular Profiles

The binning of the angular profiles has an impact on the profile measurement. Choosing bins too wide can lead to an artificially broad profile, selecting too narrow bins can result in artificial variations in the bins arising from the detector geometry. Due to the construction of the detector, defining static angular bins might result in no registered hits in some bins if no PMTs are covered by that particular angle range. Therefore, to ensure that each bin covers an array of PMTs, variable bin sizes were defined based on the number of PMTs covered by each bin.

Figures A.7 - A.9 show the angular profiles of fibres FS037, FS237 and FS155 measured with angular bins covering different amount of PMTs, from 10 PMTs per bin to 4 PMTs per bin. Each of these profiles is compared to the profile covering 5 PMTs per bin which was used for the measurement. Especially for fibre FS037 it

became apparent how important the binning of the profile is. Choosing both 10 PMTs and 7 PMTs per bin led to a wider profile, artificially enhancing the contributions at higher bin angles. Using 4 PMTs per angular bin led to more prominent variations in the profile which may be a result of the detector geometry rather than the profile of the fibre itself. Regardless of the choice of binning, this measurement will always be limited by the detector geometry. Given the resulting distributions, a binning covering 5 PMTs per angular bin was considered a good compromise between unnaturally broadening the profile and introducing artificial features to the profile.

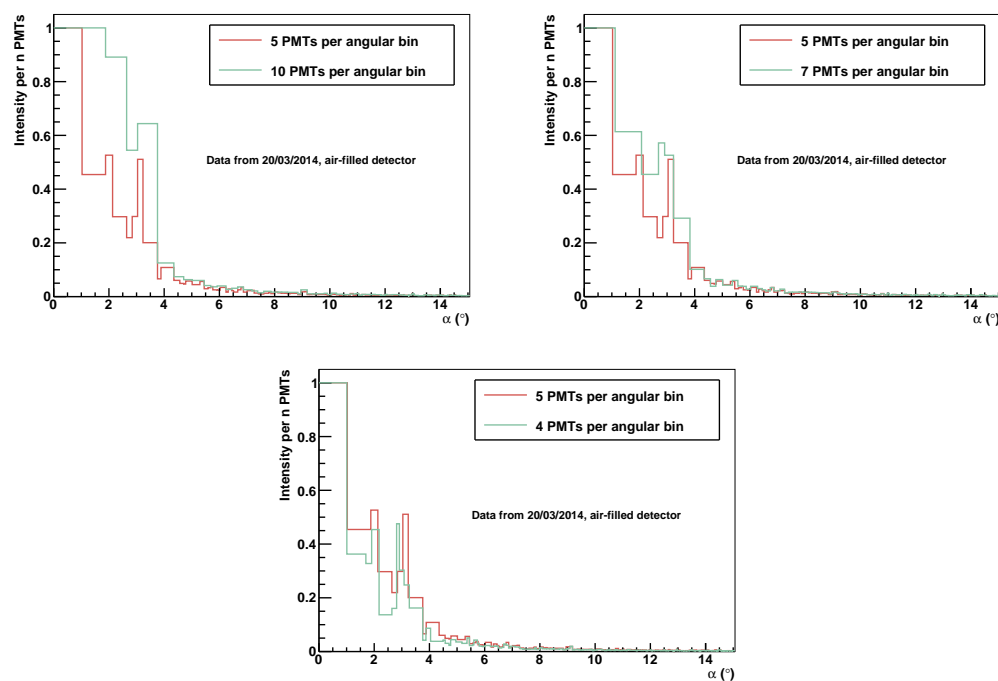


**Figure A.7:** Measured angular profiles for FS037 comparing profiles covering 10 PMTs (top left), 7 PMTs (top right) and 4 PMTs (bottom) per angular bin to the profile covering 5 PMTs per angular bin.

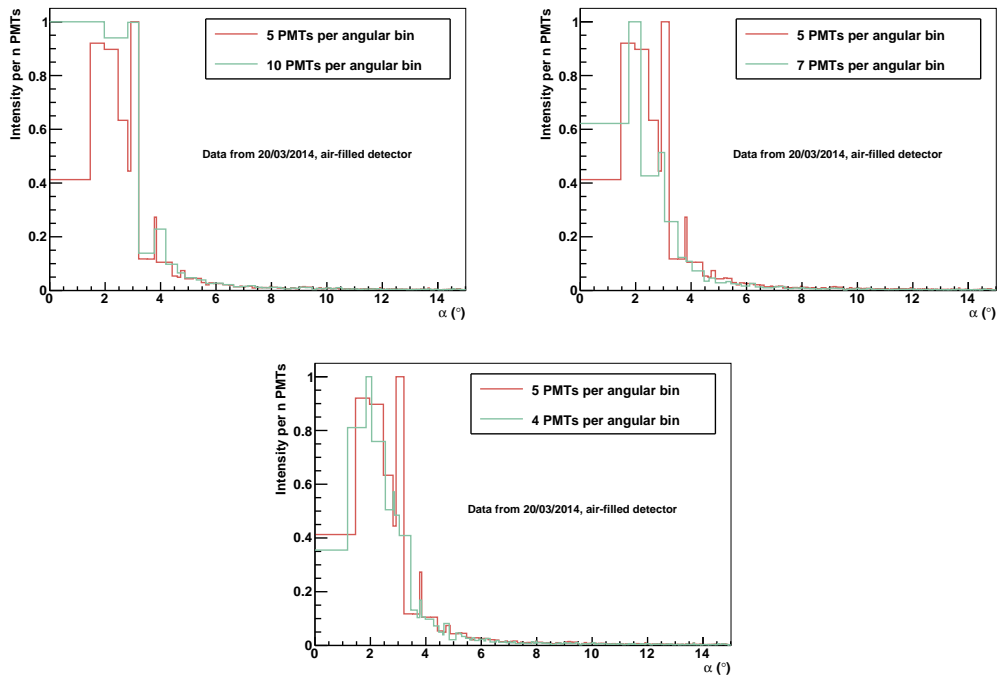


**Figure A.8:** Measured angular profiles for FS237 comparing profiles covering 10 PMTs (top left), 7 PMTs (top right) and 4 PMTs (bottom) per angular bin to the profile covering 5 PMTs per angular bin.

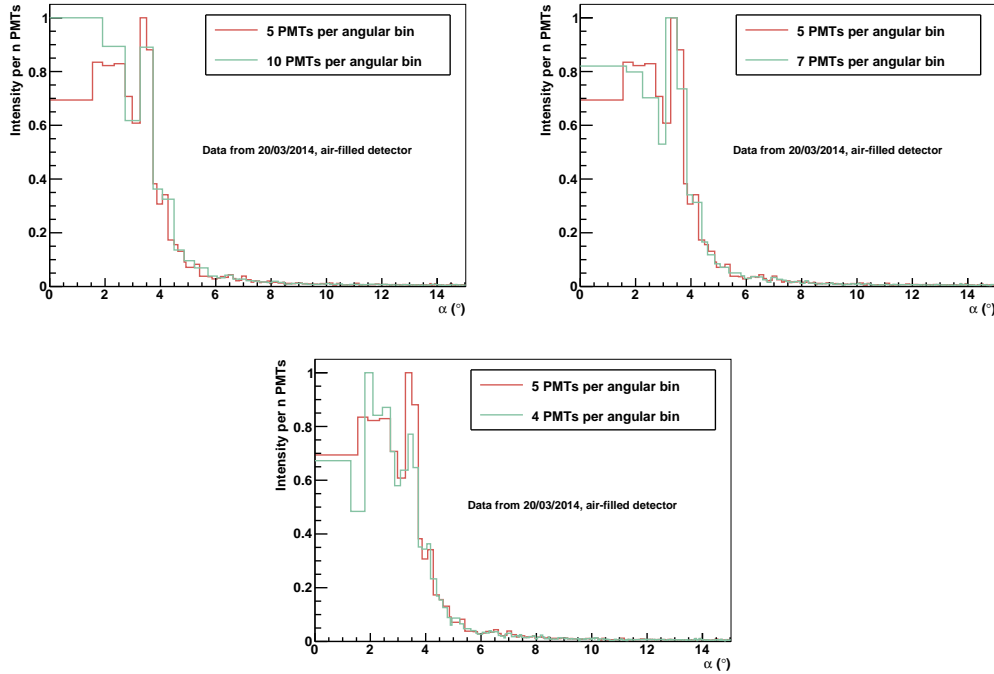


**Figure A.9:** Measured angular profiles for FS155 comparing profiles covering 10 PMTs (top left), 7 PMTs (top right) and 4 PMTs (bottom) per angular bin to the profile covering 5 PMTs per angular bin.

## A.7 Intensity Measurement

**Table A.4:** The fit parameters  $p_0$ ,  $p_1$  and  $p_2$  from Equation 5.6 for each fibre-wavelength combination.

Fibre	Wavelength (nm)	Air-fill			Water-fill		
		$p_0$	$p_1$	$p_2$	$p_0$	$p_1$	$p_2$
FS037	495	307.10	1.0102	0.00016	51.13	1.0329	0.00069
	446	342.65	1.0120	0.00017	55.40	1.0314	0.00093
	407	324.46	1.0118	0.00018	59.25	1.0302	0.00096
	375	291.85	1.0117	0.00018	62.74	1.0293	0.00083
FS237	495	248.64	1.0146	0.00020	36.70	1.0465	0.00086
	446	282.07	1.0174	0.00020	39.82	1.0445	0.00116
	407	261.33	1.0171	0.00022	42.86	1.0408	0.00120
	375	231.41	1.0170	0.00022	45.22	1.0386	0.00104
FS155	495	245.88	1.0125	0.00022	47.08	1.0353	0.00077
	446	259.13	1.0161	0.00024	48.27	1.0327	0.00111
	407	251.42	1.0145	0.00025	51.59	1.0316	0.00114
	375	227.16	1.0140	0.00025	52.97	1.0304	0.00102

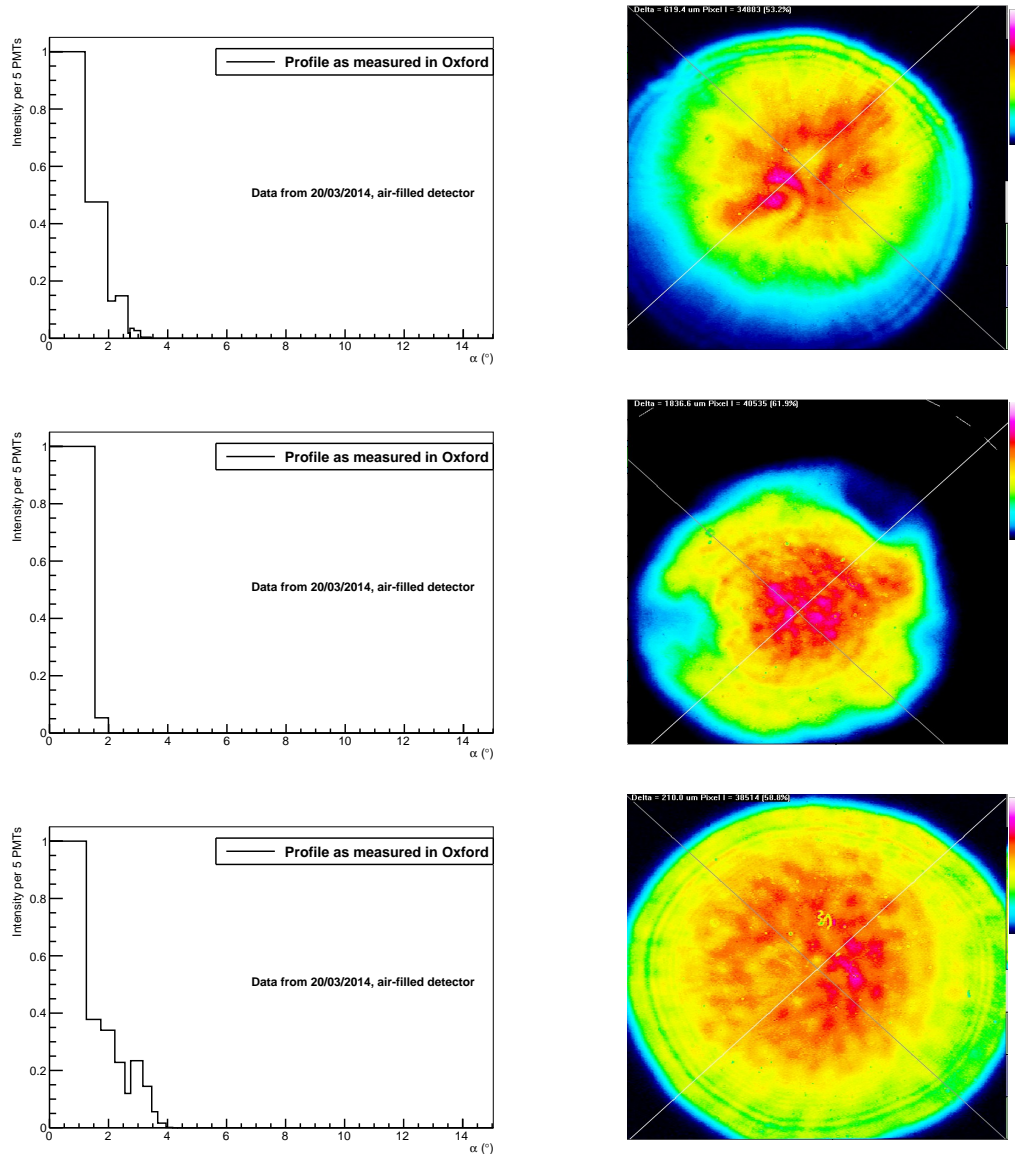


**Figure A.10:** The angular profiles as converted from the Oxford measurements for FS137 (top), FS255 (middle) and FS055 (bottom). Presented on the left are the converted profiles from the Oxford measurements. The angular bins were defined, so that each bin would cover 5 PMTs in the detector geometry, based on the directions of the fibres in the detector. The right shows the CCD images recorded in Oxford for the measurement point furthest away from the fibre. The colour scale represents how much light was exposed on each point of the CCD. Areas in red were hit by the most photons, whilst areas in blue were hit by very few photons.

**Table A.5:** The fit parameters p0, p1 and p2 from Equation 5.6 for each fibre-wavelength combination from the  $n_{\text{hits}}^{\text{mean, sim}} + \sigma^{\text{sim}}$  measurement.

Fibre	Wavelength (nm)	Air-fill			Water-fill		
		p0	p1	p2	p0	p1	p2
FS037	495	295.21	1.0197	0.00018	44.32	1.0754	0.00098
	446	336.10	1.0214	0.00019	51.63	1.0703	0.00119
	407	315.45	1.0214	0.00020	53.86	1.0671	0.00127
	375	283.28	1.0219	0.00020	56.50	1.0651	0.00110
FS237	495	243.45	1.0262	0.00022	32.64	1.1030	0.00123
	446	280.61	1.0287	0.00022	38.51	1.0958	0.00144
	407	258.77	1.0288	0.00024	40.98	1.0879	0.00151
	375	228.28	1.0296	0.00025	42.68	1.0840	0.00134
FS155	495	241.38	1.0241	0.00024	40.31	1.0824	0.00112
	446	257.34	1.0284	0.00026	44.16	1.0769	0.00147
	407	249.44	1.0266	0.00027	47.29	1.0741	0.00150
	375	224.04	1.0269	0.00028	47.33	1.0716	0.00139

**Table A.6:** The fit parameters p0, p1 and p2 from Equation 5.6 for each fibre-wavelength combination from the  $n_{\text{hits}}^{\text{mean, sim}} - \sigma^{\text{sim}}$  measurement.

Fibre	Wavelength (nm)	Air-fill			Water-fill		
		p0	p1	p2	p0	p1	p2
FS037	495	324.98	1.0014	0.00014	69.95	1.0010	0.00040
	446	352.36	1.0031	0.00015	63.10	0.9984	0.00067
	407	337.62	1.0029	0.00016	70.48	1.0001	0.00066
	375	304.67	1.0021	0.00016	76.42	1.0005	0.00056
FS237	495	256.67	1.0035	0.00018	47.21	1.0024	0.00052
	446	284.90	1.0063	0.00018	42.76	0.9984	0.00088
	407	265.53	1.0057	0.00020	46.77	0.9990	0.00090
	375	236.48	1.0048	0.00020	50.67	0.9993	0.00076
FS155	495	253.34	1.0014	0.00019	65.27	1.0007	0.00044
	446	262.47	1.0042	0.00022	56.53	0.9965	0.00077
	407	255.13	1.0027	0.00022	59.94	0.9967	0.00081
	375	232.48	1.0018	0.00022	64.83	0.9979	0.00068

**Table A.7:** Mean number of hits and Standard deviation for the March 2014 air-fill data.

Fibre	Wavelength (nm)	Laser intensity (%)	$n_{\text{hits}}^{\text{mean, data}}$	$\sigma^{\text{data}}$
FS137	495	85	173.2	12.3
	446	100	247.1	14.2
	407	100	113.0	9.5
FS037	495	85	134.0	11.1
	446	100	177.2	12.3
	407	100	67.6	7.8
FS237	495	85	146.1	11.0
	446	100	189.2	12.3
	407	100	76.7	7.9
FS255	495	85	231.5	14.1
	446	100	294.5	15.4
	407	100	131.7	9.7
FS055	495	85	192.7	12.8
	446	100	263.7	14.7
	407	100	122.0	9.6
FS155	495	85	103.7	9.3
	446	100	118.2	9.6
	407	100	42.3	6.5

**Table A.8:** Scattering length in air and water for selected wavelengths as currently implemented in RAT.

Wavelength (nm)	Scattering Length (mm)	
	Air	Water
380	$1.80 \times 10^{15}$	148 055
400	$2.25 \times 10^{15}$	181 772
440	$3.00 \times 10^{15}$	266 133
500	$4.50 \times 10^{15}$	443 781

**Table A.9:** Measured number of photons per beam pulse for the March 2014 commissioning data, runs 7151 – 7179.

Run number	Laser intensity (%)	nppb
7151	95	$4614 \pm 411$
7153	90	$4617 \pm 411$
7155	85	$4502 \pm 405$
7157	80	$4509 \pm 405$
7159	75	$4358 \pm 391$
7161	70	$4266 \pm 387$
7163	65	$4158 \pm 379$
7165	60	$4017 \pm 367$
7167	55	$3861 \pm 357$
7169	50	$3685 \pm 343$
7171	45	$3441 \pm 325$
7173	40	$3140 \pm 303$
7175	35	$2466 \pm 259$
7177	30	$934 \pm 180$
7179	28	$404 \pm 109$

# B Appendix - Rayleigh Scattering Length Measurement

## B.1 Calculating Crossing Points with the AV and PSUP

To calculate the crossing points of direct beam light with the AV, the definition of a line was used:

$$\vec{P} = \vec{f} + u \cdot \vec{r} \quad (\text{B.1})$$

with  $\vec{f}$  representing the fibre position and  $\vec{r}$  being the fibre direction. This definition was compared to the radius of a sphere (where the radius is either the radius of the AV or the radius of the PSUP)

$$R^2 = x^2 + y^2 + z^2 \quad (\text{B.2})$$

in order to achieve the intersection of the line with the sphere:

$$R^2 = (f_x + u \cdot r_x)^2 + (f_y + u \cdot r_y)^2 + (f_z + u \cdot r_z)^2 \quad (\text{B.3})$$

Equation B.3 was then re-arranged to represent a quadratic function in  $u$

$$0 = (f_x^2 + f_y^2 + f_z^2 - R^2) + 2 \cdot (f_x \cdot r_x + f_y \cdot r_y + f_z \cdot r_z) \cdot u + (r_x^2 + r_y^2 + r_z^2) \cdot u^2 \quad (\text{B.4})$$

equivalent to

$$0 = C + B \cdot u + A \cdot u^2. \quad (\text{B.5})$$

This quadratic equation was solved for  $u$  and the resulting value inserted in Equation B.1 to achieve the coordinates of the crossing point  $\vec{P}$ . For each crossing point following the first AV crossing point, the fibre direction  $\vec{r}$  needs to be adjusted using Snell's law to account for refraction on the different surfaces.

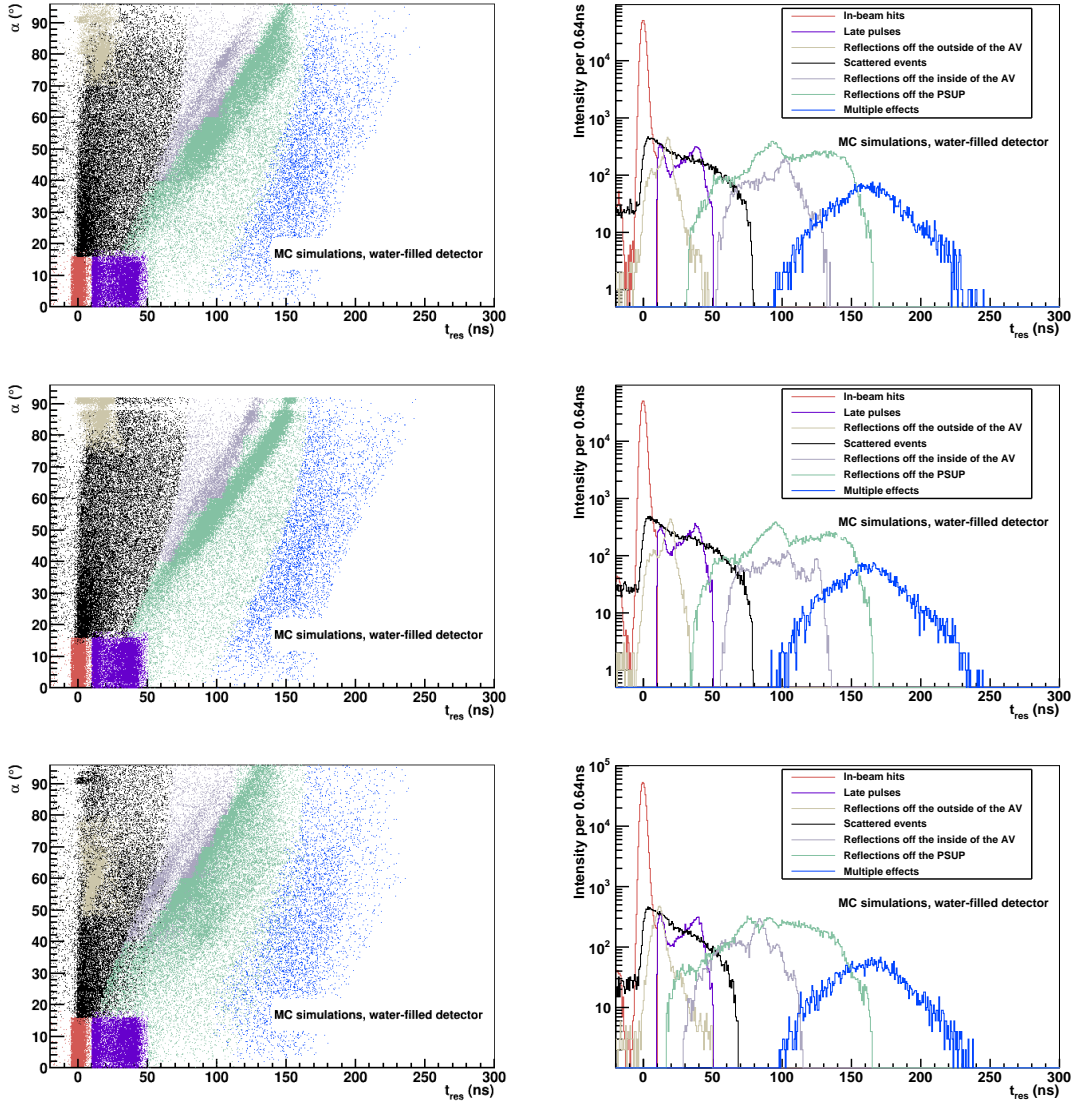


**Figure B.1:** Cut selection for the node 25 fibres at 407 nm. Shown are the  $\alpha$  vs  $t_{\text{res}}$  (left) and the  $t_{\text{res}}$  distributions (right) as defined in Equation 6.4 for FS125 (top), FS025 (middle) and FS225 (bottom).

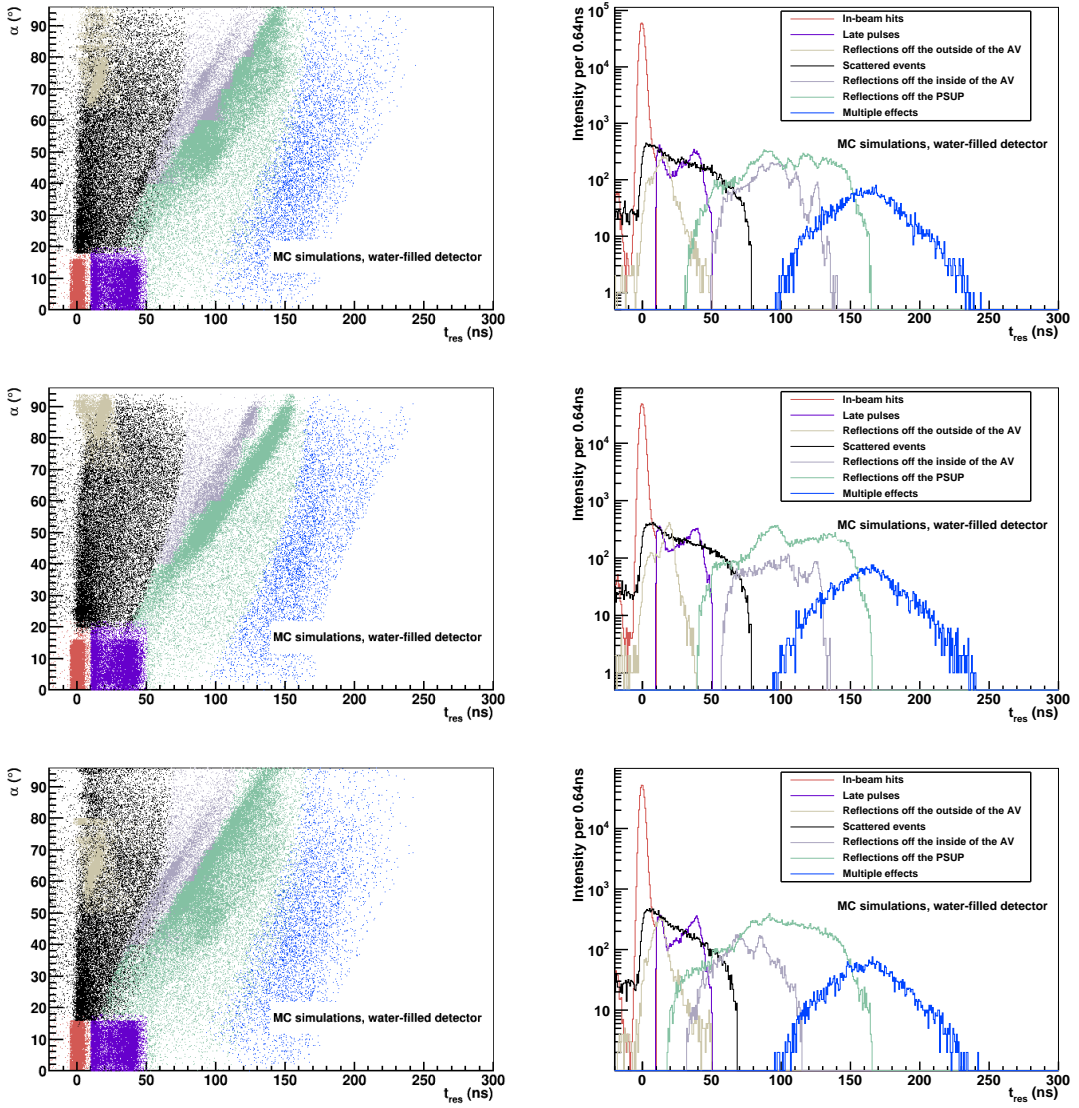


**Figure B.2:** Cut selection for the node 37 fibres at 407 nm. Shown are the  $\alpha$  vs  $t_{\text{res}}$  (left) and the  $t_{\text{res}}$  distributions (right) as defined in Equation 6.4 for FS037 (top), FS137 (middle) and FS237 (bottom).

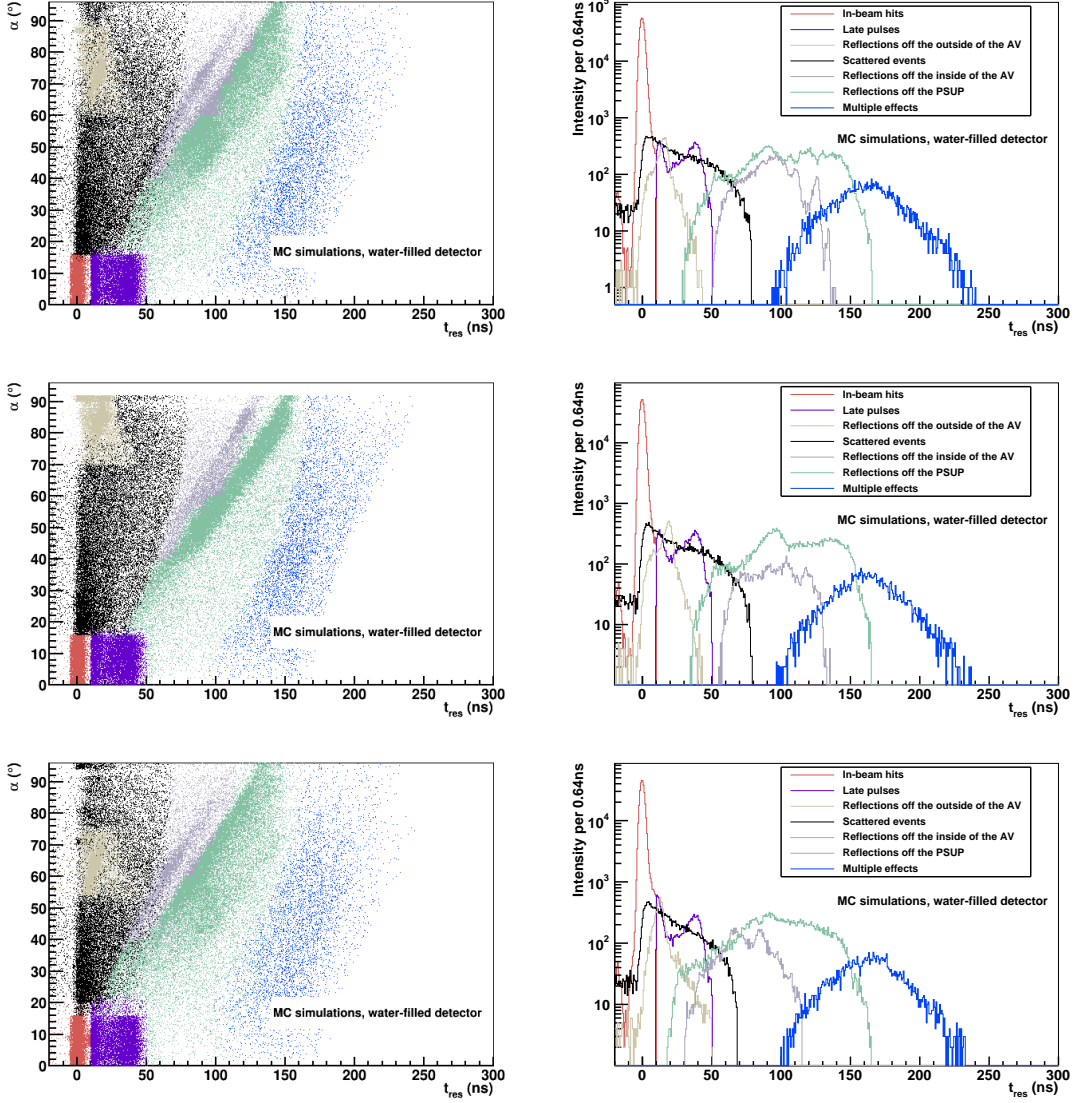


**Figure B.3:** Cut selection for the node 55 fibres at 407 nm. Shown are the  $\alpha$  vs  $t_{\text{res}}$  (left) and the  $t_{\text{res}}$  distributions (right) as defined in Equation 6.4 for FS055 (top), FS255 (middle) and FS155 (bottom).

## B.2 Evaluating the uncertainties on $c_{\text{scatt}}$ and $c_{\text{in-beam}}$

Based on the discussion in [138] for values where the numerator is a subset of the denominator, the statistical uncertainties on the measured  $c_i$  ( $i = \text{scatt}, \text{in-beam}$ )

were evaluated using a Binomial instead of a Poissonian approach. Therefore, with

$$c_i = \frac{N_i}{N_{\text{total}}} \quad (\text{B.6})$$

the uncertainty  $\Delta c_i$  is

$$\Delta c_i = \frac{1}{N_{\text{total}}} \cdot \sqrt{N_i \cdot \left(1 - \frac{N_i}{N_{\text{total}}}\right)} \quad (\text{B.7})$$

**Table B.1:** Measured intensity values in nppb from the fake data sets for each fibre-wavelength combination.

Fibre	375 nm	407 nm	446 nm	495 nm
FS007	939 ± 162	939 ± 154	936 ± 162	936 ± 208
FS107	944 ± 160	936 ± 152	940 ± 162	937 ± 195
FS207	939 ± 158	941 ± 153	939 ± 175	937 ± 191
FS025	941 ± 159	941 ± 155	935 ± 161	933 ± 195
FS125	943 ± 161	940 ± 155	940 ± 164	937 ± 197
FS225	941 ± 167	939 ± 152	937 ± 158	930 ± 199
FS037	940 ± 157	940 ± 149	938 ± 157	938 ± 192
FS137	938 ± 158	939 ± 150	937 ± 159	935 ± 191
FS237	939 ± 153	942 ± 148	935 ± 154	935 ± 188
FS055	935 ± 151	937 ± 147	936 ± 154	932 ± 185
FS155	943 ± 166	942 ± 156	939 ± 167	936 ± 203
FS255	943 ± 159	940 ± 153	940 ± 161	934 ± 195
average	941 ± 46	940 ± 44	938 ± 47	935 ± 56

**Table B.2:** The fit parameters from the  $c_{\text{scatt}}^{\text{sim}}$  vs  $s^{\text{sim}}$  fits, the ratios  $c_{\text{scatt}}^{\text{data}}$  from the fake data sets and the measured  $s_{\text{scatt}}^{\text{data}}$  for all fibre-wavelength combinations from the scattering region.

Fibre	Wavelength (nm)	$p0$	$p1$	$c_{\text{scatt}}^{\text{data}}$	$s_{\text{scatt}}^{\text{data}}$
FS007	375	$0.0610 \pm 0.0003$	$0.0307 \pm 0.0003$	$0.1125 \pm 0.0005$	$1.341 \pm 0.006$
	407	$0.0459 \pm 0.0002$	$0.0270 \pm 0.0002$	$0.0889 \pm 0.0005$	$1.349 \pm 0.006$
	446	$0.0331 \pm 0.0002$	$0.0287 \pm 0.0002$	$0.0732 \pm 0.0004$	$1.341 \pm 0.009$
	495	$0.0227 \pm 0.0003$	$0.0387 \pm 0.0003$	$0.0691 \pm 0.0005$	$1.35 \pm 0.02$
FS107	375	$0.0581 \pm 0.0002$	$0.0292 \pm 0.0003$	$0.1086 \pm 0.0005$	$1.369 \pm 0.006$
	407	$0.0441 \pm 0.0002$	$0.0256 \pm 0.0002$	$0.0838 \pm 0.0004$	$1.319 \pm 0.006$
	446	$0.0317 \pm 0.0002$	$0.0272 \pm 0.0002$	$0.0688 \pm 0.0004$	$1.312 \pm 0.009$
	495	$0.0212 \pm 0.0003$	$0.0373 \pm 0.0003$	$0.0657 \pm 0.0005$	$1.34 \pm 0.02$
FS207	375	$0.0524 \pm 0.0002$	$0.0267 \pm 0.0002$	$0.0968 \pm 0.0005$	$1.337 \pm 0.006$
	407	$0.0394 \pm 0.0002$	$0.0231 \pm 0.0002$	$0.0762 \pm 0.0004$	$1.347 \pm 0.007$
	446	$0.0286 \pm 0.0002$	$0.0243 \pm 0.0002$	$0.0628 \pm 0.0004$	$1.343 \pm 0.009$
	495	$0.0189 \pm 0.0002$	$0.0338 \pm 0.0003$	$0.0595 \pm 0.0005$	$1.36 \pm 0.02$
FS025	375	$0.0597 \pm 0.0003$	$0.0294 \pm 0.0003$	$0.1092 \pm 0.0005$	$1.337 \pm 0.006$
	407	$0.0446 \pm 0.0002$	$0.0265 \pm 0.0002$	$0.0864 \pm 0.0004$	$1.346 \pm 0.007$
	446	$0.0328 \pm 0.0002$	$0.0277 \pm 0.0002$	$0.0718 \pm 0.0004$	$1.346 \pm 0.009$
	495	$0.0221 \pm 0.0003$	$0.0382 \pm 0.0003$	$0.0675 \pm 0.0005$	$1.32 \pm 0.02$
FS125	375	$0.0579 \pm 0.0002$	$0.0291 \pm 0.0003$	$0.1073 \pm 0.0005$	$1.350 \pm 0.006$
	407	$0.0432 \pm 0.0002$	$0.0262 \pm 0.0002$	$0.0843 \pm 0.0004$	$1.346 \pm 0.007$
	446	$0.0312 \pm 0.0002$	$0.0276 \pm 0.0002$	$0.0696 \pm 0.0004$	$1.344 \pm 0.009$
	495	$0.0210 \pm 0.0003$	$0.0372 \pm 0.0003$	$0.0647 \pm 0.0005$	$1.31 \pm 0.02$
FS225	375	$0.0502 \pm 0.0002$	$0.0264 \pm 0.0002$	$0.0940 \pm 0.0005$	$1.347 \pm 0.006$
	407	$0.0377 \pm 0.0002$	$0.0233 \pm 0.0002$	$0.0737 \pm 0.0004$	$1.339 \pm 0.007$
	446	$0.0270 \pm 0.0002$	$0.0247 \pm 0.0002$	$0.0610 \pm 0.0004$	$1.35 \pm 0.01$
	495	$0.0176 \pm 0.0002$	$0.0339 \pm 0.0003$	$0.0580 \pm 0.0004$	$1.37 \pm 0.02$
FS037	375	$0.0507 \pm 0.0002$	$0.0247 \pm 0.0002$	$0.0928 \pm 0.0005$	$1.345 \pm 0.006$
	407	$0.0379 \pm 0.0002$	$0.0218 \pm 0.0002$	$0.0722 \pm 0.0004$	$1.331 \pm 0.006$
	446	$0.0272 \pm 0.0002$	$0.0234 \pm 0.0002$	$0.0589 \pm 0.0004$	$1.306 \pm 0.009$
	495	$0.0184 \pm 0.0002$	$0.0321 \pm 0.0002$	$0.0567 \pm 0.0004$	$1.34 \pm 0.02$
FS137	375	$0.0534 \pm 0.0002$	$0.0267 \pm 0.0002$	$0.0977 \pm 0.0005$	$1.329 \pm 0.006$
	407	$0.0403 \pm 0.0002$	$0.0237 \pm 0.0002$	$0.0774 \pm 0.0004$	$1.333 \pm 0.007$
	446	$0.0290 \pm 0.0002$	$0.0253 \pm 0.0002$	$0.0641 \pm 0.0004$	$1.339 \pm 0.009$
	495	$0.0195 \pm 0.0002$	$0.0348 \pm 0.0003$	$0.0609 \pm 0.0005$	$1.34 \pm 0.02$
FS237	375	$0.0533 \pm 0.0002$	$0.0256 \pm 0.0002$	$0.0967 \pm 0.0005$	$1.335 \pm 0.006$
	407	$0.0400 \pm 0.0002$	$0.0223 \pm 0.0002$	$0.0757 \pm 0.0004$	$1.333 \pm 0.007$
	446	$0.0288 \pm 0.0002$	$0.0239 \pm 0.0002$	$0.0620 \pm 0.0004$	$1.321 \pm 0.009$
	495	$0.0195 \pm 0.0002$	$0.0320 \pm 0.0003$	$0.0581 \pm 0.0004$	$1.34 \pm 0.02$
FS055	375	$0.0555 \pm 0.0002$	$0.0272 \pm 0.0002$	$0.1011 \pm 0.0005$	$1.333 \pm 0.006$
	407	$0.0414 \pm 0.0002$	$0.0245 \pm 0.0002$	$0.0803 \pm 0.0004$	$1.347 \pm 0.006$
	446	$0.0296 \pm 0.0002$	$0.0259 \pm 0.0002$	$0.0647 \pm 0.0004$	$1.311 \pm 0.009$
	495	$0.0200 \pm 0.0002$	$0.0345 \pm 0.0003$	$0.0608 \pm 0.0004$	$1.31 \pm 0.02$
FS155	375	$0.0555 \pm 0.0003$	$0.0293 \pm 0.0003$	$0.1039 \pm 0.0005$	$1.344 \pm 0.006$
	407	$0.0417 \pm 0.0002$	$0.0256 \pm 0.0002$	$0.0811 \pm 0.0005$	$1.333 \pm 0.007$
	446	$0.0303 \pm 0.0002$	$0.0269 \pm 0.0002$	$0.0679 \pm 0.0004$	$1.35 \pm 0.01$
	495	$0.0200 \pm 0.0003$	$0.0359 \pm 0.0003$	$0.0626 \pm 0.0005$	$1.33 \pm 0.02$
FS255	375	$0.0502 \pm 0.0002$	$0.0281 \pm 0.0002$	$0.1009 \pm 0.0005$	$1.334 \pm 0.006$
	407	$0.0412 \pm 0.0002$	$0.0253 \pm 0.0002$	$0.0810 \pm 0.0004$	$1.351 \pm 0.007$
	446	$0.0299 \pm 0.0002$	$0.0265 \pm 0.0002$	$0.0669 \pm 0.0004$	$1.354 \pm 0.009$
	495	$0.0197 \pm 0.0002$	$0.0360 \pm 0.0003$	$0.0622 \pm 0.0005$	$1.33 \pm 0.02$

**Table B.3:** The fit parameters from the  $c_{\text{in-beam}}^{\text{sim}}$  vs  $s^{\text{sim}}$  fits, the ratios  $c_{\text{in-beam}}^{\text{data}}$  from the fake data sets and the measured  $s_{\text{in-beam}}^{\text{data}}$  for all fibre-wavelength combinations from the in-beam region..

Fibre	Wavelength (nm)	$p0$	$p1$	$c_{\text{in-beam}}^{\text{data}}$	$s_{\text{in-beam}}^{\text{data}}$
FS007	375	$-0.082 \pm 0.001$	$0.846 \pm 0.001$	$0.737 \pm 0.002$	$1.34 \pm 0.03$
	407	$-0.062 \pm 0.001$	$0.848 \pm 0.001$	$0.764 \pm 0.002$	$1.36 \pm 0.03$
	446	$-0.044 \pm 0.001$	$0.844 \pm 0.001$	$0.784 \pm 0.002$	$1.35 \pm 0.05$
	495	$-0.030 \pm 0.001$	$0.831 \pm 0.002$	$0.791 \pm 0.002$	$1.34 \pm 0.09$
FS107	375	$-0.079 \pm 0.001$	$0.846 \pm 0.001$	$0.739 \pm 0.002$	$1.36 \pm 0.03$
	407	$-0.059 \pm 0.001$	$0.845 \pm 0.001$	$0.766 \pm 0.002$	$1.33 \pm 0.04$
	446	$-0.043 \pm 0.001$	$0.842 \pm 0.001$	$0.785 \pm 0.002$	$1.32 \pm 0.05$
	495	$-0.028 \pm 0.001$	$0.829 \pm 0.002$	$0.792 \pm 0.002$	$1.29 \pm 0.09$
FS207	375	$-0.069 \pm 0.001$	$0.842 \pm 0.001$	$0.750 \pm 0.002$	$1.35 \pm 0.03$
	407	$-0.051 \pm 0.001$	$0.842 \pm 0.001$	$0.772 \pm 0.002$	$1.35 \pm 0.04$
	446	$-0.037 \pm 0.001$	$0.837 \pm 0.001$	$0.788 \pm 0.002$	$1.34 \pm 0.06$
	495	$-0.024 \pm 0.001$	$0.824 \pm 0.001$	$0.791 \pm 0.002$	$1.4 \pm 0.1$
FS025	375	$-0.082 \pm 0.001$	$0.848 \pm 0.001$	$0.738 \pm 0.002$	$1.34 \pm 0.03$
	407	$-0.061 \pm 0.001$	$0.848 \pm 0.001$	$0.766 \pm 0.002$	$1.33 \pm 0.03$
	446	$-0.045 \pm 0.001$	$0.845 \pm 0.001$	$0.785 \pm 0.002$	$1.34 \pm 0.05$
	495	$-0.029 \pm 0.001$	$0.830 \pm 0.002$	$0.791 \pm 0.002$	$1.34 \pm 0.09$
FS125	375	$-0.079 \pm 0.001$	$0.844 \pm 0.001$	$0.738 \pm 0.002$	$1.34 \pm 0.03$
	407	$-0.059 \pm 0.001$	$0.844 \pm 0.001$	$0.763 \pm 0.002$	$1.35 \pm 0.04$
	446	$-0.043 \pm 0.001$	$0.840 \pm 0.001$	$0.783 \pm 0.002$	$1.34 \pm 0.05$
	495	$-0.028 \pm 0.001$	$0.828 \pm 0.002$	$0.789 \pm 0.002$	$1.4 \pm 0.1$
FS225	375	$-0.068 \pm 0.001$	$0.843 \pm 0.001$	$0.751 \pm 0.002$	$1.35 \pm 0.03$
	407	$-0.051 \pm 0.001$	$0.843 \pm 0.001$	$0.775 \pm 0.002$	$1.33 \pm 0.04$
	446	$-0.036 \pm 0.001$	$0.837 \pm 0.001$	$0.789 \pm 0.002$	$1.35 \pm 0.06$
	495	$-0.024 \pm 0.001$	$0.825 \pm 0.001$	$0.792 \pm 0.002$	$1.4 \pm 0.1$
FS037	375	$-0.071 \pm 0.001$	$0.865 \pm 0.001$	$0.769 \pm 0.002$	$1.35 \pm 0.03$
	407	$-0.052 \pm 0.001$	$0.865 \pm 0.001$	$0.794 \pm 0.002$	$1.34 \pm 0.04$
	446	$-0.037 \pm 0.001$	$0.860 \pm 0.001$	$0.811 \pm 0.002$	$1.33 \pm 0.06$
	495	$-0.025 \pm 0.001$	$0.846 \pm 0.001$	$0.813 \pm 0.002$	$1.4 \pm 0.1$
FS137	375	$-0.077 \pm 0.001$	$0.856 \pm 0.001$	$0.752 \pm 0.002$	$1.34 \pm 0.03$
	407	$-0.059 \pm 0.001$	$0.857 \pm 0.001$	$0.778 \pm 0.002$	$1.34 \pm 0.04$
	446	$-0.042 \pm 0.001$	$0.852 \pm 0.001$	$0.796 \pm 0.002$	$1.34 \pm 0.05$
	495	$-0.028 \pm 0.001$	$0.839 \pm 0.002$	$0.800 \pm 0.002$	$1.38 \pm 0.10$
FS237	375	$-0.075 \pm 0.001$	$0.848 \pm 0.001$	$0.747 \pm 0.002$	$1.34 \pm 0.03$
	407	$-0.056 \pm 0.001$	$0.848 \pm 0.001$	$0.773 \pm 0.002$	$1.34 \pm 0.04$
	446	$-0.040 \pm 0.001$	$0.843 \pm 0.001$	$0.789 \pm 0.002$	$1.34 \pm 0.06$
	495	$-0.026 \pm 0.001$	$0.831 \pm 0.001$	$0.796 \pm 0.002$	$1.3 \pm 0.1$
FS055	375	$-0.075 \pm 0.001$	$0.852 \pm 0.001$	$0.752 \pm 0.002$	$1.34 \pm 0.03$
	407	$-0.055 \pm 0.001$	$0.851 \pm 0.001$	$0.776 \pm 0.002$	$1.34 \pm 0.04$
	446	$-0.039 \pm 0.001$	$0.846 \pm 0.001$	$0.795 \pm 0.002$	$1.33 \pm 0.06$
	495	$-0.027 \pm 0.001$	$0.835 \pm 0.001$	$0.800 \pm 0.002$	$1.3 \pm 0.1$
FS155	375	$-0.080 \pm 0.001$	$0.833 \pm 0.001$	$0.726 \pm 0.002$	$1.33 \pm 0.03$
	407	$-0.060 \pm 0.001$	$0.832 \pm 0.001$	$0.751 \pm 0.002$	$1.35 \pm 0.04$
	446	$-0.043 \pm 0.001$	$0.828 \pm 0.001$	$0.769 \pm 0.002$	$1.37 \pm 0.05$
	495	$-0.028 \pm 0.001$	$0.815 \pm 0.002$	$0.777 \pm 0.002$	$1.3 \pm 0.1$
FS255	375	$-0.082 \pm 0.001$	$0.846 \pm 0.001$	$0.737 \pm 0.002$	$1.34 \pm 0.03$
	407	$-0.061 \pm 0.001$	$0.845 \pm 0.001$	$0.763 \pm 0.002$	$1.35 \pm 0.04$
	446	$-0.043 \pm 0.001$	$0.842 \pm 0.001$	$0.783 \pm 0.002$	$1.37 \pm 0.05$
	495	$-0.029 \pm 0.001$	$0.830 \pm 0.002$	$0.793 \pm 0.002$	$1.27 \pm 0.09$

**Table B.4:** Fibre directions for the node 07 and 25 fibres.

Fibre	$\vec{r}$
FS007	$\begin{pmatrix} 0.8555 \pm 0.0214 \\ -0.2790 \pm 0.0428 \\ -0.4363 \pm 0.0391 \end{pmatrix}$
FS107	$\begin{pmatrix} 0.8540 \pm 0.0200 \\ -0.1096 \pm 0.0468 \\ -0.5086 \pm 0.0332 \end{pmatrix}$
FS207	$\begin{pmatrix} 0.7767 \pm 0.0237 \\ -0.5718 \pm 0.0284 \\ -0.2641 \pm 0.0515 \end{pmatrix}$
FS025	$\begin{pmatrix} -0.8523 \pm 0.0214 \\ -0.2859 \pm 0.0411 \\ -0.4380 \pm 0.0391 \end{pmatrix}$
FS125	$\begin{pmatrix} -0.7569 \pm 0.0254 \\ -0.4026 \pm 0.0377 \\ -0.5148 \pm 0.0338 \end{pmatrix}$
FS225	$\begin{pmatrix} -0.9645 \pm 0.0136 \\ 0.0087 \pm 0.0430 \\ -0.2638 \pm 0.0499 \end{pmatrix}$

# C Appendix - Background Evaluation

## C.1 Pure Scintillator Phase

**Table C.1:** Internal backgrounds for the pure scintillator phase, including the target rates from [92] and the subsequent event yield expected in 181 days.

Isotope	rate (Hz)	Events in 181 days
$^{228}\text{Ac}$	0.0000216	338
$^{39}\text{Ar}$	0.0027106	42 390
$^{210}\text{Bi}$	0.0013531	21 160
$^{212}\text{Bi}$	0.0000216	338
$^{214}\text{Bi}$	0.0001553	2 429
$^{14}\text{C}$	129.3759513	$2.02 \times 10^9$
$^{40}\text{K}$	0.0002689	4 205
$^{234m}\text{Pa}$	0.0001553	2 429
$^{210}\text{Pb}$	0.0013531	21 160
$^{212}\text{Pb}$	0.0000216	338
$^{214}\text{Pb}$	0.0001553	2 429
$^{210}\text{Po}$	0.5390664	$8.4 \times 10^6$
$^{212}\text{Po}$	0.0000138	216
$^{214}\text{Po}$	0.0001553	2 429
$^{216}\text{Po}$	0.0000216	338
$^{218}\text{Po}$	0.0001553	2 429
$^{224}\text{Ra}$	0.0000216	338
$^{226}\text{Ra}$	0.0001553	2 429
$^{228}\text{Ra}$	0.0000216	338
$^{220}\text{Rn}$	0.0000216	338
$^{222}\text{Rn}$	0.0001553	2 429
$^{228}\text{Th}$	0.0000216	338
$^{230}\text{Th}$	0.0001553	2 429
$^{232}\text{Th}$	0.0000216	338
$^{234}\text{Th}$	0.0001553	2 429
$^{208}\text{Tl}$	0.0000078	122
$^{210}\text{Tl}$	$3.2 \times 10^{-8}$	0
$^{234}\text{U}$	0.0001553	2 429
$^{238}\text{U}$	0.0001553	2 429

**Table C.2:** Pure scintillator RAT 4.5.0 Monte Carlo production files. All listed files were merged from all available runs for the isotope in question for the 4.5.0 production.

File name	Events in files	Events in fiducial volume
Ac228.ntuple.root	100 074	36 163
Ar39.ntuple.root	100 002	35 241
Bi210.ntuple.root	100 007	34 842
Bi212.ntuple.root	103 757	37 997
Bi214.ntuple.root	101 488	34 804
C14.ntuple.root	4 080 054	577 138
K40.ntuple.root	80 018	29 594
Pa234m.ntuple.root	100 034	36 875
Pb210.ntuple.root	100 000	7 317
Pb212.ntuple.root	100 002	40 126
Pb214.ntuple.root	100 005	40 800
Po210.ntuple.root	1 707 650	679 903
Po212.ntuple.root	157 684	43 641
Po214.ntuple.root	142 492	43 202
Po216.ntuple.root	124 170	42 602
Po218.ntuple.root	109 289	42 035
Ra224.ntuple.root	105 126	41 657
Ra226.ntuple.root	100 795	41 626
Ra228.ntuple.root	100 000	426
Rn220.ntuple.root	114 161	42 268
Rn222.ntuple.root	103 448	40 717
Th228.ntuple.root	102 953	41 889
Th230.ntuple.root	100 472	41 805
Th232.ntuple.root	100 125	40 832
Th234.ntuple.root	100 001	19 783
Tl208.ntuple.root	114 584	37 515
Tl210.ntuple.root	106 453	36 354
U234.ntuple.root	100 614	41 770
U238.ntuple.root	100 156	40 777
PEP.ntuple.root	100 009	38 827
Be7.ntuple.root	100 002	37 701
B8.ntuple.root	11 096	3 881
CNO.ntuple.root	100 003	33 560

**Table C.3:** Bi-Po coincidence cut selection on RAT 4.5.0 Monte Carlo production files. The files were merged from all available runs for the isotope in question for the 4.5.0 production. The row denoted “all” is a count of all events in the file, so a sum of all  $^{21x}\text{Bi}$  and  $^{21x}\text{Po}$  decays. Hence, to get the number of coincidence decays contained in the file, this number needs to be divided by 2. These numbers were used to determine  $\epsilon(\Delta r)$  and  $\epsilon^{\text{Bi}}(r_{fidvol})$ .

Cut	Bi212Po212.ntuple.root	Bi214Po214.ntuple.root
all	178 347	228 797
$r_{fidvol}$	87 028	95 010
$n_{\text{hits}}^{\text{Po}}$	14 426	32 710
$\Delta t$	9 779	30 459
$r_{fidvol}$ on Bi	8 909	26 690
$\Delta r$	7 216	20 979
$n_{\text{hits}}^{\text{Bi}}$	6 878	19 313

**Table C.4:** Measurement uncertainty ( $\frac{\Delta N_{\text{Bi}^{21x}\text{Po}^{21x}}}{N_{\text{Bi}^{21x}\text{Po}^{21x}}}$ ) on the  $^{212}\text{Bi}^{212}\text{Po}$  and  $^{214}\text{Bi}^{214}\text{Po}$  coincidences over time. These numbers are based on the rates in Table C.1. The effect of mistagged events is not included.

Measurement duration	$^{212}\text{Bi}^{212}\text{Po}$	$^{214}\text{Bi}^{214}\text{Po}$
31 days	60.00 %	12.15 %
59 days	43.51 %	8.86 %
90 days	35.25 %	7.21 %
120 days	30.54 %	6.29 %
151 days	27.24 %	5.64 %
181 days	24.88 %	5.18 %
365 days	17.58 %	3.77 %

**Table C.5:** Polonium cut efficiencies  $\epsilon^i$  ( $n_{\text{nhits}}$ ) for the Bi-Po coincidence measurements.

Isotope	$\epsilon^{\text{Po}214}$ ( $n_{\text{nhits}}$ )	$\epsilon^{\text{Po}212}$ ( $n_{\text{nhits}}$ )
$^{228}\text{Ac}$	$(9.6 \pm 0.2) \times 10^{-2}$	$0.174 \pm 0.002$
$^{39}\text{Ar}$	$(1.6 \pm 0.2) \times 10^{-3}$	0
$^{210}\text{Bi}$	$0.135 \pm 0.002$	$(1.66 \pm 0.07) \times 10^{-2}$
$^{212}\text{Bi}$	$0.304 \pm 0.003$	$(9.0 \pm 0.2) \times 10^{-2}$
$^{214}\text{Bi}$	$(3.8 \pm 0.1) \times 10^{-2}$	$(3.3 \pm 0.1) \times 10^{-2}$
$^{14}\text{C}$	0	0
$^{40}\text{K}$	$0.272 \pm 0.003$	$0.136 \pm 0.002$
$^{234m}\text{Pa}$	$0.224 \pm 0.003$	$0.144 \pm 0.002$
$^{210}\text{Pb}$	0	0
$^{212}\text{Pb}$	$(1.0 \pm 0.2) \times 10^{-3}$	0
$^{214}\text{Pb}$	$0.274 \pm 0.003$	$(2.11 \pm 0.07) \times 10^{-2}$
$^{210}\text{Po}$	$(7 \pm 1) \times 10^{-5}$	$(3 \pm 2) \times 10^{-6}$
$^{212}\text{Po}$	$0.228 \pm 0.003$	$0.767 \pm 0.006$
$^{214}\text{Po}$	$0.946 \pm 0.007$	$(7.4 \pm 0.4) \times 10^{-3}$
$^{216}\text{Po}$	$0.816 \pm 0.006$	0
$^{218}\text{Po}$	$0.152 \pm 0.002$	0
$^{224}\text{Ra}$	$(5.0 \pm 0.1) \times 10^{-2}$	$(1.4 \pm 0.6) \times 10^{-4}$
$^{226}\text{Ra}$	$(8.0 \pm 0.4) \times 10^{-3}$	$(2.4 \pm 2.4) \times 10^{-5}$
$^{228}\text{Ra}$	0	0
$^{220}\text{Rn}$	$0.470 \pm 0.004$	$(8 \pm 1) \times 10^{-4}$
$^{222}\text{Rn}$	$(1.6 \pm 0.2) \times 10^{-3}$	$(2.5 \pm 0.8) \times 10^{-4}$
$^{228}\text{Th}$	$(1.99 \pm 0.07) \times 10^{-2}$	0
$^{230}\text{Th}$	0	0
$^{232}\text{Th}$	0	0
$^{234}\text{Th}$	0	0
$^{208}\text{Tl}$	$(9.7 \pm 0.5) \times 10^{-3}$	$(7.2 \pm 0.4) \times 10^{-3}$
$^{210}\text{Tl}$	$(6.3 \pm 0.4) \times 10^{-3}$	$(1, 10 \pm 0.06) \times 10^{-2}$
$^{234}\text{U}$	0	0
$^{238}\text{U}$	0	0
PEP	$0.250 \pm 0.003$	$0.158 \pm 0.002$
$^7\text{Be}$	$0.116 \pm 0.002$	0
$^8\text{B}$	$(6.8 \pm 0.4) \times 10^{-2}$	$(4.8 \pm 0.4) \times 10^{-2}$
CNO	$(8.8 \pm 0.2) \times 10^{-2}$	$(3.2 \pm 0.3) \times 10^{-3}$

**Table C.6:** Bismuth cut efficiencies  $\epsilon^i$  ( $n_{\text{nhits}}$ ) for the Bi-Po coincidence measurements.

Isotope	$\epsilon^{\text{Bi}214}$ ( $n_{\text{nhits}}$ )	$\epsilon^{\text{Bi}212}$ ( $n_{\text{nhits}}$ )
$^{228}\text{Ac}$	$0.590 \pm 0.005$	$0.985 \pm 0.007$
$^{39}\text{Ar}$	0	$0.594 \pm 0.005$
$^{210}\text{Bi}$	$(1.1 \pm 0.6) \times 10^{-4}$	$0.684 \pm 0.006$
$^{212}\text{Bi}$	$0.174 \pm 0.002$	$0.956 \pm 0.007$
$^{214}\text{Bi}$	$0.869 \pm 0.007$	$0.988 \pm 0.008$
$^{14}\text{C}$	0	$(5 \pm 1) \times 10^{-5}$
$^{40}\text{K}$	$0.102 \pm 0.002$	$0.905 \pm 0.008$
$^{234m}\text{Pa}$	$0.195 \pm 0.003$	$0.902 \pm 0.007$
$^{210}\text{Pb}$	0	0
$^{212}\text{Pb}$	0	$0.915 \pm 0.007$
$^{214}\text{Pb}$	0	$0.966 \pm 0.007$
$^{210}\text{Po}$	0	$0.997 \pm 0.002$
$^{212}\text{Po}$	$(2 \pm 2) \times 10^{-5}$	$0.997 \pm 0.007$
$^{214}\text{Po}$	$(7 \pm 4) \times 10^{-5}$	$0.997 \pm 0.007$
$^{216}\text{Po}$	$(2 \pm 2) \times 10^{-5}$	$0.997 \pm 0.007$
$^{218}\text{Po}$	0	$0.997 \pm 0.007$
$^{224}\text{Ra}$	0	$0.997 \pm 0.007$
$^{226}\text{Ra}$	0	$0.997 \pm 0.007$
$^{228}\text{Ra}$	0	0
$^{220}\text{Rn}$	0	$0.997 \pm 0.007$
$^{222}\text{Rn}$	0	$0.997 \pm 0.007$
$^{228}\text{Th}$	0	$0.997 \pm 0.007$
$^{230}\text{Th}$	0	$0.997 \pm 0.007$
$^{232}\text{Th}$	0	$0.989 \pm 0.007$
$^{234}\text{Th}$	0	$(4.0 \pm 0.5) \times 10^{-3}$
$^{208}\text{Tl}$	$0.968 \pm 0.007$	$0.995 \pm 0.007$
$^{210}\text{Tl}$	$0.968 \pm 0.007$	$0.996 \pm 0.007$
$^{234}\text{U}$	0	$0.997 \pm 0.007$
$^{238}\text{U}$	0	$0.995 \pm 0.007$
PEP	$(4.1 \pm 0.1) \times 10^{-2}$	$0.861 \pm 0.006$
$^7\text{Be}$	0	$0.699 \pm 0.006$
$^8\text{B}$	$0.76 \pm 0.02$	$(9.7 \pm 0.2) \times 10^{-2}$
CNO	$(1.5 \pm 0.7) \times 10^{-4}$	$0.622 \pm 0.005$

**Table C.7:** Number of mistagged events  $N_{\text{mis}}^{\text{coinc}}$  for the  $^{212}\text{Bi}^{212}\text{Po}$  and  $^{214}\text{Bi}^{214}\text{Po}$  coincidence measurements expected in 181 days at different rate scenarios based on the rates in Table C.1 and the leaching rates as calculated in Chapter 8.

Scenario	$^{212}\text{Bi}^{212}\text{Po}$	$^{214}\text{Bi}^{214}\text{Po}$
expected rates	9.94	3.11
$10 \times$ solar rates	9.96	3.89
$10 \times$ Th chain rates	9.94	3.32
$10 \times$ U chain rates	9.95	3.38
$10 \times$ leaching rates	993.44	282.64
$10 \times$ rates of other backgrounds	9.97	3.35

## C.2 Statistical Uncertainties on $^{21x}\text{Bi}^{21x}\text{Po}$ coincidence Measurements

Applying the cut selection to a data sample, the measured value is  $N_{\text{Bi}^{21x}\text{Po}^{21x}}^{\text{allcuts}}$  (as shown in Equation 7.10), with a statistical uncertainty of

$$\Delta N_{\text{Bi}^{21x}\text{Po}^{21x}}^{\text{allcuts}} = \sqrt{N_{\text{Bi}^{21x}\text{Po}^{21x}}^{\text{allcuts}}} \quad (\text{C.1})$$

The statistical uncertainty of  $\epsilon$  arises from Gaussian error propagation using the statistical uncertainties on all efficiency values determined using Monte Carlo simulations:

$$\begin{aligned} \Delta\epsilon = & \left( \frac{r_{\text{fidvol}}}{r_{AV}} \right)^3 \cdot \epsilon(\Delta t) \cdot \sqrt{ \left( \Delta\epsilon^{\text{Po}21x}(n_{\text{hits}}) \cdot \epsilon(\Delta r) \cdot \epsilon^{\text{Bi}21x}(r_{\text{fidvol}}) \cdot \epsilon^{\text{Bi}21x}(n_{\text{hits}}) \right)^2 \\ & + \left( \epsilon^{\text{Po}21x}(n_{\text{hits}}) \cdot \Delta\epsilon(\Delta r) \cdot \epsilon^{\text{Bi}21x}(r_{\text{fidvol}}) \cdot \epsilon^{\text{Bi}21x}(n_{\text{hits}}) \right)^2 \\ & + \left( \epsilon^{\text{Po}21x}(n_{\text{hits}}) \cdot \epsilon(\Delta r) \cdot \Delta\epsilon^{\text{Bi}21x}(r_{\text{fidvol}}) \cdot \epsilon^{\text{Bi}21x}(n_{\text{hits}}) \right)^2 \\ & + \left( \epsilon^{\text{Po}21x}(n_{\text{hits}}) \cdot \epsilon(\Delta r) \cdot \epsilon^{\text{Bi}21x}(r_{\text{fidvol}}) \cdot \Delta\epsilon^{\text{Bi}21x}(n_{\text{hits}}) \right)^2 } \end{aligned} \quad (\text{C.2})$$

Combining Equations C.1 and C.2 leads to an uncertainty for the measurement of the  $^{21x}\text{Bi}^{21x}\text{Po}$  coincidence abundance of

$$\Delta N_{\text{Bi}^{21x}\text{Po}^{21x}} = \sqrt{\left(\frac{\Delta N_{\text{Bi}^{21x}\text{Po}^{21x}}^{\text{all cuts}}}{\epsilon}\right)^2 + \left(\frac{N_{\text{Bi}^{21x}\text{Po}^{21x}}^{\text{all cuts}}}{\epsilon^2} \Delta \epsilon\right)^2} \quad (\text{C.3})$$

### C.3 Statistical Uncertainties on Mistagged events

The uncertainty  $\Delta N_{\text{mis}}^{\text{coinc}}$  as described in Equation 7.17 on the mistagging evaluation follows from the uncertainty propagation

$$\begin{aligned} \Delta N_{\text{mis}}^{\text{coinc}} = & \sqrt{(\Delta N_{\text{true}}^{\text{Po}} \cdot P_{\text{mis}}^{\text{Bi}})^2 + (N_{\text{true}}^{\text{Po}} \cdot \Delta P_{\text{mis}}^{\text{Bi}})^2} \\ & + (\Delta N_{\text{mis}}^{\text{Po}} \cdot P_{\text{true}}^{\text{Bi}})^2 + (N_{\text{mis}}^{\text{Po}} \cdot \Delta P_{\text{true}}^{\text{Bi}})^2 \\ & + (\Delta N_{\text{mis}}^{\text{Po}} \cdot P_{\text{mis}}^{\text{Bi}})^2 + (N_{\text{mis}}^{\text{Po}} \cdot \Delta P_{\text{mis}}^{\text{Bi}})^2 \end{aligned} \quad (\text{C.4})$$

Since

$$N_{\text{mis}}^{\text{Po}} = \sum_i^{\text{all isotopes}} N^i \quad (\text{C.5})$$

and

$$N^i = N_{\text{full}}^i \cdot \epsilon^i (n_{\text{hits}}) \quad (\text{C.6})$$

$$\Delta N_{\text{mis}}^{\text{Po}} = \sqrt{\sum_i^{\text{all isotopes}} \left( (N_{\text{fidvol}}^i \cdot \Delta \epsilon^i (n_{\text{hits}}))^2 + (\Delta N_{\text{fidvol}}^i \cdot \epsilon^i (n_{\text{hits}}))^2 \right)}, \quad (\text{C.7})$$

with  $\Delta N_{\text{fidvol}}^i = \sqrt{N_{\text{fidvol}}^i}$ . The uncertainty on  $P_{\text{mis}}^{\text{Bi}}$  can be evaluated using

$$\Delta P_{\text{mis}}^{\text{Bi}} = \Delta t \cdot \Delta r \cdot e^{-R_{\text{bckg}} \cdot \Delta t \cdot \Delta r} \cdot \Delta R_{\text{bckg}} \quad (\text{C.8})$$

with

$$\Delta R_{\text{bckg}} = \sqrt{\sum_i^{\text{all isotopes}} (R^i \Delta \epsilon^i (n_{\text{hits}}))^2} \quad (\text{C.9})$$

All  $n_{\text{hits}}$  cut efficiencies and their respective uncertainty are listed in Tables C.5 and C.6 for each isotope.

## C.4 Tellurium Loaded Phase

**Table C.8:** Tellurium loaded scintillator RAT 5.0.2 Monte Carlo production files. All listed files were merged from all available runs for the isotope in question for the 5.0.2 production.

File name	Events in files	Events in fiducial volume
TeLoadedAlphan.ntuple.root	14 292 899	123 797
TeLoadedBi210.ntuple.root	20 714 589	4 371 742
TeLoadedBi212.ntuple.root	40 003	11 249
TeLoadedBi214.ntuple.root	36 482	10 457
TeLoadedC14.ntuple.root	7 796 795	105 326
TeLoadedPo210.ntuple.root	120 003	34 829
TeLoadedPo212.ntuple.root	70 006	20 394
TeLoadedPo214.ntuple.root	60 005	17 548
TeLoaded0n2b.ntuple.root	973 292	285 513
TeLoaded2n2b.ntuple.root	7 771 884	2 242 539
TeLoadedExternals.ntuple.root	12 478 006	1 850

**Table C.9:** Bi-Po coincidence cut selection on RAT 5.0.2 Monte Carlo production files. The files were merged from all available runs for the isotope in question for the 5.0.2 production. The row denoted “all” is a count of all events in the file, so a sum of all  $^{21x}\text{Bi}$  and  $^{21x}\text{Po}$  decays. Hence, to get the number of coincidence decays contained in the file, this number needs to be divided by 2. These numbers were used to determine  $\epsilon(\Delta r)$  and  $\epsilon^{\text{Bi}}(r_{fidvol})$ .

Cut	TeLoadedBi212Po212.ntuple.root	TeLoadedBi214Po214.ntuple.root
all	789 538	13 368 984
$r_{fidvol}$	254 487	3 973 160
$n_{\text{hits}}^{\text{Po}}$	132 368	2 059 365
$\Delta t$	53 957	1 833 289
$r_{fidvol}$ on Bi	48 662	1 722 182
$\Delta r$	48 278	1 721 579
$n_{\text{hits}}^{\text{Bi}}$	42 315	1 429 244

**Table C.10:** Polonium cut efficiencies  $\epsilon^i$  ( $n_{\text{nhits}}$ ) for the Bi-Po coincidence measurements for selected backgrounds during the Tellurium loaded phase.

Isotope	$\epsilon^{\text{Po}214}$ ( $n_{\text{nhits}}$ )	$\epsilon^{\text{Po}212}$ ( $n_{\text{nhits}}$ )
$(\alpha, n)$	$0.400 \pm 0.002$	$0.474 \pm 0.002$
$^{210}\text{Bi}$	$(7.30 \pm 0.01) \times 10^{-2}$	$(1.12 \pm 0.01) \times 10^{-2}$
$^{212}\text{Bi}$	$0.354 \pm 0.007$	$0.27 \pm 0.01$
$^{214}\text{Bi}$	$0.093 \pm 0.003$	$0.188 \pm 0.005$
$^{14}\text{C}$	0	0
$^{210}\text{Po}$	$(4 \pm 1) \times 10^{-4}$	0
$^{212}\text{Po}$	$1.00 \pm 0.01$	$0.907 \pm 0.009$
$^{214}\text{Po}$	$0.96 \pm 0.01$	$0.301 \pm 0.004$
$0\nu\beta\beta$	0	0
$2\nu\beta\beta$	$0.545 \pm 0.001$	$0.411 \pm 0.001$
Externals	$0.015 \pm 0.003$	$0.012 \pm 0.003$

**Table C.11:** Bismuth cut efficiencies  $\epsilon^i$  ( $n_{\text{nhits}}$ ) for the Bi-Po coincidence measurements for selected backgrounds during the Tellurium loaded phase.

Isotope	$\epsilon^{\text{Bi}214}$ ( $n_{\text{nhits}}$ )	$\epsilon^{\text{Bi}212}$ ( $n_{\text{nhits}}$ )
$(\alpha, n)$	$0.380 \pm 0.002$	$0.620 \pm 0.003$
$^{210}\text{Bi}$	0	$0.9999 \pm 0.0007$
$^{212}\text{Bi}$	$0.076 \pm 0.003$	$0.92 \pm 0.01$
$^{214}\text{Bi}$	$0.83 \pm 0.01$	$0.172 \pm 0.004$
$^{14}\text{C}$	0	$0.996 \pm 0.004$
$^{210}\text{Po}$	0	$1.000 \pm 0.008$
$^{212}\text{Po}$	0	$1.00 \pm 0.01$
$^{214}\text{Po}$	0	$1.00 \pm 0.01$
$0\nu\beta\beta$	$0.999 \pm 0.002$	$(8.0 \pm 0.5) \times 10^{-4}$
$2\nu\beta\beta$	$0.0541 \pm 0.0002$	$0.76 \pm 0.03$
Externals	$0.020 \pm 0.003$	$0.774 \pm 0.003$

# D Appendix - Partial-fill Background Estimation

**Table D.1:** Volume and Area covered by the scintillator volume per day during the partial-fill period for the first 45 fill days. Due to the detector symmetry, the area covered for the remaining fill days followed from the full sphere area of the AV and the numbers listed in this Table (e.g  $A_{46} = A_{\text{full}} - A_{45}$ ,  $A_{47} = A_{\text{full}} - A_{44}$  and so on). The remaining volumes can be achieved using Equation 8.2.

Day $k$	$A_{\text{partial},k}$ [m $^2$ ]	$V_{\text{partial},k}$ [m $^3$ ]
1	21.54	9.93
2	32.52	19.86
3	42.10	29.79
4	48.75	39.72
5	57.49	49.65
6	64.27	59.58
7	70.60	69.51
8	76.59	79.44
9	82.33	89.37
10	87.83	99.3
11	93.09	109.23
12	98.21	119.16
13	103.14	129.09
14	107.97	139.02
15	113.26	148.95
16	117.19	158.88
17	121.62	168.81
18	125.99	178.74
19	130.26	188.67
20	134.46	198.6
21	138.58	208.53
22	142.63	218.46
23	146.61	228.39
24	150.55	238.32
25	154.40	248.25
26	158.23	258.18
27	161.98	268.11
28	165.71	278.04
29	169.39	287.97
30	173.03	297.9
31	176.63	307.83
32	180.18	317.76
33	183.71	327.69
34	187.20	337.62
35	190.70	347.55
36	194.09	357.48
37	197.55	367.41
38	200.96	377.34
39	204.34	387.27
40	207.70	397.2
41	211.07	407.13
42	214.41	417.06
43	217.72	426.99
44	221.03	436.92
45	224.35	446.85

**Table D.2:** Fill levels  $z_k$  used for the RAT 5.3.1 partial-fill production.

Day	$k$	$z_k$ (mm)	Day	$k$	$z_k$ (mm)
	1	4392		46	-47
	2	3943		47	-94
	3	3636		48	-142
	4	3364		49	-190
	5	3174		50	-240
	6	2988		51	-291
	7	2822		52	-342
	8	2670		53	-394
	9	2531		54	-448
	10	2401		55	-503
	11	2279		56	-559
	12	2165		57	-616
	13	2057		58	-674
	14	1954		59	-734
	15	1862		60	-795
	16	1762		61	-857
	17	1672		62	-921
	18	1585		63	-987
	19	1502		64	-1054
	20	1421		65	-1124
	21	1343		66	-1195
	22	1268		67	-1268
	23	1195		68	-1343
	24	1124		69	-1421
	25	1054		70	-1502
	26	987		71	-1585
	27	921		72	-1672
	28	857		73	-1762
	29	795		74	-1862
	30	734		75	-1954
	31	674		76	-2057
	32	616		77	-2165
	33	559		78	-2279
	34	503		79	-2401
	35	448		80	-2531
	36	394		81	-2670
	37	342		82	-2822
	38	291		83	-2988
	39	240		84	-3174
	40	190		85	-3364
	41	142		86	-3636
	42	94		87	-3943
	43	47		88	-4392
	44	1		89	-4928
	45	-1		90	-5464

**Table D.3:** Internal backgrounds for the pure water phase.

Isotope	rate (Hz)
$^{228}\text{Ac}$	0.0128425
$^{210}\text{Bi}$	0.3932014
$^{212}\text{Bi}$	0.0128425
$^{214}\text{Bi}$	0.3932014
$^{40}\text{K}$	0.0856164
$^{234m}\text{Pa}$	0.3932014
$^{210}\text{Pb}$	0.3932014
$^{212}\text{Pb}$	0.0128425
$^{214}\text{Pb}$	0.3932014
$^{228}\text{Ra}$	0.0128425
$^{234}\text{Th}$	0.3932014
$^{208}\text{Tl}$	0.00462960
$^{210}\text{Tl}$	$(8.2763 \times 10^{-5})$

**Table D.4:** Partial-fill RAT 5.3.1 Monte Carlo production files for events simulated in the scintillator volume. All listed files were merged from all available runs/fill-levels for the isotope in question for the 5.3.1 production.

File name	Events in files	Events in fiducial volume
Ac228_Scint.ntuple.root	10 805	3 140
Ar39_Scint.ntuple.root	921 270	280 813
Bi210_Scint.ntuple.root	637 987	191 865
Bi212_Scint.ntuple.root	11 346	3 340
Bi214_Scint.ntuple.root	62 248	18 476
C14_Scint.ntuple.root	2 589 339	856 861
K40_Scint.ntuple.root	102 429	31 386
Kr85_Scint.ntuple.root	941 173	288 528
Pa234m_Scint.ntuple.root	58 992	17 817
Pb210_Scint.ntuple.root	1 505 582	627 622
Pb212_Scint.ntuple.root	10 282	3 120
Pb214_Scint.ntuple.root	60 517	18 247
Po210_Scint.ntuple.root	620 683	185 086
Po212_Scint.ntuple.root	14 756	4 165
Po214_Scint.ntuple.root	91 288	27 722
Po216_Scint.ntuple.root	14 222	4 037
Po218_Scint.ntuple.root	68 008	20 207
Ra224_Scint.ntuple.root	11 942	3 508
Ra226_Scint.ntuple.root	62 049	18 834
Ra228_Scint.ntuple.root	108	43
Rn220_Scint.ntuple.root	12 715	3 596
Rn222_Scint.ntuple.root	64 439	19 456
Th228_Scint.ntuple.root	11 397	3 360
Th230_Scint.ntuple.root	61 495	18 691
Th232_Scint.ntuple.root	11 052	3 321
Th234_Scint.ntuple.root	32 246	10 203
Tl208_Scint.ntuple.root	11 177	3 086
Tl210_Scint.ntuple.root	11 399	3 186
U234_Scint.ntuple.root	62 371	18 977
U238_Scint.ntuple.root	61 243	18 724
PEP_Scint.ntuple.root	31 859	9 919
Be7_Scint.ntuple.root	2 095 280	650 091
B8_Scint.ntuple.root	41 207	12 388
CNO_Scint.ntuple.root	88 340	24 697

**Table D.5:** Partial-fill RAT 5.3.1 Monte Carlo production files for events simulated in the water volume. All listed files were merged from all available runs/fill-levels for the isotope in question for the 5.3.1 production.

File name	Events in files	Events in fiducial volume
Ac228_Water.ntuple.root	98 051	669
Ar39_Water.ntuple.root	349	2
Bi210_Water.ntuple.root	478	7
Bi212_Water.ntuple.root	19 943	416
Bi214_Water.ntuple.root	165 913	1 967
C14_Water.ntuple.root	300	0
K40_Water.ntuple.root	16 239	142
Kr85_Water.ntuple.root	673	7
Pa234m_Water.ntuple.root	15 012	461
Pb210_Water.ntuple.root	1 345	16
Pb212_Water.ntuple.root	32 931	396
Pb214_Water.ntuple.root	57 717	368
Ra228_Water.ntuple.root	170	1
Th234_Water.ntuple.root	1 393	36
Tl208_Water.ntuple.root	625 462	7 585
Tl210_Water.ntuple.root	531 882	5 165
PEP_Water.ntuple.root	60	3
Be7_Water.ntuple.root	402	1
B8_Water.ntuple.root	18 012	37
CNO_Water.ntuple.root	43 954	11 508

**Table D.6:** Bi-Po coincidence cut selection on RAT 5.3.1 Monte Carlo production files for events occurring in the scintillator volume. The files were merged from all available runs for the isotope in question for the 5.3.1 production. The row denoted “all” is a count of all events in the file, so a sum of all  $^{21x}\text{Bi}$  and  $^{21x}\text{Po}$  decays. Hence, to get the number of coincidence decays contained in the file, this number needs to be divided by 2. These numbers were used to determine  $\epsilon(\Delta r)$  and  $\epsilon^{\text{Bi}}(r_{fidvol})$ .

Cut	Bi212Po212_Scint.ntuple.root	Bi214Po214_Scint.ntuple.root
all	19 763	153 633
$r_{fidvol}$	6 137	46 327
$n_{\text{hits}}^{\text{Po}}$	1 301	16 078
$\Delta t$	983	15 362
$r_{fidvol}$ on Bi	910	14 217
$\Delta r$	909	14 180
$n_{\text{hits}}^{\text{Bi}}$	858	13 044

**Table D.7:** Bi-Po coincidence cut selection on RAT 5.3.1 Monte Carlo production files for events occurring in the water volume. The files were merged from all available runs for the isotope in question for the 5.3.1 production. The row denoted “all” is a count of all events in the file, so a sum of all  $^{21x}\text{Bi}$  and  $^{21x}\text{Po}$  decays. Hence, to get the number of coincidence decays contained in the file, this number needs to be divided by 2. These numbers were used to determine  $\epsilon(\Delta r)$  and  $\epsilon^{\text{Bi}}(r_{fidvol})$ .

Cut	Bi212Po212_Water.ntuple.root	Bi214Po214_Water.ntuple.root
all	19 943	16 4094
$r_{fidvol}$	416	2 014
$n_{\text{hits}}^{\text{Po}}$	0	26
$\Delta t$	0	0
$r_{fidvol}$ on Bi	0	0
$\Delta r$	0	0
$n_{\text{hits}}^{\text{Bi}}$	0	0

**Table D.8:** Polonium cut efficiencies  $\epsilon^i$  ( $n_{\text{nhits}}$ ) for the Bi-Po coincidence measurements for events occurring in the partial-fill scintillator volume.

Isotope	$\epsilon^{\text{Po}214}$ ( $n_{\text{nhits}}$ )	$\epsilon^{\text{Po}212}$ ( $n_{\text{nhits}}$ )
$^{228}\text{Ac}$	$0.047 \pm 0.005$	$0.099 \pm 0.006$
$^{39}\text{Ar}$	$0.0067 \pm 0.0002$	0.0
$^{210}\text{Bi}$	$0.180 \pm 0.001$	$0.0319 \pm 0.0006$
$^{212}\text{Bi}$	$0.40 \pm 0.01$	$0.081 \pm 0.006$
$^{214}\text{Bi}$	$0.020 \pm 0.001$	$0.020 \pm 0.001$
$^{14}\text{C}$	0	0.0
$^{40}\text{K}$	$0.281 \pm 0.004$	$0.178 \pm 0.003$
$^{85}\text{Kr}$	$0.0685 \pm 0.0006$	0
$^{234m}\text{Pa}$	$0.214 \pm 0.005$	$0.151 \pm 0.004$
$^{210}\text{Pb}$	0	0
$^{212}\text{Pb}$	$0.029 \pm 0.009$	0
$^{214}\text{Pb}$	$0.370 \pm 0.006$	$0.046 \pm 0.002$
$^{210}\text{Po}$	$0.0046 \pm 0.0002$	0
$^{212}\text{Po}$	$0.028 \pm 0.008$	$0.97 \pm 0.03$
$^{214}\text{Po}$	$0.82 \pm 0.01$	$0.181 \pm 0.004$
$^{216}\text{Po}$	$0.84 \pm 0.02$	0
$^{218}\text{Po}$	$0.606 \pm 0.008$	0
$^{224}\text{Ra}$	$0.192 \pm 0.009$	0
$^{226}\text{Ra}$	$0.024 \pm 0.001$	$0.007 \pm 0.007$
$^{228}\text{Ra}$	0	0
$^{220}\text{Rn}$	$0.83 \pm 0.02$	$0.02 \pm 0.02$
$^{222}\text{Rn}$	$0.038 \pm 0.002$	$0.005 \pm 0.002$
$^{228}\text{Th}$	$0.097 \pm 0.006$	0
$^{230}\text{Th}$	0	0
$^{232}\text{Th}$	$0.013 \pm 0.001$	0
$^{234}\text{Th}$	0	0
$^{208}\text{Tl}$	$0.04 \pm 0.02$	$0.05 \pm 0.03$
$^{210}\text{Tl}$	$0.011 \pm 0.001$	$0.03 \pm 0.01$
$^{234}\text{U}$	$0.004 \pm 0.003$	0
$^{238}\text{U}$	0	0
PEP	$0.237 \pm 0.006$	$0.180 \pm 0.005$
$^7\text{Be}$	$0.202 \pm 0.001$	0
$^8\text{B}$	$0.069 \pm 0.008$	$0.059 \pm 0.007$
CNO	$0.104 \pm 0.008$	$0.012 \pm 0.003$

**Table D.9:** Bismuth cut efficiencies  $\epsilon^i$  ( $n_{\text{nhits}}$ ) for the Bi-Po coincidence measurements for events occurring partial-fill scintillator volume.

Isotope	$\epsilon^{\text{Bi}214}$ ( $n_{\text{nhits}}$ )	$\epsilon^{\text{Bi}212}$ ( $n_{\text{nhits}}$ )
$^{228}\text{Ac}$	$0.73 \pm 0.02$	$0.992 \pm 0.026$
$^{39}\text{Ar}$	0	$0.662 \pm 0.002$
$^{210}\text{Bi}$	$0.0006 \pm 0.0001$	$0.733 \pm 0.004$
$^{212}\text{Bi}$	$0.197 \pm 0.009$	$0.93 \pm 0.02$
$^{214}\text{Bi}$	$0.91 \pm 0.01$	$0.98 \pm 0.01$
$^{14}\text{C}$	0	$(1.9 \pm 0.2) \times 10^{-4}$
$^{40}\text{K}$	$0.149 \pm 0.003$	$0.923 \pm 0.009$
$^{85}\text{Kr}$	0	$0.717 \pm 0.002$
$^{234m}\text{Pa}$	$0.270 \pm 0.005$	$0.92 \pm 0.01$
$^{210}\text{Pb}$	0	0
$^{212}\text{Pb}$	0	$0.95 \pm 0.03$
$^{214}\text{Pb}$	0	$0.97 \pm 0.01$
$^{210}\text{Po}$	0	$0.977 \pm 0.004$
$^{212}\text{Po}$	$0.02 \pm 0.01$	$0.99 \pm 0.03$
$^{214}\text{Po}$	$0.004 \pm 0.002$	$0.99 \pm 0.01$
$^{216}\text{Po}$	0	$0.84 \pm 0.02$
$^{218}\text{Po}$	0	$0.92 \pm 0.01$
$^{224}\text{Ra}$	0	$0.95 \pm 0.02$
$^{226}\text{Ra}$	0	$0.99 \pm 0.01$
$^{228}\text{Ra}$	0	0
$^{220}\text{Rn}$	0	$0.89 \pm 0.02$
$^{222}\text{Rn}$	0	$0.97 \pm 0.01$
$^{228}\text{Th}$	0	$0.97 \pm 0.03$
$^{230}\text{Th}$	0	$0.99 \pm 0.01$
$^{232}\text{Th}$	0	$0.998 \pm 0.023$
$^{234}\text{Th}$	0	$0.013 \pm 0.002$
$^{208}\text{Tl}$	$0.93 \pm 0.02$	$0.93 \pm 0.02$
$^{210}\text{Tl}$	$0.93 \pm 0.02$	$0.94 \pm 0.02$
$^{234}\text{U}$	0	$0.99 \pm 0.01$
$^{238}\text{U}$	0	$0.997 \pm 0.012$
PEP	$0.082 \pm 0.003$	$0.86 \pm 0.01$
$^7\text{Be}$	0	$0.736 \pm 0.003$
$^8\text{B}$	$0.68 \pm 0.03$	$0.91 \pm 0.03$
CNO	$0.02 \pm 0.02$	$0.65 \pm 0.02$

**Table D.10:** Fiducial volume cut efficiencies  $\epsilon^i$  ( $r_{\text{fidvol}}$ ) for the partial-fill water volume events.

Isotope	$\epsilon$ ( $r_{\text{fidvol}}$ )
$^{228}\text{Ac}$	$(8.50 \pm 0.03) \times 10^{-4}$
$^{210}\text{Bi}$	$(2.6 \pm 0.2) \times 10^{-6}$
$^{212}\text{Bi}$	$(1.20 \pm 0.01) \times 10^{-4}$
$^{214}\text{Bi}$	$(1.142 \pm 0.004) \times 10^{-3}$
$^{40}\text{K}$	$(1.52 \pm 0.01) \times 10^{-4}$
$^{234m}\text{Pa}$	$(5.70 \pm 0.09) \times 10^{-5}$
$^{210}\text{Pb}$	$(1.50 \pm 0.04) \times 10^{-5}$
$^{212}\text{Pb}$	$(2.46 \pm 0.02) \times 10^{-4}$
$^{214}\text{Pb}$	$(4.55 \pm 0.02) \times 10^{-4}$
$^{228}\text{Ra}$	$(3.6 \pm 0.7) \times 10^{-7}$
$^{234}\text{Th}$	$(9.5 \pm 0.3) \times 10^{-6}$
$^{208}\text{Tl}$	$(2.262 \pm 0.006) \times 10^{-3}$
$^{210}\text{Tl}$	$(1.905 \pm 0.005) \times 10^{-3}$
PEP	$(0.8 \pm 0.3) \times 10^{-5}$
$^7\text{Be}$	$(1.8 \pm 0.4) \times 10^{-6}$
$^8\text{B}$	$(1.22 \pm 0.09) \times 10^{-3}$
CNO	$0.0132 \pm 0.0001$

**Table D.11:** Polonium cut efficiencies  $\epsilon^i$  ( $n_{\text{nhits}}$ ) for the Bi-Po coincidence measurements for events occurring in the partial-fill water volume.

Isotope	$\epsilon^{\text{Po}214}$ ( $n_{\text{nhits}}$ )	$\epsilon^{\text{Po}212}$ ( $n_{\text{nhits}}$ )
$^{228}\text{Ac}$	$0.142 \pm 0.002$	$0.127 \pm 0.002$
$^{210}\text{Bi}$	$0.12 \pm 0.03$	0
$^{212}\text{Bi}$	$0.109 \pm 0.004$	$0.024 \pm 0.002$
$^{214}\text{Bi}$	$0.090 \pm 0.001$	$0.0439 \pm 0.0008$
$^{40}\text{K}$	$0.081 \pm 0.007$	$0.065 \pm 0.004$
$^{234m}\text{Pa}$	$0.021 \pm 0.002$	$0.018 \pm 0.002$
$^{210}\text{Pb}$	0	0
$^{212}\text{Pb}$	0	0
$^{214}\text{Pb}$	$0.0124 \pm 0.0007$	$0.0019 \pm 0.0003$
$^{228}\text{Ra}$	0	0
$^{234}\text{Th}$	0	0
$^{208}\text{Tl}$	$0.0337 \pm 0.0004$	$0.0127 \pm 0.0002$
$^{210}\text{Tl}$	$0.0478 \pm 0.0005$	$0.0264 \pm 0.0003$
PEP	$0.3 \pm 0.2$	0
$^7\text{Be}$	0	0
$^8\text{B}$	0	0
CNO	$0.136 \pm 0.007$	$0.010 \pm 0.002$

**Table D.12:** Bismuth cut efficiencies  $\epsilon^i (n_{\text{nhits}})$  for the Bi-Po coincidence measurements for events occurring in the partial-fill water volume.

Isotope	$\epsilon^{\text{Bi}214} (n_{\text{nhits}})$	$\epsilon^{\text{Bi}212} (n_{\text{nhits}})$
$^{228}\text{Ac}$	$0.055 \pm 0.001$	$0.618 \pm 0.005$
$^{210}\text{Bi}$	0	$0.45 \pm 0.07$
$^{212}\text{Bi}$	$0.055 \pm 0.003$	$0.324 \pm 0.007$
$^{214}\text{Bi}$	$0.164 \pm 0.002$	$0.475 \pm 0.003$
$^{40}\text{K}$	$0.316 \pm 0.009$	$0.67 \pm 0.01$
$^{234m}\text{Pa}$	$0.0059 \pm 0.0009$	$0.080 \pm 0.003$
$^{210}\text{Pb}$	0	0
$^{212}\text{Pb}$	0	$0.181 \pm 0.004$
$^{214}\text{Pb}$	0	$0.409 \pm 0.005$
$^{228}\text{Ra}$	0	0
$^{234}\text{Th}$	0	0
$^{208}\text{Tl}$	$0.1035 \pm 0.0006$	$0.222 \pm 0.001$
$^{210}\text{Tl}$	$0.0661 \pm 0.0006$	$0.230 \pm 0.001$
PEP	0	$0.5 \pm 0.3$
$^7\text{Be}$	0	$0.4 \pm 0.2$
$^8\text{B}$	$0.003 \pm 0.002$	$0.030 \pm 0.006$
CNO	0	$0.66 \pm 0.02$

# Bibliography

- [1] W. Pauli. Offener Brief an die Gruppe der Radioaktiven bei der Gauvereins-Tagung zu Tübingen (German) [Open letter to the group of radioactive people at the Gauverein-meeting in Tübingen]. [http://symmetrymagazine.org/sites/default/files/legacy/pdfs/200703/logbook\\_letter.pdf](http://symmetrymagazine.org/sites/default/files/legacy/pdfs/200703/logbook_letter.pdf), 1930. Accessed: 14/08/2016.
- [2] E. Fermi. Versuch einer Theorie der  $\beta$ -Strahlen (German) [Attempt of a Theory of  $\beta$ -Radiation]. *Zeitschrift für Physik*, 88:161–177, 1934.
- [3] J. Chadwick. Possible Existence of a Neutron. *Nature*, 129:312, 1932.
- [4] D. Decamp et al. [ALEPH Collaboration]. A precise determination of the number of families with light neutrinos and of the Z boson partial widths. *Phys. Lett. B*, 235:399–411, 1990.
- [5] M. Goldhaber et al. Helicity of Neutrinos. *Phys. Rev.*, 109:1015–1017, 1958.
- [6] C. L. Cowan Jr. et al. Detection of the Free Neutrino. *Phys. Rev.*, 92:830–831, 1953.
- [7] C. L. Cowan Jr. et al. Detection of the Free Neutrino: a Confirmation. *Science*, 124:103–104, 1956.
- [8] C. M. G. Latted et al. Observations on the Tracks of Slow Mesons in Photographic Emulsions. *Nature*, 160:486–492, 1947.
- [9] G. Danby et al. Observations of High-Energy Neutrino Reactions and the Existence of Two Kinds of Neutrinos. *Phys. Rev. Lett.*, 9:36, 1962.

- [10] M. L. Perl et al. Evidence for Anomalous Lepton Production in  $e^+ - e^-$  Annihilation. *Phys. Rev. Lett.*, 35:1489, 1975.
- [11] K. Kodama et al. [DONUT Collaboration]. Observation of tau neutrino interactions. *Phys. Lett. B*, 504:218–224, 2001.
- [12] B. Pontecorvo. Mesonium and anti-mesonium. *Soviet. Phys. JETP*, 6:429, 1958.
- [13] Z. Maki et al. Remarks on the Unified Model of Elementary Particles. *Progress of Theoretical Physics*, 28:870–880, 1962.
- [14] Z. Xing and Y. Zhou. Majorana CP-violating phases in neutrino-antineutrino oscillations and other lepton-number violating processes. *arXiv:1305.5718*, 2013.
- [15] K. Zuber. *Neutrino Physics*. CRC Press, 2nd edition, 2012.
- [16] A. B. Balantekin et al. Neutrino oscillations. *Progress in Particle and Nuclear Physics*, 71:150–161, 2013.
- [17] S. P. Mikheev et al. Resonance enhancement of oscillations in matter and solar neutrino spectroscopy. *Soviet Journal of Nuclear Physics*, 42:913–917, 1985.
- [18] L. Wolfenstein. Neutrino oscillations in matter. *Phys. Rev. D*, 17:2369, 1978.
- [19] W. C. Haxton et al. Solar neutrinos: status and prospects. *Ann. Rev. Astron. Astrophys.*, 51:21, 2013.
- [20] V. Castellani et al. Solar neutrinos: beyond standard solar models. *Phys. Rep.*, 281(5):309–398, 1997.
- [21] V. Lozza. Scintillator phase of the SNO+ Experiment. *Journal of Physics: Conference Series*, 375(4), 2012.
- [22] C. Galbiati et al. Cosmogenic  $^{11}\text{C}$  production and sensitivity of organic scintillator detectors to pep and CNO neutrinos. *Phys. Rev. C*, 71:055805, 2005.
- [23] B. T. Cleveland et al. Measurement of the Solar Electron Neutrino Flux with the Homestake Chlorine Detector. *Astrophys. J.*, 496:505–526, 1998.

- [24] Y. Fukuda et al. Solar Neutrino Data Covering Solar Cycle 22. *Phys. Rev. Lett.*, 77:1683, 1996.
- [25] M. B. Smy et al.[Super Kamiokande Collaboration]. Precise measurement of the solar neutrino day-night and seasonal variation in Super-Kamiokande-I. *Phys. Rev. D*, 69:011104, 2004.
- [26] B. Aharmim et al. [SNO Collaboration]. Electron energy spectra, fluxes and day-night asymmetries of  ${}^8\text{B}$  solar neutrinos from measurements with NaCl dissolved in the heavy-water detector at the Sudbury Neutrino Observatory. *Phys. Rev. C*, 72:055502, 2005.
- [27] Y. Fukuda et al.[Kamiokande Collaboration]. Atmospheric  $\nu_\mu/\nu - e$  ratio in the multi-GeV energy range. *Phys. Lett. B*, 335:237–245, 1994.
- [28] Y. Fukuda et al.[Super Kamiokande Collaboration]. Evidence for Oscillation of Atmospheric Neutrinos. *Phys. Rev. Lett.*, 81:1562, 1998.
- [29] M. Apollonio et al.[CHOOZ Collaboration]. Limits on Neutrino Oscillations from the CHOOZ Experiment. *Phys. Lett. B*, 466:415, 1999.
- [30] T. Araki et al.[KamLAND Collaboration]. Measurement of Neutrino Oscillation with KamLAND: Evidence of Spectral Distortion. *Phys. Rev. Lett.*, 94:081801, 2005.
- [31] E. Aliu et al. [K2K Collaboration]. Evidence for Muon Neutrino Oscillation in an Accelerator-Based Experiment. *Phys. Rev. Lett.*, 94:081802, 2005.
- [32] D. G. Michael et al. [MINOS Collaboration]. Observation of Muon Neutrino Disappearance with the MINOS Detectors in the NuMI Neutrino Beam. *Phys. Rev. Lett.*, 97:191801, 2006.
- [33] A. Aguilar et al. [LSND Collaboration]. Evidence for neutrino oscillations from the observation of  $\bar{\nu}_e$  appearance in a  $\bar{\nu}_\mu$  beam. *Phys. Rev. D*, 64:112007, 2001.
- [34] S. Bilenky et al. Neutrinoless double-beta decay. A brief review. *Mod. Phys. Lett. A*, 27, 2012.

- [35] H. Tanaka. Status, recent results and plans for T2K. Neutrino 2016 – XXVII International Conference on Neutrino Physics and Astrophysics, July 2016.
- [36] S. Moriyama. New atmospheric and solar results from Super-Kamiokande. Neutrino 2016 – XXVII International Conference on Neutrino Physics and Astrophysics, July 2016.
- [37] A. Cabrera. Double Chooz first multi-detector results. Neutrino 2016 – XXVII International Conference on Neutrino Physics and Astrophysics, July 2016.
- [38] K. Abe et al. [The T2K Collaboration]. Neutrino Oscillation Physics Potential of the T2K Experiment. *Prog. Theor. Exp. Phys.*, 043C01, 2015.
- [39] Y. Abe et al. [Double Chooz Collaboration]. Indication for the disappearance of reactor  $\bar{\nu}_e$  in the Double Chooz experiment. *PRL*, 108:131801, 2012.
- [40] P. Vahle. New results from NOvA. Neutrino 2016 – XXVII International Conference on Neutrino Physics and Astrophysics, July 2016.
- [41] U. F. Katz. The ORCA Option for KM3NeT. *PoS(Neutel 2013)057*, arXiv:1402.1022, 2014.
- [42] F. Capozzi et al. PINGU and the neutrino mass hierarchy: Statistical and systematic aspects. *Phys. Rev. D*, 91:073011, 2015.
- [43] M. M. Devi et al. Enhancing sensitivity to neutrino parameters at INO combining muon and hadron information. *JHEP*, 1410:189, 2014.
- [44] [JUNO collaboration]. Neutrino Physics with JUNO. *J. Phys. G*, 43(3):030401, 2016.
- [45] V. N. Aseev et al. An upper limit on electron antineutrino mass from Troitsk experiment. *Phys. Rev. D*, 84:112003, 2011.
- [46] Ch. Kraus et al. Final Results from phase II of the Mainz Neutrino Mass Search in Tritium  $\beta$  Decay. *Eur. Phys. J.*, C40:447–468, 2005.

- [47] N. Steinbrink et al. Neutrino mass sensitivity by MAC-E-Filter based time-of-flight spectroscopy with the example of KATRIN. *New J. Phys.*, 15:113020, 2013.
- [48] M. C. Gonzalez-Garcia et al. Phenomenology with Massive Neutrinos. *Phys. Rept.*, 460:1–129, 2008.
- [49] P. A. R. Ade et al. [Planck Collaboration]. Planck 2015 results. XIII. Cosmological parameters. *arXiv:1502.01589*, 2015.
- [50] M. Goeppert-Mayer. Double Beta-Disintegration. *Phys. Rev.*, 48:512–516, 1935.
- [51] T. Tomoda. Double beta decay. *Reports on Progress in Physics*, 54, 1991.
- [52] B. Povh et al. *Teilchen und Kerne: Eine Einführung in die physikalischen Konzepte (German) [Particles and Nuclei: An Introduction to the Physical Concepts]*. Springer Verlag Berlin Heidelberg, 8th edition, 2009.
- [53] E. Majorana. Symmetric theory of the electron and the positron. *Il Nuovo Cimento*, 14:171–184, 1937.
- [54] W. H. Furry. On Transition Probabilities in Double Beta-Disintengration. *Phys. Rev.*, 56:1184–1193, 1939.
- [55] P. Bhupal et al. Constraining Neutrino Mass from Neutrinoless Double Beta Decay. *Phys. Rev. D*, 88:091301, 2013.
- [56] S. M. Bilenky. Neutrinoless double-beta decay. *Phys. Part. Nuclei*, 41:690, 2010.
- [57] A. Gando et al. [KamLAND-Zen Collaboration]. Search for Majorana Neutrinos near the Inverted Mass Hierarchy Region with KamLAND-Zen. *arXiv:1605.02889*, 2016.
- [58] J. Shirai. Results and Future plans for the KamLAND-Zen. Neutrino 2016 – XXVII International Conference on Neutrino Physics and Astrophysics, July 2016.

- [59] M. Agostini et al. [GERDA collaboration]. Search of Neutrinoless Double Beta Decay with the GERDA Experiment. *Nucl. Part. Physics Procs.*, 273-275:1876, 2016.
- [60] M. Agostini. First results from GERDA Phase II. Neutrino 2016 – XXVII International Conference on Neutrino Physics and Astrophysics, July 2016.
- [61] R. Arnold et al. Limits on different Majoron decay modes of  $^{100}\text{Mo}$  and  $^{82}\text{Se}$  for neutrinoless double beta decays in the NEMO-3 experiment. *Nucl. Phys. A*, 765:483–494, 2006.
- [62] J. Argyriades et al. Measurement of the two neutrino double beta decay half-life of Zr-96 with the NEMO-3 detector. *NPA*, 847:168, 2010.
- [63] R. Arnold et al. Probing New Physics Models of Neutrinoless Double Beta Decay with SuperNEMO. *Eur. Phys. J. C*, 70:927–943, 2010.
- [64] C. Alduino et al. [CUORE Collaboration]. CUORE-0 detector: design, construction and operation. *Journal of Instrumentation*, 11:P07009, 2016.
- [65] L. Canonica. Status and prospects for CUORE. Neutrino 2016 – XXVII International Conference on Neutrino Physics and Astrophysics, July 2016.
- [66] G. Lefevre. From SNO to SNO+, upgrading a neutrino experiment. *Nucl. Instrum. Methods A*, 718:506–508, 2013.
- [67] B. vKrosigk. Status of the SNO+ experiment, 2012.
- [68] Particle Data Group. Review of Particle Physics. *Phys. Rev. D*, 86:010001, 2012.
- [69] S. J. M. Peeters. The SNO+ experiment: status and overview. *Nucl. Phys. B (Proc. Suppl.)*, 237-238:98–100, 2013.
- [70] S. Andringa et al. Current Status and Future Prospects of the SNO+ Experiment. *Advances in High Energy Physics*, 2016:6194250, 2016.
- [71] The SNO Collaboration. The Sudbury Neutrino Observatory. *Nucl. Instrum. Methods A*, 449:172–207, 2000.

- [72] M. Askins et al. *Background Information for the Tellurium Loading Down Select*. Internal SNO+ document: SNO+-doc-3505-v1, 2015.
- [73] R. Ford et al. SNO+ scintillator purification and assay. *AIP Conference Proceedings*, 1338:183–194, 2011.
- [74] R. Ford [SNO+ Collaboration]. A scintillator purification plant and fluid handling system for SNO+. *AIP Conference Proceedings*, 1672(080003), 2015.
- [75] I. Coulter. *Proposed Nucleon Decay Plots*. Internal SNO+ document: SNO+-doc-2595-v6, 2015.
- [76] C. Arpesella et al. [Borexino Collaboration]. Direct measurement of the  $^7\text{Be}$  solar neutrino flux with 192 days of Borexino data. *Physical Review Letters*, 90(2):091302, 2008.
- [77] G. Alimonti et al. [Borexino Collaboration]. The liquid handling systems for the solar neutrino detector. *Nucl. Instrum. Methods A*, 609(1):58–78, 2009.
- [78] R. Bonventure. *Solar sensitivity studies*. Internal SNO+ document: SNO+-doc-3690-v1, 2016.
- [79] M. Hodak. *High Level Schedule Overview*. Internal SNO+ document: SNO+-doc-3896-v2, 2016.
- [80] E. Leming. *Neutrinoless double beta decay at SNO+*. Internal SNO+ document: SNO+-doc-3532-v3, 2016.
- [81] T. Kaptanoglu. *Te Diol 0.5% Loading Approved BB Sensitivity Plots and Documentation*. Internal SNO+ document: SNO+-doc-3689-v1, 2016.
- [82] A. Mastbaum. *Electronics Overview and Status*. Internal SNO+ document: SNO+-doc-1339-v1, 2012.
- [83] P. Harvey. *SNO+ Event Builder*. Internal SNO+ document: SNO+-doc-1348-v1, 2012.
- [84] S. Seibert et al. The RAT user’s Manual. [http://snopl.us/docs/rat/user\\_manual/html/UserGuide.html](http://snopl.us/docs/rat/user_manual/html/UserGuide.html). Accessed: 12/07/2016.

- [85] G. Orebi Gann. *Dealing With Time in RAT - From Universal Time to PMT hit times*. Internal SNO+ document: SNO+-doc-481-v2, 2010.
- [86] S. Peeters. *Calibration Overview*. Internal SNO+ document: SNO+-doc-1614-v1, 2012.
- [87] G. D. Orebi Gann et al. *Calibration & Analysis Plan*. Internal SNO+ document: SNO+-doc-1698-v6, 2013.
- [88] K. Singh et al. *Camera System for SNO+*. Internal SNO+ document: SNO+-doc-1680-v3, 2013.
- [89] J. R. Sinclair. *Scintillator Phase Laserball Hardware Status*. Internal SNO+ document: SNO+-doc-2901-v1, 2015.
- [90] S. J. Peeters. *Electronics specification of the ELLIE system*. Internal SNO+ document: SNO+-doc-544-v2, 2010.
- [91] J. Maneira. *SNO+ ELLIE Fibers: Summary of UG installation work plan*. Internal SNO+ document: SNO+-doc-1865-v1, 2012.
- [92] M. Chen et al. *Expected radioactive backgrounds in SNO+*. Internal SNO+ document: SNO+-doc-507-v30, 2015.
- [93] F. Alessandria et al. CUORE crystal validation runs: Results on radioactive contamination and extrapolation to CUORE background. *Astroparticle Physics*, 35(12):839–949, 2012.
- [94] G. Alimonti et al. [Borexino Collaboration]. Measurement of the  $^{14}\text{C}$  abundance in a low-background liquid scintillator. *Physics Letters B*, 422(1-4):349–358, 1998.
- [95] V. Lozza. *Note on newNd cosmogenic induced background*. Internal SNO+ document: SNO+-doc-1588-v16, 2013.
- [96] M. Yeh. *Purification of Telluric Acid for SNO+ Neutrinoless Double-beta Decay Search*. Internal SNO+ document: SNO+-doc-2932-v1, 2015.

- [97] C. Dock. *Instrumental Background Elimination and Alpha Beta Discrimination UPdate*. Internal SNO+ document: SNO+-doc-2643-v1, 2014.
- [98] J. Walker. *Instrumental Backgrounds: From SNO to SNO+*. Internal SNO+ document: SNO+-doc-3098-v3, 2015.
- [99] J. Wilson. *RAT*. Internal SNO+ document: SNO+-doc-207-v1, 2008.
- [100] K. Majumdar. *Functional-Form Energy Reconstruction*. Internal SNO+ document: SNO+-doc-2782-v2, 2016.
- [101] I. Coulter. *Modelling and reconstruction of events in SNO+ related to future searches for lepton and baryon number violation*. Ph.D. Thesis, University of Oxford, 2013.
- [102] H. Wan Chan Tseung et al. Measurement of the dependence of the light yields of linear alkylbenzene-based and ej-301 scintillators on electron energy. *arXiv:1105.2100*, v2, 2011.
- [103] E. Arushanova et al. *A Summary document about the use of Perylene as secondary wavelength shifter in Te-loaded phase*. Internal SNO+ document: SNO+-doc-3468-v2, 2015.
- [104] K. Majumdar.  *$^{208}Tl$  Background Rejection using  $\alpha$ -Tagging*. Internal SNO+ document: SNO+-doc-1456-v3, 2013.
- [105] K. Singh.  *$^{85}Kr$  Tagging*. Internal SNO+ document: SNO+-doc-1745-v1, 2013.
- [106] J. Wilson. *Mistagging and Efficiency studies for the  $^{214}Bi$  and  $^{212}Bi$  tags*. Internal SNO+ document: SNO+-doc-2836-v2, 2014.
- [107] J. R. Wilson. *A Measurement of the  $^8B$  Solar Neutrino Energy Spectrum at the Sudbury Neutrino Observatory*. Ph.D. Thesis, University of Oxford, 2004.
- [108] P. G. Jones. *Background Rejection for the Neutrinoless Double Beta Decay Experiment SNO+*. Ph.D. Thesis, University of Oxford, 2011.
- [109] X. Zhou et al. Rayleigh scattering of linear alkylbenzene in large liquid scintillator detectors. *Rev. Sci. Instrum.*, 86:073310, 2015.

- [110] G. Mie. Beiträge zur Optik trüber Medien, speziell kolloidaler Metallösungen (German) [Contributions to the Optics of Turbid Media, particularly of Colloidal Metal Solutions]. *Annalen der Physik*, 330:377–445, 1908.
- [111] A. Morel. Optical properties of pure water and pure sea water. *Optical aspects of oceanography*, 1:1–24, 1974.
- [112] K. Majumdar. *On the Measurement of Optical Scattering and Studies of Background Rejection in the SNO+ Detector*. Ph.D. Thesis, University of Oxford, 2015.
- [113] L. Cavalli et al. *The SMELLIE Hardware Manual*. Internal SNO+ document: SNO+-doc-3511-v2, 2016.
- [114] S. Biller. SNO+ with Tellurium. *Physics Procedia*, 61:205–210, 2015.
- [115] S. D. Biller et al. Measurements of photomultiplier single photon counting efficiency for the Sudbury Neutrino Observatory. *Nucl. Instrum. Methods Phys. Res. A*, 432(2-3):364–373, 1999.
- [116] K. Clark. *ELLIE Fibre Radioactivity*. Internal SNO+ document: SNO+-doc-1223-v1, 2011.
- [117] K. Clark. *SMELLIE Installation Note*. Internal SNO+ document: SNO+-doc-931-v1, 2011.
- [118] J. R. Wilson. *SMELLIE - A Scattering Module in the Embedded LED Light Injection Entity*. Internal SNO+ document: SNO+-doc-463-v1, 2010.
- [119] S. Andriga. *ELLIE fibers positions and directions*. Internal SNO+ document: SNO+-doc-1730-v1, 2013.
- [120] K. Majumdar. *SMELLIE Sanity Checks*. Internal SNO+ document: SNO+-doc-2527-v1, 2014.
- [121] N. Gagnon et al. SNOPLUS Cavity Shift report from 21/05/2014. <https://www.snolab.ca/snoplus/TWiki/bin/view/Cavity/CavityDiary2014x05x21>. Accessed: 09/10/2014.

- [122] S. Langrock. *Position Verification of SMELLIE in RAT*. Internal SNO+ document: SNO+-doc-2000-v3, 2013.
- [123] S. Langrock. *SMELLIE dark runs March 2014*. Internal SNO+ document: SNO+-doc-2483-v1, 2014.
- [124] K. Clark et al. SMELLIE Fibre Beam Profiles and Opening Angles. 2016.
- [125] ROOT. Class index. <https://root.cern.ch/root/html/ClassIndex.html>. Accessed: 21/04/2016.
- [126] D. Halliday et al. *Physik (German) [Fundamentals of Physics]*, page 985/993. Wiley-VCH GmbH & Co. KGaA, extended 6th edition, 2005.
- [127] W. S. Rodney and R. J. Spindler. Index of Refraction of Fused-Quartz Glass for Ultraviolet, Visible, and Infrared Wavelengths. *J. Research Natl. Bur. Standards*, 53:185, 1954. RP2531.
- [128] M. Chen et al. *Optical Properties in RAT*. Internal SNO+ document: SNO+-doc-1664-v1, 2012.
- [129] J. Cameron. *The Photomultiplier Tube Calibration of the Sudbury Neutrino Observatory*. Ph.D. Thesis, University of Oxford, 2001.
- [130] J. Waterfield. *The PMT Calibration System of SNO+*. Internal SNO+ document: SNO+-doc-3102-v1, 2015.
- [131] J. R. Wilson. *Bias Tests of Scintillator Scattering Measurement*. Internal SNO+ document: SNO+-doc-3440-v1, 2015.
- [132] L. Segui. *Mistagging external events in alphas energy window, updated*. Internal SNO+ document: SNO+-doc-2817-v1, 2014.
- [133] J. Wilson. *A first look at the Full BiPo rejection (in and out of window together)*. Internal SNO+ document: SNO+-doc-3756-v1, 2016.
- [134] K. Boudjemline et al. The calibration of the Sudbury Neutrino Observatory using uniformly distributed radioactive sources. *Nucl. Instrum. Meth. A*, 620:171–181, 2010.

- [135] I. Coulter et al. *Summary of Month's Mixed Data Set Analysis*. Internal SNO+ document: SNO+-doc-3504-v1, 2015.
- [136] S. Langrock et al. *Internal Background studies for the pure liquid scintillator and partial fill phase*. Internal SNO+ document: SNO+-doc-3866-v2, 2016.
- [137] J. Huwaldt. PlotDigitizer, Version 2.6.1. <http://plotdigitizer.sourceforge.net>. Accessed: 03/11/2012.
- [138] M. Paterno. *Calculating Efficiencies and Their Uncertainties*. No. FERMILAB-TM-2286-CD. United States. Department of Energy, 2004.